



**ScuDo**  
Scuola di Dottorato - Doctoral School  
WHAT YOU ARE, TAKES YOU FAR



Doctoral Dissertation  
Doctoral Program in Materials Science and Technologies (31<sup>st</sup> Cycle)

# **Innovative ozone sensors for environmental monitoring working at low temperature**

**Daniele Ziegler**

\* \* \* \* \*

## **Supervisors**

Prof. Paola Palmero, Supervisor  
Prof. Jean-Marc Tulliani, Co-Supervisor

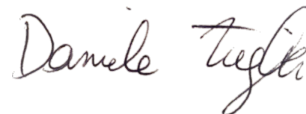
## **Doctoral Examination Committee:**

Prof. Carlo Cantalini, Università degli studi dell'Aquila  
Prof. Jean-Paul Viricelle, École des Mines de Saint-Étienne  
Prof.ssa Ornella Abollino, Università degli studi di Torino  
Prof.ssa Sara Biamino, Politecnico di Torino  
Prof.ssa Sonia Fiorilli, Politecnico di Torino

Politecnico di Torino

This thesis is licensed under a Creative Commons License, Attribution - Noncommercial - NoDerivative Works 4.0 International: see [www.creativecommons.org](http://www.creativecommons.org). The text may be reproduced for non-commercial purposes, provided that credit is given to the original author.

I hereby declare that, the contents and organisation of this dissertation constitute my own original work and does not compromise in any way the rights of third parties, including those relating to the security of personal data.



.....  
Daniele Ziegler  
Turin,09/07/2019



# Summary

Ozone ( $O_3$ ), a gas that is well known for its oxidant properties, has drastically incremented its amount in the troposphere in the last decenniums. Considering that high  $O_3$  concentration is well-known to be hazardous for the human health (especially for the respiratory system), the development of valid strategies to detect it appears an urgent need.

The analytical techniques available in the market for measuring  $O_3$  are expensive and they require expert technicians (e.g. spectroscopic UV adsorption). For this reason, cheap alternatives have been investigated for online measurement of  $O_3$ . Among them, chemical gas sensors exhibit a great potential because they are cost-effective, easy to use, stable in time, reliable and integrable in portable electronics.

The features of a gas sensor could save human health and the environment respectively from diseases and disasters, controlling continuously the air pollution. For this reason, human generation is intimately related to the potential of gas sensors.

The aim of this PhD thesis is the investigation of innovative materials to produce gas sensors able to detect  $O_3$  and the main interfering gases: humidity, ammonia and nitrogen dioxide. To reach this goal, chemical sensors were realized by techniques like screen printing and dip coating. The sensitive materials were successfully obtained by different synthesis methods (i.e. hydrothermal synthesis and auto-combustion sol-gel route) and fully characterized. In this way, an understanding of the relations between the structural characteristics of the materials and the gas sensing phenomena was accomplished. The proposed sensitive materials can find application in an array of sensors able to distinguish the presence of  $O_3$  in a real environment.

This PhD thesis is composed by 7 parts that here are explained more in details

In the **chapter 1** the issues related to O<sub>3</sub> in troposphere are described in detail, including the effect on the human health and the recommended threshold limit values.

**Chapter 2** discusses the gas sensors principles that are depicted with a special focus on Semiconducting Metal Oxide (SMOx) and carbon-based sensors. Advantages and disadvantages of both types of gas sensing systems are elucidated, and a preliminary presentation of the material selected in this work is given.

**Chapter 3** reports the technologies for chemical sensor preparation and the principles of the instruments used for materials characterization.

In **chapter 4** results of O<sub>3</sub> tests achieved firstly with BaFe<sub>12</sub>O<sub>19</sub> thick films, synthesized by auto-combustion sol gel method and innovative spray-coated detectors based on functionalized single-walled CNTs by covalent modification with octadecylamine (ODA).

In **chapter 5**, the best results among O<sub>3</sub> sensors were presented by using n-type indium oxide (In<sub>2</sub>O<sub>3</sub>): a commercial In<sub>2</sub>O<sub>3</sub> powder was doped with different contents of tungsten trioxide (WO<sub>3</sub>) by impregnation method to enhance its sensing capability. With the aim to diminish the size of crystallites and agglomerates and to enhance the specific surface area of the nano-powder, In<sub>2</sub>O<sub>3</sub> and WO<sub>3</sub> doped-In<sub>2</sub>O<sub>3</sub> were synthesized by hydrothermal synthesis and used as O<sub>3</sub> sensitive materials working close to room temperature. Moreover, DRIFT (Diffuse Reflectance Infrared Fourier Transform spectroscopy) analysis were performed on In<sub>2</sub>O<sub>3</sub> and WO<sub>3</sub> doped-In<sub>2</sub>O<sub>3</sub> for understanding which species are generated during the interaction of the metal oxide in oxidant atmospheres like NO<sub>2</sub> and O<sub>3</sub>.

The main drawback of SMOx sensors is the modest selectivity. For this reason, in **chapter 6** novel solutions for the monitoring of humidity are described. For humidity measurements, three different biochars were used for the first time: SWP-Softwood pellets, OSR-Oil Seed Rape and WCG-waste coffee ground.

Finally, the final **chapter 7** displays the results of sensors realized for N-based interferences: ammonia and nitrogen dioxide. For ammonia detection, a spinel type Co<sub>3</sub>O<sub>4</sub> realized by auto-combustion sol-gel route was utilized, whereas different ZnO-based screen-printed sensors were applied for the detection of NO<sub>2</sub> at relatively low temperatures.

This PhD work has been developed through relationships with various research groups: Carbon group directed by prof. Tagliaferro with the supervision of dr. Pravin Jagadale, the groups of prof. Specchia and prof. Cauda in Politecnico di Torino. Moreover, international collaborations were fulfilled: the Weimar group in the University of Tübingen with the supervision of Dr. Barsan, E. Bekyarova from Carbon Solutions company and K. Naishadam from Georgia Tech University.

# Acknowledgments

At the end of this extraordinary path, my deep thanking to all the persons that have helped me to reach this important goal.

I would like to extend my sincere gratitude to my supervisor **Prof.ssa Paola Palmero** and to my co-supervisor **Prof. Jean-Marc Tulliani**. In these four years of Research Activity in the LINCE group, they have provided to me scientific advices and guideliness in the organization of research activities, as well as in the preparation of conferences and in writing scientific articles. Many thanks Paola and Jean Marc, I simply cannot express the gratitude in words for your support.

I would like also to thank Prof.ssa Mariangela Lombardi and Prof.ssa Laura Montanaro for their kindness in every precious moment.

I would like to thank all the Carbon Group with prof. Alberto Tagliaferro, **Pravin Jagadale**, Mauro Giorcelli and Massimo Rovere for their profitable collaboration about carbon-based materials in gas sensing.

I am grateful to Prof. Stefania Specchia and to Giuliana Ercolino for providing us the  $\text{Co}_3\text{O}_4$  powder that was used as ammonia sensitive and selective material.

I would like to thank prof. Valentina Cauda and Diego Pugliese that gave us ZnO flower-like powder as nitrogen dioxide great sensors.

I thank also Elena Bekyarova and Krishna Naishadham for the profitable collaboration and a wider knowledge about carbon nanotubes materials.

I am grateful also to the Weimar Group in the University of Tübingen for the wonderful experience where I learnt quickly many competences in gas sensor technology and particularly to **Dr. Nicolae Barsan**, Prof. Udo Weimar, Dr. Alexandru Oprea, **Dr. Anna Staerz** for their continuous help and patience. I really have learned a lot from all of them.

I was very lucky to meet a great researcher from KIT of Japan: Keishi Yamaguchi. I am sure we will see each other soon.

In addition, I would like to thank the rest of LINCE group (**Andrea Marchisio**, Mehdi Mohammadi, Federico Bosio, Bartolomeo Coppola, Giulia Molinaro, Barbara Inserra, Alberto Belli, Enrico Virgillito, Alessandra Formia, Marco Di Donato, Riccardo Grisotti, Luca Capurso, Michelangelo Blasi, Roberto Nisticò, Luca Ferrante, Gabriele Zocchi, Andrea Cibirin, Carmine Dimaggio, Anna Gianturco, Laura Leotta) for their kind help during my days in Politecnico.

In Politecnico I have also found new friends like Mojtaba Alidoost, Kristen Meiburger, Vincenzo Randazzo and Roberta Bardini.

Special thanks to my parents for their love and prayers. I cannot express gratitude in words to my father and mother for their sacrifices for me.

Finally, I would like to thank my wife **Gabriella** to be exactly as she is...my truly love! I would simply say that it is just thanks to her endless affection and love that permitted me to complete in time my PhD and to bring this thesis into its definitive shape.

*I would like to dedicate  
this thesis to all  
family: my parents and  
my wife*

*Even matter, which is called inorganic,  
deemed dead, responds to the disbelievers  
and gives irrefutable proof of the living  
principle within itself. Everything that  
exists, organic or inorganic, living and non-  
living is sensitive to outside stimuli.*

*Nikola Tesla*



# Contents

Chapter1-Ozone.....	1
Abstract.....	1
1.1 Characteristics of ozone.....	1
1.2 Production of ozone.....	3
1.2.1 Corona Discharge Ozone Generation.....	4
1.2.2 Cold plasma ozone generation.....	5
1.2.3 Ultraviolet Ozone Generators.....	5
1.2.4 Electrochemical ozone generators.....	6
1.2.5 Radiochemical Ozone Generation.....	7
1.3 Toxicity of O <sub>3</sub> .....	7
1.4 Limits of ozone exposure.....	8
1.5 Need of ozone measurements.....	9
1.6 Methods to measure ozone in air.....	10
1.6.1 UV adsorption-photochemical method.....	11
1.6.2 Iodometric titration.....	12
1.7 Conclusions.....	13
References.....	14
Chapter 2 - Chemical sensors.....	19
Abstract.....	19
2.1 General aspects of sensors.....	19
2.1.1 Historic view.....	19
2.1.2 Basic principle of sensors.....	22
2.1.3 Classification of sensors.....	23
2.2 MOS.....	26
2.2.1 Reactions involved in MOS.....	31
2.2.2 Adsorption of reducing gases.....	35
2.2.3 Adsorption of oxidant gases.....	36
2.2.4 Desorption of gases.....	38
2.2.5 Performance of gas sensors.....	38
2.2.6 Factors affecting the gas sensing properties.....	39

2.3 Carbon-based chemical sensors .....	42
2.3.1 CNTs.....	42
2.3.2 Sensing mechanism .....	45
2.3.3 Functionalization of CNTs .....	46
2.4 Conclusions .....	47
Chapter 3 - Fabrication of sensors and materials characterization .....	54
3.1 Fabrication of sensors .....	54
Abstract.....	54
3.1.1 Substrate .....	54
3.1.2 Electronic circuit.....	55
3.1.3 Active layers .....	55
3.1.4 Influence of layer parameters on gas sensing.....	56
3.1.5 Sol-gel technique .....	58
3.1.6 Sputtering technique .....	59
3.1.7 Thermal spraying technique .....	60
3.1.8 Spin coating method .....	62
3.1.9 Drop coating route .....	63
3.1.10 Screen printing technique .....	64
3.2 Sensors test .....	71
3.3 Material characterization .....	72
3.3.1 Laser granulometry.....	72
3.3.2 DTA .....	73
3.3.3 N <sub>2</sub> adsorption .....	75
3.3.4 XRD.....	77
3.3.5 XPS.....	81
3.3.6 SEM.....	82
3.3.7 TEM.....	85
3.4 Conclusions.....	86
References.....	87
Chapter 4 - BaFe <sub>12</sub> O <sub>19</sub> and SWCNTs O <sub>3</sub> sensors .....	91
4.1 BaFe <sub>12</sub> O <sub>19</sub> sensors .....	91
4.1.1 BaFe <sub>12</sub> O <sub>19</sub> characteristics.....	92
4.1.2 BaFe <sub>12</sub> O <sub>19</sub> synthesis .....	94
4.1.3 BaFe <sub>12</sub> O <sub>19</sub> powder and film characterization .....	95
4.1.4 BaFe <sub>12</sub> O <sub>19</sub> gas sensing properties .....	100

4.2 SWCTs-ODA sensors .....	105
4.2.1 Introduction .....	106
4.2.2 Sensor preparation .....	107
4.2.3 ODA-CNTs characterization .....	108
4.3 Conclusions.....	113
References.....	114
Chapter 5 - In <sub>2</sub> O <sub>3</sub> -based O <sub>3</sub> sensors .....	123
Abstract.....	123
5.1 In <sub>2</sub> O <sub>3</sub> and WO <sub>3</sub> -doped In <sub>2</sub> O <sub>3</sub> powders.....	123
5.1.1 General aspects of In <sub>2</sub> O <sub>3</sub> .....	124
5.1.2 Sensing properties of In <sub>2</sub> O <sub>3</sub> .....	125
5.1.3 Strategies to optimize In <sub>2</sub> O <sub>3</sub> sensors -surface modification .....	130
5.1.4 Strategies to optimize In <sub>2</sub> O <sub>3</sub> sensors – bulk doping .....	132
5.1.5 General aspects of WO <sub>3</sub> .....	133
5.2 Sensors based on In <sub>2</sub> O <sub>3</sub> nanostructures.....	134
5.2.1 Synthesis of In <sub>2</sub> O <sub>3</sub> .....	135
5.2.2 Characterization of In <sub>2</sub> O <sub>3</sub> .....	136
5.3 Sensor performances of In <sub>2</sub> O <sub>3</sub> and WO <sub>3</sub> -In <sub>2</sub> O <sub>3</sub> .....	148
5.4 Influence of film thickness on sensor response .....	156
5.5 DRIFT measurements .....	168
5.5.1 H <sub>2</sub> O/D <sub>2</sub> O test .....	169
5.5.2 NO <sub>2</sub> test .....	170
5.5.3 O <sub>3</sub> test .....	172
5.6 Conclusions.....	175
References.....	176
Appendix A.....	182
Abbreviations .....	182
Chapter 6 - Humidity sensors .....	185
6.1 Humidity detection .....	185
6.1.1 Some definition about humidity .....	185
6.1.2 Methods to measure humidity .....	187
6.1.3 Chemical humidity sensors.....	189
6.1.4 Carbon-based humidity sensors.....	191

6.2 Humidity sensors measurements .....	192
6.3 SWP-OSR Humidity sensors .....	193
6.3.1 OSR-SWP biochars .....	193
6.3.2 Biochars powder and film characterization .....	194
6.3.3 Biochars gas sensing properties .....	200
6.4 Waste coffee ground sensors .....	205
6.4.1 Coffee ground biochar (CGB) .....	206
6.4.2 CGB powder and film characterization .....	206
6.4.3 CGB gas sensing properties .....	212
6.5 Conclusions .....	217
References .....	218
Appendix A .....	224
Abbreviations .....	224
Chapter 7 - NH <sub>3</sub> and NO <sub>2</sub> sensors .....	228
Abstract .....	228
7.1 Ammonia detection .....	228
7.1.1 NH <sub>3</sub> issue .....	228
7.1.2 Co <sub>3</sub> O <sub>4</sub> characteristics and synthesis .....	231
7.1.3 Co <sub>3</sub> O <sub>4</sub> powder and film characterization .....	232
7.1.4 Co <sub>3</sub> O <sub>4</sub> gas sensing properties .....	237
7.2 Nitrogen dioxide detection .....	245
Abstract .....	245
7.2.1 NO <sub>2</sub> issue .....	246
7.2.2 ZnO characteristics and synthesis .....	248
7.2.3 ZnO powder and film characterization .....	252
7.2.4 ZnO gas sensing properties .....	256
7.3 Conclusions .....	261
References .....	262
Appendix A .....	269
Abbreviations .....	269
General Conclusions .....	270

# List of Tables

**Table 1:** Ozone physical and chemical data.

**Table 2:** Ozone safety and regulatory data

# List of Figures

**Figure 1.** Oxygen and ozone molecules.

**Figure 2.** Mechanism of production of ozone molecules.

**Figure 3.** Ozone cycle in troposphere.

**Figure 4.** Adsorption spectrum of O<sub>3</sub>.

# Chapter 1 - Ozone

## Abstract

In this first chapter, the main characteristics of ozone are described, as well as different methods to produce  $O_3$ , with a special focus on those used in this thesis in order to perform ozone measurements (corona discharge and UV generation). The limits of exposure connected with its toxicity are discussed, with the state of art of methods currently used to measure this oxidant gas in troposphere.

## 1.1 Characteristics of ozone

Ozone is a chemical compound with three oxygen atoms ( $O_3$  – triatomic oxygen), an extremely energetic form compared to the normal atmospheric biatomic oxygen ( $O_2$ ). In addition, the two forms have a different in structure, as depicted in Figure 1.

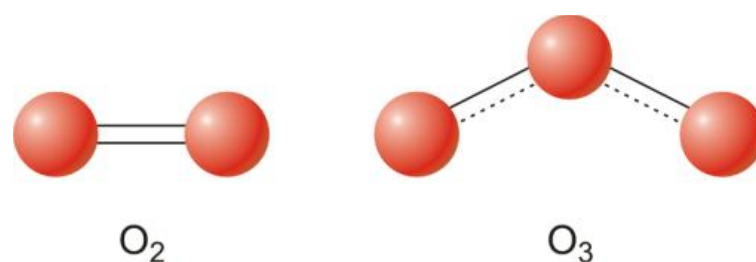


**Figure 1.** Oxygen and ozone molecules [1].

$O_3$  is one of the most significant gases in the atmosphere, and in the stratosphere (i.e. the layer between 15 and 50 km) it is essential due its ability to filter UV rays in the range 200-320 nm, with an absorption signal at 254 nm. This value is critical

for the preservation of biologic equilibrium inside the biosphere. In particular, the radiation of the sun in the range 200-290 nm is the most harmful to DNA [2].

As a result, the protective layer of stratospheric O<sub>3</sub> impedes that highly energetic radiation to reach the surface of the earth, furnishing protection for terrestrial life and resulting in the well-known blue-colored sky.

The main physical-chemical data of O<sub>3</sub> are tabulated in the next Table 1.

**Table 1.** Physical-chemical data for O<sub>3</sub>.

PROPERTY	VALUE
<b>CHEMICAL/PHYSICAL [3]</b>	
Molecular formula	O <sub>3</sub>
Molar mass	47.998 g·mol <sup>-1</sup>
Density	2.144 g·mL <sup>-1</sup> (0°C)
Melting point	-195.5
Boiling point	-111.9
Solubility in H <sub>2</sub> O	0.104 g/100 mL at 0°C
Critical pressure	5460 kPa
Critical temperature	-12.1 at 0°C
Half time in air	4-12 h
Half time in water	1-20 min

Furthermore, O<sub>3</sub> is a '*secondary*' pollutant generated from other species like volatile organic compounds (VOC<sub>s</sub>) and nitrogen oxides (NO<sub>x</sub>) under solar light. O<sub>3</sub> concentrations usually are higher in areas with ere significant emissions of NO<sub>x</sub> and VOC<sub>s</sub> under high temperatures, elevated levels of solar radiation together with stagnant meteorological conditions.

Its cycle in troposphere is depicted in Figure 2.



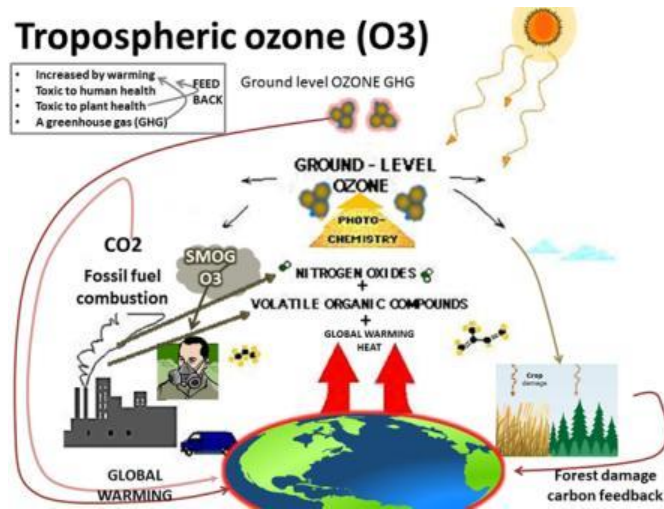


Figure 2. Ozone cycle in troposphere [4].

The O<sub>3</sub> cycle is strictly linked to Global Warming process, since O<sub>3</sub> amounts in troposphere results in higher concentrations of pollutants that are responsible of its presence at ground level.

Moreover, O<sub>3</sub> due to its high oxidizing potential is used in many applications like hospital operating rooms, in freshwater disinfection, process and cooling water, for sterilization in fish farms. Thus. It is utilized in deodorization, detoxification and disinfection of wastewater from industry [5]. For instance, in Western Europe 95% of potable water is currently processed by O<sub>3</sub>.

## 1.2 Production of ozone

O<sub>3</sub> is produced naturally by two main methods:

- From **electrical discharges** following thunderstorms. O<sub>3</sub> is formed due to electrical discharge, breacking an oxygen molecule (O<sub>2</sub>) into two separated atoms of oxygen. An O<sub>3</sub> molecule is formed when the individual oxygen atoms combine with another oxygen molecule, as displayed in Figure 3.

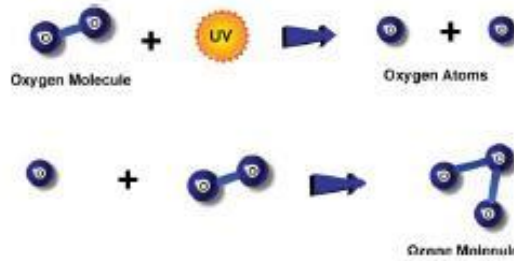


**Figure 3.** Mechanism of production of ozone molecules [6].

- From **ultraviolet rays** coming from the sun, which generates and electrical discharge over oxygen molecules in the stratosphere. This generates the O<sub>3</sub> layer, that absorbs most of the UV radiation of the sun.

These two natural processes are exploited for industrial purposes. For its applications, O<sub>3</sub> must be generated on site immediately before using because is inherently unstable. To this aim, even if a wide range of methods are now available to generate O<sub>3</sub>, only few of them appear practical for market applications. In fact, those technologies are corona discharge, ultraviolet and electrolytic/electrochemical systems, adopted in recent years. In this PhD thesis, corona was utilized for O<sub>3</sub> measurements in University of Tubingen, while UV generator to perform O<sub>3</sub> measurements in Politecnico di Torino.

### 1.2.1 Corona Discharge Ozone Generation

Nowadays, O<sub>3</sub> generators based on corona discharge are the reference method of production in the major part of commercial applications in medium-large scale. They produce up to 10 wt% of O<sub>3</sub> in a stream of feed gas [7]. The central criterion of operation is the production of a corona, that is an area of ionized gas, between a high tension (5 kV-20 kV) and a ground electrode. The separation is established by a dielectric, consisting in a ceramic or a glass, and a shrink air gap where the corona discharge is established [3].

O<sub>2</sub>, diatomic oxygen, in air or concentrated in a stream, passes across the high-voltage of the discharge gap. In this place, a fraction of the O<sub>2</sub> is divided into atomic oxygen (O). A portion of the as formed O reacts with O<sub>2</sub> in the gas stream forming O<sub>3</sub> that is the triatomic form of oxygen. One other fraction of the atomic oxygen can react with other atomic oxygen reforming molecular oxygen.

In order to maintain a corona, a significant amount of heat is required. This must be pulled out to prevent thermal decomposition of O<sub>3</sub> [3].

The feed gas must be cleaned by contaminants that could affect the generator's performances [3]. In addition, its consumption is critical that moisture-like water vapour could be pulled out from the gas stream, since it exhibits two main adverse consequences in the yield of O<sub>3</sub> generation. Firstly, the presence of humidity in the feed gas will drastically decrease the concentration of O<sub>3</sub> produced. Secondly the formation of HNO<sub>3</sub> can occur, which can corrode the dielectric materials and the electrodes inside the generator.

For this reason, even in relatively dry environments, humidity could be enough to cause the problems previously described in air preparation in any commercial-scale corona discharge generator. In order to remove moisture in ambient air, sorbents are utilized, or it is common to apply heating to the air for lowering the dew point [3]. Since the conditioning of feed gas is required in any case, many operators are employing gas preparation systems that furnish higher O<sub>2</sub> amounts (more than 90%) producing higher quantity of O<sub>3</sub> per unit of power.

### **1.2.2 Cold plasma ozone generation**

In this method, a plasma generated by a dielectric barrier discharge interacts with pure O<sub>2</sub>. O<sub>2</sub> is splitted into two oxygen atoms, that recombine in triplets forming O<sub>3</sub>.

Pure O<sub>2</sub> is used in cold plasma machines as the source producing a maximum percentage of around 5% of O<sub>3</sub>. They generate great amounts of O<sub>3</sub>, but they are not widely used because of their cost.

The discharges are filamentary migration of electrons in a gap between two electrodes. A dielectric insulator is adopted for separating the electrodes preventing arcing phenomena. In some cases, cold plasma units can produce others short-lived allotropes of oxygen (e.g. O<sub>4</sub>, O<sub>5</sub>, O<sub>6</sub>, O<sub>7</sub>, etc).

### **1.2.3 Ultraviolet Ozone Generators**

O<sub>3</sub> generators employing UV radiation act on the analogous base as that working in the stratosphere to generate the '*safety ozone layer*'. O<sub>2</sub> molecules absorb high frequency UV radiations (i.e. < 200 nm) and those are characterized by an adequate energy consumpt to rive the bonds between oxygen atoms. As previously seen with generators of corona-discharge, the as formed atomic oxygen reacts with molecular

oxygen to generate O<sub>3</sub>. This is easily accomplished by settling a quartz sleeve between the the air stream and the bulb. [7].

In the case of UV generators, the yield in ozone production is lower compared to the other two main methods of production, corona discharge and electrolytic generators. In fact, the O<sub>3</sub> yield from a UV device is generally lower than 1 wt%. Despite those aspects concerning the yield, this kind of systems are not complicated, and they do not present an absolute demand for feed conditioning [7]. For these motivations, UV systems are useful for solutions at small-scale. Thus, this system was used for the major part of experiments in this PhD thesis, those carried out in Politecnico.

## 1.2.4 Electrochemical ozone generators

The creation of O<sub>3</sub> using electrolytic methods has been recognized from the beginning of ozone generation processes [8].

Nevertheless, it has only been in the last 20 years that the right materials have been promoted for allowing a reliable and commerciable electrochemical generator.

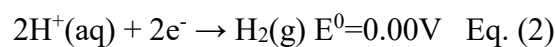
There are two general types of this technology, that are classified as Type-I and Type-II. In type-I generators, two not reactive electrodes are submerged in a lectrolytes solution, whose composition can be tailored to satisfy specific requirements [9]. In type-II generators, the electrolysis of water is exploited. A solid polymer electrolyte (SPE) is the proton exchange membrane (PEM) and Naphion-117 is often utilized for this scope. PEM is coated on each side with catalysts able to form O<sub>3</sub> [9].

Generally, PbO<sub>2</sub> and Pt are used for anode and cathode for these kind of generators [10].

When high purity water passes above the anode of PbO<sub>2</sub> at an adequately tension (i.e. higher than 1.51 V) and current density, O<sub>3</sub> is developed in accordance with equation (1):



H<sup>+</sup> that is generated passes through the PEM and gains electrons at the cathode, generating H<sub>2</sub>, as in equation (2):



High O<sub>3</sub> concentrations (up to 47 wt%) can be produced by electrochemical O<sub>3</sub> without requiring feed gas infrastructure. [8].

Nowadays this technology is not as mature as the previous two and commercial reliability remains to be established, even if the O<sub>3</sub> gas amounts generated are elevated and can lead to consistent mass transfer. Further, when the absolute O<sub>3</sub> generation is higher, H<sub>2</sub> gas generation and consumption must be addressed. Despite this, some researchers recommend that H<sub>2</sub> could be used in fuel cell devices as a combustible, hereby offsetting some of the expenses for disinfection [10].

### **1.2.5 Radiochemical Ozone Generation**

The last method for ozone production is the radiochemical generator. Radioactive rays that irradiate oxygen at high-energy can favor the ozone formation. This ozone production procedure has not yet become a significant application in water treatment because of its extremely complicated process requirements, even though high thermodynamic yields are reached, and it has an intriguing use of waste fission isotopes.

## **1.3 Toxicity of O<sub>3</sub>**

O<sub>3</sub>, is toxic above certain concentration thresholds as any oxidizing species.

O<sub>3</sub> gas present an odour threshold of around 0.02 mg·m<sup>-3</sup>, that is over toxic limits for work: light, medium and heavy. Nevertheless, desensitization can occur in some cases, constituting a serious risk for the human health [11].

The inhalation of O<sub>3</sub> can be toxic for the pulmonary system and other apparatus. The symptoms of exposure of O<sub>3</sub> depend on the amount and period of exposure. In fact, after short time exposure typical symptoms are headaches and dryness of the eyes, throat and nose. Moreover, ozone prolonged exposure can result in lassitude, tightness, retarded edema of lungs, or constriction in the breast and acid-mouth [11]. Coughing, tachycardia, vertigo, dyspnea, sensation of suffocation, decreased blood pressure, serious breast ache and general body pain can be proved as symptoms of severe exposures. The lung function can be suppressed in case of chronic exposures and trigger other respiratory dysfunctions like asthma.

When a patient is intoxicated by O<sub>3</sub>, he must be placed quickly in the supine position, thus inhaling humid oxygen and taking ascorbic acid, vitamin E and acetylcysteine.

## 1.4 Limits of ozone exposure

Ozone can seriously harm people's health if it is present in high concentration for its negative powerful oxidization effect. This gas is often produced in everyday life, like in laser printers as well as by older generation photocopiers. The exposure in the range between 100 and 1000 ppb (parts per billion) results in headache, burning eyes, and irritation to the respiratory apparatus. A person staying in a place under 100 ppb of O<sub>3</sub> environment for a period higher than two hours will suffer a decrease of 20% in breath capability, while if he/she remains under 1000 ppb of ozone for more than six hours, he/she will undergo a crisis of bronchitis. A rat maintained under 10 ppm of ozone is going to die in few minutes [12].

The O<sub>3</sub> regulatory data in accordance with Air Quality Directive 2008/50/EC, are tabulated in Table 2, together with some effects on human health. This Directive set some thresholds for O<sub>3</sub> concentrations at European level.

**Table 2.** Ozone safety and regulatory data.

<b>REGULARITY/ SAFETY</b>	
	90 ppbv information threshold (IT)
	120 ppbv alert threshold (AT)
	60 ppbv long term objective (LTO)
	to protect human health
Detectable odour	0.005-0.04 ppmv
Health and safety limits (Italy) [13,7]	0.2 ppmv for maximum period of 2 h
	0.1 ppmv TWA (8h, 5d/w) for light work
	0.08 ppmv TWA (8h, 5d/w) for moderate work
	0.05 ppmv TWA (8h, 5d/w) for heavy work
Dry cough, lung irritation, chest pain, severe fatigue	600-1000 ppbv over 1-2 h
Immediately dangerous for life and health (IDLH)	5 ppmv
Expected to be fatal	50 ppmv

Several standards for the protection of human health from pollution by O<sub>3</sub> have been defined by the European Union (EU). They include four parameters: information threshold, alert threshold, long-term objective (LTO) and the target value [14].

The first standard, information threshold (IT), is defined as one-hour mean O<sub>3</sub> level of 180 µg/m<sup>3</sup> (90 ppb) and an obligation is triggered with the aim to inform the population on possible associated risks.

The second parameter, the alert threshold (AT), is triggered when 1-hour average level of ozone overcomes 240 µg/m<sup>3</sup> (120 ppb) and necessitates cities to take actions immediately.

The third one is the long-term objective (LTO), i.e. the highest 8-hour average in a day level of O<sub>3</sub> should not surpass 120 µg/m<sup>3</sup> (60 ppb).

The last value is the Target Value (TV) that should not be exceeded on more than 25 days per each year, and it is a mean over 3 years.

Furthermore, the maximum O<sub>3</sub> concentration in workplaces should not exceed 200 µg/m<sup>3</sup> (~ 100 ppb).

In 2015 in the USA, United States Environmental Protection Agency (EPA) modified the National Ambient Air Quality Standards (NAAQS) at ground-level not to surpass 70 ppb of ozone. This review was taken for improving public health protection [15], while previously the maximum O<sub>3</sub> concentration for hourly exposure was set at 80 ppb in accordance with the air quality standard in U.S [16].

## **1.5 Need of ozone measurements**

Because of its toxicity, it appears of the highest importance to measure O<sub>3</sub> at ground level. With the aim of monitoring the O<sub>3</sub> amounts in the troposphere, it is necessary to consider some aspects.

Firstly, O<sub>3</sub> is unstable and it is converted to oxygen with a half-life of around 1 hour at 25°C [17].

As previously described, O<sub>3</sub> can react quickly with other species donating a free oxygen to hydrogen, chlorine or nitrogen. Moreover, the amount of O<sub>3</sub> differ considerably with time and place.

It is consequently necessary to monitor environmental O<sub>3</sub> amount either in workplaces and in everyday life. In the former case a prevention of O<sub>3</sub> leaks from

the generators is required, whereas in the latter case environmental monitoring of this gas is fundamental to protect the health of the people. Consequently, nowadays the actions of monitoring the amount of O<sub>3</sub> becomes strictly necessary.

Tropospheric O<sub>3</sub> is typically measured by spectroscopic methods that exploit the ability of O<sub>3</sub> to adsorb UV light around 254 nm.

The O<sub>3</sub> measuring stations are typically expensive and big. It is not possible to situate a huge number of these measuring stations in a urban place to detect O<sub>3</sub> anywhere and anytime. However, O<sub>3</sub> monitoring now is an urgent demand.

Considering environmental monitoring, ozone episodes can often occur. An ozone episode is a period of up to 2-3 weeks with elevated O<sub>3</sub> levels, characterized by quotidian exceedances of the thresholds determined to preserve human health. Those phenomena take place upon peculiar meteorological regimes characterized by wide areas of stagnant air and elevated pressure in atmosphere. Those are more frequent during summer since the formation of O<sub>3</sub> is promoted by the presence of the sunlight [18].

## **1.6 Methods to measure ozone in air**

The analytical techniques progressed to measure O<sub>3</sub> amounts should be sensitive in a broad range of concentration, between 10-10000 ppb. In fact, environmental monitoring requires instruments with an accuracy of few ppb, while in industrial usages, the precision is not such rigorous, since the expected concentration are in the order of thousands of ppb.

Up to now, a wide range of papers has been published about determination of ozone amount [19-23].

For accomplishing this purpose, many analytical methods were presented in papers like optical sensing [24], ultraviolet (UV) light absorption [25] chemiluminescence analyzers [26], fluorescence tests [27], KI [28] and direct amperometry determination [29].

However, most of these procedures are not peculiar only for O<sub>3</sub> but they typically determine the amount of oxidation reagents. Generally, techniques for measuring the concentration of ozone could be split into two groups: i.e. photochemical and chemical methods.



In the major part of the recently published works about ozone production [13, 24, 25] and its quantitative determination, the '*photochemical method*' of UV light absorption is adopted. The biggest pro of this method is the possibility to determine continuously the amount of ozone. This property could be useful for the automatic regulation of ozone production by ozonizer according to the actual need.

By means of '*chemical methods*', the absolute determination of O<sub>3</sub> amount (in oxygen) can be evaluated. For instance, the iodometric titration belongs to this group of methods. However, chemical methods disable continuous measurements of O<sub>3</sub>.

Both types of methods could be adopted without any other requirements only in the case of ozone generation using oxygen as a source because when air is flowed, the absorption of other molecules such as nitrogen and nitrogen oxides can happen. Nevertheless, in the case of UV generation of ozone by means of a mercury lamp, the influence of such absorption can be neglected because it occurs only between excited metastable species. The mostly used techniques – UV adsorption and iodine titration – will be briefly described in this section.

### **1.6.1 UV adsorption-photochemical method**

The most used photochemical method and recommended route for the evaluation of O<sub>3</sub> gas concentration is direct UV absorption [7]. As previously described, O<sub>3</sub> absorbs UV radiation between 190 – 310 nm and it has an absorption peak at 254 nm (Figure 4), that is near the  $\lambda = 253.7$  nm mercury (Hg) resonance line [30]. O<sub>2</sub> absorb exclusively the highest energy of UV light generated by the sun, principally below 200 nm. Thus, the specific absorption characteristics of O<sub>3</sub> has been exploited to develop ozone sensors.

By means of a Hg lamp, UV is produced very close to the absorption peak of O<sub>3</sub>. By introducing O<sub>3</sub> into the sample stream, a drop in the UV signal at 254 nm of  $\lambda$  is registered. It is proportional to the O<sub>3</sub> amount in the specimen in accordance with the Beer-Lambert law [31].

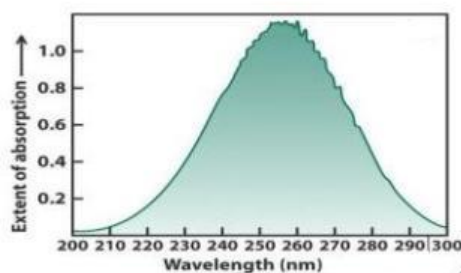


**Figure 4.** Adsorption spectrum of O<sub>3</sub> [32].

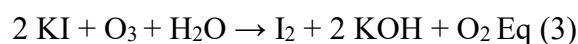
O<sub>3</sub> streams between two cuvette windows in the same direction of sapphire or quartz, transparent until 254 nm, with a carrier gas (air or oxygen) Two UV detectors measure electrically the UV radiation. The first detector measures the reference signal that is the radiation without O<sub>3</sub>, whereas the second detector quantifies the radiation as the O<sub>3</sub> passes the cuvette. Moreover, by varying the cuvette width, the sensitivity and the measurable concentration range of O<sub>3</sub> gas is easily adjustable. There is no interference from oxygen adsorption at 254 nm. The O<sub>3</sub> spectrometer is extremely heavy and can achieve a lifetime of more than a decade. It is necessary to prevent dust that contaminate the equipment.

Thanks to its noticeable resolution, this is without any doubts the dominating commercially available product for accurate ozone measurement in air. This technology allows a widerange of measure from 1 ppb up to 2500 ppm. Nevertheless, the weight of this type of ozone photometer is a disadvantage, because it is in the range of tens of kilograms. In the last years, the need to produce portable devices led to diminishing the size and the weight until 6 kg, including the electrical unit.

In addition, the required electrical power, is extremely high (more than 20 W). Furthermore, the ozone photometers are too heavy, expensive and big, and they require high energy consumption for employing as portable devices, despite of its wide measuring range, high resolution and extended life time.

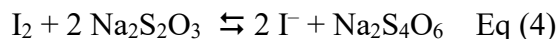
### **1.6.2 Iodometric titration**

In the iodometric titration reaction, O<sub>3</sub> is added into an alkali iodide solution (KI) in accordance with the following reaction (eq 3):



In this reaction, iodine is formed from iodide. The initial presence of iodine result in a yellow or even brown solution.

The amount of iodide is consequently determined by the titration with sodium thiosulphate in acidic conditions, as presented in equation 4:



where it is easy to follow the reduction of iodine to iodide by a remarkable decoloration of the yellow-brownish solution. For making this reaction more sensitive, the starch solution is typically added before the end of the titration. This solution changes color of the titrated mixture into blue.

Flowing gas is led from the ozonizer into the bubbling vessel containing potassium iodide solution. The as-formed  $\text{O}_3$  reacts with iodide forming.

The above-mentioned methods require expert technicians for the set up of the instrumentation (photochemical methods) and to fulfill the chemical reaction (chemical methods). In order to realize cheap and ease-to use on-line  $\text{O}_3$  sensors, chemical sensors have an intriguing potential. For this reason, ceramic and carbon based-chemical sensors able to detect ozone and its interferences at low concentrations (ppm and ppb level) will be propose in this thesis.

## 1.7 Conclusions

Ozone is a strong oxidant that has drastically raised its amounts in the troposphere in recent years.  $\text{O}_3$  is generated by the interaction between sunlight and many chemicals released by human activities, such as vehicles and industries. Furthermore,  $\text{O}_3$  in troposphere is a byproduct of both urban and industrial pollution. Since high  $\text{O}_3$  tropospheric levels are hazardous for the human health, monitoring its amount at ground level appears crucial.

The actual analytical techniques available in the market for ozone control are expensive and they require expert technicians. For this reason, cheap alternatives have been deeply investigated for online measurement of pollutants, and among them, chemical gas sensors have a great potential for their modest cost, facility of operation, great reliability and the possibility to integrate them in portable electronics. In fact, nowadays, low-cost and energy-saving  $\text{O}_3$  detectors are widely required.

In this thesis, the development of many types of small-size, cheap and energy efficient O<sub>3</sub> sensors are described. In the next chapter, the basic work principle of SMO<sub>x</sub> (semiconductor metal oxides) and carbon-based chemical sensors will be illustrated together with the advantage and disadvantages of this technology.

## References

- [1] [https://www.periodni.com/gallery/allotropic\\_forms\\_of\\_oxygen.png](https://www.periodni.com/gallery/allotropic_forms_of_oxygen.png) visited on 18th September 2018.
- [2] Jiang Y., Ke C. H., Mieczkowski P. A., Marszalek P. E. (2007). UVA generates pyrimidine dimers in DNA directly. *Biophys. J.* pages 1758-1767.
- [3] Rakness K. L. (2005). Ozone in drinking water treatment: process design, operation and optimization. 1st ed. *American Water Works Association*. Denver, CO.
- [4] <http://www.climatechange-foodsecurity.org>, visited on 18th September 2018.
- [5] Horvath M., Bilitzky L., Hüttner J., (1985). Ozone, Monograph 20th serie: *Topics in Anorganic and General Chemistry* (pages 350). Amsterdam: Elsevier.
- [6] Aucamp P. J. (2007). Questions and answers about the effects of the depletion of the ozone layer on humans and the environment. *Photochem. Photobiol. Sci.* pages 319-330.
- [7] Harrison J. P. (2004). Ozone for point-of-use, point-of-entry, and small water system water treatment application. *Water Quality Association*. Lisle, IL.
- [8] Franco D. V., Jardim W. F., Boodts J. F. C., Da Silva L. M. (2008) Clean – soil air water. pages 34-44.
- [9] McDonald G. V. (2007) Ozone (O<sub>3</sub>) efficacy on reduction of *Phytophthora capsici* in recirculated horticultural irrigation water. Texas A&M, College Station, PhD Diss. 121.
- [10] Han S., Kim J., Myung K., Rana R. K., Singh K. C. (2006). Electro-chemical production of ozone using water electrolysis cell of solid polymer electrolyte (SPE). *Ind. J. Chem. Techol.* pages 156-161.

- [11] Gottschalk C., Libra J. A., Saupe A. (2000). Ozonation of water and wastewater – a practical guide.
- [12] Seiyama T. (1988) Chemical Sensor Technology. Tokyo: Kodansha LTD.
- [13] Decreto Legislativo n. 15-2010.
- [14] EEA European Environment Agency (2014) Air Pollution by ozone.
- [15] <https://www.epa.gov/ozone-pollution/2015-national-ambient-air-quality-standards-naaqs-ozone>, visited on 18th September 2018.
- [16] Wongwiriyapan W., Honda S., Konishi H., Mizuta T., Ikuno T., Ohmori T., Ito T., Shimazaki R., Maekawa T. (2006) *Jpn. J. Appl. Phys. A*. pages 3669-3671.
- [17] Koike K., Inoue G., Fukuda T. (1999) *J. Chem. Eng. Jpn.* pages 295-299.
- [18] Harrison R. V. (2010) Chemical Sensors: properties, performance and applications, Chemistry Research and Applications.
- [19] Bader H., Hoigné J. (1981) Determination of ozone in water by the indigo method. *Water research* pages 449-456.
- [20] Daumont D., Brion J., Charbonnier J. (1992) Ozone UV spectroscopy I: Absorption cross-sections at room temperature *Atmos Chem.* pages 145.
- [21] Nederbragt W., van der Horst A., van Duijn J. (1965) Rapid ozone determination near an accelerator. *Nature* pages 87.
- [22] Birdsall C. M., Jenkins A. C., Spadinger E. (1952) Iodometric determination of ozone. *Anal. Chem.* pages 662-664.
- [23] Straka M. R., Pacey G. E., Gordon G. (1984). Residual ozone determination by flow injection analysis *Anal. Chem.* pages 1973-1975.
- [24] Ando M., Swart C., Pringsheim E., Mirsky V. M., Wolfbeis O. S. (2002). Optical ozone detection by use of polyaniline film, *Solid State Ionics*. pages 819–822.
- [25] Potyrailo R. A., Hobbs S. E., Hieftje G. M (1998). A simple, highly stable scintillator light source for ultraviolet absorption-based sensors. *Anal. Chim. Acta*. pages 153–157.
- [26] Eipel C., Jeroschewski P., Steinke I. (2003) Determination of ozone in ambient air with a chemiluminescence reagent film detector, *Anal. Chim. Acta*. pages 145–153.
- [27] Takayanagi T., Dasgupta P. K. (2005) A chemiluminescence-based continuous flow aqueous ozone analyzer using photoactivated chromotropic acid, *Talanta* pages 823–830.
- [28] Doll T., Lechner J., Eisele I., Schierbaum K.-D., Göpel W. (1996). Ozone detection in the ppb range with work function sensors operating at room temperature, *Sens. Actuators B*. pages 506–510.

- [29] Stergiou D. V., Stergiopoulos T., Falaras P., Prodromidis M. I. (2009). Solid redox polymer electrolyte-based amperometric sensors for the direct monitoring of ozone in gas phase, *Electrochem. Commun.* pages 2113–2116.
- [30] Matsumi Y., Kawasaki M. (2003) Photolysis of atmospheric ozone in the ultraviolet region. *Chem. Rev.* pages 4767–4782.
- [31] Gottschalk C., Libra J.A., Saupe A. (2000). Ozonation of water and waste water – a practical guide to understanding ozone and its applications. Wiley-VCH, Weinheim, Germany.
- [32] <https://www.slideserve.com/aquene/chemistry-of-the-stratosphere>, visited on 18th September 2018.

# List of Tables

**Table 1.** Advantages and disadvantages of methods based on electrical variation.

**Table 2.** Response mechanism of n-type and p-type semiconductor sensors.

# List of Figures

**Figure 1.** Scheme of different gas sensing methods.

**Figure 2.** Electronic core–shell structures in (a) n-type and (b) p-type MOS.

**Figure 3.** Studies based on n- and p-type MOS chemical sensors.

**Figure 4.** Functions of receptor and transducer of MOS chemical sensor.

**Figure 5.** Functions of receptor and transducer for MOS gas sensor.

**Figure 6.** Functions of receptor and transducer of MOS sensor (a) SnO<sub>2</sub> sensors response as a function of crystallite size (b) SnO<sub>2</sub>, WO<sub>3</sub> sensor response as a function of SiO<sub>2</sub> amount (c). Influence of noble metal content Pd (d) influence of working T on In<sub>2</sub>O<sub>3</sub> sensor response and response time (e). Influence of SnO<sub>2</sub> film thickness on sensor response and response time (f) SnO<sub>2</sub> layer resistance.

**Figure 7.** Scheme of band bending after chemisorption of charged species (in this example the ionosorption of oxygen). EC, EV, and EF denote respectively the energy of the conduction band, valence band, and the Fermi level, whereas  $\Lambda_{\text{air}}$  describes the thickness of the space-charge layer, and  $eV_{\text{surface}}$  is the potential barrier.

**Figure 8.** Structural and band model for mechanism of conduction of a polycrystalline MOS: (a) initial state (b) effect of CO for large crystallites.

**Figure 9.** The different mechanisms of crystallite size dependence of conductance in MOS (a)  $D \gg 2dl$ , crystallite boundary control (b)  $D = 2dl$ , neck control (c)  $D < 2dl$ , crystallite control [51].

**Figure 10.** Scheme of SWCNT (left) and MWCNT (right).

**Figure 11.** Scheme of configuration of chemoresistive CNT sensors.

**Figure 12.** Three ways of interaction between analytes and CNTs that result in a change in the conductivity of CNTs. (a) SWNT-electrode junction; (b) charge transfer among the SWNT and target gases; (c) intertube junction.



# Chapter 2 - Chemical sensors

## Abstract

In this chapter, the principal properties of chemical sensors are discussed. Starting with an historical view of chemical sensors, the basic principle and the classification of these devices are presented. Thus, metal oxide semiconductor and carbon-based chemical sensor properties, performances and sensing mechanism are described with both advantages and limits of those techniques.

## 2.1 General aspects of sensors

### 2.1.1 Historic view

After the consequences of many dangerous gases on human health were distinguished, different methods of gas leak detection became of great importance. Early detection systems relied on less precise sensors, before the development of modern electronic devices. During the 19th and the beginning of 20th centuries, coal miners used to taking canaries with them below to the tunnels as a primitive measuring system for protection towards gaseous species like  $\text{CO}_2$ ,  $\text{CO}$  and  $\text{CH}_4$ . The canary, that normally are a songbird, would stop to sing and then die in some cases. This happened if they were not removed in time from these harmful species, warning the workers to leave the mine immediately.

The earliest gas sensor that found application in industry was the *Flame Safety Lamp* (FSL), invented in 1815 by Sir Humphry Davy for measuring  $\text{CH}_4$  in underground coal mines. The FSL was made of an oil flame adapted to a characteristic height under fresh air. For preventing ignition, FSL was held in a glass sleeve equipped with a mesh flame arrestor. The height of the flames changed if  $\text{CH}_4$  or a lack of oxygen were present. Nowadays, FSL systems are still operating in some parts of the world.

In 1926, the '*modern era of gas detection*' began by the progress of the catalytic combustion *Lower Explosive Limit* (LEL) detector. This device was developed by Dr. Oliver Johnson at Standard Oil Company in California, USA.

His aim was to avoid detonations in storage tanks of gasoline and oil.

This sensor shows the minimum gas amount in air that will explosively blaze in case of ignition's sources. The atmosphere burns if it contains a certain amount of fuel and oxygen, an ignition's source and a proper energy to support the fire chain reaction.

The first practical '*electric vapor indicator*' meter started to be manufactured in 1927.

In 1928, the World's first gas detection company, Johnson-Williams Instruments was founded by Phil Williams and Oliver Johnston. J-W Instruments is known as the earliest electronics firm established in Silicon Valley. Over the following four decades, the company pioneered several '*firsts*' in the modern age of gas sensors, covering more portable instruments, the realization of a portable oxygen detector and the first instrument able to measure oxygen, vapors and combustible gases.

Prior to the progress of electronic household CO sensors in the 1980s, the presence of this harmful gas was evaluated with a chemically infused paper that after exposition to the gas turned into brown. From that point on, several electronic systems have been realized to measure alerting the leak of many gases.

When electronic gas sensors's performances and prizes improved, they have been incorporated into various systems. For instance, in automobiles they were initially used for engine emissions monitor. Nowadays, gas detectors may be utilized to guarantee passenger safety and comfort. CO detectors are being introduced into buildings in demand-controlled ventilation schemes. Thus, in medical diagnostic, sophisticated gas sensor systems have been investigated well besides their early scope in operating rooms. Alarms and gas monitors for CO and other dangerous gases are disposable also for both domestic and working utilizations and they are now legally demanded in some countries.

At the beginning of their development, sensors were developed for detection of a unique gas. Nowadays, modern systems can detect many combustible or toxic gases, together with an arrangement of them [1].

It is not possible that gas detectors solve the constituent signals from a complex aroma to distinguish many gases at the same time [2].

The 1962 could be considered the first year of the era of chemical sensor technology. Taguchi delivered the first patent on SnO<sub>2</sub> as the first metal oxide based chemoresistive gas sensor [3].

In the same year, Seiyama et al. [4] developed an innovative type of detector for gaseous components.

In this kind of sensor, the adsorption and desorption of gases generate the variation in the electrical conductance of SnO<sub>2</sub> film demonstrating that gas detection is feasible with facile electrical devices. Although this phenomenon was already known in some degree, the authors found that at the temperature of 485°C, the adsorption and the succeeding desorption processes on the surface of semiconductors take place quickly and may indicate a marked variation in the electrical conductivity.

The response of this system towards propane was about 100 times larger in comparison with the thermal conductivity sensors utilized at that time.

Moreover, this property of thin films was found to be widely applicable to the detection of gaseous components.

At the beginning of the 1950s, Bardeen and Brattain, two workers of Bell Laboratories, firstly demonstrated for the first time that some semiconductors like germanium varies their resistance, in dependence of the surrounding atmosphere [5].

In 1954, Heiland reported that metal oxides like zinc oxide alter their semiconducting characteristics by a variation in the concentration of O<sub>2</sub> or other species in the ambient. Nevertheless, these findings were not further studied [6].

Subsequently Shaver in 1967 delineated the effects of adding noble metals such as Pt, Pd, Ir and Rh on the semiconductors [7].

Thence, selectivity and sensitivity of semiconductor sensitive materials have been improved remarkably, thanks to an intensification in searching new formulations for gas sensing materials.

Four years later, Taguchi patented the first device of chemoresistive gas sensors, ready for useful applications, with SnO<sub>2</sub> as the ceramic sensing element [8].

He discovered that SnO<sub>2</sub> possess many intriguing features such a great sensitivity at low working temperature and a structure that is thermally stable. Considering thick film sensors, the first generation was developed with a mixture of stearic acid and tin chloride painted onto the substrate and then fired at 700 °C. This step was necessary to evaporate the organic vehicle, releasing a porous layer of SnO<sub>2</sub>. Taguchi utilize also Pd as a metal catalyst to enhance the sensor stability, selectivity and sensitivity. These sensors were commercialized by Figaro Inc, and they found application in alarms for preventing accidents such as gas leakages and fire formation in houses by detecting the presence of harmful amounts of explosive species. As a result, a diffused utilization of semiconductor gas detectors take place. In fact, at the end of 1980s, the use of semiconductors in gas sensing field experienced a significative growth becoming one of the most dynamic area of reserach in the sensor community.

The request for gas detectors with high-performance and enhanced sensitivity, selectivity and reliability, quicker response and modest power dissipation, generated accelerated strengths for realizing innovative sensing elements.

The fast expansion of materials chemistry together with the materials science, has brought to a significant enhancement in the quantity of new sensitive elements disposable. This favored the realization of high-efficient solid-state gas sensors.

Nowadays, it appears evident that the research on chemoresistive devices is playing a fundamental role in daily life.

In fact, chemical sensors have experienced an expansion in their exploitation to a wide range of areas, from vehicle control of emissions and environmental monitoring to industrial emission control and household security, together with agricultural, biomedical utilizations, over the last five decades. This is a result of their ease to use, extremely cheap, small volume being able to be equipped into electronic systems [7, 9–11].

Nowadays, novel nanoscale technologies provide opportunities for the development of semiconducting sensing materials. Nanoscience, permitting manageable manipulation of materials at the molecular level, is a crucial source for novelties in elaboration of materials. Moreover, developing nanotechnologies are generating deep modifications in sensor designs and applicabilities. The essential achievements from gas sensor research are a considerably smaller size, lower weight and power consumption and enhanced sensitivity and specificity for the target gas.

Gas detectors based on metal oxides have been broadly utilized and studied in the measurement of a wide range of species. Studies have confirmed that the gas detection mechanism is highly connected to surface phenomena. For this reason, one of the essential parameters of gas detectors, i.e. the sensitivity, will vary with the factors that influence the surface phenomena. Those are the chemical components, microstructures and surface-modifications of sensing film, as well as humidity and temperature of the ambient [12].

The operating mechanism of semiconductor metal oxide sensors (SMOs) is associated to the alteration of the electrical conductivity of the material after oxidation/reduction reactions for the adsorption/desorption of interfering gases on the material surface. An electronic device measures the variation of resistance through a well-defined transfer function and determines the true value of the gas concentration by transmitting the output signal. Gas selectivity and reactions caused by interference from other gases or by humidity are partially attenuated by careful formulation of the composition and chemical nature of the basic oxides using catalysts and through selecting a suitable working temperature by means of a heating circuit.

### **2.1.2 Basic principle of sensors**

Intelligent systems with sensors can be utilized for many applications, as previously described.

Generally, sensors are electronical systems that turn physical-chemical phenomena into electrical outputs [13].

In addition, an actuator converts an electric signal to a physical output.

There are many possible classifications of sensors, which often are guided by application perspectives. Typically, a sensor acquires a stimulus and return with an electrical output [14].

A different definition describes a sensor as a system that is suitable to turn a physical quantity into an output readable by an instrument or an external observer [15].

A slightly diverse definition from the IEC (International Electrotechnical Committee) affirms '*the sensor is the primary part of a measuring chain which converts the input variable into a signal suitable for measurement*' [16].

Therefore, the necessity to control and monitor has driven the research and development of numerous sensors with several materials and technologies [14].

### **2.1.3 Classification of sensors**

The classifications of sensors can be of different types, from the easiest until the most complex. In dependence on the classification type, variegated criteria can be picked. Here, there are many practical methods to look at the sensors.

A first classification of sensors is between two kinds: passive and active, where the former kind does not require additional source of energy and produces an electric output responding to an external stimulus: the sensor converts the energy of the stimulus into the outcome signal [17].

Some types of this group of sensors are thermocouples, photodiodes and piezoelectric sensors. The major part of passive sensors are direct sensors requiring an excitation signal as an external power for their performance. This signal is altered by the detector in order to produce an outcome.

On the opposite, the properties of active sensors are modified responding to an external stimulus and those are transformable afterwards into measurable electric outputs.

A sensor modulates the excitation signal and this signal conveys informations about the measured value. Some examples are constituted by a thermistor and a resistive gauge.

The former is a temperature-sensitive resistor. By flowing a current across it, its resistance is measurable by alterations in voltage/current through the thermistor. The thermistor does not produce any electric output. These modifications are directly related to the temperature.

The later case of an active detector is a resistive strain gauge where the resistance is associated to a strain. In this case, an electrical current is applied from a power supply in order to quantify the sensor resistance.

In dependence on the reference choosed, sensors are categorized into absolute and relative devices. The former measures a stimulus referring to an absolute physical range. This quantity is not dependent on conditions of the test, while a relative detector sensor generates a signal referrable to a certain event.

The thermistor is a typical absolute sensor: it is a resistor sensitive to the temperature. Its resistance is related to the absolute temperature range (in Kelvin). The thermocouple is a further widely used temperature sensor. This kind sensor produces a voltage that depends on a gradient of temperature through the wires of the thermocouple. In addition, a thermocouple outcome requires to be referred to a known baseline.

Talking about pressure sensors, they can be both absolute and relative sensors. The former one generates a signal referred to vacuum (where the pressure is zero), whereas a relative detector sensor generates a signal in reference to a baseline that is different from 0 P (e.g. can be the P of the atmosphere).

It is also possible to consider other properties, such as which conversion mechanism is used, which physical phenomenon the sensor is sensitive to and which stimulus is detecting [18].

With the aim to provide a definite description of sensing criteria, in this section many technologies are separated in two classes: those related to alterations of electrical features and other characteristics, as illustrated in Figure 1.

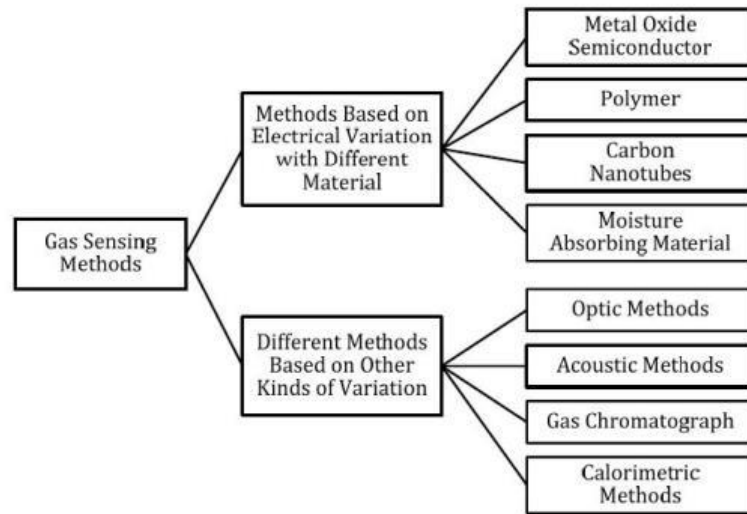


**Figure 1.** Scheme of different gas sensing methods [18].

Among those gas sensing methods, those related to electrical alterations with diverse materials were chosen, due to several advantages. In Table 1 pros and cons of sensors based on electrical variation are tabulated.

**Table 1. Table 1.** Advantages and disadvantages of methods based on electrical variation.

METHODS	PRO	CONS	APPLICATIONS
MOS	Cheap, fast, several gases, extended lifetime, low power consumption	Low selectivity, sensitive to environmental factors	Industrial and civil use
Carbon nanotubes	Sensitive, fast, great adsorption, large s/V	Low repeatability and difficulties in preparation	Detection of partial discharge
Polymers	Sensitive, fast, cheap, simple, low power consumption	Long term instability, irreversibility and poor selectivity	Indoor air monitoring, chemical industries
Moisture adsorbing material	Cheap, low weight, selective to water vapor	Irreversibility at high water vapor, vulnerable to friction	Humidity monitoring

NB: s: surface, V: volume.

## 2.2 MOS

The most used sensitive elements are MOS - metal oxide semiconductors, that furnish chemical sensors with many pros, as described in table 1: their cost is low, they present high sensitivity, quick response and recovery times, they find application in the measurement of several gases and it is possible to reuse them after a long period of time.

Semiconductors are characterized by an electrical conductivity in the range  $10^{-8}$  and  $10^3$  S/cm, in the middle between a conductor and an insulator. Generally, their electrical resistance decreases by increasing the temperature. Thus, the energy band gap between valence band (VB) and conduction band (CB) makes it easy to energize valence electrons sending them to the conduction band. Semiconductors are classified in two groups, depending on the presence of impurities in the crystalline lattice.

- n-type (e.g. SnO<sub>2</sub>, ZnO, WO<sub>3</sub>, In<sub>2</sub>O<sub>3</sub>)
- p-type (e.g. CuO, Co<sub>3</sub>O<sub>4</sub>, NiO, Mn<sub>3</sub>O<sub>4</sub>)

In the n-type semiconductor materials, free electrons ( $e^-$ ) are the main carriers and holes ( $p^+$ ) are the minority ones. A vacancy is created in the broken bond whenever a free electron is formed during breakdown of a semiconductor to another covalent bond. These vacancies are related to holes. Each hole is a positive equivalent of an electron since it is formed from a lack of an electron. In a n-type semiconductor, there are both free holes and electrons, but the number of the latter is considerably higher when comparing with the former.

Therefore, this brings to a variation of the Fermi level towards the n-type side to maintain the equilibrium (i.e. the product of electrons and holes must be a constant). The opposite is true for the p-type semiconductors. A p-type semiconductor has several holes that move randomly in the crystal. Besides the holes produced from trivalent impurity atoms in the p-type semiconductor crystal, there are thermally produced electron-hole pairs too. They are referred to those formed during the breakdown of covalent bonds in the thermal excitation at room temperature. These electrons furnish free electrons in the p-type crystal.

Consequently, the whole quantity of holes in a p-type semiconductor is the sum of  $p^+$  generated by impurity atoms and those formed in the thermal excitation. On the contrary, free electrons are only generated by thermal excitation. For this reason, the number of free electrons in a p-type metal oxide is considerably smaller than that of holes.  $p^+$  here are the main carriers and  $e^-$  are the minority ones [20].



The two mechanisms of interaction for n-type and for p-type metal oxide semiconductors is illustrated in Figure 2.

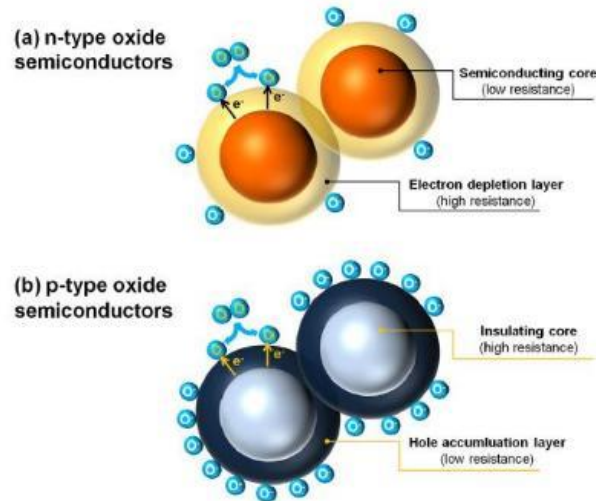


**Figure 2.** Electronic core–shell structures in (a) n-type and (b) p-type MOS. Reproduced with permission from [19], published by Elsevier, 2014.

Generally, the ionosorbed species  $O_2^-$ ,  $O^-$ , and  $O^{2-}$  are predominant respectively at  $T < 150^\circ C$ , in the temperature range  $150^\circ C - 400^\circ C$ , and at  $T > 400^\circ C$ , respectively [19]. This led to the generation of an electronic core–shell structure (Figure 2). In a n-type semiconductor, the area at the cores of grains has low resistance, and a resistive layer at the shells of the crystallites is formed: the EDL (electron depletion layer). When oxygen ions are adsorbed in p-type semiconductors, a HAL (hole accumulation layer) close to the material surface is generated. This is a result of the electrostatic interplay between the oppositely charged species, that determine the electronic core–shell structure: the non-conductive area at the centers of crystallites and the semiconducting HALs near the crystallites’s surface.

Several materials has been studied to find application in gas sensing, from mono-component metal oxides to multi-component oxides, like  $BiFeO_2$ ,  $MgAl_2O_4$ , and  $SrTiO_3$  [21].

Generally, metal oxide semiconductors can be divided into two groups: non-transition and transition ones. The former (e.g.,  $In_2O_3$ ,  $Al_2O_3$ ,  $SnO_2$ ) are constituted by with only one oxidation state-elements, whereas the latter (e.g.,  $CuO$ ,  $ZnO$ ,  $Fe_2O_3$ ) consists of elements with more than one oxidation states [22].

In this case, transition-metal oxides can generate differnt oxidation states on the surface, a phenomenon that is used in the sensor mechanism. More in detail,

transition-metal oxides having an electronic configuration of  $d_0$  and  $d_{10}$  can be deployed in chemical sensing exploitations [23].

The  $d_0$  is present in transition metal oxides like  $WO_3$ ,  $TiO_2$  and  $V_2O_5$ , while  $d_{10}$  was found in post-transition-metal oxides, like  $ZnO$  and  $SnO_2$ . The major part of MOS belong to n-type semiconductors, even if there are some kinds of p-type semiconductors such as  $NiO_x$ ,  $Co_3O_4$  and  $CuO$  that show promising features as gas sensing elements. For instance, it is demonstrated that 10 wt% of  $NiO_x$  amount in  $TiO_2$  is necessary for the conversion of n-type into p-type conductivity. The principle distinction between n-type  $TiO_2$  and p-type  $NiO_x$  doped  $TiO_2$  layer is that at higher temperatures the n-type material exhibits an enhanced sensitivity towards reducing species, whereas for the p-type the response is dropped [24].

An interesting advantage of p-type semiconductors is that usually they present a higher sensitivity at relatively lower working temperatures compared to n-type ones.

Sensors made up of MOS are principally used to monitor gases across redox reactions between the metal oxide's surface and the analyte [25].

This is a two-stages process [22]:

- A serie of redox reactions, where  $O^-$  allocated on the surface of the semiconductor, interact with analyte gas, resulting in an electronic alteration of its surface due to a charge transfer.
- This alteration is transduced into a sensor electrical resistance modification. This can be recognized by measuring the resistance, the impedance but also the variation of capacitance, mass, work function, optical properties or the reaction energy [22].

Metal oxide semiconductors, like  $SnO_2$ ,  $ZnO$ ,  $In_2O_3$ ,  $WO_3$ ,  $V_2O_5$ ,  $CuO$ ,  $Cr_2O_3$ , and  $TiO_2$ , can find application in monitoring of reductants and oxidants. Furthermore, they can be handled as combustibles with sensors, that are principally measuring the variations in resistance after the interaction with the target gas [26].

$SnO_2$  is the most utilized gas sensing metal oxide, as clearly described in Figure 3.

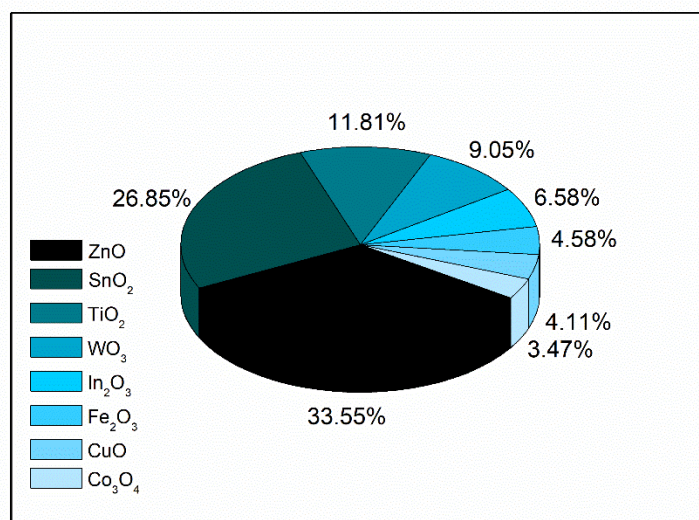


**Figure 3.** Studies based on n- and p-type MOS chemical sensors (internet search of Web of Knowledge on October 9, 2018).

The resistance of SnO<sub>2</sub> film variations with the variation of gas amount, from liquefied petroleum gas (LPG) to methane (CH<sub>4</sub>); from carbon monoxide (CO) to other reductants [27].

Other metal oxide semiconductors are also extensively investigated for their interesting gas sensing properties, like tungsten trioxide WO<sub>3</sub>. For example, anodic WO<sub>3</sub> by applying electrochemical etching of W exhibit superior responses when exposed to hydrogen (H<sub>2</sub>) and nitrogen oxide (NO) [28].

Regarding a different reducing gas, NH<sub>3</sub>, the response of undoped WO<sub>3</sub> to ammonia is slightly low, the WO<sub>3</sub> sensor displayed a moderate selectivity for ammonia regarding the interference from NO<sub>x</sub>.

A successful way to improve WO<sub>3</sub> properties in gas sensing, is to decorate it with Cu and V as catalysts to increase the response towards ammonia, eliminating the abnormal behavior of the sensor [29].

Another example of well-studied MOS is titanium dioxide (TiO<sub>2</sub>) that is handled as sensing layer for its sensing performance due to the high dielectric permittivity suitable for gas adsorption [30].

There are many influencing factors, like the structure and characteristics of the sensitive film, affecting the redox phenomena and influencing the semiconductor's sensitivity as gas sensitive elements, and those characteristics will be elucidated in detail in the next session. The sensitivity of SnO<sub>2</sub>-based sensors is rather elevated,

driving to its widespread and its wide presence in the market (e.g. in Figaro sensors).

However, this sensitivity is due to the elevated working temperature, that is typically accomplished through an external heated filament or an internal heater. For the major part of oxides, the elevated working temperature is a result of the reaction temperature of  $O^-$  [21]. The sensitive film requires preheating to a certain T to enhance the possibility of adsorption of target gas molecules on the layer surface consuming ions from the sensitive element. After depletion of ions, the film conductivity arises forrealizing the sensing function. Thus, the use of a micro-hotplate is a further option to maintain the sensing elements at high temperatures [31].

Heating the sensing element is not the unique way to improve the sensitivity of the chemical sensors, like pre-concentration technology or UV-illumination [32].

An interesting strategy to ameliorate the gas sensing properties is to develop composites like  $SnO_2$ -ZnO or  $FeO_3$ -ZnO because they advice a synergic effect between the components [21]. Consequently, the sensitivity can be manipulated by adjusting the amount of every component into the composite. For instance, the operating T of sensors based on  $SnO_2$  in composites varies from room temperature to 500 °C and the optimum operational T to different gases change [32].

This aspect must be considered since when the temperature deviates a lot from its optimal value, other gases could be more reactive towards  $SnO_2$ . This led to a drop in the selectivity for the target gas. Nevertheless, in the case of high differences between these two temperatures, a unique sensor should be selected to measure two species by varying the temperature. For instance, the best operative T of  $SnO_2$  towards  $CH_4$  is 400 °C whereas that for CO is equal to 90 °C. This necessitate a thermostatic cycle of the sensing layer at the two temperatures to detect both gases by considering the resistance variations of the sensing element during each gas exposure [34].

Some strategies to ameliorate the selectivity of the sensing film involve doping the surface of the sensing film with an appropriate catalyst [21, 25]. Besides, an additional way to improve the selectivity is by adopting a sensor array based on various sensing materials [35, 36].

A gas sensor array is constituted by different sensing elements for the detection of a single specie. In the case of an array with many elements, a gas recognition circuit is typically adopted to improve the selectivity [36].

A further methodology to enhance the selectivity includes the use of catalytic filters for the detection of combustible gases [37, 38].

Metal oxide semiconductors have been universally utilized in sensor technology. Nonetheless in some cases, their need of high working temperature requires higher costs and tricky configurations, when comparing with room-temperature technologies. With the aim to overcome those issues, researchers have proposed some methodologies like the exploitation of micro-sized materials with micro-heaters realized by silicon IC technology [39] and T-pulse mode with quick heat steps [40] to decrease the sensor power consumption.

Another issue could be represented by long recovery times required after each gas adsorption. This is not practical for some sensors limiting their application where the gas concentrations mutate quickly. In conclusion, the research in SMO sensors should discover novel solutions to overcome their limits. Researches on metal oxides have displayed that nanostructures could refine the sensitivity and the kinetic of response of gas sensors [41].

### 2.2.1 Reactions involved in MOS

In the gas sensing of MOS, two main mechanisms are involved: the receptor and transducer functions. The receptor concerns the recognition of an analyte gas in the interface between gas and solid, including electronic changes in the metal oxide surface, whereas the transducer includes transduction of the phenomenon on the surface in an electrical alteration of the film's resistance [42].

Figure 4 illustrates both receptor and transducer functions in MOS sensors.

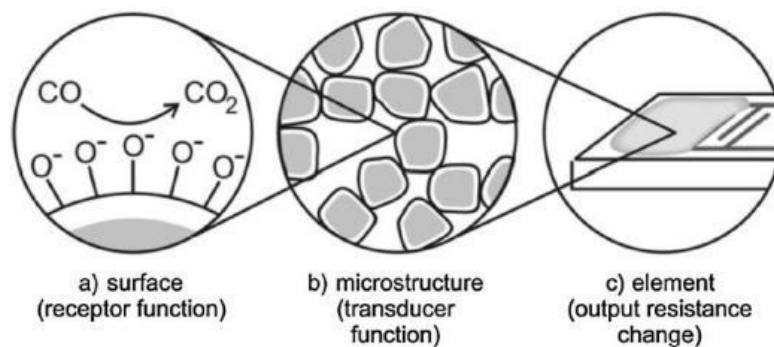


**Figure 4.** Functions of receptor and transducer of MOS chemical sensor. Reproduced with permission from [43], published by John Wiley and Sons, 2005.

According to Korotcenkov [44], chemical characteristics of the surface oxygens of the metal oxide are accountable for the receptor function since it accounts the capability of the oxide to interact with the gas species.

The receptor function can be modulated by loading the metal oxide with noble metals, acid or basic oxides. Modifications in the receptor function causes a large alteration in sensor performance. The transducer function converts the signal due to chemical interactions of the oxide surface corresponding to a variation in work function, into a measurable electrical output. This is generated by every crystallite boundary. In the next Figure 5, a useful scheme of receptor and transducer functions is summarized, together with the physicochemical and material characteristics related to semiconductor gas sensors.

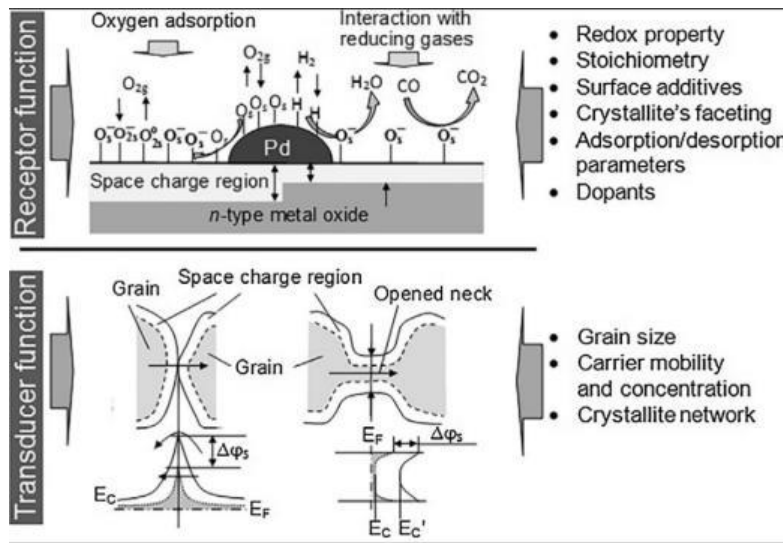


**Figure 5.** Functions of receptor and transducer for MOS gas sensor. Reproduced with permission from [44], published by Elsevier, 2017.

Gas sensing in MOS sensors involved ionosorbed surface oxygen and the target gas. The gas causes an alteration in the equilibrium of the reaction involving surface oxygens and corresponds to the transducer function. The alteration in chemisorbed oxygen is responsible to a variation in the conductivity of the SMO materials [45].

In the Figure 6, the receptor and transducer functions are illustrated with factors that influence the properties of the sensor.

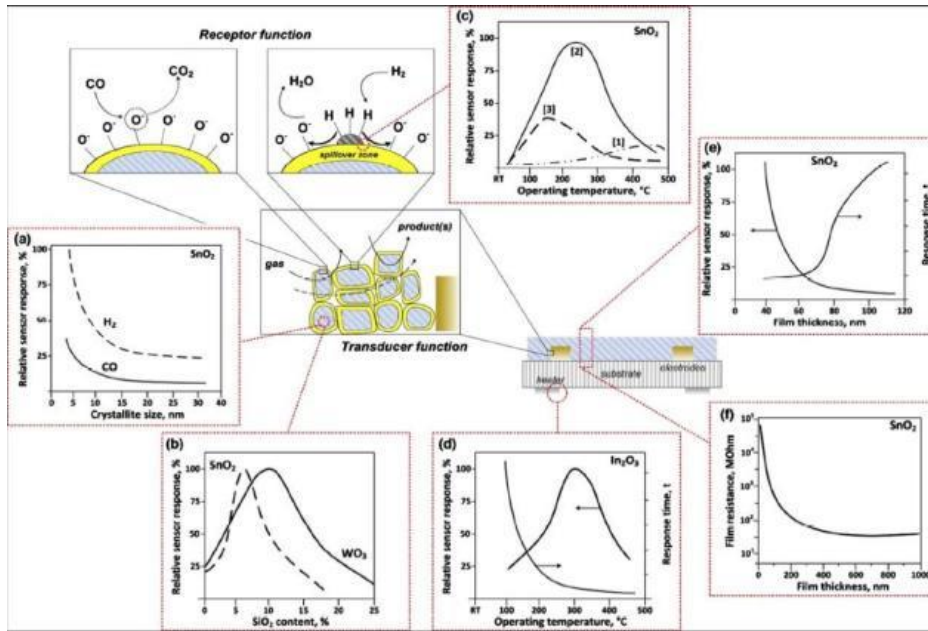
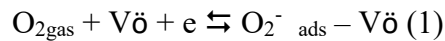


**Figure 6.** Functions of receptor and transducer of MOS sensor (a) SnO<sub>2</sub> sensors response as a function of crystallite size (b) SnO<sub>2</sub>, WO<sub>3</sub> sensor response as a function of SiO<sub>2</sub> amount (c). Influence of noble metal content Pd (d) influence of working T on In<sub>2</sub>O<sub>3</sub> sensor response and response time (e). Influence of SnO<sub>2</sub> film thickness on sensor response and response time (f) SnO<sub>2</sub> layer resistance. Reproduced with permission from [45], published by Elsevier, 2015.

The sensitivity of a sensor is directly correlated to the capability to vary its surface conductivity after interaction with the analyte. Oxygen ions adsorb on the solid-gas interface at the active adsorption sites, that are the superficial oxygen atoms, V<sub>o</sub>.

In this adsorption process, the conducting electrons of the solid are depleted for the formation of ionic species adsorbed following the reaction (1):



In this equation, O<sub>2gas</sub> is the gaseous oxygen, whereas O<sub>2ads</sub><sup>-</sup> represents the adsorbed oxygen ion on the vacancy at the surface of the MOS. This process assesses that an electron depletion layer is created after adsorption of oxygen and as a result, a reduction of charge density in the grain zone close to the depletion layer is formed. This produces a drop in the amount of charge near the surface and a potential barrier of the Schottky barrier is generated [46], as depicted in Figure 7.

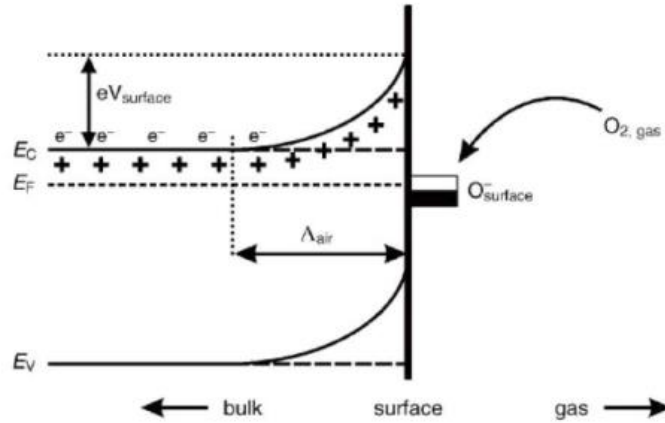


**Figure 7.** Scheme of band bending after chemisorption of charged species (in this example the ionosorption of oxygen).  $E_C$ ,  $E_V$ , and  $E_F$  denote respectively the energy of the conduction band, valence band, and the Fermi level, whereas  $\Lambda_{air}$  describes the thickness of the space-charge layer, and  $eV_{surface}$  is the potential barrier. [46].

The mechanism involves the  $e^-$  trapping at adsorbed oxygens and a band bending (BB) is formed due to these anions that are responsible for an alteration in conductivity. These anions trapped results in an upward BB and the resistance is increased in comparison with the flat band. If  $O_2$  molecules are absorbed on the MOS surface,  $e^-$  are extracted from the CB - $E_C$ - trapping the  $e^-$  at the surface as ions. Weisz limitation states a maximum degree of coverage of charged ions in the case of chemisorption of oxygen that is limited to a small fraction of a monolayer between  $10^{-3}$  and  $10^{-2}$   $cm^{-1}$  ions, describing the equilibrium between the energy of surface-adsorbed sites and the Fermi level.

This results in a BB with an  $e^-$ -depleted region, and a surface potential barrier in the range 0.5-1.0 eV is formed.

This  $e^-$ -depleted region is the '*space-charge layer*', and its thickness is the length of the BB area. The height ( $eV_{Surface}$ ) and depth ( $\Lambda_{air}$ ) of the BB are a function of the surface charge, that depends on the amount and typology of adsorbed oxygen. In addition, the depth of band bending is a function of the Debye length  $Ld$ , according to equation 2:

$$Ld = \sqrt{\frac{\epsilon\epsilon_0KT}{e^2\eta d}} \quad (2)$$



In this equation,  $\epsilon$  is the dielectric constant,  $\epsilon_0$  is the permittivity of free space,  $K$  represent the Boltzmann's constant,  $T$  is the operational temperature,  $e$  is the charge of electron, and  $\eta d$  stands for the concentration of carriers, corresponding to the donor concentration in a fully ionized situation.

In polycrystalline materials, the electronic conductance takes place over percolation paths through contacts between crystallites and consequently is a function of the  $eV_{\text{Surface}}$  of the nearby crystallites.  $eV_{\text{Surface}}$  is the Schottky barrier. For this situation, the conductance of the sensitive element can be extracted by the next equation (3) [47]:

$$G = \exp\left(\frac{-eV_{\text{Surface}}}{KT}\right) \quad (3)$$

### 2.2.2 Adsorption of reducing gases

When reducing or oxidizing gases interact with the surface of the MOS, the base line resistance will change after an exchange of electrons. Based on the typology of metal oxide semiconductor (n-type or p-type) and interfering gas, oxiditants or reductants, such variation causes an increase or in a decrease of the resistance value. Among reducing species, carbon monoxide is one of the most investigated because of its hazardous effect on human health [48].

When CO interacts with the surface of a n-type MOS at a temperature of around 300 °C, it is oxidized to CO<sub>2</sub> delivering electrons in the CB of the MOS and the surface of the semiconductor is reduced following the reaction (4):



When CO takes part to the interaction with the adsorbed oxygen molecules, electrons are inserted into the MOS and so the amount of charge carriers is enhanced, with a drop in the thickness of the depletion layer and in the  $eV_{\text{Surface}}$ , as illustrated in Figure 8 for the band and structural models.

As a result,  $R_g$  that is defined as the resistance of the semiconductor at equilibrium when it interacts with CO gas, decreases as compared with the resistance when exposed to air  $R_o$  ( $R_g < R_o$ ).

After the interaction between CO and chemisorbed oxygen, the generation of unidentately and/or bidentately bound carbonates takes place, desorbing as CO<sub>2</sub> [16]. The concentration of adsorbed oxygen is reduced considerably even under traces of reductants and the trapped  $\text{e}^-$  at the surface are delivered back to the bulk. Thereafter, the Schottky barrier height is attenuated, enhancing the conductivity of

the whole sensitive film. The band model concerning the conductive mechanism in polycrystalline MOS are depicted in Figure 8.

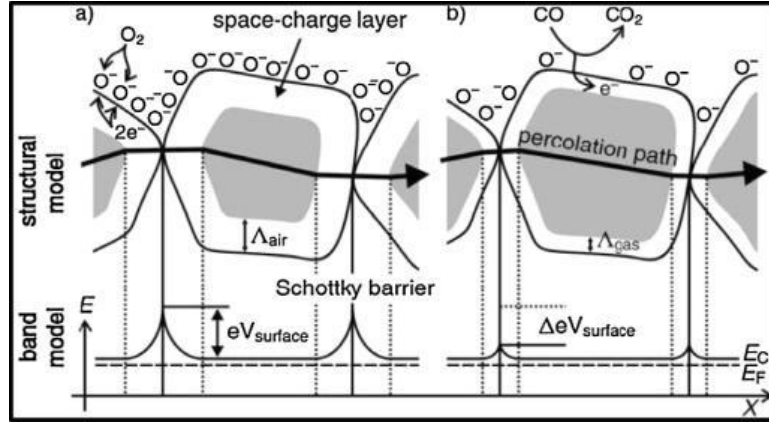
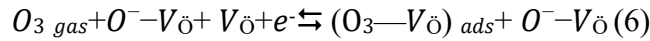
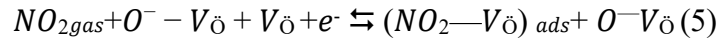


**Figure 8.** Structural and band model for mechanism of conduction of a polycrystalline MOS: (a) initial state (b) effect of CO for large crystallite [46].

### 2.2.3 Adsorption of oxidant gases

Among oxidant gases, a great attention is paid for  $\text{NO}_2$  and  $\text{O}_3$  because of their strong oxidant interactions for the human health. For instance, when  $\text{NO}_2$  is adsorbed on the semiconductor surface, it follows the reactions (5-6):



From these reactions,  $\text{O}_3$  and  $\text{NO}_2$  have a huge affinity for the reaction with oxygen vacancies ( $\text{V}_{\text{O}}$ ) compared with the adsorbed oxygen species,  $\text{O}^- - \text{V}_{\text{O}}$ . As a result,  $e^-$  of the CB of the MOS are depleted. Subsequently to the interaction of  $\text{O}_3$  and  $\text{NO}_2$ , the depletion layer thickness is increased, the amount of the charge carrier is decreased, and the potential barrier ( $\Delta E$ ) is enhanced. In terms of resistance,  $R_g$  is higher than the resistance when exposed to air  $R_o$ , ( $R_g > R_o$ ).

In the next Table 2, the reactions and the correlated resistance variations after exposure to reducing (CO) and oxidant ( $\text{O}_3$ ) gases for n-type and p-type semiconductors are summarized.

**Table 2.** Response mechanism of an n-type and p-type semiconductor sensors.

TARGET GAS	REACTION WITH THE SURFACE	RESISTANCE n-type (In <sub>2</sub> O <sub>3</sub> , WO <sub>3</sub> , ZnO)	RESISTANCE p-type (BaFe <sub>12</sub> O <sub>19</sub> , Co <sub>3</sub> O <sub>4</sub> , CNT)
REDUCING	CO <sub>gas</sub> + O <sup>-</sup> - V <sub>o</sub> ⇌ CO <sub>2gas</sub> + V <sub>o</sub> + e <sup>-</sup>	Increase	Decrease
OXIDIZING	O <sub>3gas</sub> + O <sup>-</sup> - V <sub>o</sub> + V <sub>o</sub> + e <sup>-</sup> ⇌ (O <sub>3</sub> - V <sub>o</sub> ) <sub>ads</sub> + O <sup>-</sup> - V <sub>o</sub>	Decrease	Increase

The depletion layer thickness ( $dl$ ) is calculated by means of the Debye's equation (equation 7):

$$dl = \frac{Q_s}{N_{de}} \quad (7)$$

In this equation,  $N_{de}$  represents the quantity of donors per volume of material, and  $Q_s$  is defined in the equation 8:

$$Q_s = (\sum_j N_{s,j} q_j \theta_j) \quad (8)$$

Where  $N_s$  is the sum of the surface states having unitary electronic charge per unit of surface ( $q_j$ ) and  $\theta_j$  is the fraction of adsorbed area corresponding to the states surface tipe  $j$ .

The surface potential together with the height of Schottky barrier are determined using the equation 9:

$$\Delta\phi_S = \frac{(Q_s)^2}{2\varepsilon\varepsilon_0 N_{de}} \quad (9)$$

where  $Q_s$  defines the charge associated with surface oxygen coverage,  $\varepsilon$  and  $\varepsilon_0$  are the dielectric constant of the MOS and the dielectric constant relative to the vacancy, respectively.

Generally,  $\varepsilon\varepsilon_0 = 10^{-12} \text{ F/cm}$ ,  $N_d$  around  $10^{18} \text{ cm}^{-3}$ ,  $\Delta\phi_S$  close to  $1 \text{ V}$ , implying a depletion layer thickness of  $dl$  in the range between 1 and 100 nm.

Oxygen adsorption depends on both the environmental partial pressure and of the amount of active site on the semiconductor's surface. The material resistance depends on the coverage degree by adsorbed oxygen ions and varies only by altering the amount of oxygen anions at the surface. In dependece on the working temperature, oxygen is present as  $O_2^-$ ,  $O^-$  and  $O^{2-}$ . The alterations in the level of

charge carriers results in the alterations in the layer resistance. It is possible to assess that, for a certain temperature at the equilibrium, every value of the resistance of the MOS corresponds to a certain concentration of oxygen gas [49].

#### 2.2.4 Desorption of gases

When the target gas, reducing or oxidizing, is removed from the surface of the MOS, the surface of the MOS tends to desorb the adsorbed species, restoring the equilibrium conditions of the ion adsorbate oxygen species, and this process is favored by increasing the operating temperature.

For instance, for the interaction of CO with the MOS surface, when this gas is lifted, the atmospheric oxygen tends to be absorbed and restores the balance concentration of the species  $O^- - V_{\text{O}}$ . The equilibrium moves to the left part of the equation previously described, and the resistance of the material recovers the initial value [49].

#### 2.2.5 Performance of gas sensors

The performances of chemical sensors are analyzed by means of parameters such as:

- sensitivity
- selectivity
- long term stability
- response and recovery times
- fabrication cost.

The '*Limit of Detection*' (*LOD*) is defined as the smallest concentration in volume of the analyte that a sensor is able to detect during the exposure time. A method to define the '*sensor response*' is  $R_g/R_0$  for oxidant species and  $R_0/R_g$  for reducing gases with n-type MOS, and the opposite occurs for p-type ones.  $R_g$  stands for the resistance value under target gas at the equilibrium, while  $R_0$  represents the resistance of the film under a reference gas (usually dry air) at the equilibrium. Another method to express the sensor response is the SR% (sensor response %) that is expressed in the equation 10 [50].

$$SR (\%) = 100 * \frac{|Z_o - Z_g|}{Z_o} \quad (10)$$

In the equation 6,  $Z_0$  is the impedance under reference gas at the equilibrium and  $Z_g$  its impedance when it interacts with the target gas at the equilibrium. The ‘*sensitivity*’ is the ratio of the incremental variation in the sensor response to the incremental variation of concentration of target gas. The calibration curve’s slope is used for the calculation of sensitivity, expressed in [ppm<sup>-1</sup>].

The ‘*selectivity*’ is the capability of the device to distinguish a unique specie in a mixture of gas species.

Normally, one gas sensor can detect several species, especially if it consists in chemiresistive metal oxides. The selectivity is defined as equation 11:

$$\text{Selectivity} = \frac{R_{\text{target gas}}}{R_{\text{interfering gas}}} \quad (11)$$

The ‘*stability*’ is a crucial criterion required for gas sensors, because chemical sensors should operate considerably under repeated cycles of exposure to the target gas at different concentrations, and sometimes in harsh environments. The achievement of a stable performance without a drift is another essential parameter to proof the performance of gas sensor devices.

Parameters such as ‘*Response time*’ and ‘*recovery time*’ are describing how fast are the adsorption and desorption steps for a sensor that interacts with the target gas. The first one is the time required to obtain 90% of the saturation in resistance when the sensor interacts with the analyte and is described by  $\tau_{\text{ads}}$ . The second one corresponds to the amount of time needed for a sensor to drop back to 10% of the saturation in resistance when the sensor is placed in reference gas and it is defined by  $\tau_{\text{des}}$ . Both  $\tau_{\text{ads}}$  and  $\tau_{\text{des}}$  should be as small as possible for practical applications.

In summary, a model sensor should own the highest sensitivity, selectivity and long-term stability, the lowest response and recovery times together with the minimum fabrication costs possible.

## 2.2.6 Factors affecting the gas sensing properties

There are several ways for optimizing the above-mentioned sensor parameters. Firstly, the sensor sensitivity could be improved essentially by modifications in the microstructure, e.g. the crystallite size. Three scenarios are possible and shown in Figure 9:

- If  $D$ , the crystallite size, is  $\gg 2dl$  (the space charge layer thickness), the conductivity is restrained by the Schottky barrier at crystallite boundaries: here, the conductivity is governed by the crystallite boundaries.
- If  $D=2dl$ , the conductivity is restrained by necks among crystallites, and the conduction is controlled by necks.
- If  $D < 2dl$ , the conductivity is determined by each crystallite (crystallite control).

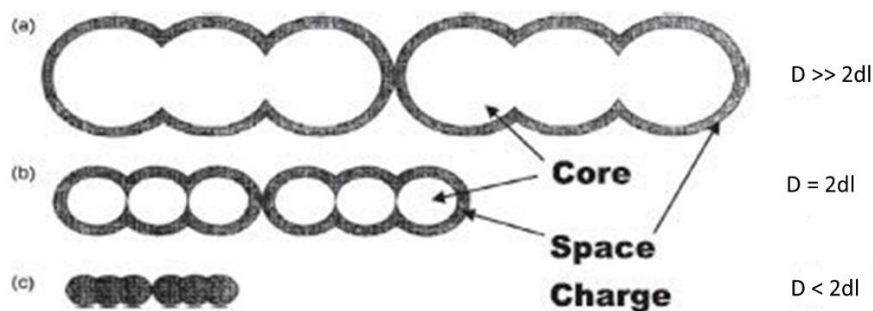


**Figure 9.** The different mechanisms of crystallite size dependence of conductance in MOS (a)  $D \gg 2dl$ , crystallite boundary control (b)  $D = 2dl$ , neck control (c)  $D < 2dl$ , crystallite control [51].

A different approach to increase the sensitivity of the MOS is by modifying its microstructure and porosity. Porous MOS with an enhanced surface area result in an improved sensitivity towards analytes [7].

The sensitivity of the MOS sensors can be increased also by adding impurities or dopants like noble metals such as Pt [52], metal oxide PdO [53] and rare earth oxide like  $CeO_2$  [54].

There are two different routes accountable for the improvements of gas sensing characteristics. The first one is a chemical modification, caused principally by spillover phenomenon and the second one is an electronic route [51].

In general, smaller crystallite size of the MOS improves the gas sensors's sensitivity, especially in the case of  $D < dl$ . However, an excessive drop in the crystallite size could result in a decrease in the sensor stability. Indeed, if the metal oxide is dispersed in too finely crystallites, an adverse effect on the stability in time of the sensor is noticed due to the agglomeration of nanoparticles (NPs).

The principal drawback of the technology based on MOS is the modest selectivity. As a consequence, one of the challenges for SMOs is to achieve a remarkable selectivity for the target gas. For this purpose, two main strategies for increasing

the selectivity of metal oxides are possible. The first consist in obtaining a MOS capable to be selective towards one gas with a low cross-sensitivity for other species. Usually this is quite hard to obtain since the mechanism of interaction between the MOS surface and the oxidant or reductant gases are analogous. The second approach consist in the discrimination between several analytes in the mixture. This result could be accomplished by temperature modulation usually achieved by modulating the temperature with a single sensor [51] or by using sensor arrays [49]. With an array of sensors that detect different analytes, it is possible to discriminate the contribution of the target gas in a real environment by means of statistical methods.

The addition of dopants to the SMO is a third strategy to ameliorate the sensor selectivity since each material is more sensitive for a certain gas specie. In many cases, by adding impurities and dopants it is possible to refine the sensing performance of the sensors.

A further key parameter in the advancement of gas sensors for the market is the long-term stability because sensors should produce a signal both stable and reproducible. In order to be ready for a large-scale presence in the market, the sensor signal should be constant at least for 2–3 years corresponding to an operation time between 17,000 h and 26,000 h [44].

The stability of the sensor should be associated to the reproducibility of its performances among a defined time at operative conditions (i.e. high temperature and in presence of analytes). An additional type of sensor stability is evaluated over a certain time under normal storage conditions (i.e. ambient humidity and room temperature). According to Korotcenkov et al [44] there are many factors that define the sensors instability such as structural and phase transformations, degradation of heaters and contacts, poisoning, errors in the design, variation in the amount of humidity, bulk diffusion, modification in the temperature of the ambient atmosphere and interference effects. A post processing process like calcination is an efficient method to ameliorate the sensor stability. In this way, a decrease of the sensing element working temperature is achieved. Doping is a first valid strategy to increase the stability of the sensor materials [7]. This is a consequence of the new thermally stable structures formed by doping. They lost their surface area slower, stabilizing the sensor performances. A wide range of engineering approaches could be accomplished for increasing the stability. For example, by a drift compensation, or by selecting correct gas system elements, adding specific filters and by stabilizing the temperature [44].

## 2.3 Carbon-based chemical sensors

Although multiple advantages, SMO sensors usually require high operational temperatures, usually in the range 150-400 °C. For this reason, carbon-based chemoresistive sensors have been attracting wide interest for the detection of different species: humidity, NO<sub>2</sub>, NH<sub>3</sub>, H<sub>2</sub>, greenhouse gases like CH<sub>4</sub> and CO<sub>2</sub>, VOCs and explosives [55].

Carbon films (resistive or capacite) are often characterized by an extended sensing area and they are chemical inertness [56]. Moreover, carbon nanomaterials, like carbon nanotubes (CNTs), carbon nanofibers, graphene and carbon black are also extensively utilized for the design of chemical sensors with great performances. Particularly, graphene and CNTs can be accomplished into 1D fibers, 2D films and 3D architectures. In this way, an simple design of chemical sensors can be realized and used for many practical applications [56]. Carbon-based materials can work at ambient temperature, it is possible to functionalize them to increase the specificity and they are characterized by a modest thermal mass providing fast heating with modest energy dissipation [57]. The main disadvantages of carbon-based materials are their poor reproducibility and selectivity, the susceptibility to poisoning and along-term drift in some cases [57].

Recently, other carbon elements produced from bio-materials by pyrolysis processes have been studied as sensitive elements, like silk [58] and cotton [59]. Biomass can also be a valuable source of carbon, available in high quantity, and it is accounted as an ecological and renewable reserve [60]. Additionally, diverse biochars, i.e. byproducts of biomass pyrolysis, are accessible directly from pilot plants generating energy and biogas [61, 62]. In recent years, the applications of biochars included several areas [63]. Besides, biochar has been investigated broadly as replcement for high-priced carbon powders such as carbon nanotubes, graphene and others [64].

### 2.3.1 CNTs

Recently, carbon nanotubes (CNTs) have been accounted ideal materials in the area of chemical sensors for their peculiar characteristics. CNTs were realized by Iijima and co-workers in 1991 [65]. CNTs are classified in single-walled carbon nanotubes (SWCNTs) and multi-walled carbon nanotubes (MWCNTs). The former ones are constituted on a single rolled layer of graphene, having diameters between 0.4 nm



and 6 nm, while the length is extending towards few microns [66]. The latter ones whereas are constituted by multiple rolled layers of graphene, having diameters of tens of nm and few  $\mu\text{m}$ -length. SWCNTs and MWCNTs structures are reproduced in Figure 10.

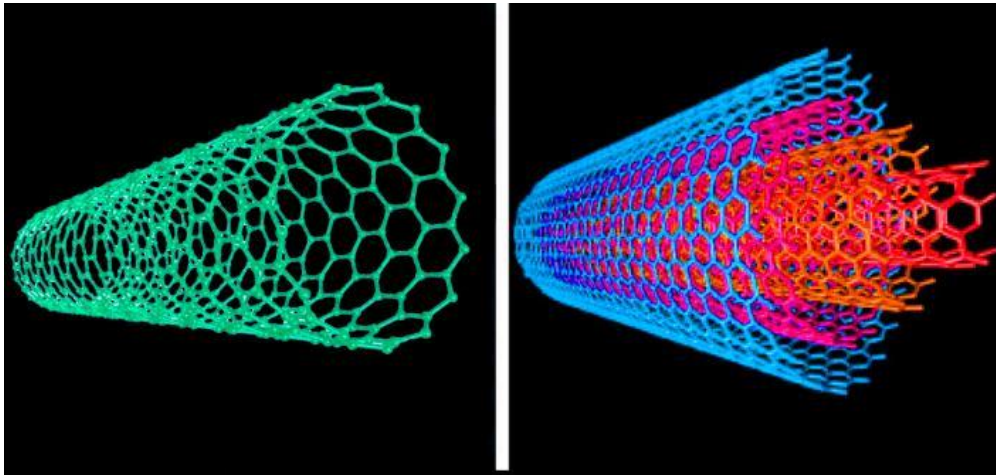


**Figure 10.** Scheme of SWCNT (left) and MWCNT (right) [55].

CNTs generally are subjected to aggregation forming tube bundles for the strong interaction between the nanotubes and they exhibit outstanding electronic and mechanical and electronic features. For instance, SWCNTs have an elastic modulus up to 1 TPa, that is comparable to diamond, their strength is more than 100 times compared to steel, and a density of one-sixth. Moreover, one of the exceptional properties of this material is the great electrical conductivity for a remarkable conjugation effect.

Approximately two-third of SWCNTs present semiconducting properties, while the remaining CNTs are characterized by metallic properties. The latter ones are utilized as single electron transistors, while the former ones find application in field effect transistors (FETs).

MWCNTs are promising sensing elements because they can be miniaturized in portable electronics for their compactness and they present low prizes of production together with lower operating temperatures compared to MOS sensors.

Firstly, CNTs are nearly completely constituted of surface atoms, and usually they display outstanding sensitivity to various adsorbates. CNT sensors display considerable advantages over conventional MOS sensor elements considering their lower working temperatures, great sensitivity and the possibility to miniaturize them in the design and production of massive sensor arrays.

SWCNTs are characterized by elevated environmental stability and aspect ratio, together with excellent electronic and mechanical features. Probably the most interesting aspect is the ultrahigh S/V ratios of these materials. From the work of Kong et al. in 2004 where SWNT field-effect transistors (FETs) were utilized for the measurement of NO<sub>2</sub> and NH<sub>3</sub>, SWCNT-based chemical sensors have been utilized to sense several species, gases and chemical vapors, like O<sub>2</sub>, VOCs, NO<sub>2</sub>, HCl and explosive analytes.

Different typologies of CNT-based sensor devices have been realized, in the three main categories such as field-effect-transistors (FETs), chemicapacitors and chemiresistors. The latter ones are becoming extremely appealing for their not complex structure, low price and the precision of the measurements.

A scheme of chemoresistive CNT sensors is displayed in Figure 11.

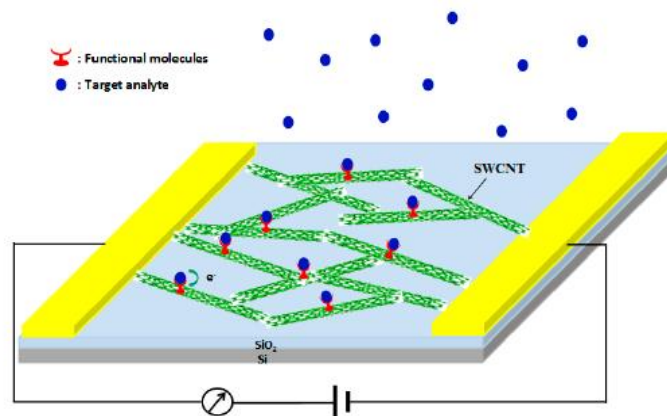


**Figure 11.** Scheme of configuration of chemoresistive CNT sensors [55].

In the chemiresistive sensor showed in figure 11, CNTs act as conductive channels within the electrodes. The variations in conductivity between those two electrodes are measured for studying the sensing performances towards different species.

There are some principal methods that are typically used for the deposition of CNTs between the electrodes: by solid transfer, spraying, printing, drop casting or chemical vapor deposition (CVD) growth. The high sensitivity of CNTs sensors is a consequence of the fact that CNTs are constituted almost completely of surface atoms, and an extremely little variation in the surrounding environment can result in a measurable conductance variation.

### 2.3.2 Sensing mechanism

The CNTs sensing mechanism has been widely described by Fennell et al. [67]. According to this work, the adsorption of analytes onto the CNTs surface generate a variation in the conductivity caused by the phenomena depicted in Figure 12: the adjustment of the Schottky barrier at electrode-CNT junctions, the charge transfer between gas molecules and CNTs, and the increase in the CNTs–CNTs junction distance.

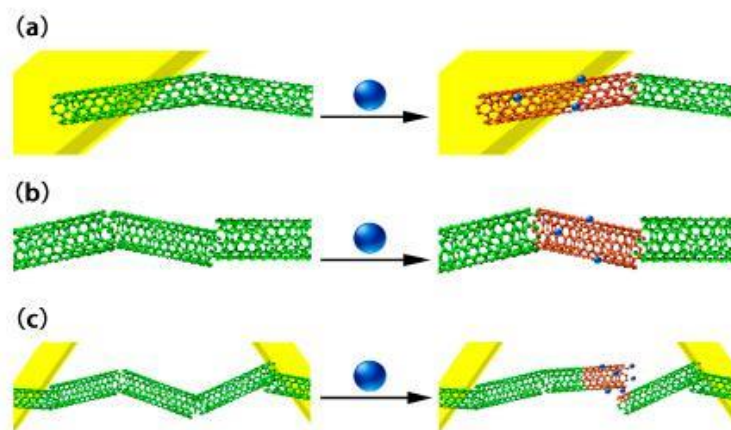


**Figure 12.** Three ways of interaction between analytes and CNTs that result in a change in the conductivity of CNTs. (a) SWNT-electrode junction; (b) charge transfer among the SWNT and target gases; (c) intertube junction [55].

CNTs act as p-type semiconductors under ambient conditions. Reducing species that furnish  $e^-$  into the VB of CNTs, dropping the hole amount, cause a drop in the film conductivity. On the opposite, oxidant species like  $O_3$  and  $NO_2$  withdraw electrons from CNTs valence bond enhancing the amounts of holes in the CNTs, enhancing the conductance of the sensing film. An introduction of scattering sites can induce a reduction of the charge of CNTs, creating a variation in the conductance. A modification of the Schottky barrier can occur when analytes are adsorbed on the CNTs-metal interface. Generally, individual CNTs have not the required elongation to create conducting channels, so a connection of many tubes for the conducting channels take place during the sensing of target molecules. In the case gas molecules are successfully adsorbed on the junction between tubes, the conductivity of CNTs can be modified by manipulating the intertube junctions too.

### 2.3.3 Functionalization of CNTs

CNTs exhibit great properties when they are used as sensing elements, even though the selectivity and the sensitivity for a specific gas is usually low since the interaction between target gas and the CNTs is weak.

A successful method to enhance both the sensitivity and the selectivity of this kind of material is through functionalization [68, 69].

Two principal strategies for the functionalization of CNTs surface are currently available: covalent and non-covalent functionalization [70]. In the former small organic species or metal NPs are covalently linked on the surface of CNTs, while in the latter one supramolecular complexation through wrapping and adsorptive forces are involved, like Van der Waals forces and stacking interactions.

Generally, functionalized CNT sensors show higher sensitivity and selectivity towards target analytes comparing with the pristine CNT sensors.

The covalent functionalization of CNTs could be realized with oxygen-containing groups like OH, COOH, CO onto the CNTs surface in order to link covalently specific molecules on the CNTs surface. When species like carbenes, diazonium ions and free radicals interact with the CNTs surface, they react immediately with the carbons of CNTs forming covalent bonds. The non-covalent functionalization doesn't modify the configuration of the sidewalls of the nanotubes and the right electronic characteristics can be preserved.

Organic polymers are widely utilized in carbon nanotubes gas sensors as sensitive film. The sensing mechanism of those functionalized CNT detectors involve a change in physical-chemical features of the polymers when they interact with target gas molecules. This phenomenon can perturb the conductivity of CNTs. Conducting polymers (e.g., polyaniline, polythiophene, polypyrrole and others) [71] are utilized widely thanks to the semiconducting properties, and in some cases even metallic. The density of  $e^-$  in the conducting polymer can be modified after the adsorption of certain analytes. Metal nanoparticles present also interesting features that are applied in field such as chemistry, physics and electronics [72]. Some studies confirm that when CNTs interact strongly with metallic nanoparticles cluster of Au, Ag, Cu, Co, Ni Pt or Pd a consistent charge reorganization occurs on the surface of CNTs [73, 74]. This type of CNTs exhibit great sensitivity and selectivity to some analytes, like CO, NH<sub>3</sub>, H<sub>2</sub> and others. Moreover, metal functionalization of CNTs results in a higher resistance to temperature and to harsher environments when comparing with the organic molecule-functionalized CNT sensors.

## 2.4 Conclusions

In the last years, the demand for cheap, portable and ease-to use gas sensors for environmental ozone monitoring have increased sharply. In this chapter, a classification of different sensors was firstly proposed. Thus, the main characteristics of chemoresistive gas sensors were presented, with a special focus on ceramic and carbon-based materials. Advantages and disadvantages of those sensors were then discussed.

The basic working principles and the effect of microstructure of the SMO<sub>x</sub> on the sensing features were reviewed. Furthermore, an overview of the main strategies to enhance the sensor response and the selectivity of the sensitive material were explained.

In the next chapter, other methods for sensor preparation will be examined together with the measurement principles of the instruments utilized to characterize the selected materials.

## References

- [1] <https://www.thomasnet.com/articles/instruments-controls/How-Gas-Detectors-Work>, visited on 17th October 2018.
- [2] Wali R. P. (2012) An electronic nose to differentiate aromatic flowers using a real-time information-rich piezoelectric resonance measurement. *Procedia Chem.* pages 194–202.
- [3] Taguchi N., (1962) Patent, 45-38200.
- [4] Seiyama T., Kato A., Fujiishi K. Nagatani M. (1962) *Anal. Chem.* pages 1502.

- [5] Brattain W.H.; Bardeen J. (1952) Surface properties of germanium. *Bell Syst. Tech. J.* pages 1–41.
- [6] Heiland G. (1954) On the influence of hydrogen on the electrical conductivity of ZnO crystals. *Z. Phys.* pages 459–464.
- [7] Yamazoe N. New approaches for improving semiconductor gas sensors. *Sens. Actuators B* pages 7–19.
- [8] Taguchi N. (1971) Gas Detecting Devices. U.S. Patent 3,631,436.
- [9] Seiyama T. (1988) Chemical sensors—Current status and future outlook. *Chemical Sensor Technology*; in Elsevier: Amsterdam, The Netherlands.
- [10] Shimizu Y.; Egashira M. (1999) Basic aspects and challenges of semiconductor gas sensors. *MRS Bull.* pages 18–24.
- [11] Yamazoe N. (2005) Toward innovations of gas sensor technology. *Sens. Actuators B* pages 2–14.
- [12] Jones E. (1987). The pellistor catalytic gas detection, in: P. Moseley, B. Tofield (Eds.), *Solid State Gas Sensors*, Adam Hilger, Bristol pages 17-31.
- [13] Nenov T. G.; Yordanov S. P. (1996). *Ceramic Sensors, Technology and Applications*, Technomic Publishers, Lancaster, pages 138-144.
- [14] Fraden J. (2010) *Handbook of Modern Sensors*, 4th ed. New York: Springer.
- [15] Chen K. Y., Janz K. F., Zhu W., Brychta R.J. (2012). Redefining the roles of sensors in objective physical activity monitoring, *Med Sci Sports Exerc*, pages 13.
- [16] *Terms and Definitions in Industrial Process Measurement and Control*, (IEC draft 65/84) International Electrotechnical Committee (1982).
- [17] Norton H. N. (1989). *Handbook of Transducers*. Prentice-Hall, Englewood Cliffs, NJ.
- [18] White R. W. (1991). A sensor classification scheme. In: *Microsensors*. IEEE Press, New York pages 3–5.
- [19] Kim H. J., Lee J. H. (2014). Highly sensitive and selective gas sensors using p-type oxide semiconductors: Overview, *Sens Actuators B* pages 607–627.
- [20] Lang I., Firsov Y.A. (1963). Kinetic theory of semiconductors with low mobility. *Sov Phys JETP*, pages 1301.
- [21] Hoffheins B. (1996). Solid State, Resistive Gas Sensors, in *Handbook of chemical and biological Sensors*, R.F. Taylor and J.S. Schultz, eds., Philadelphia: Institute of Physics.
- [22] Sofian M. K.; Oussama M. E.; Imad A. A.; Marsha C. K. (2009) Semiconducting metal oxide-based sensors for selective gas pollutant detection. *Sensors* pages 8158–8196.
- [23] Wang C., Yin L., Zhang L., Xiang D., Gao R. (2010). Metal oxide gas sensors: Sensitivity and influencing factors. *Sensors* pages 2088–2106.

- [24] Wisitsoraat A., Tuantranont A., Comini E., Sberveglieri G., Wlodarski W. (2009). Characterization of n-type and p-type semiconductor gas sensors based on NiO<sub>x</sub> doped TiO<sub>2</sub> thin films. *Thin Solid Films* pages 2775–2780.
- [25] Yamazoe N., Shimano K. (2002). Theory of power laws for semiconductor gas sensors. *Sens. Actuators B* pages 566–573.
- [26] Batzill M., Diebold U. (2005) The surface and materials science of tin oxide. *Prog. Surf. Sci.* pages 47–154.
- [27] Hofer U., Böttner H., Felske A., Kühner G., Steiner K., Sulz G. (1997). Thin-film SnO<sub>2</sub> sensor arrays controlled by variation of contact potential-A suitable tool for chemometric gas mixture analysis in the TLV range. *Sens. Actuators B* pages 429–433.
- [28] Jarmo K., Jani M., Niina H., Teemu K., Géza T., Maria S., Andrey S., Jyri-Pekka M., Heli J., Krisztián K. (2011). Gas sensors based on anodic tungsten oxide. *Sens. Actuators B* pages 293–300.
- [29] Wisitsoraat A., Tuantranont A., Comini E., Sberveglieri G. (2007). Gas sensing properties of CNT-SnO<sub>2</sub> nanocomposite thin film prepared by E-beam evaporation. Proceedings of 2007 IEEE Sensors, Atlanta, GA, USA, pages 550–553.
- [30] Hallil H.; Chebila F.; Menini P.; Pons P.; Aubert H. (2010). Feasibility of wireless gas detection with an FMCW RADAR interrogation of passive RF gas sensor. Proceedings of 2010 IEEE Sensors, Kona, HI, USA, pages 759–762.
- [31] Niskanen A. J., Varpula A., Utriainen M., Natarajan G., Cameron D. C., Novikov S., Airaksinen V., Sinkkonen J., Franssila, S. (2010). Atomic layer deposition of tin dioxide sensing film in microhotplate gas sensors. *Sens. Actuators B* pages 227–232.
- [32] Harrison R. V. (2010). Chemical Sensors: properties, performance and applications, Chemistry Research and Applications.
- [33] Berger F., Sanchez J., Heintz O. (2009). Detection of hydrogen fluoride using SnO<sub>2</sub>-based gas sensors: Understanding of the reactional mechanism. *Sens. Actuators B* pages 152–157.
- [34] Cordos E., Ferenczi L., Cadar S., Costiug S., Pitl G., Aciu A., Ghita A., Chintoanu M. (2006). Methane and carbon monoxide gas detection system based on semiconductor sensor. In Proceedings of 2006 IEEE International Conference on Automation, Quality and Testing, Robotics, Cluj-Napoca, Romania, pages 208–211.
- [35] Dong H. Y., Chul H. K., Hyung-Ki H., Seung-Ryeol K., Kyuchung L., Ho G. S., Ji E. K. (1997). Highly sensitive and selective ammonia gas Sensor. Proceedings of 1997 International Conference on Solid State Sensors and Actuators, Chicago, IL, USA, pages 959–962.

- [36] Kwan T. N., Boussaid F., Bermak A. (2011). A CMOS single-chip gas recognition circuit for metal oxide gas sensor arrays. *IEEE Trans. Circuit. Syst. I* pages 1569–1580.
- [37] Kwon C. H., Yun D. H., Hong H., Kim S., Lee K., Lim H. Y., Yoon K. H. (2000). Multi-layered thick-film gas sensor array for selective sensing by catalytic filtering technology. *Sens. Actuators B* pages 327–330.
- [38] Portnoff M. A., Grace R. G., Guzman A. M., Runco P. D., Yannopoulos L. N. (1990). Enhancement of MOS gas sensor selectivity by ‘on-chip’ catalytic filtering. Proceedings of Technical Digest of the 3rd International Meeting on Chemical Sensors, Cleveland, OH, USA.
- [39] Lee D. D., Chung W. Y., Choi M. S., Baek J. M. (1996). Low-power micro-gas sensor. *Sens. Actuators B* pages 147–150.
- [40] Jaegle N., Meisinger T., Bottner H., Muller G., Becker T., Braunmuhl C.B. (1999). Micromachined thin film SnO<sub>2</sub> gas sensors in temperature-pulsed operation mode. *Sens. Actuators B* pages 130–134.
- [41] Comini E. (2005). Metal oxide nano-crystals for gas sensing. *Analyt. Chim. Acta* pages 28–40.
- [42] Kanan S., El Kadri O. M., Abu-Yousef I. A., Kanan M. C. (2009). Semiconducting metal oxide-based sensors for selective gas pollutant detection. *Sensors* pages 8158–8196.
- [43] Franke M. E., Koplín T. J., Simon U. (2006). Metal and Metal Oxide Nanoparticles in Chemiresistors: Does the Nanoscale Matter? *Small*. Pages 36–50.
- [44] Korotcenkov G., Cho B. K. (2017). Metal oxide composites in conductometric gas sensors: achievements and challenges, *Sens. Actuators B* pages 182–210.
- [45] Righettoni M., Amann A., Pratsinis S.E. (2015). Breath analysis by nanostructured metal oxides as chemo-resistive gas sensors, *Mater. Today* pages 163–171.
- [46] Wang C. (2010). Metal oxide gas sensors: sensitivity and influencing factors. *Sensors* pages 2088-2106.
- [47] Madou M. J.; Morrison S. R. (2012). Chemical sensing with solid state devices. Elsevier.
- [48] <https://ephtracking.cdc.gov/showCoRisk.action>, visited on 10<sup>th</sup> October 2018.
- [49] Liu X. (2012). A survey on gas sensing technology. *Sensors* pages 9635-9665.
- [50] Patil S. J., Patil A. V., Dighavkar V. G., Thakare K. S., Borase R. Y., Nandre S. Y., Deshpande N. G., Ahire R. R. (2015). Semiconductor metal oxide compounds-based gas sensors: a literature review. *Front. Mater. Sci.* pages 14–37.



- [51] Bochenkov V. E., Sergeev G. B. (2010). Metal oxide nanostructures and their applications, in: A. Umar, Y.B. Hahn (Eds.), *Metal Oxide Nanoparticles and Their Applications*, American Scientific Publication, pages 31–52.
- [52] Zhang M., Yuan Z., Song J., Zheng C. (2010). Improvement and mechanism for the fast response of a Pt/TiO<sub>2</sub> gas sensor, *Sens. Actuators B* pages 87–92.
- [53] Yuasa M., Masaki T., Kida T., Shimano K., Yamazoe N. (2009). Nanosized PdO loaded SnO<sub>2</sub> nanoparticles by reverse micelle method for highly sensitive CO gas sensor, *Sens. Actuators B* pages 99–104.
- [54] Mohammadi M. R., Fray D. J. (2010). Nanostructured TiO<sub>2</sub>–CeO<sub>2</sub> mixed oxides by an aqueous sol–gel process: Effect of Ce: Ti molar ratio on physical and sensing properties. *Sens. Actuators B* pages 631–640.
- [55] Tang R, Shi Y., Hou Z., Wei L. (2017). Carbon nanotube-based chemiresistive sensors. *Sensors* pages 882.
- [56] Jian M., Wang C., Wang Q., Wang H., Xia K., Yin Z., Zhang M., Liang X., Zhang Y. (2017). Advanced carbon materials for flexible and wearable sensors. *Sci China Mater.* pages 1026–1062.
- [57] Korotcenkov G., Brinzari V., Ham M.-H. (2018). Materials Acceptable for Gas Sensor Design: Advantages and Limitations. *Key Eng. Mater.* pages 80–89.
- [58] Wang C., Li X., Gao E., Jian M., Xia K., Wang Q., Xu Z., Ren T., Zhang Y. (2016). Carbonized Silk Fabric for Ultrastretchable, Highly Sensitive, and Wearable Strain Sensors. *Adv. Mater.* pages 6640–6644.
- [59] Zhang M., Wang C., Wang H., Jian M., Hao X., Zhang Y. (2017). Carbonized Cotton Fabric for High-Performance Wearable Strain Sensors. *Adv. Funct. Mater.* pages 1604795.
- [60] Nanda S., Dalai A. K., Berruti F., Kozinski J. A. (2015). Biochar as an exceptional bio resource for energy, agronomy, carbon sequestration, activated carbon and specialty materials. *Waste Biomass Valor* pages 201–235.
- [61] [https://www.biochar.ac.uk/cms/i/user/standard\\_materials/21\\_SWP%20700-web.pdf](https://www.biochar.ac.uk/cms/i/user/standard_materials/21_SWP%20700-web.pdf) (Visited on 19<sup>th</sup> February 2017).
- [62] [https://www.biochar.ac.uk/cms/i/user/standard\\_materials/19\\_OSR\\_700-web.pdf](https://www.biochar.ac.uk/cms/i/user/standard_materials/19_OSR_700-web.pdf) (Visited on 19<sup>th</sup> February 2017).
- [63] Ahmad S., Khushnood R.A., Jagdale P., Tulliani J.-M., Ferro G. A. (2015). High performance self-consolidating cementitious composites by using micro carbonized bamboo particles. *Mater. Des.* pages 223–229.
- [64] Ziegler D., Palmero P., Giorcelli M., Tagliaferro A., Tulliani J.-M. (2017). Biochars as innovative humidity sensing materials. *Chemosens.* pages 35.

- [65] Iijima S. (1991). Helical microtubules of graphitic carbon. *Nature* pages 56–58.
- [66] Merkoçi A., Pumera M., Llopis X., Pérez B., del Valle M., Alegret S. (2005) New materials for electrochemical sensing VI: Carbon nanotubes. *Trac. Trend. Anal. Chem.* pages 826–838.
- [67] Fennell J. F. Jr., Liu S. F., Azzarelli J. M., Weis J. G., Rochat S., Mirica K. A., Ravnsbaek J. B., Swager T. M. (2016). Nanowire chemical/biological sensors: Status and a roadmap for the future. *Angew. Chem. Int. Ed. Engl.* pages 1266–1281.
- [68] Hu H., Zhang T., Yuan S., Tang S. (2016). Functionalization of multi-walled carbon nanotubes with phenylenediamine for enhanced CO<sub>2</sub> adsorption. *Adsorption* pages 73–85.
- [69] Kim E., Jeong H. S., Kim B. M. (2014). Studies on the functionalization of MWNTs and their application as a recyclable catalyst for CC bond coupling reactions. *Catal. Commun.* pages 71–74.
- [70] Ihsanullah, Asmaly H. A., Saleh T. A., Laoui T., Gupta V. K., Atieh M. A. (2015). Enhanced adsorption of phenols from liquids by aluminum oxide/carbon nanotubes: Comprehensive study from synthesis to surface properties. *J. Mol. Liq.* pages 176–182.
- [71] Srivastava S., Sharma S. S., Kumar S., Agrawal S., Singh M., Vijay Y. K. (2009). Characterization of gas sensing behavior of multi walled carbon nanotube polyaniline composite films. *Int. J. Hydrogen Energy* pages 8444–8450.
- [72] Kumar S., Ahlawat W., Kumar R., Dilbaghi N. (2015). Graphene, carbon nanotubes, zinc oxide and gold as elite nanomaterials for fabrication of biosensors for healthcare. *Biosens. Bioelectron.* pages 498–503.
- [73] Penza M., Rossi R., Alvisi M., Signore M. A., Cassano G., Dimaio D., Pentassuglia R., Piscopiello E., Serra E., Falconieri M. (2009). Characterization of metal-modified and vertically-aligned carbon nanotube films for functionally enhanced gas sensor applications. *Thin Solid Films* pages 6211–6216.
- [74] Saha K., Agasti S. S., Kim C., Li X., Rotello V. M. (2012). Gold nanoparticles in chemical and biological sensing. *Chem. Rev.* pages 2739–2779.

# List of Figures

- Figure 1.** Interdigitated electrode chemical sensor.
- Figure 2.** Models of diffusion processes in (a) thick layer and (b, c) thin layer.
- Figure 3.** Sol gel method scheme.
- Figure 4.** Scheme of sputtering process.
- Figure 5.** Scheme of flame spray process.
- Figure 6.** Scheme of the four stages-spin coating deposition.
- Figure 7.** The four stages of dip coating method.
- Figure 8.** Components of the screen-printing technique.
- Figure 9.** A plain weave pattern of a typical thick layer screen.
- Figure 10** Cross-sectionional side view illustration of the process from top to bottom chronologically in the fabrication of a screen-printed device supported by a substrate.
- Figure 11.** Schematic diagram of sensors preparation by means of the screen-printing technique.
- Figure 12.** Changes in the ink viscosity at different stages of the printing process.
- Figure 13.** Scheme of the chemical sensor fabricated by screen printing: (a) front view, (b) side view. The proportions between the components are exaggerated for explanatory purpose, whereas the quotes are referred to the real sizes. In the image, solid black lines are platinum interdigitated electrodes, dark grey is the film of the sentivite material, and the white area represent the  $\alpha$ -Al<sub>2</sub>O<sub>3</sub> substrate.
- Figure 14.** Home made system for sensing testing.
- Figure 15.** Scheme of a laser granulometer.
- Figure 16.** Scheme of DTA cell.
- Figure 17.** Representation of a BET plot.
- Figure 18.** Scheme of an X-ray tube for the production of X-rays.
- Figure 19.** XRD pattern of Mo vs the applied tension.
- Figure 20.** Interaction of X-rays with materials.
- Figure 21.** Schematic of a typical diffractometer.
- Figure 22.** Interference of X-rays scattered by crystals.
- Figure 23.** XPS analyser.
- Figure 24.** Schematic setup of Scanning Electron Microscope.
- Figure 25.** Volume and mechanism of interaction between e<sup>-</sup> and matter (SEM).
- Figure 26.** Scheme of a TEM, imaging mode (left), diffraction mode (right).

# Chapter 3 - Fabrication of sensors and materials characterization

## 3.1 Fabrication of sensors

### Abstract

Sensitive films are divided in thin film ( $<1\mu\text{m}$  of thickness) and thick film ( $>1\mu\text{m}$  of thickness). In this chapter, different deposition techniques are detailed, with a special focus of those used in this thesis for thick film preparation: i.e. dip coating and screen-printing techniques. A chemical sensor thick film typically consist on three parts: the sensitive film, the electronic circuit and the dielectric substrate. Thus, the operative conditions of a home-made dynamic system for sensor test towards different gases are displayed, and the main analytical technique used for material characterization are presented: laser granulometry, DTA-TG,  $\text{N}_2$  adsorption, XRD, XPS, FESEM and TEM analysis.

### 3.1.1 Substrate

The main requirement for a substrate is to provide electrical insulation and mechanical support for the sensitive films and the electronic circuit. The principle considerations to choose the substrate are the following:

- *Dielectric constant*: This parameter defines the capacitance of various materials prepared onto the substrate.
- *Thermal conductivity*: If this parameter is high, substrates are suitable for applications at high temperature.
- *Thermal coefficient of expansion*: It should be closely aligned to the sensitive elements and the other constituents.

The most utilized materials for thick film technique are alumina ( $\text{Al}_2\text{O}_3$ ), beryllia ( $\text{BeO}$ ) and aluminium nitride ( $\text{AlN}$ ), three ceramic materials. Thus, Si has also been adopted in some transducer exploitations. Among them,  $\text{Al}_2\text{O}_3$  is the most used substrate because of its physical-chemical properties and for its low price.  $\text{Al}_2\text{O}_3$  of 96% purity indeed find application in the major part of commercial circuits all over the world.  $\text{BeO}$  has a great thermal conductivity but it is toxic, and it find application only in limited areas.

AlN is also characterized by great thermal conductivity and excellent mechanical properties. Finally, substrates of insulated stainless steel are adopted in some exploitations where a superior thermal dissipation and mechanical roughness are needed [1].

In this work, laser-cutted  $\alpha$ -alumina substrates were used. They are manufactured by Al<sub>2</sub>O<sub>3</sub> powder, mixtured with low quantity of SiO<sub>2</sub>, Mg (OH)<sub>2</sub> and Ca (OH)<sub>2</sub>. These are also ball- or roll-milled for around 10 hours with solvents, lubricants and binders to provide precise mixing. Typically, the thickness of thick film substrates is lower than 1 millimeter (in the substrates utilized, it was equal to 0.38 mm), and the preferable way of fabrication is sheet casting. A slurry flows out onto a girde, passing under a metal doctor blade able to control precisely the obtained thickness. Thus, the material is successfully dried in air for removing the solvent. Finally, the substrates are fired for at least 12 h at 1500°C to sinter properly the material.

### **3.1.2 Electronic circuit**

Their main function of the electronic circuit is to furnish interconnection between the different elements. Conductors supply the terminations for thick film resistors. The features of the electronic circuit depend on the composition of the active part of the ink. In general, these comprehend precious metals like Ag, Au, Pt or Pd. The size, shape and distribution of the particles impact the electrical characteristics of the fired layer too.

Among electronic circuits, of interdigitated electrodes ehibit an enhanced contact area between the sensitive matarial and the electronic circuit. There are two types of layers: capacitive and resistive.

### **3.1.3 Active layers**

Considering capacitive sensors, the sensitive film is a dielectric between two electrodes that are parallel each others, whereas in resistive chemical sensors, the sensitive film is a resistor between the same electrodes. As a consequence, the response of a capacitive sensor to stimuli is evaluated by a variation in the sensor capacitance, while the reaction of a resistive sensor to analytical stimuli is evaluated by alterations in the film resistance [2].

Capacitive chemical sensors usually necessitate a sensing element with modest conductivity for an efficient use as dielectric material. On the other side, resistive sensors are subjected to a current flow accross the sensing layer to accomplish an analytical measurement. When the sensing layer interacts with an analyte, its

conductance exhibits an alteration. Consequently, the resistance across a length of the layer is altered too. The film resistance varies when the sensor interacts with different quantities of analyte gas. A big serpentine gap area between the electrodes is an important advantage for both capacitive and resistive chemical sensors. Interdigitated electrode sensor can be patterned as a string of single resistors ordered in parallel. In Figure 1 an image of interdigitated electrode chemical sensor is illustrated.

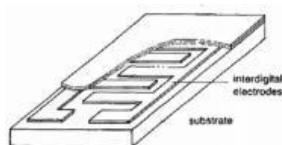


**Figure 1.** Interdigitated electrode chemical sensor [3].

In this thesis, thick films were fabricated by screen-printing technology onto  $\alpha$ -alumina ceramic substrates (Coors Tek, Golden, CO, USA, ADS-96, 96%  $\text{Al}_2\text{O}_3$ , 0.85 cm x 1.7 cm) with Pt electrodes that are interdigitated each others (5545-LS, ESL, King of Prussia, PA, USA) over the dielectric substrate. The circuit was fired at 980°C (2°C/minute of rate) for 18 min obtaining a satisfying adhesion. In addition, the electrical conductance was optimized, in accordance with the recommendations of the manufacturer.

The pastes for screen-printing were obtained by adding the sensitive elements with an organic vehicle (ethylene glycol monobutyl ether, Emflow, Emca Remex, USA), to obtain the right rheology and a proper viscosity, and polyvinyl butyral (PVB, Sigma Aldrich), acting as a momentary binder previously to firing stage.

Subsequently to the screen-printing step with a 325-mesh mask of steel, sensors were dried at 80°C for 12 h. Thus, they were fired at the proper T for removing all the organic components and to guarantee the adequate adhesion onto the substrate at the same time.

### **3.1.4 Influence of layer parameters on gas sensing**

The specific characteristic of film structure is depicted in Figure 2.

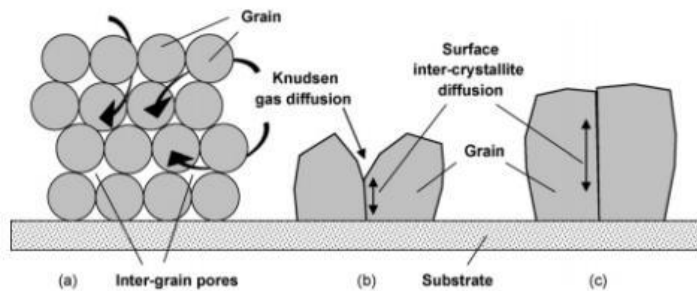


**Figure 2.** Models of diffusion processes in (a) thick layer and (b, c) thin layer. Reproduced with permission from [4], published by Elsevier, 2009.

In evaluating the experimental results in literature, sensors realized by thin and thick film techniques possess their specific characteristics when interacting with the analyte, despite the type of the gas sensing material.

In accordance with [4], an enhancement of the layer thickness is correlated by either a decrease in  $O_3$  sensor response and a drop in sensitivity to the reductants. Those results were obtained at  $300^\circ\text{C}$ . In addition, an enhancement in the layer thickness is associated to a decrease in the optimum working  $T$  of the sensor. For instance, when the film thickness is equal to several microns, under  $O_3$  exposure, the top layers of the  $\text{SnO}_2$  exploit as a filter [5], preventing a deep penetration of  $O_3$  into the sensing element.

Improving the sensitivity at low working  $T$  is a way to decrease energy consumption increasing the service life of thick film sensors. Nonetheless, such a variation is matched with higher response and recovery times, in agreement with an investigation of the velocity of sensor response.

However, thin films are not characterized by the same porosity of sensors realized by ceramic or thick film techniques [6].

For decreasing sensor  $\tau_{\text{ads}}$  and  $\tau_{\text{des}}$ , thin films can be selected. Here, the sensitivity is delimited by the performance of surface phenomena, whereas the gas diffusion in the sensing layer (that restricts the velocity of sensor response) has no impact on the sensor response. However, when the velocity of sensor response is not a crucial parameter, thick films can be selected for the sensor design, since they furnish higher sensitivity at lower operating temperatures.

Finally, the decrease of film thickness and grain size are the preferred methods to optimize the time constants of the major part of gas sensors.

The adhesion of the film over the substrate is essential for practical use in environmental monitoring. This ensures an efficient ohmic contact between the sensitive film and the circuit.

According to their structural characteristics, thin films are classified into two different categories: single crystals and polycrystals. The former ones are not commonly utilized as gas sensors since they do not present grain boundaries and as a result, they exhibit only modest changes of electrical resistance when exposed to oxidants and reductants [7]. Furthermore, the later ones are more appropriate as gas sensors. Charge transport occurs through grain boundaries. This is one of the principal phenomena that govern the sensor response towards oxidant and reducing gasses. For instance, Dibbern et al. [8] demonstrates that the growth parameters of thin films deposited by r.f. sputtering strongly influence their response to gasses. The deposition of an active layer into a substrate is one of the crucial steps for the realization of the sensor device. After that, firing is a necessary step for achieving a film that is homogeneous and stable. Structural alterations can occur to the material during the process of firing (e.g. increasing the grain size by heating). Moreover, the concentration of grain boundaries is a critical parameter in the sensing characteristics. The alteration of the crystallite size could affect directly the mobility and the amount of charge carriers modifying the sensitivity of a metal oxide towards a target gas.

Nowadays, a wide range of deposition techniques for preparing chemical sensors devices are available: from sol-gel techniques to sputtering, from thermal spraying to screen-printing, from spin-coating to drop-coating methods.

The actual limits of existing chemoresistive sensors have involved the requirement of valid options and in the last years, nanomaterials have exhibited the possibility to transform deeply the gas sensor technology [9].

### **3.1.5 Sol-gel technique**

A sol is a stable suspension consisting in colloidal particles in a liquid, and a gel is a porous 3-D network that evolves into a liquid. Gel is produced in the case the dispersion into the suspension becomes rigid [10].

The sol-gel chemistry is divided in two different routes:

- gelation of colloidal particles
- alkoxide precursors hydrolyzed and then polycondensated succeeded by a hypercritical drying or aging at room T.

Through sol-gel steps, distinct coatings can be developed, from thicknesses of a few nm to tens of  $\mu\text{m}$  on distinguishing substrates. A scheme of this procedure is displayed in Figure 3.



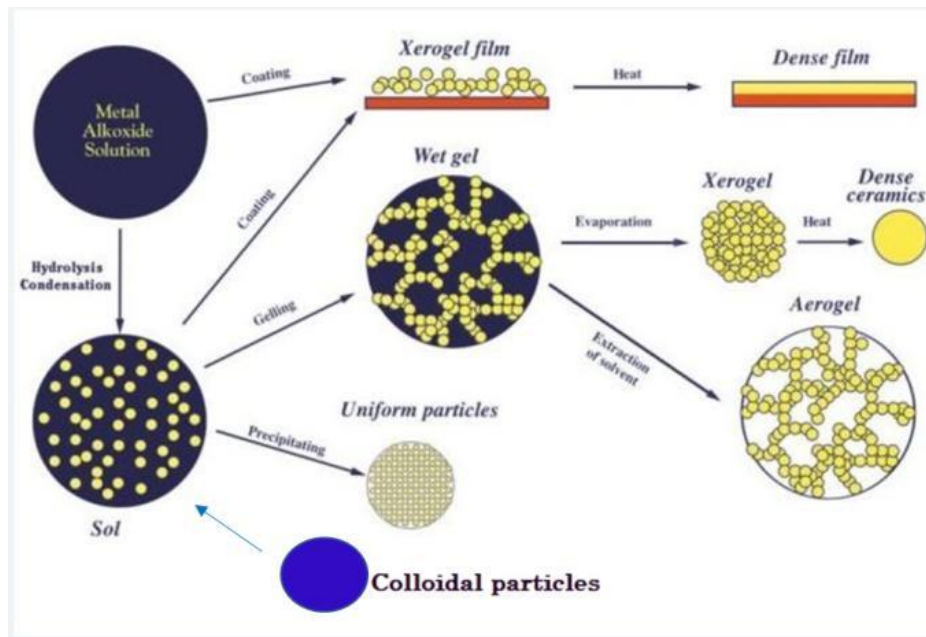


**Figure 3.** Sol gel method scheme [11].

Firstly, a mixture is prepared. It is generable by mechanical blending of colloidal particles in H<sub>2</sub>O in a pH range that prevent any precipitation or by hydrolyzing a precursor of metal alkoxide, following the  $M(OR)_x$  where R is indicating a hydrocarbon and M the metallic compound.

Different synthesys routes can be followed, together several reagents and operative conditions.

The gelation is a certain period (from hours to days), in which the poly-condensation keep on decreasing significantly the porosity. After the aging of the gel, a drying step must be performed resising to crack formation. During the drying stage, stresses could result in cracks except if the drying stage is checked by decreasing the liquid surface energy with surfactants or by pores elimination [12].

The last step for sol–gel coatings is the densification. In many studies an enhancement of the crystallite size when the temperature of calcination was raised and succeeded by a drop in the sensing behavior was reported.

### 3.1.6 Sputtering technique

Sputter deposition is an extensively utilized technique for thin layer deposition into substrates. The tecnology consist on a bombardment of ions on a source material, i.e. the target. This results into a vapor phase for totally physical process, i.e. the s target sputtering. This is a physical vapor deposition technique. They include both

thermal evaporation and pulsed laser deposition. The most used methodology to grow thin films by sputtering consist in the utilization of a magnetron source whose target is bombarded by cations in plasma of a magnetically enhanced glow discharge. An image of PVD (Physical Vapor Deposition) is displayed in Figure 4.

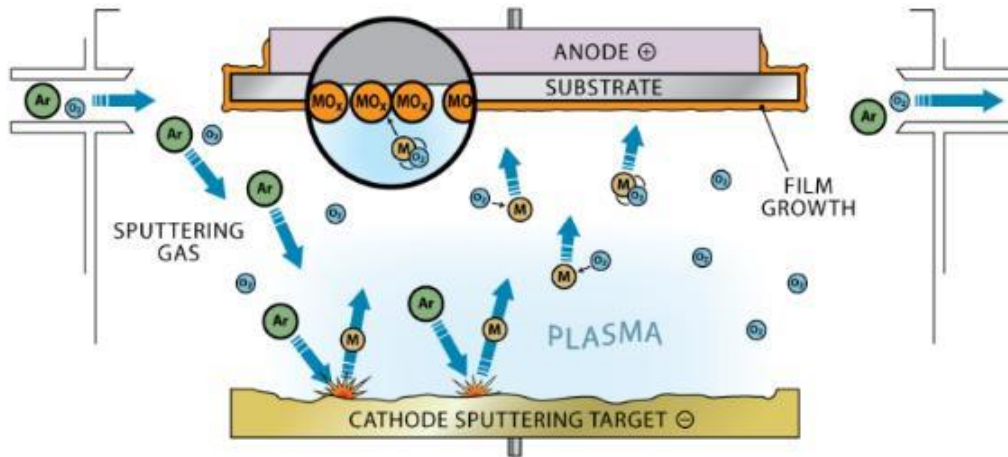


**Figure 4.** Scheme of sputtering process [13].

The target can be supplied in diverse modes, using radio frequency (RF) for targets that are nonconductive, or direct current (DC) for targets that are conductive, until different methods of applying voltage and/or current impulses to the target. The addition of specific chemical compounds for the deposition of a layer should be performed ad hoc by adding reactive gas to the plasma, i.e. reactive sputtering. The unpleasant interaction between reactive species and the target material results in a nonlinear behavior of the deposition parameters in dependence of the reactive gas flow. For modeling this attitude, the fluxes of the different species to the target should be defined. At the same time, it is important to adjust the flows of the incident species on the substrate since they impact the reactive sputter deposition procedure controlling at the same time the growth of the desired film [14].

### 3.1.7 Thermal spraying technique

The thermal spraying techniques consists in the preparation of a coating where materials that are heated or melted are sprayed onto a surface. The "*feedstock*", i.e. the precursor of the coating, is heated by an electrical carry - plasma or an arc- or with a chemical agent like a combustion flame.

With this technique, it is possible to obtain thick coatings (from 20  $\mu\text{m}$  to many mm of thickness) over a large area at high rate of deposition in comparison to other procedures of coating, i.e. physical and chemical vapor deposition. There are many materials accessible for thermal spraying: from ceramics to metals, from alloys to plastics and composites. They are in different conditions, from powder or wire, heated to a molten state. Then they are speeded up towards substrates in the form of microparticles. The most utilized energetic sources of energy for thermal spraying are combustion and electrical arc discharge. The obtained coatings consist in an accumulation of a great number of sprayed particles. The surface usually does not heat up significantly, permitting to coat flammable substances too.

The quality of coating is typically improved by controlling its content in oxide, its porosity, macro and micro-hardnesses, together with the bond strength and the surface roughness. In general, the grade of the coating is higher when the speed of the particles is increased to more than 40 m/s.

Amongst the thermal spray approaches, the cheapest and simplest for the deposition of the coating is the flame spraying (combustion spraying). An illustration of this technology is displayed in Figure 5.

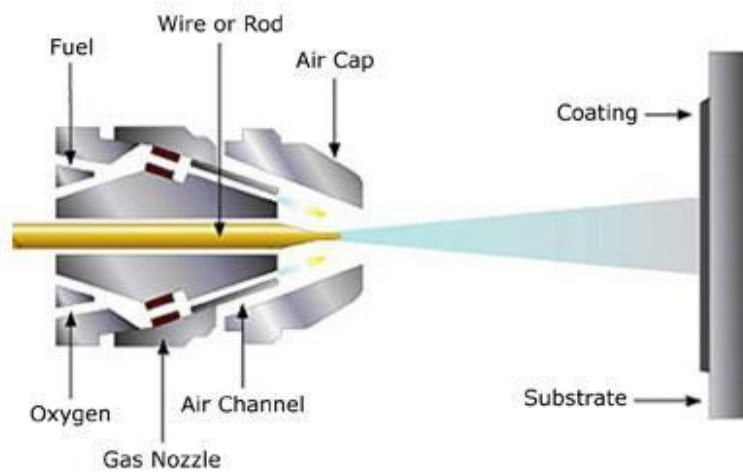


**Figure 5.** Scheme of flame spray process [15].

The process consists in the reaction of  $\text{O}_2$  with a fuel of combustion ( $\text{H}_2$  or  $\text{C}_2\text{H}_2$ ) to generate a heat source that produces a gas stream.

The feedstock that is sprayed is fed into the flame as a wire, and compressed air is utilized subsequently in order to atomise the molten with the accelerated particles into the substrate. In the combustion powder process, the only differentiation is that the powder substitutes the wire feed stock. This technique may also be utilized to create porous structures. The main advantage of this technology is that a large

choice of coatings can be prepared from an overall range of materials in the powder form. The limit of the flame spray process is the use of materials with elevated temperature of melting compared to the flame and the decompositions must be avoided. It is possible to obtain porous coatings with low bond strength of deposit and low adhesive power between coating and the substrate.

### 3.1.8 Spin coating method

Spin-coating is a widely utilized approach to apply liquid coatings upon a rotating substrate. A characteristic spin-coating method is constituted by four basic stages that are schematically illustrated in Figure 6.

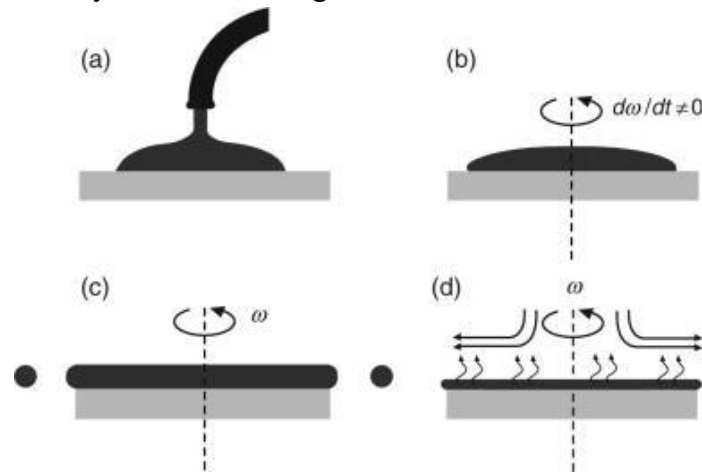


**Figure 6.** Scheme of the four stages-spin coating deposition [16].

Spin coating typically includes the exploitation of a film (from few nm to few  $\mu\text{m}$ ) regularly through the surface of a substrate by coating a solution of the desirable sensitive element in a solvent (an 'ink') when the system is spinning.

- In the deposition step (a), the coating ink with the desired material and a proper solvent is firstly applied onto the substrate. The quantity of applied liquid is a function of the liquid viscosity and on the dimension of the substrate.
- During the acceleration stage (b), a centrifugal force disperses the ink through the substrate. The rotating velocity is regulated at a proper value based on the requested layer thickness, since the thickness of a spin coated film is inversally proportional to the rotating speed squared.
- The coated substrate is spun quicker (c). The ink flows radially outer, while the surplus liquid streams to the perimeter and get off as droplets.

- In the last step (d), the solvent evaporates leaving just the target molecules on the surface.

This method finds application in several industries and technology areas. The pros of this technique are their possibility to generate very uniform films in an easy and quick way.

The utilization of spin coating in nanotechnology and organic electronics is increasing in last decades.

It is employed to coat substrates with many materials, from organic semiconductors to photoresistors, from insulators to nanomaterials, from synthetic metals to transparent conductive oxides and metal oxide precursors. It is omnipresent across the semiconductor R&D/Industrial sectors.

The pros of spin coating are the simplicity of the process formulation and the thin and uniform coating achievable. In addition, the high airflow brings fast drying due to the high spin speeds, resulting in a great constancy at either macroscopic and nanometric levels.

The main limit of this technique is that the quick drying procedure can also result in modest performance for some specific nano-technologies (e.g. small molecule OFETs). They need time to crystallize and/or self-assemble. Finally, the actual material uses in this process is generally less than 10%, and the remaining is wasted. Despite these drawbacks, spin coating is an effective and important technology for realization of thin film and with a little practise it can be used to produce film that are uniform and of high-quality.

### **3.1.9 Drop coating route**

In addition to spin coating technique, another deposition method that is extremely suitable for thin film realization is dip-coating method.

This method needs to immerse the substrate in a solution of precursor. After interaction with the liquid, the substrate is tuck up realizing the deposition of a thin film. In this method, the velocity of removal has a relevant effect in the thickness of the coating. A scheme of dip coating technique is displayed in Figure 7.

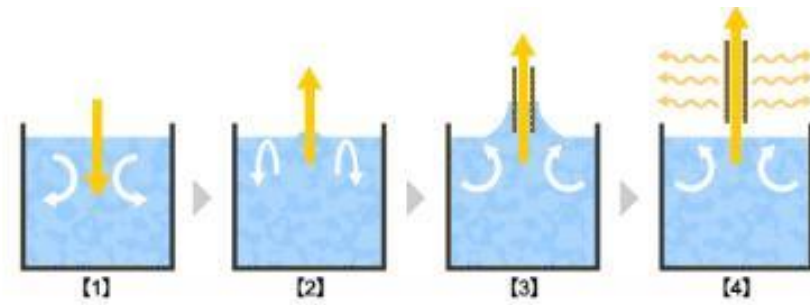


**Figure 7.** The four stages of dip coating method [17].

Firstly, a sample is submerged vertically into the coating solution. Subsequently, it is withdrawn at a speed adjusted according to some parameters such as the surface tension, the viscous force and the gravity of the solution.

In dependence of the speed of sample withdraw, film thickness is adjustable considering the relation between the viscosity and the gravity causing adhered liquid to fall. A uniform thin film is generated after removing the surplus of solution by drying and firing. By dip coating method, it is possible to coat both sides of the substrate in a single process, with smaller loss of coating liquid and lower quantity of coating liquid needed. Moreover, comparing with spin coating methods, it is compatible with all shapes of substrates. Furthermore, it is a cost-effective approach since, differently from dry processing approaches, expensive facilities such as vacuum furnaces are not requested. With dip coating, increased processing volumes and capacity of production can be accomplished.

In this thesis, screen-printing and dip coating methods were deployed to produce thick-film sensors in a cheap, easy and reproducible way.

### 3.1.10 Screen printing technique

The manufacture of the thick-film sensors is an additive process involving the deposition of one or more layers of the ink onto an electrically insulating substrate. It is well known that printing technologies find application in high-tech form and are used to produce a broad range of devices and components which are:

- Electric discrete components (wirings, bus-bars, electrodes, resistors, inductors, antennas, capacitors)
- Active electronic devices (solar cells, transistors, photo-diodes, OLED)
- Memory devices (ferroelectric capacitors)
- Energy storage (batteries)
- Sensors (physical, chemical)

➤ Flexible hybrid systems (printing+SMD)

Moreover, by screen-printing technique sensors based on different sensing principles are printable: capacitive, resistive, inductive, amperometric, voltammetric, impedance, thermoelectric, piezoresistive, piezoelectric, photoelectric, pyroelectric, resonant and optical.

Also known as serigraph printing, serigraphy and silkscreen, the screen-printing technique is one of the ancient methods of printing – and at the same time, one of the methods with the greatest future ahead of it. The first serigraphic fabrics were made of silk, that generates the name of this technology. It is based on a simple idea that could be easily transferred to a huge variety of materials.

In this method, a screen is utilized for keeping the ink applied from certain areas of a surface being printed: i.e. only regions permit the paste through onto the substrate. In fact, the screen is impermeable to the ink, except for the designed image. The ink passes through the screen, under the action of a squeegee, resulting in a printed image of the desired design transferred on the substrate. It is a versatile technique with a reliable control on the film thickness and a great durability, even if it requires usually the machine to set up. In the last years, screen printing has become a widely used commercial process. A scheme of the component of a screen-printing machine is depicted in Figure 8.

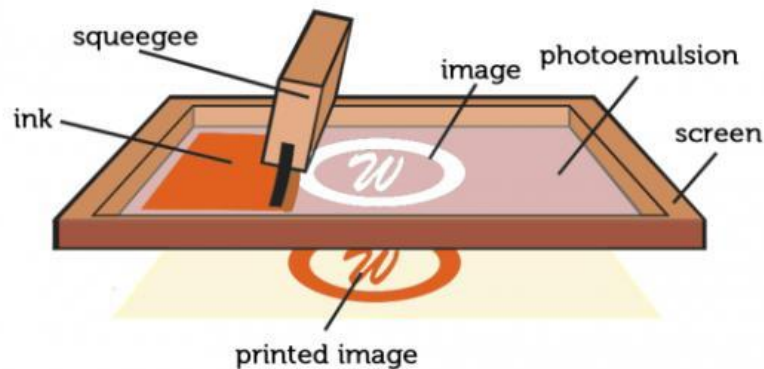


**Figure 8.** Components of the screen-printing technique Image: Harry Wad [18].

Nowadays, the screens are produced with synthetic polyester or steel mesh. The mesh is pre-processed, by immersing it in a purpose-blended emulsion sensitive to light and kept for drying in a dark-room. After the emulsion preparation, a dark print-out negative of the model to be printed is placed on the mesh and it is exposed to a strong light: the light hardens further the emulsion, but the dark color avoids the light from reaching the regions across which paste will need to be cut out. The screen is subsequently washed with H<sub>2</sub>O, and the non-hardened regions are flushed

away, leaving non-coated membrane gaps that can hold paste, but cross which paste can also be pressed.

The screen-printing technique is a non-contact-type of printing technology and can be applied to almost any kind of material: conductors (Ag, Cu, Au, Pt...), organic and inorganic semiconductors (Poly (3,4-ethylenedioxythiophene)- PEDOT, Poly(3-hexylthiophene)- P3HT, Silicon...), organic and inorganic materials and dielectrics (Polystyrene PS, Poly(methyl methacrylate)-PMMA, benzocyclobutene-BCB, oxides...).

The screen fixed the pattern of the printed film measuring at the same time the amount of ink deposited upon the insulating substrate. Typically, the screen comprehends a frame, made in stainless steel or cast aluminum, where a finely woven mesh is tightened.

The mesh is generally constituted by a flat surface weave pattern, as shown in Figure 9.

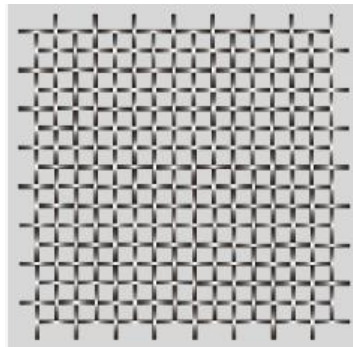


**Figure 9.** A plain weave pattern of a typical thick layer screen [19].

Generally, there are 200 strands per inch in a typical mesh: the mesh opening is dependent on the mesh number and on the diameter of the filament. For a fixed mesh count, a shorter filament diameter results in a bigger mesh opening that permit a higher volume of paste to be deposited on the selected substrate. Therefore, the gap between the mesh furnishes a way to control the thickness of the deposit.

The following equation 1 quantifies the percentage open area of mesh across which the paste can pass through (%):

$$\%: \frac{100A^2}{(A+D)^2} \quad (1)$$

where A represent the aperture of the mesh and Dis the diameter of the filament.

A cross-section of a mesh is depicted in Figure 10.



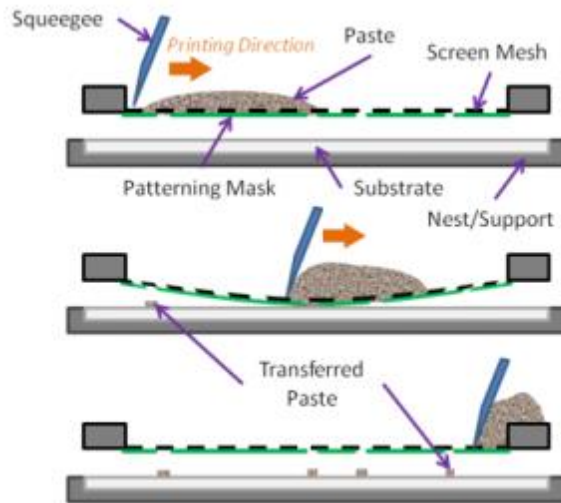


**Figure 10.** Cross-sectional side view illustration of the process from top to bottom chronologically in the fabrication of a screen-printed device supported by a substrate [20].

The schematic diagram of the sensors preparation by means of the semi-automatic screen-printing instrument utilized in Politecnico's laboratory is outlined in Figure 11, together with the screen-printing masks of the platinum electrodes and the sensitive film. Particularly, the screen's patterns can be diversified depending on which materials has to be deposited.

The utilized screens were all constituted by stainless steel having apertures of 270 mesh, that corresponds to 53  $\mu\text{m}$ .

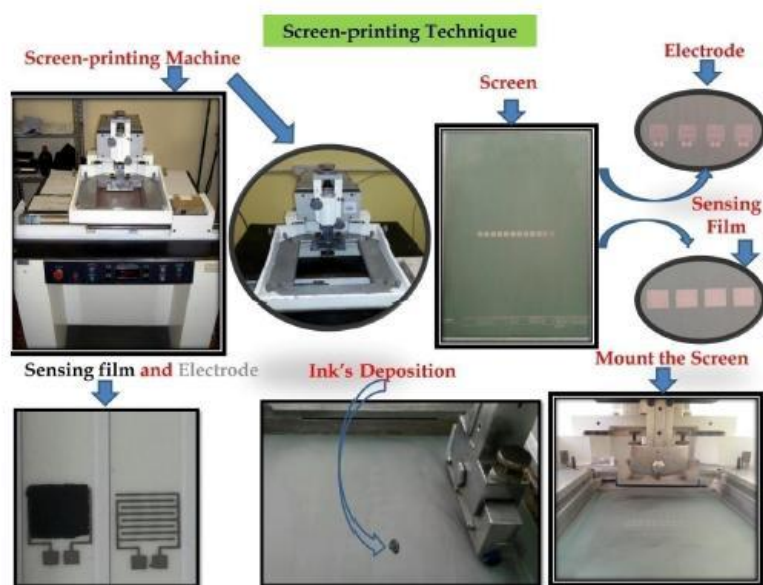


**Figure 11.** Schematic diagram of sensors preparation by means of the screen-printing technique [21].

Each paste utilized to produce thick films is constituted by three main components: the sensing material, the solvent and the binding phase. The solvent is typically an organic vehicle, that furnishes a homogeneous suspension of the sensing material particles achieving a suitable rheology to print the desired film pattern. The organic vehicle is therefore a momentary, *'sacrificial component'*, that must be fully eliminated in the successive stages of the process, when the film microstructure is structured.

The rheological behavior characteristic of a screen-printing paste is represented in the next Figure 12.

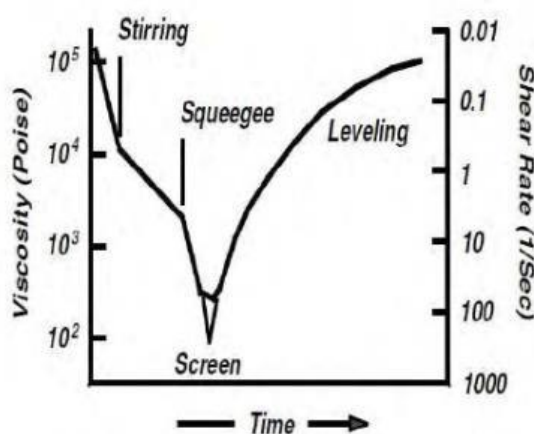


**Figure 12.** Changes in the ink viscosity at different stages of the printing process [22].

An ink presents a thixotropic reological behavior, since it must simply pass across the weaves of the screen. The action of squeegee should reach its initial viscosity. In this way, the deposit held the shape of the apertures of the screen when it is on the substrate. In accordance with figure 8, the viscosity of the ink must decrease during the action of the squeegee, and later it must quickly augment passing through the screen, returning to its initial condition.

The process of removal of the sacrificial components consists in two stages: the drying and the firing steps.

Typically, these two processes are essential for the sensor fabrication: after deposition, the electrodes and/or the film are placed in air for few hours, to allow the paste to level out and stand. The objective of drying is to produce an adherent printed film onto the substrate without removing the organic solvents at this step.

The organic vehicle is still present in the paste and drying takes place at 80-150°C in an oven.

After drying, the firing stage takes place. It is a step where the electrodes or the printed films are heated at elevated temperatures and the components of the paste are decomposed thermally. This led to a visible shrinkage of the film: the thermal program is typically studied depending on the sample considering the efficiency of adhesion between the sensitive film and the ceramic substrate.

In laboratory, a mixture of terpineols, ethylene glycol monobutyl ether (Emflow, Emca Remex, USA) was utilized as organic vehicle for realizing the inks of the screen-printing deposition. In addition, the binding phase was poly-(vinyl butyral-co-vinyl alcohol-co-vinyl acetate) (PVB, Aldrich, USA), that provides the plasticity to the ink guaranteeing the proper adhesion of the film onto the substrate at the

same time. Typically, for the preparation of 1 g of the basic component ink, 0.053 g of PVB and 1.2 cm<sup>3</sup> of Emflow were added: the binder and the solvent were mixed together for obtaining a homogeneous viscous liquid. Subsequently the sensing material powder was added to the solution forming a dense paste, printable onto the substrate. In the architecture developed to create the ceramic sensors devices, the sensing films were deposited onto 0.38 mm thick commercial  $\alpha$ -Al<sub>2</sub>O<sub>3</sub> substrates (Coors Tek, USA, ADS-96 R, 96% alumina, 0.85 cm × 1.7 cm<sup>2</sup>) equipped with Pt electrodes that are interdigitated and screen-printed over the substrate, where the sensitive film overlapped them. The size of the interdigitated circuit is 6 × 8 mm<sup>2</sup> with 0.45  $\mu$ m of electrode width, 1.6 mm of inter-electrode spacing and 6  $\mu$ m of electrode thickness as shown in the next Figure 13.

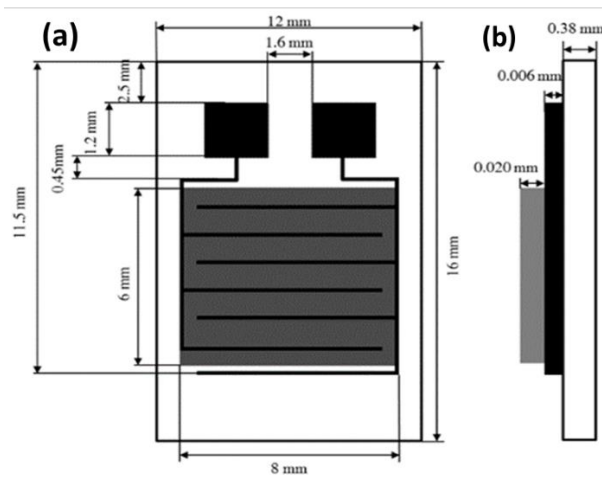


**Figure 13.** Scheme of the chemical sensor fabricated by screen printing: (a) front view, (b) side view. The proportions between the components are exaggerated for explanatory purpose, whereas the quotes are referred to the real sizes. In the image, solid black lines are platinum interdigitated electrodes, dark grey is the film of the sentivite material, and the white area represent the  $\alpha$ -Al<sub>2</sub>O<sub>3</sub> substrate [23].

Starting from a commercial platinum-Pt paste (5545-LS, ESL, King of Prussia, PA, USA), the Pt paste was screen-printed onto  $\alpha$ -Al<sub>2</sub>O<sub>3</sub> substrate by means of a rubber squeegee after cleaning the substrate in ethanol by 5 minutes of sonication. The electrodes, after drying for 12 h, were fired at 980°C for 18 min (2°C/min of heating ramp) in order to optimise their electrical conductance and their adhesion over the ceramic substrate, in accordance with the recommendations of the paste's manufacturer.

## 3.2 Sensors test

After fabrication of the sensors, they were tested in a regulated home-made gas flow system schematized in Figure 14.

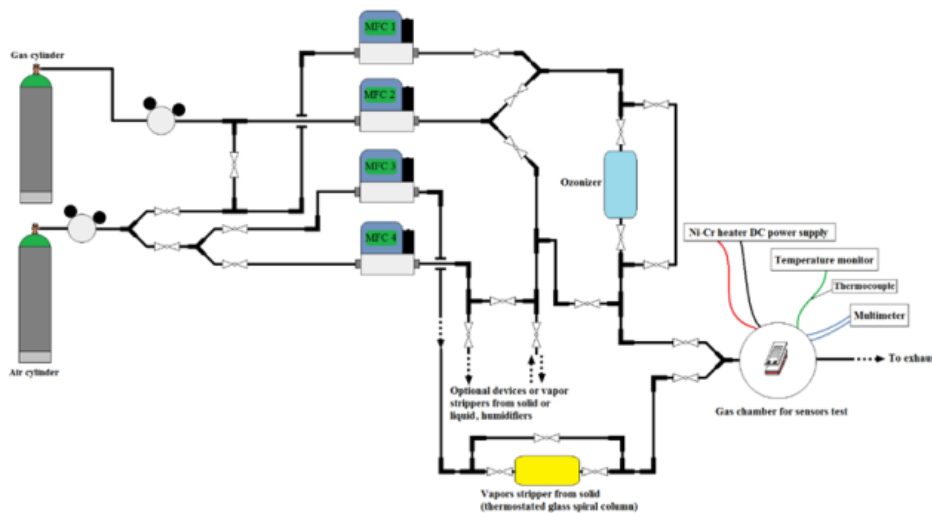


Figure 14. Home made system for sensing testing [24].

O<sub>3</sub> was produced from synthetic dry air bottles (SIAD, Bergamo, Italy; research quality gases) by the UV lamp (SOG-01, Ultra-Violet Products LTD, Cambridge, UK), through concentration amounts from 0.2 until 0.5 ppm in step of 0.1 ppm. The O<sub>3</sub> generators use the photochemical reaction of the 185 nm emission line of Hg to generate O<sub>3</sub> from O<sub>2</sub>. A unit is based on a persistent source of radiation at 185 nm, a reaction tube in quartz and a radiation housing. The radiation source is a Pen-Ray Hg lamp put into the radiation housing and an external power supply. This arrangement can be equipped both with a supply of oxygen or dry air, providing a strong source of O<sub>3</sub> for hundreds of hours of operation. In the device a shield is present, and by modulating the length of lamp exposed, it is possible to generate a precise O<sub>3</sub> concentration in accordance with the manufacturer's calibration curves. O<sub>3</sub> possible losses caused by reactions in pipelines and in the testing chamber were avoided by using proper polymers such as polyvinylidene fluoride (PVDF) and polytetrafluoroethylene (PTFE) tubes.

Tests were realized under a uniform airflow rate of 1000 SCCM (standard cubic centimeter) of dry air. The analyte gas was diluted with air through four flow meters (Teledyne Hastings Instruments HFM 300, HFC 302, USA).

In the course of measurements in a dynamic flow apparatus, film impedance (magnitude and phase) and resistance were measured with LCR meter (Hioki 3533-01, Nagano, Japan). Impedance was recorded at a constant frequency of 1 kHz imposing an AC tension equal to 1 V. The fabricated devices were put in a glassy chamber of 100 mL covered with silver paper in order to avoid interaction of the sunlight in the test chamber. A Ni-Cr wire was situated underneath the device in the glass bottle with the heater, and the sensor T was checked with accuracy by modulating the DC power (Peak Tech, China) through the coil in accordance with the power/temperature calibration plot carried out with a Pt1000 thermistor.

Different analyte gases were injected singly into the test chamber for cross-sensitivity test at the optimum operating temperature.

At the selected temperature, the measured impedance under synthetic dry air was observed for 4 minutes, after stabilization of the baseline impedance in dry air for a couple of hours. The analyte gas was then inserted in the test chamber until the equilibrium was reached. Finally, the desorption of the target molecules was also studied by injecting dry air in the testing chamber until a new equilibrium is reached.

### **3.3 Material characterization**

In this paragraph, the experimental procedures realized for the characterization of the gas sensitive materials are described. Nano and micro-characterizations were accomplished by laser granulometry, DTA-TG, N<sub>2</sub> adsorption, XRD, XPS, FESEM and TEM analysis.

#### **3.3.1 Laser granulometry**

When a laser ray beats the particles suspended in a medium (in these analysis ethanol), the produced scattered rays have an intensity and a scattering angle that is dependent on the particle size.

In Figure 15, a scheme of a laser granulometer is depicted.

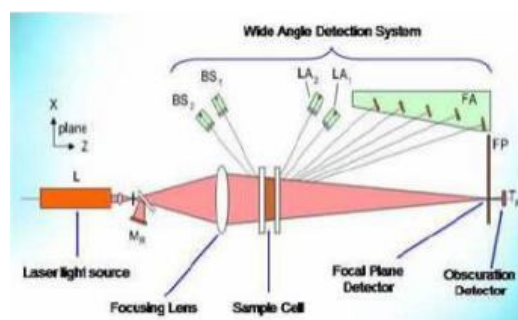


**Figure 15.** Scheme of a laser granulometer [21].

The instrument used was a Mastersizer 3000. It is constituted by the principal optical section, a dispersion unit and a measurement cell.

The optical unit transmit red and blue lights across a sample, and it uses its detectors (photodiodes) to produce data about the light scattering pattern generated by the particles that constitutes the sample.

The data are analyzed by the Mastersizer software to furnish informations about particle size with accuracy. The additional blue light utilized on Mastersizer 3000 supplies enhancements in the analysis resolution under 1 micron in size. The Mie theory is adopted by the instrument to extrapolate the particle size distribution in volume. It considers either the diffraction and the refractive indexes of the solvent and the sample.

A wet dispersion unit was used controlling the dispersion of a sample suspended in a solvent.

The measurement cell is the interface between the dispersion and the optical units. The sample is directed between test windows in the cell to permit the laser to pass across it by performing a measurement.

The Mastersizer application software is the heart of the system. It commands the optical and dispersion units processing the raw data assembled by the system, furnishing data analysis and reports.

In this thesys, the particle size distribution of samples was measured through laser granulometry technique (Mastersizer 3000, Malvern, Worcestershire, UK). The analysis wer carried out after dispersion of the powders in EtOH and subsequently sonication for 5 min.

### 3.3.2 DTA

DTA consists typically in heating or cooling a powder together with a reference under the same conditions, measuring any variation in temperature between the

reference and the sample. This variation depends on the time and/or temperature. Variations in the sample that are related to adsorption or evolution of heat are detectable. Alterations in T can spring out between two samples that are inert in the case their response towards the selected heat ramp is not the same. DTA is exploitable to investigate thermal characteristics and phase alterations without variations in enthalpy. The baseline of the DTA signal should displays discontinuities at the transition temperatures and the slope of the curve is dependent on the microstructure at each temperature.

The area beneath a DTA signal can be generated by variations in enthalpy and it is not influenced by the heat capacity of the powder. The principle characteristics of a DTA are the following:

- Sample holder equipped with thermocouples, sample holders and a metallic or ceramic block
- Furnace
- T programmer
- Recording system.

The last three elements are the crucial conditions of the furnace are that it should supply a stable and large hot area and should respond quickly to instructions from the temperature programmer too. It is fundamental to achieve constant rates of heating. The recording system must have a modest inertia to reliably repeat changes in the experimental set up. In the Figure 16, a scheme of DTA cell is portrait.

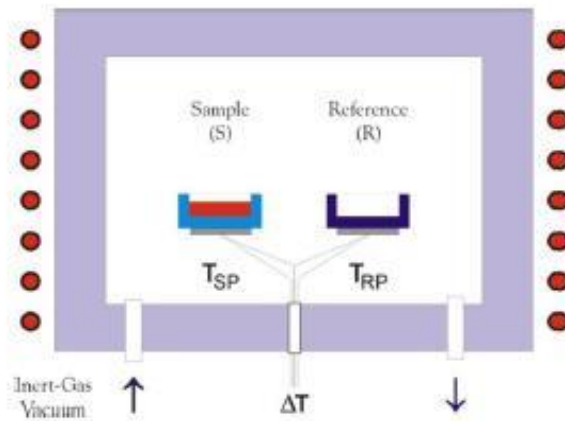


**Figure 16.** Scheme of DTA cell [21].

The sample holder is based on a thermocouple for either the sample and the reference, surrounded by a slab to allow distribution of heat. The sample is put in a little crucible (in this case made of Pt) equipped with an indentation on the base to permit a compact fit over the thermocouple bead. The crucible is realized by



materials such as Pyrex, silica, alumina, nickel or platinum, in dependence on the type of the tests. The thermocouples should not be placed directly in contact with the sample to prevent contamination.

Metallic blocks are less affected by drift on the baseline comparing with ceramics that contain residual porosity. Nevertheless, their great thermal conductivity brings to smaller DTA signals. The sample assembly is detached from any electrical interference by the furnace wiring with an earthed case, often fabricated with Pt-coated ceramic materials. It can also be utilized for containing the sample in a regulated atmosphere. When the test temperature is between 200 and 500°C, issues can arise in transferring heat equally away from the specimen. These can be controlled with thermocouples as flat discs to guarantee optimum thermal contact with the flat-bottomed sample holder, made of Al or Pt sheet. Finally, it is mandatory to assure that the thermocouple and holder are compatibly put with respect to each other to guarantee reproducibility of measurement.

DTA-TG (STA 409, Netzsch, Selb, Germany) was carried out on powders with a rate of heating equal to 10°C/min in static air.

### 3.3.3 N<sub>2</sub> adsorption

In 1938, S. Brunauer, P. H. Emmett and E. Teller presented a scientific article about their theory ‘*BET*’ [25] where the acronym describes their family names initials.

This work was the starting point for a crucial analysis for the measurement of the specific surface area (SSA) of a material.

This theory extends the Langmuir theory (that is valid for molecular adsorption of monolayers) to adsorption of multilayer with some assumptions:

- Gas molecules can adsorb physically onto a solid in infinite layers.
- No interactions between different layers occur.
- The Langmuir theory is exploitable at each layer. The resulting BET relation is explicit by equation (2):

$$\frac{1}{[(P_0/P)-1]} = \frac{c-1}{V_m c} \left( \frac{P}{P_0} \right) + \frac{1}{V_m c} \quad (2)$$

In the equation, P and P<sub>0</sub> are respectively the equilibrium and the saturation pressure of adsorbates at the adsorption T, V<sub>m</sub> is the monolayer adsorbed amount and c is the BET constant, coming from the following relationship (3):

$$c = \exp\left(\frac{E_1 - E_L}{RT}\right) \quad (3)$$

Here,  $E_1$  is the adsorption heat of the top layer, and  $E_L$  is the adsorption heat of the second layer and corresponds to the liquefaction's heat.

The equation (2) represent an isotherm of adsorption and can be draw as a straight line with  $1/v[(P_0/P)-1]$  in the y-axis and  $\phi: (P/P_0)$  in the x-axis in accordance with the experimental results as illustrated in Figure 17.

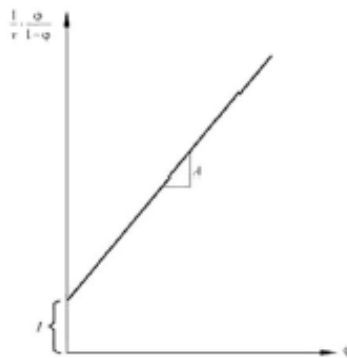


**Figure 17.** Representation of a BET plot [25].

The figure 17 represent the BET plot. The linear correlation of this equation is kept solely in the interval  $0.05 < P/P_0 < 0.35$ . The slope  $A$  and the intercept with y-axis  $I$  are utilized to estimate the monolayer adsorbed gas quantity  $V_m$  and the BET constant. The equation (4) and (5) are used:

$$V_m = \frac{1}{A+1} \quad (4)$$

$$c = 1 + \frac{A}{I} \quad (5)$$

The BET theory is largely utilized in surface science for the calculus of surface regions of solids by physical adsorption of different gas species. A whole surface area  $S_{total}$  and a specific surface area  $S$  are calculated by (6):

$$S_{BET, total} = \frac{V_m NS}{V} \quad (6)$$

In which  $V_m$  is in volume units, that are the units of molar volume of the adsorbate gas too (7):

$$S_{BET} = \frac{S_{total}}{a} \quad (7)$$

Where  $N$  is number of Avogadro,  $s$  is the adsorption cross-section of the adsorbing gases,  $V$  corresponds to the molar volume of adsorbate gas in the mass of adsorbent in (g).

$N_2$  adsorption and desorption isotherms were recorded with an ASAP2020, Micromeritics ASAP 2020 Plus Physisorption (Norcross, GA, USA), at the constant  $T$  of  $-196^\circ\text{C}$ . Before  $N_2$  adsorption–desorption analysis, samples were degassed at  $150^\circ\text{C}$  for 8 h. In addition, Brumauer–Emmett–Teller (BET) theory was exploited to define the SSA of the investigated materials.

### 3.3.4 XRD

X-rays are electromagnetic waves with  $\lambda$  between 0.01 and 10 nm and energies between 100 eV and 10 MeV. These can act as particles in accordance with the quantum theory. X-rays were found by Roentgen in 1885. They are generated in an X-ray tube consisting in a filament of tungsten.  $E^-$  are produced by the  $W$  filament by thermionic discharge and they are constituted to hit on the anode by supplying a tension. After the bombardment of electrons on the target, X-rays are generated to escape from the tube as displayed in Figure 18.

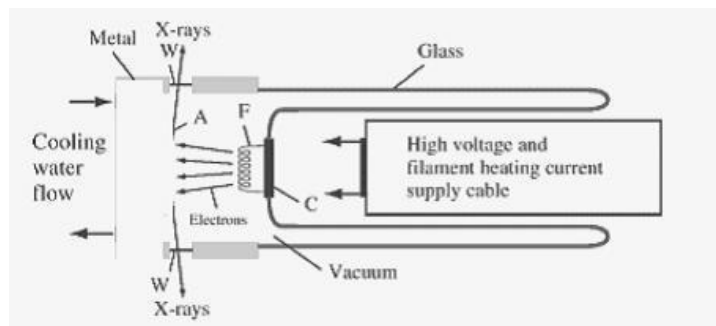


**Figure 18.** Scheme of an X-ray tube for the production of X-rays [26].

In the figure, the X-ray tube holds the filament  $F$ , the target  $T$  and the windows  $W$  across which X-rays leave the tube generated from  $Mo$  target as a consequence of

the supplied tension. Two typologies of signals are possible. The formers are the white signals whereas the latters are characteristic radiations  $K_{\alpha}$  and  $K_{\beta}$ . In X-ray diffraction investigation, solely the characteristic part of the X-ray spectrum is suitable. For this reason, it is necessary to eliminate the white part. This is accomplished by the application of filters. Typically, the filter chosen is of 1 atomic number smaller compared to the anode utilized for the production of X-rays. A scheme of Cu radiation before and after going through a Ni filter is represented in the Figure 19.

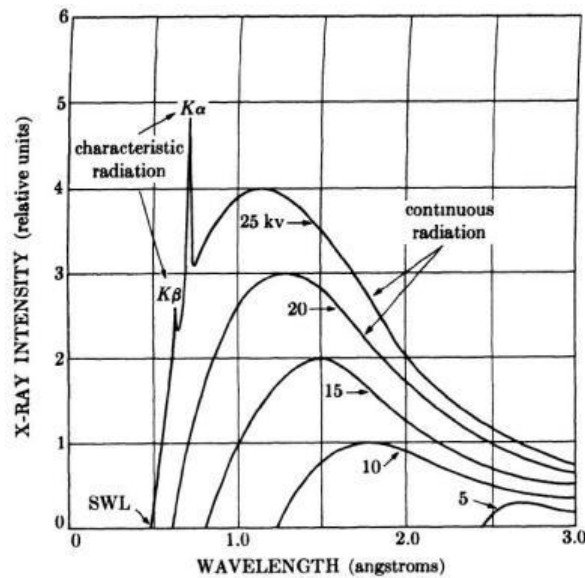


**Figure 19.** XRD pattern of Mo vs the applied tension [27].

When X-ray beam is incident onto the samples, four processes can happen in accordance with the Figure 20.

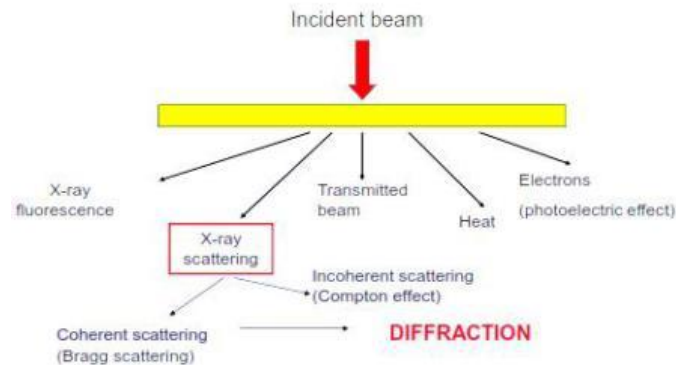


**Figure 20.** Interaction of X-rays with materials [28].

In fact, part of the X-rays go by the incident material (transmittance), others result  $e^-$  that are injected for photoelectric effect, some generate X-ray fluorescence whereas others are scattered in several directions coherently or incoherently. The formers are utilized in the standard X-ray diffractometry in the analysis of materials composition.

The X-ray tubes are set up in the X-ray diffractometer apparatus utilized to perform the XRD investigation. A monochromatic ray of  $K\alpha$  radiations is attached to the samples after going across the collimator and an antiscatter slit. X-rays are scattered in several directions and they come into a counter of X-ray typically put at the identical angle of the incident beam.

The main elements of an X-ray diffractometer are depicted in the Figure 21.

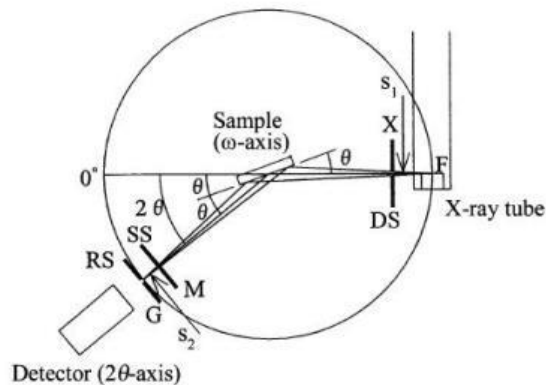


**Figure 21.** Schematic of a typical diffractometer [28].

They embrace an X-ray source F, a sample holder S and a detector G, Rowland circle going across F (target focal spot), S (center point of diffractometer) and G

(the focal point of the diffracted ray), the divergent slits DS, the scattering slits SS and the receiving slit RS [28].

The X-rays elastically scattered from a crystal lattice are erasable each others in a destructively, or they can sum each others in constructive interference. Bragg's law explains these diffractions as (equation 8) and Figure 22:

$$n\lambda: 2dsen\theta \quad (8)$$

Equation 8 is the notorious equation of Bragg in which  $d$  is interplanar distance,  $\theta$  is the incident angle,  $\lambda$  is the wavelength of the incident X-rays and  $n$  is an integer number.

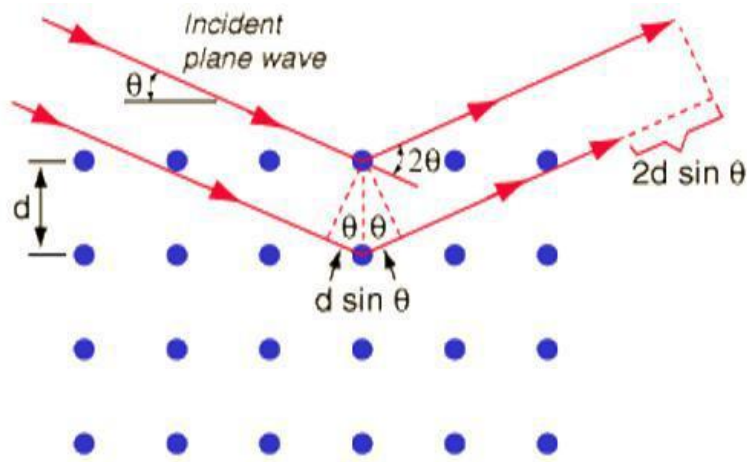


**Figure 22.** Interference of X-rays scattered by crystals [28].

In our case, the sample holder is fixed and both X-ray source and the detector spin with a velocity  $\omega$ , and  $I-\theta$  are obtained. The diffractometer is called  $\theta-\theta$  type diffractometer.

The diffraction patters attained through the XRD investigation can be analyzed to gain useful informations about the material. From angular position ( $2\theta$ ) of the diffraction pattern signals, the crystal system can be studied, together with the spatial group symmetry, phases and unit cell. From the intensity ( $I$ ) of the diffraction peaks, informations concerning the nature of the unit cell, quantitative composition of the mixture, point symmetry and the preferred orientation and texture are achieved. Thus, from studies of the width peak and profile, informations about the crystallite size between 1 and 100 nm, defects, texture and residual stresses can be obtained.

XRD was also carried out on the most interesting powders. In some cases, the analysis was performed adding quartz ( $\text{SiO}_2$ ) acting as an internal standard, in order to investigate possible shifts in the diffraction spectrum afer doping. Spectra were recorded on a Pan'Analytical X'Pert Pro instrument (Pan'Analytical, Almelo, The

Netherlands) with Cu K radiation (0.154056 nm) between 5 and 70° of 2θ, with a 0.0065° of 2θ step size and 23 s of acquisition time per step. Diffraction patterns were then indexed with the Powder Data File database (P.D.F. 2000, International Centre of Diffraction Data, Newtown Square, PA, USA). The generator tension and current were fixed respectively to 40 kV and 40 mA.

The mean crystallite size was evaluated in accordance with the Scherrer equation, with the aim to compare the obtained results with those available in the state of the art (eq. 9):

$$D = k\lambda / \beta \cos\theta \quad (\text{eq. 9})$$

where  $k$  is a constant = 0.9,  $\lambda$  is the Cu K $\alpha$  wavelength (0.154056 nm),  $\theta$  is the half of Bragg (radians) and  $\beta$  is the full width at half maximum of the signals, that are usually correlated with the crystallite size, defects of the sample and signal broadening produced by the instrument [29].

### 3.3.5 XPS

A scheme on an X-ray photoelectron spectrometer (XPS) is illustrated in Figure 23.

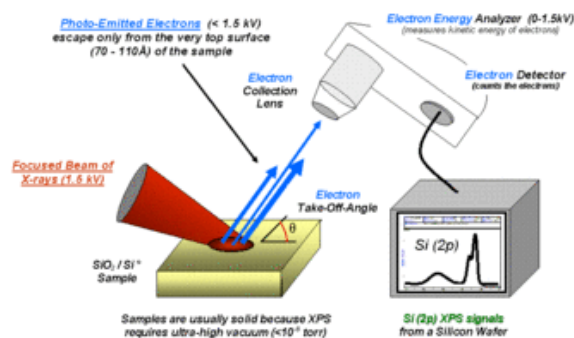


**Figure 23.** XPS analyser [30].

X-ray photoelectron spectroscopy (XPS) is a surface qualitative and quantitative spectroscopic technology that evaluate the elemental composition at ppt range, empirical formula, electronic and chemical states of the elements. Furthermore, with XPS it is possible to measure which bonds are presents between the elements. The denetration is around 20 nm into a material.

XPS analysis is realized after irradiation of a sample with a beam of X-rays. In the meanwhile, the kinetic energy and  $e^-$  that outflow from the material are measured. XPS needes high ( $P \sim 10^{-8}$  millibar) or ultra-high vacuum (UHV;  $P < 10^{-9}$  millibar). XPS is a valuable tool to investigate the surface chemical properties of a sample.

XPS is called ESCA (electron spectroscopy for chemical analysis), an acronym invented by the research group of Kai Siegbahn to accentuate the chemical informations that this technique can provides.

By XPS all elements are in principle detectable. LOD of ppm are feasible, but it requires particular conditions like the concentration at topmost of the surface or prolonged collection time.

In the present thesis, XPS investigations were carried out with a PHI 5000 Versaprobe (Physical Electronics, Chanhassen, MN, USA) scanning X-ray photoelectron spectrometer (monochromatic Al K $\alpha$  X-ray source with 1486.6 eV energy, 15 kV of tension, and 1 mA of anode current) to study the chemistry at the surface of the selected materials.

### **3.3.6 SEM**

Scanning electron microscopes (SEM) have grown as an essential technique in materials characterization. SEM is a microscope that use a focused beam of  $e^-$  to produce particulars in HR of the materials under investigation. For the extremely short wavelength of bombarding electron beams, SEM possess a superior resolving power than the optical microscopes [31]. The scheme of a SEM labeled with the main components is depicted in Figure 24.



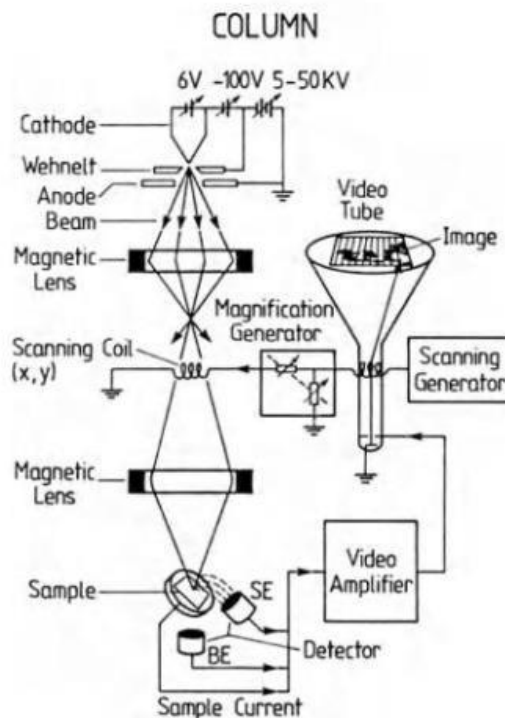


**Figure 24.** Schematic setup of Scanning Electron Microscope [32].

There are seven main steps for this process of imaging:

- A flow of free  $e^-$  is generated in an electron gun. It is based on a tungsten filament cathode that produces these  $e^-$  by thermionic emission.
- The flow of  $e^-$  from the electron gun is accelerated in an optical column with an elevated tension at the anode.
- Condenser lenses transform this flow of  $e^-$  into a beam of electrons.
- The current of the beam is managed by the condenser lenses and the regulation of the aperture of the beam.
- A stigmator is utilized to get rid of the ellipticity of the  $e^-$  beam.
- An ultimate condensing lens set the beam onto a probe spot.
- The  $e^-$  beam interacts with the material surface and consequently, the different output are generated:

**Secondary electrons (SE):** They are characterized by a low energy and they are emitted from the near surface of the material. These  $e^-$  are collectable in a secondary electron detector to extract informations about the topography of the material.

**Back scattered electrons (BSE):** They are the  $e^-$  that are scattered back from the inner section of the sample beneath the surface. They have higher density compared

to the SE. Since these  $e^-$  arise for the fretest part from the material's bulk, they possess information circa the mean atomic mass. Thus, the image contains information circa the chemical composition of the material components.

**X-rays:** X-rays are produced too from the sample resolvavle considering their energies or wavelengths. The typical waves resolved based on energy are recorded in the Energy Dispersive X-ray (EDX) analyzer for studies of the composition.

However, X-rays are resolvable by diffraction process across a regular and periodic solid material. It is collectable in a gas-filled counter named Wavelength Dispersive Spectrometer (WDS) analyser.

Furthermore to the SE, BSE and X-rays, heat or light photons are produced as a consequence of the electron beam bombardment onto the material. Typically, the SE arises from top few nm of the sample volume, while the BSE derive from top 40% of the sample volume and X-rays are discharged from the whole area of bombardment. A scheme of the volume and mechanism of the interactions between electrons and material in SEM is displayed in Figure 25.

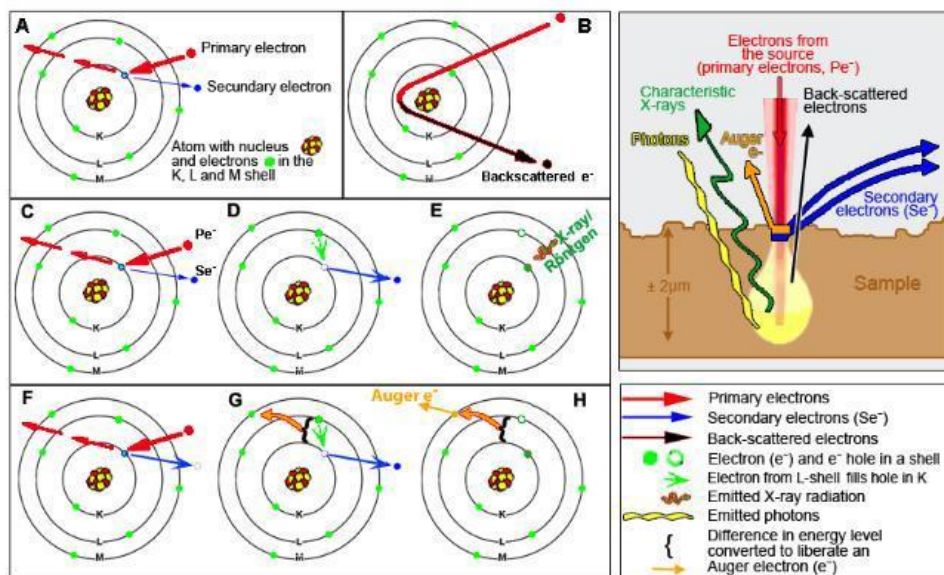


**Figure 25.** Volume and mechanism of interaction between  $e^-$  and matter (SEM) [32].

In this thesis, morphologies of both powders and layers were investigated with a FESEM (Zeiss Supra-40, Oberkochen, Germany) equipped with an Oxford Energy Dispersive X-ray detector. These analyses were carried out after Cr sputtering. Observations were carried out on the powders and films with an IN-LENS detector

while for low resolution and EDS an ETD detector (EVERHART-THORNLEY) and HV 12 to 25 Kv was used.

### 3.3.7 TEM

Transmission electron microscopy (TEM) consist in a beam of  $e^-$  that are transmitted across a sample forming an image. In Figure 26, a scheme of the main constituents of a TEM are depicted.

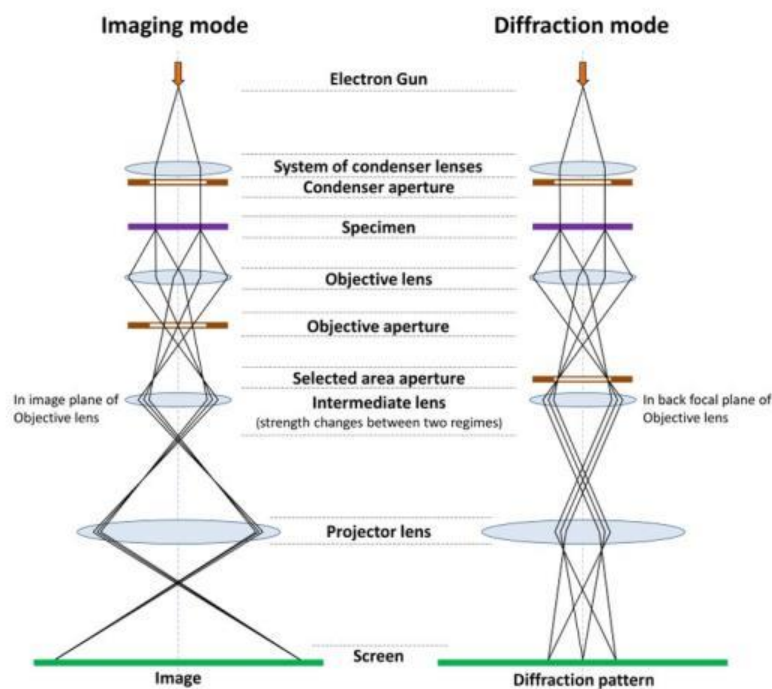


**Figure 26.** Scheme of a TEM, imaging mode (left), diffraction mode (right) [33].

The sample is typically an ultrathin area (<100 nm of thickness) or a suspension onto a grid. An image is generated after the interaction of the  $e^-$  with the material since the  $e^-$  beam is transmitted across the sample. Thus, the image is magnified and focused into an imaging system. This can be a sensor, a fluorescent screen or a layer of photographic film.

M. Knoll and E. Ruska fabricated the first TEM in 1931 with high resolution. Then, the first commercial TEM was ready in 1939.

TEM can image at a significantly higher magnification compared to the other microscopes. This allows the instrument to appreciate details—even as little as a unique column of atoms, that is thousands of times smaller compared to a resolvable object view in an optical microscope. For this reason, TEM is one of the main analytical techniques in the chemical, physical and biological sciences.

At elevated resolutions, complex wave interactions adjust the image intensity, demanding appropriate analysis of the resulting images. Alternate modes of utilization permit to resolve adjustments in electronic chemical nature, structure, crystal orientation and  $e^-$  phase shift due to the sample.

In this thesis, chemical analysis and observations of the powders were carried out by HR-TEM coupled with energy dispersive X-ray spectroscopy (TEM-EDS). Characterizations were accomplished with a JEOL 3010-UHR (Peabody, MA, USA) instrument, working with a tension of acceleration of 300 kV and an Oxford Inca Energy TEM 200 EDS X-rays analyser. In addition, quantitative studies of the chemical composition were accomplished by means of an Oxford INCA Microanalysis Suite software and the average chemical composition after a mean of 5 tests in diverse areas of the sample.

### **3.4 Conclusions**

In this chapter, the constituents of a chemical sensor were described together with the influence of film properties towards gas sensing mechanism.

Furthermore, the main deposition techniques were analysed in detail, with a special focus on those used in this thesis, i.e. dip coating and screen-printing techniques.

Thus, the home-made system for dynamics test of the realized sensors upon diverse gases and at different working temperature was delineated.

In the final part, the experimental procedures realized for the characterization of the gas sensitive materials were portrayed. Nano and micro-characterizations were accomplished by laser granulometry, DTA-TG,  $N_2$  adsorption, XRD, XPS, FESEM and TEM analysis.

In the next chapter, the first results of barium hexaferrite and SWCNTs functionalized with an Octadecylamine group for ozone sensing will be discussed.

# References

- [1] White N. (2017). Thick Films. In: Kasap S., Capper P. (eds) Springer handbook of electronic and photonic materials. Springer Handbooks.
- [2] Grover W. H. (1999). Interdigitated array electrode sensors: their design, efficiency, and applications University of Tennessee Honors Thesis Projects.
- [3] Hauptmann P. (1991). Sensors: principles and applications. Prentice Hall International: Hertfordshire, UK.
- [4] Korotcenkov G., Cho B. K. (2009). Thin film SnO<sub>2</sub>-based gas sensors: film thickness influence. *Sens and Actuators B* pages 321–330.
- [5] Pijolat C., Viricelle J. P., Tournier G., Montmeat P. (2005). Application of membranes and filtering films for gas sensors improvements. *Thin Solid Films* pages 7–16.
- [6] Barsan N., Schweizer-Berberich M., Göpel W. (1999). Fundamental and practical aspects in the design of nanoscaled SnO<sub>2</sub> gas sensors: a status report, *J. Anal. Chem.* pages 287–304.
- [7] Madou M. J. and Morrison S. R. (1986). Chemical sensing with solid state devices, Academic Press, San Diego, pages 424-426.
- [8] Dibbern U., Kuersten G., Willich P. (1986). Gas sensitivity, sputter conditions and stoichiometry of pure tin oxide layer, Proc. 2nd Int. Meet. Chemical Sensors, Bordeaux, France, pages 127-130.
- [9] Gardon M., Guilemany J. M. (2013). A review on fabrication, sensing mechanisms and performance of metal oxide gas sensors. *J Mater Sci: Mater Electron* pages 1410–1421.
- [10] Pierre A. C. (1998). Introduction to sol-gel processing, Kluwer, Massachussets).
- [11] <https://www.gelest.com/applications/sol-gel-applications/>(accessed on 22th February 2019).
- [12] Hench L. L., West J. K. (1990). The sol-gel process. *Chem. Rev.* pages 33–72.
- [13] [http://lnf-wiki.eecs.umich.edu/wiki/File:Sputter\\_Deposition.png](http://lnf-wiki.eecs.umich.edu/wiki/File:Sputter_Deposition.png) (accessed on 20th February 2019).
- [14] Barlow F. D., Elshabini A. (2007). Ceramic interconnect technology handbook. CRC Press, New York.
- [15] <http://www.advanced-coating.com/english/spraying-flame.htm#top> (accessed on 21th February 2019).
- [16] Charoen T. K., Suk C. W.(2013) In Semiconductor gas sensors, Woodhead Publishing Series in Electronic and Optical Materials.

- [17] [http://www.dip-coater.com/english/about\\_dip\\_coating.html](http://www.dip-coater.com/english/about_dip_coating.html) (accessed on 23th February 2019).
- [18] <https://commons.wikimedia.org/wiki/File:Silketrykk.svg> (accessed on 24th February 2019).
- [19] White N. (2017). Thick Films. In: Kasap S., Capper P. (eds) Springer handbook of electronic and photonic materials. Springer Handbooks. Springer, Cham.
- [20] Lee J. (2014). Electrochemical sensing of oxygen gas in ionic liquids on screen printed electrodes. PhD thesis in Applied Chemistry, Electrochemistry, Sensors.
- [21] Afify A. (2016). Elaboration and characterization of humidity sensors for environmental monitoring. PhD thesis in Materials Science, Sensors.
- [22] Martin P. (2010). Handbook of Deposition Technologies for Films and Coatings Science, Applications and Technology 3rd Edition•2010.
- [23] Ziegler D., Marchisio A., Ercolino G., Specchia S., Tulliani J. M. (2019) Ammonia selective sensors based on cobalt spinel prepared by combustion synthesis. *Solid State Ionics*. Pages 91-100.
- [24] Ziegler D., Marchisio A., Montanaro L., Palmero P., Tulliani J. M. (2018) Barium hexaferrite thick-films for ozone detection at low temperature. *Solid state ionics*. Pages 24-32.
- [25] Brunauer S., Emmett P. H., Teller E. (1938). BET theory aims to explain the physical adsorption of gas molecules on a solid surface *J. Am. Chem. Soc.* pages 309.
- [
- [26] De Graef M., McHenry M. E. (2007). Structure of Materials: An Introduction to crystallography, Diffraction and Symmetry, Cambridge, UK: Cambridge University Press.
- [27] Cullity, B. D. (1956). Elements of X-Ray Diffraction, USA: Addison.
- [28] Waseda Y., Matsubara E., Shinoda, K. (2011). X-Ray Diffraction Crystallography, New York, NY: Springer New York Dordrecht Heidelberg London.
- [29] Ho W. H., Yen S. K. (2006). Preparation and characterization of indium oxide film by electrochemical deposition, *Thin Solid Films*. pages 80-84.
- [30] <https://upload.wikimedia.org/wikipedia/commons/f/f2/System2.gif> (accessed on 24th February 2019).
- [31] Rochow T.G., Rochow, E.G. (1995). An introduction to microscopy by means of light, electrons, X-Rays, or ultrasound, Boston, MA: Springer US.
- [32] Luth H. (1995). In Surfaces and interfaces of solid materials 3rd ed., NY: Springer.

[33][https://en.wikipedia.org/wiki/Transmission\\_electron\\_microscopy#/media/File:Schematic\\_view\\_of\\_imaging\\_and\\_diffraction\\_modes\\_in\\_TEM.tif](https://en.wikipedia.org/wiki/Transmission_electron_microscopy#/media/File:Schematic_view_of_imaging_and_diffraction_modes_in_TEM.tif) (accessed on 21th February 2019).

## List of Tables

**Table 1.** Metallic sub-lattices of BaM, with coordinations, locations in the lattice, and orientations of the spin.

**Table 2.**  $d_{10}$ ,  $d_{50}$  and  $d_{90}$  values of the cumulative distribution.

**Table 3.** Response and recovery times for BaM under different  $O_3$  concentrations at 250°C.

**Table 4.** The best performances of Fe-based  $O_3$  MOS sensors.

**Table 5.** The best features of CNTs- $O_3$  sensors.

# List of Figures

**Figure 1.** The S block in BaM: (a) Top oxygen R layer from above. (b) The two layers of the S-block with the oxygen ions and metal cations in the interstitial sites.

**Figure 2.** The R block structure in BaFe<sub>12</sub>O<sub>19</sub> with metal cations at the intersitial sites.

**Figure 3.** Particle size distribution of BaFe<sub>12</sub>O<sub>19</sub>.

**Figure 4.** TG-DTA curve of BaFe<sub>12</sub>O<sub>19</sub> before (a) and after (b) annealing at 350°C. TG: dashed line; DTA: continue line.

**Figure 5.** XRD spectra of BaM precursors calcined for 1 h at 350°C, 650°C and 900°C.

**Figure 6.** FESEM images at different magnification, BaFe<sub>12</sub>O<sub>19</sub> powder: 25,000× (a), 100k× (b); BaFe<sub>12</sub>O<sub>19</sub> sensor: 25k× (c) and 100k× (d).

**Figure 7.** TEM (a, b) and HRTEM (c) micrographs of BaFe<sub>12</sub>O<sub>19</sub>.

**Figure 8.** BaFe<sub>12</sub>O<sub>19</sub> sensor (1x2 cm).

**Figure 9.** Sensor response of BaFe<sub>12</sub>O<sub>19</sub> thick-film at different working T (150-350°C) upon 0.5 ppm of O<sub>3</sub> (a) and impedance's changes after exposing BaFe<sub>12</sub>O<sub>19</sub> film to different levels of O<sub>3</sub> at 250°C (200-500 ppb) (b).

**Figure 10.** Sensor response vs O<sub>3</sub> concentration for BaFe<sub>12</sub>O<sub>19</sub> sensor.

**Figure 11.** Cross sensitivity tests for BaFe<sub>12</sub>O<sub>19</sub> sensor.

**Figure 12.** Structure of ODA-CNTs (a) and dispersion of ODA-CNTs in THF.

**Figure 13.** Characterization for ODA-CNTs: (a) SEM micrograph displaying the porous nanotube networks, (b) TGA investigation, (c) Mid IR and (d) Near IR Spectroscopy.

**Figure 14.** Sensor response at different operating temperatures (a) and adsorption and desorption of 0.2 ppm of O<sub>3</sub> for ODA-SWCNTs sensor in the temperature range 25-100°C.

**Figure 15.** Impedance (a) and conductance (b) variation under 200-500 ppb of O<sub>3</sub> and calibration curve at 75°C (c).

**Figure 16.** Cross sensitivity tests for ODA-SWCNTS sensor.



# Chapter 4 - BaFe<sub>12</sub>O<sub>19</sub> and SWCNTs O<sub>3</sub> sensors

## Abstract

In this chapter, results of the development of O<sub>3</sub> sensors with two different p-type semiconductors, a ceramic and a carbon-based material, are presented. Since only in a study [1] BaFe<sub>12</sub>O<sub>19</sub> was used as ozone sensitive material in the form of thin film, this ozone sensor was realized by screen printing deposition in the form of thick layer, with the goal to compare the sensor performances with respect to thin film technology. The sensor shows a good response and complete recovery at 250°C at sub-ppm level. The ceramic powder was obtained by sol-gel auto-combustion synthesis. In order to decrease the operating temperature, octadecylamine ODA-functionalized Single-walled Carbon Nanotubes (SWCNTs) sensors were realized by spray-coating technique and tested towards O<sub>3</sub> 200 ppb. The sensor exhibits great response and acceptable recovery at 75°C.

## 4.1 BaFe<sub>12</sub>O<sub>19</sub> sensors

In this section, the results of a thick film sensor based on polycrystalline BaFe<sub>12</sub>O<sub>19</sub> are presented. The goal is to study the characteristics of an innovative p-type MOS based on barium hexaferrite (BaFe<sub>12</sub>O<sub>19</sub>) towards O<sub>3</sub> exposure under sub-ppm concentration level, since only few works have shown the gas sensing performances of doped ferrites, such as SmFeO<sub>3</sub> and BaFe<sub>12</sub>O<sub>19</sub> towards oxidant species [1-3]. This chemical sensor was fabricated by screen-printing method, instead of thin layer technology which have been examined previously as a material for O<sub>3</sub> detection [1].

Among diverse synthesis such as hydrothermal method and solid-state reaction [4-6], BaFe<sub>12</sub>O<sub>19</sub> powder was obtained by a sol-gel auto-combustion synthesis by gelling and combustion of a mixture with salts and an organic fuel, where citric acid that is both a chelating agent and a fuel.

This technique exhibits the benefits of the utilization of cheap precursors, a quick and easy synthesis and an excellent scalability.

The pre-combusted powder was then annealed at 900°C for 1 h and analyzed by laser granulometry, thermal analysis, X-ray diffraction, N<sub>2</sub> adsorption, scanning electron microscopy, and transmission electron microscopy. Sensors were realized by screen-printing deposition on  $\alpha$ -Al<sub>2</sub>O<sub>3</sub> substrates equipped with Pt electrodes. Sensors were tested after drying for 12 h and firing at 600°C for 1 h in air. The response of the sensor was evaluated between 150°C – 350°C and from 200 ppb until 500 ppb of O<sub>3</sub>.  $\tau_{\text{ads}}$  and  $\tau_{\text{des}}$  were determined, as well as the cross-sensitivity of the sensor by exposing it towards reducing species (NH<sub>3</sub>, CH<sub>4</sub> and humidity) and oxidant ones (CO<sub>2</sub>, N<sub>2</sub>O and NO<sub>2</sub>) at the optimum operating temperature.

#### 4.1.1 BaFe<sub>12</sub>O<sub>19</sub> characteristics

BaFe<sub>12</sub>O<sub>19</sub> is a magnetic material that is extensively utilized in the everyday life, finding applications in constituents from electronic systems to refrigerator labels and components of children plaything. Ferrites display magnetic features and they are constituted by iron oxides, existing in diverse crystalline structures like cubic, hexagonal, orthoferrites and garnets. They constituted a type of fundamental magnetic materials for their chemical inertness, desirable electrical and magnetic properties, and modest cost of manufacture.

These elements are essential in industrial and technological advancement, and the development of novel applications like radar and telecommunication technologies, motor industry and digital storage devices. The increasing demand for innovative cheap magnetic materials with appropriate features for specific demands had consequently arisen a high demand in the preparation and characterization of ferrites with hexagonal crystal structure for their excellent characteristics [7-9].

The M-type BaFe<sub>12</sub>O<sub>19</sub> (BaM) is a ferrimagnetic characterized by 1390°C of melting point and a density equal to 5.3 g/cm<sup>3</sup>. The BaM crystal structure symmetry is described by the P6<sub>3</sub>/mmc space group characterized by lattice parameters  $a = b = 0.589\text{nm}$ ,  $c = 2.317\text{ nm}$ ,  $\alpha = \beta = 90^\circ$ ,  $\gamma = 120^\circ$  [21]. Two molecules of BaM are present in the unit cell of BaM and the unit cell is assembled by piling S and R structural blocks lengthwise the hexagonal c-axis in the RSR\*S\* sequence, where \* denotes 180° rotation with respect to the c-axis [8, 10].

The S block is shown in Figure 1 and it is described by Fe<sub>6</sub>O<sub>8</sub> molecules consisting in two close-packed oxygen sheets accommodated in a face-centered cubic (fcc) piling sequence, every layer with 4 oxygen anions.

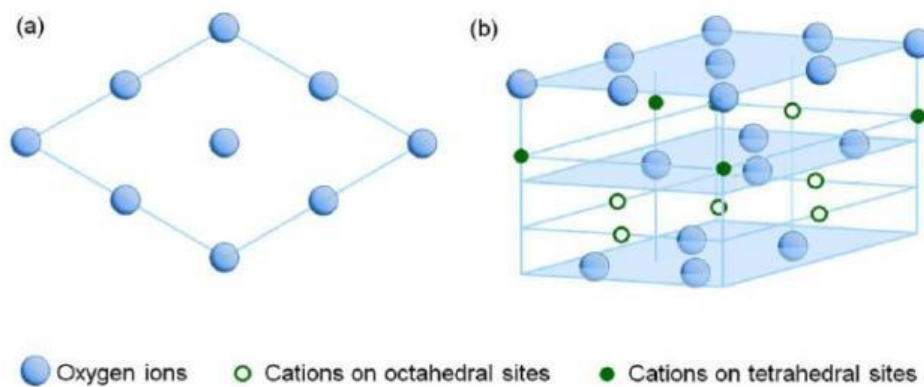


**Figure 1.** The S block in BaM: (a) Top oxygen R layer from above. (b) The two layers of the S block with the oxygen ions and metal cations in the interstitial sites [11].

The block R is depicted in the Figure 2 and it is characterized by  $\text{BaFe}_6\text{O}_{11}$  units, consisting in three close-packed sheets in a piling sequence where  $\text{Ba}^{2+}$  ions that replace an  $\text{O}^{2-}$  ion substitutionally at the center of the layer. The metallic sub-lattices of BaM, with their coordinations, position in the lattice, and orientations of the spin are tabulated in Table 1.

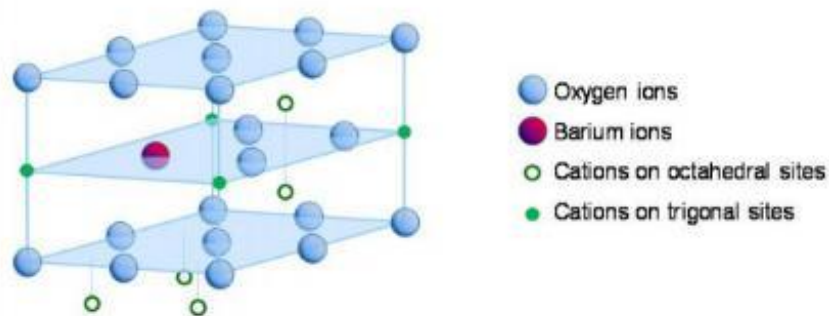


**Figure 2.** The R block structure in  $\text{BaFe}_{12}\text{O}_{19}$  with metal cations at the intersitial sites [11].

**Table 1.** Metallic sub-lattices of BaM, with coordinations, locations in the lattice, and orientations of the spin [11].

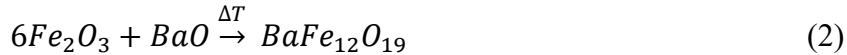
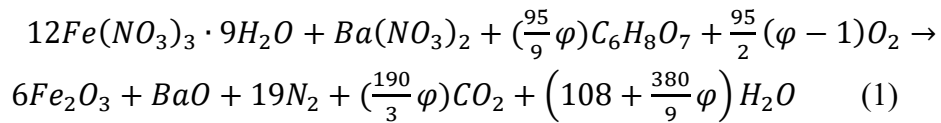
Block	Sublattice	Coordination	Cations	Spin
S	2a	octahedral	1	↑
S	4f <sub>1</sub>	tetrahedral	2	↓
R	2b	by-piramidal	1	↑
R	4f <sub>2</sub>	octahedral	2	↓
S-R	12k	octahedral	6	↑

#### 4.1.2 BaFe<sub>12</sub>O<sub>19</sub> synthesis

BaFe<sub>12</sub>O<sub>19</sub> nano-particles was obtained by sol-gel auto-combustion method [12] using iron nitrate nonahydrate and barium nitrate, as metal precursors, citric acid, and a solution of ammonium hydroxide for adjusting the pH (28% v/v).

Here, Fe (NO<sub>3</sub>)<sub>3</sub>·9H<sub>2</sub>O (ACS reagent, >98%, Aldrich) and Ba (NO<sub>3</sub>)<sub>2</sub> (ACS reagent, <99%, Aldrich) were admixed at 50°C in the right molar ratio of 12:1 in H<sub>2</sub>O, till a red-coulored solution was formed. Then, C<sub>6</sub>H<sub>8</sub>O<sub>7</sub> (99%, Alfa Aesar) was combined into the mixture, with a molar ratio equal to 1 between nitrates and citric acid [13].

By adding NH<sub>4</sub>OH (Fluka, 28%), the pH was adjusted to 7.0. In this process, C<sub>6</sub>H<sub>8</sub>O<sub>7</sub> act as chelating agent for Fe<sup>3+</sup> and Ba<sup>2+</sup> ions and as fuel where nitrates are the oxidizing agents [10]. According to [12], the whole reaction of combustion can be described like in equations 1 and 2, since the synthetized BaFe<sub>12</sub>O<sub>19</sub> particles are represented by the formula BaO·6Fe<sub>2</sub>O<sub>3</sub>:



In those equations, some simplifications were carried out with the aim to outline the whole combustion process. Firstly, the two oxides formation (Fe<sub>2</sub>O<sub>3</sub> and BaO) was accounted distinctly in the reaction in agreement with solution combustion synthesis (SCS) [14].

In addition, the contribution of NH<sub>4</sub>OH to the whole balance of reducing and oxidizing agents was ignored since it is present in extremely little amounts compared to other species in the combustion process.

The solution was then evaporated at 80°C under permanent stirring, after 1 h stirring at 50°C, till a brownish viscous gel was generated. In the final stages of the evaporation step, some EtOH ( $\geq 99.8\%$ , Aldrich) was added up to diminish the particle agglomeration. The precursor was subsequently pre-combusted at 180°C. After a violent ignition step, a brownish fibrous arrangement was quickly generated. Nevertheless, the as-prepared metal oxide exhibited magnetic properties, as checked by a little magnet. Finally, the pre-combusted powders were annealed at 900°C for 1 h with 5°C/min of rate, to provide crystallinity of the obtained BaM powder [11].

### 4.1.3 BaFe<sub>12</sub>O<sub>19</sub> powder and film characterization

Particle size distribution of BaM was established by laser granulometry measurement. BaM powder was manually milled with an agate mortar and agata pestle, and then sieved <45  $\mu\text{m}$ .

Laser granulometry showed that BaM displays a bimodal distribution, with two maxima respectively at 5 and 17.5  $\mu\text{m}$ , and a  $d_{50}$  of 12  $\mu\text{m}$ . These outputs are outlined in Figure 3 and in Table 2 where the values that corresponds to the 10, 50 and 90% of the cumulative distribution are shown.

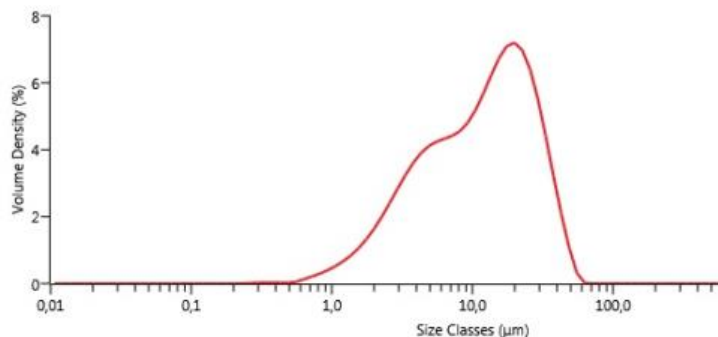


**Figure 3.** Particle size distribution of BaFe<sub>12</sub>O<sub>19</sub> [15].

**Table 2.**  $d_{10}$ ,  $d_{50}$  and  $d_{90}$  values of the cumulative distribution.

Cumulative (%)	BaFe <sub>12</sub> O <sub>19</sub> ( $\mu\text{m}$ )
10	2.79
50	12.00
90	30.40

The TG-DTA investigation was performed either on the precursor of BaM and sunsequently to a pre-calcination step carried out at 350°C. The prime test, depicted

in Figure 4a, outlined two endothermic and exothermic signals. An initial large endothermic signal, situated from 50°C and 189°C, is due to a mass loss of 8% and it could be a consequence of the release of the remaining H<sub>2</sub>O present the dry gel [12]. At 193°C, an extremely sharp exothermic peak corresponds to a 72% of mass loss, generated by a strong auto-combustion stage involving citric acid and nitrates [12]. After this step, no consistent weight loss is noticeable. In addition, at around 330°C, a further exothermic signal was detected, which denotes that magnetite began to crystallize (as demonstrated by XRD analysis performed on the powder calcined for 1 h at 350°C, as depicted in Figure 5. Finally, an endothermic peak is situated at 410°C, indicating the crystallization of BaFe<sub>2</sub>O<sub>4</sub>, in accordance with the literature [12]. Furthermore, the TG-DTA investigation executed upon the pre-calcined BaM at 350°C is depicted in Figure 4b. From this investigation, a novel exothermic signal at 800°C was related to BaFe<sub>12</sub>O<sub>19</sub> that starts to crystallize, in agreement with XRD analysis. The signal present at 256°C is affiliated to a weight loss of around 0.5%, is possibly generated by the decomposition of some precursor residues such as citric acid and nitrates. From the TG curve, a 2.2% of weight loss in the range 620°C-730°C is attributable to release of CO<sub>2</sub> from BaCO<sub>3</sub> generated in the combustion since Fe<sub>2</sub>O<sub>3</sub> acts as catalyst [13]. This signal could also be attributed to the simultaneous composition of the intermediate phase barium monoferrite (BaFe<sub>2</sub>O<sub>4</sub>) [13].

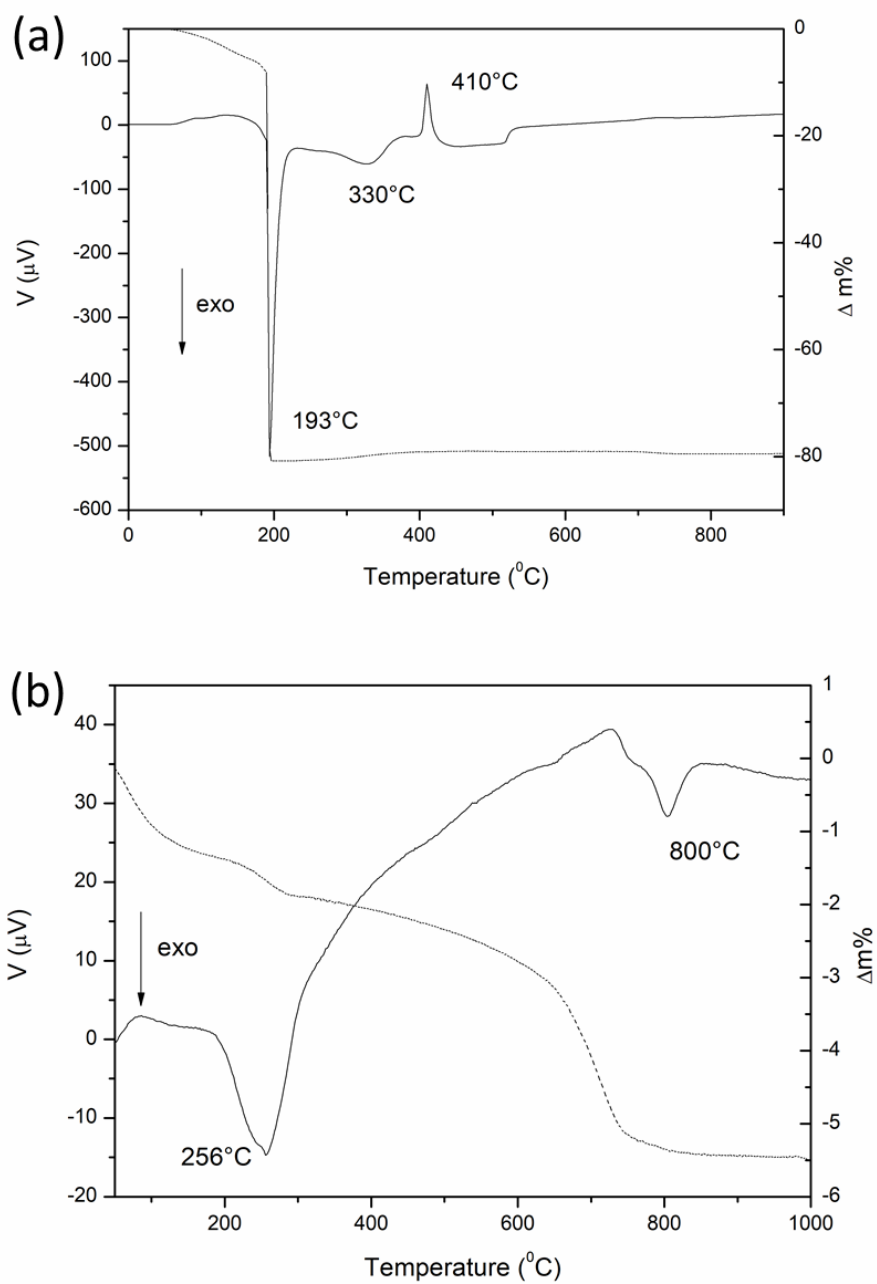


**Figure 4.** TG-DTA curve of BaFe<sub>12</sub>O<sub>19</sub> before (a) and after (b) annealing at 350°C. TG: dashed line; DTA: continue line [15].

Starting from the TG-DTA results, precursors were annealed for 1 h at three diverse temperature: 350°C, 650°C and 900°C. The XRD patterns of those pre-calcined powders are presented in Figure 5.

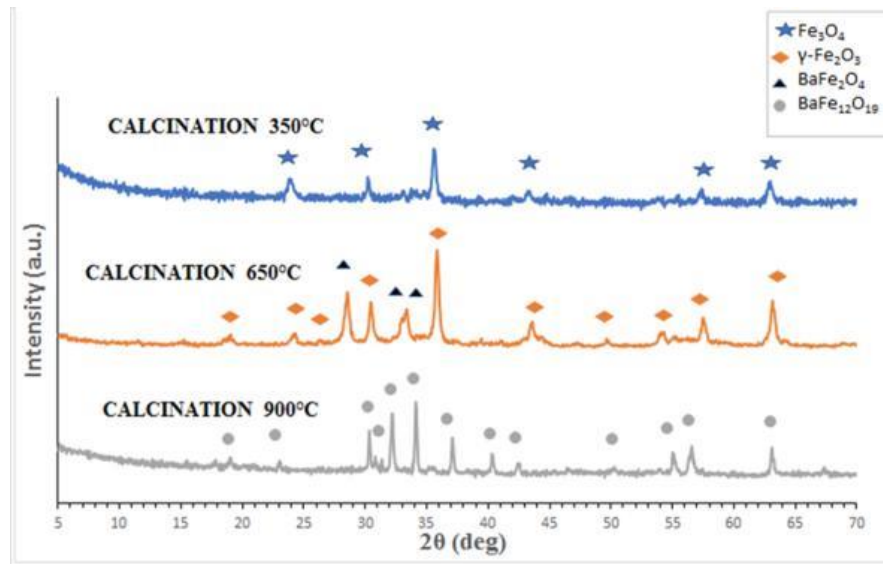


**Figure 5.** XRD spectra of BaM precursors calcined for 1 h at 350°C, 650°C and 900°C [15].

Firstly, the powder pre-combusted at 350°C showed solely the formation of magnetite (JCPDS file n°026-1136), whereas the powder annealed at 650°C was constituted by maghemite (JCPDS file n°039-1346) and of barium monoferrite, BaFe<sub>2</sub>O<sub>4</sub> (JCPDS file n° 046-0113), in accordance with TG-DTA investigations. As expected, the rate of crystallization enhanced at higher temperatures and the crystallization of maghemite at 650°C was established by the finding of two signals at 23.77° (210) and 26.10° (211), in agreement with the state of art [12]. In conclusion, BaM precursor calcined at 900°C was constituted exclusively of barium hexaferrite (JCPDS file n°039-1433). According to these results, the powder synthesized by auto-combustion sol-gel route was then annealed at 900°C for 1 h, for crystallizing pure BaM phase.

The mean crystallite size in the obtained BaM was calculated to be 44 nm, in accordance with the Scherrer equation 3. This value agrees with a previous study [12], where a crystallite size of 42 nm was obtained after firing at 950°C. However, in ref. [13, 16] a finer crystallite size of 16 nm was calculated. Nevertheless, in the latter references, BaM was synthesized after pre-annealing at 450°C for 4h, in experimental conditions rather diverse from this thesis.



From N<sub>2</sub> adsorption test, the specific surface area (SSA) of the BaFe<sub>12</sub>O<sub>19</sub> powder annealed at 900°C/1h was equal to 7.40 m<sup>2</sup>/g, and a median size of pores of 1.07 nm.

By FESEM observations, BaFe<sub>12</sub>O<sub>19</sub> treated at 900°C exhibited small primary particles, this size in the range 75-110 nm. Those particles were slightly agglomerated, generating ‘worm like’, submicronic structures as illustrated in Figure 6a, b. In the same figure (c, d) the morphology of the BaFe<sub>12</sub>O<sub>19</sub> film, subsequently to the firing at 600°C for 1 h to enhance its adhesion to the alumina substrate, is depicted as well. We can observe that the BaFe<sub>12</sub>O<sub>19</sub> nanoparticles underwent a moderate sintering. The microstructure was composed by primary particles with dimensions between 60 and 150 nm, with either spherical and prolonged morphology (Figure 6c, d) comprehending a widespread residual porosity. FESEM images carried out orthogonally to the sensors permitted to measure film thickness equal to 22.9 ± 2.4 μm.

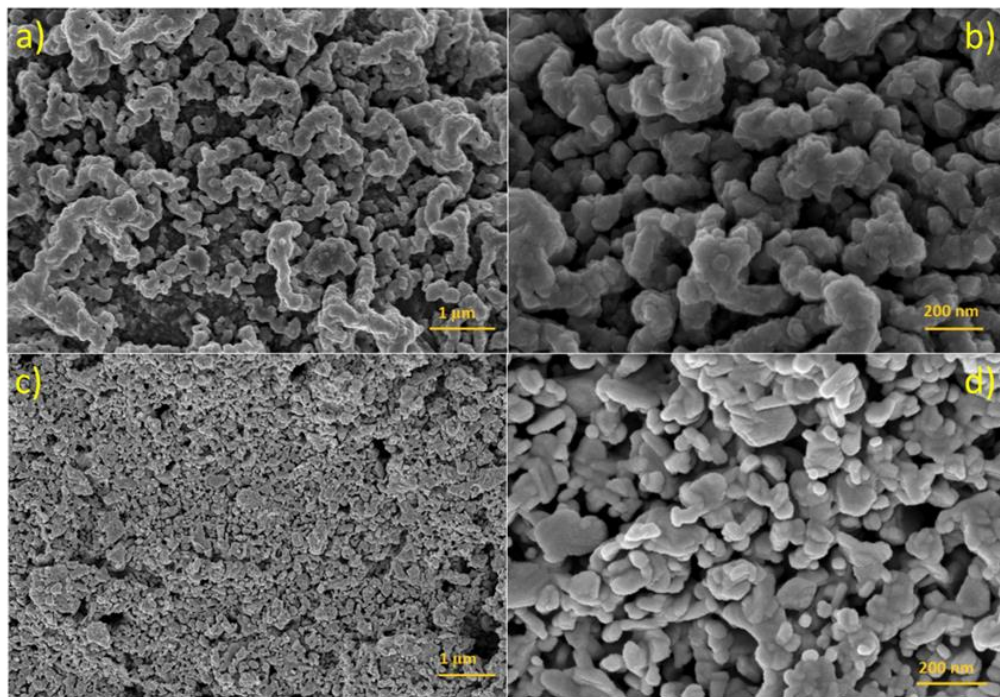


**Figure 6.** FESEM images at different magnification, BaFe<sub>12</sub>O<sub>19</sub> powder: 25k× (a), 100k× (b); BaFe<sub>12</sub>O<sub>19</sub> film: 25k× (c) and 100k× (d) [15].

Images of BaM particles annealed at 900 °C from TEM) and HR-TEM are displayed in Figure 7. Generally, particles appear considerably agglomerated with a lamellar form and the crystallite size was around 40 nm, accordingly to the value determined by the Scherrer equation. From HR-TEM, the lattice fringes confirmed

the strong crystalline character of the auto-combustion sol-gel obtained crystallites. The lattice spacing obtained from these observations equal to 0.278 nm coincides to (1 0 7) plane, i.e the main signal of BaM pattern (JCPDS-card n° 39-1433). In conclusion, either XRD and TEM investigations coherently confirm the nano-crystalline character of the synthesized BaM powders.

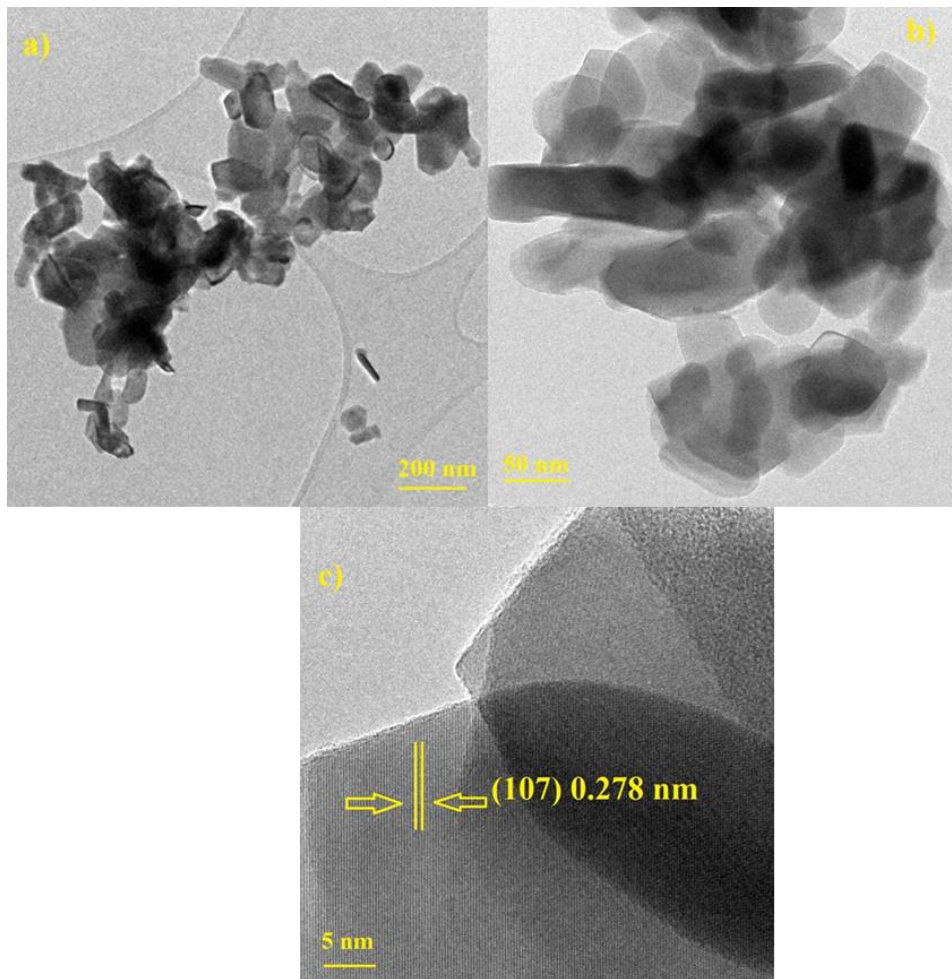


**Figure 7.** TEM (a, b) and HRTEM (c) micrographs of BaFe<sub>12</sub>O<sub>19</sub> [15].

#### 4.1.4 BaFe<sub>12</sub>O<sub>19</sub> gas sensing properties

Screen printed BaM sensors were firstly tested towards 500 ppb of O<sub>3</sub> concentration in a wide range of temperatures (150-350°C). A photo of the as-prepared sensor is illustrated in Figure 8.

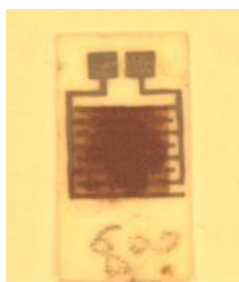


**Figure 8** BaFe<sub>12</sub>O<sub>19</sub> sensor (1x2 cm) [15].

Results of the changes of the sensor response at different T are represented in figure 9a. The selection of this range of temperature was motivated according with the results achieved in two previous works on BaM sensors under oxiditants respectively as pellets and thin films (NO<sub>2</sub> and O<sub>3</sub>) [3, 1].

The variation in impedance at the constant frequency of 1 kHz was investigated for BaM sensor, assessing the optimum working temperature, equal to 250°C (Figure 9a), a temperature close to the other two studies [3, 1]. So, from now on, sensor performances were evaluated at 250°C. Variations in impedance of BaM film after interaction towards diverse O<sub>3</sub> amounts (between 200 and 500 ppb) are depicted in Figure 9b.

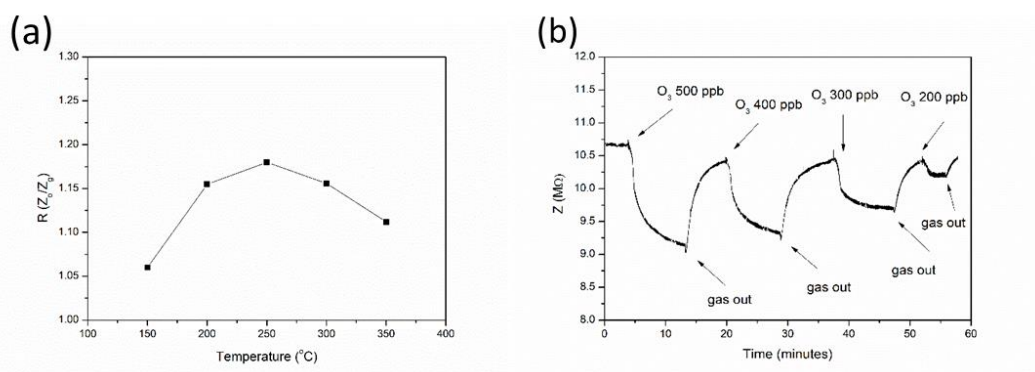


**Figure 9.** Sensor response of BaFe<sub>12</sub>O<sub>19</sub> thick-film at different working T (150-350°C) upon 0.5 ppm of O<sub>3</sub> (a) and impedance's changes after exposing BaFe<sub>12</sub>O<sub>19</sub> film to different levels of O<sub>3</sub> at 250°C (200-500 ppb) (b) [15].

Sensors impedance decreased from around 10.7 MΩ in dry conditions until 9 MΩ under 0.5 ppm of O<sub>3</sub>, showing a p-type semiconducting behaviour in all the investigated concentration range. The relation between the sensor response and [O<sub>3</sub>] is represented with the curve of calibration in Figure 10, that is linear in the studied range of concentration.

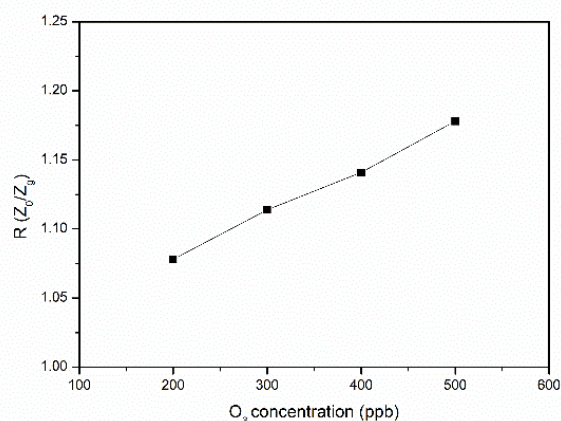


**Figure 10.** Sensor response vs O<sub>3</sub> concentration for BaFe<sub>12</sub>O<sub>19</sub> sensor [15].

In accordance with the IUPAC definition, the sensor's sensitivity is determined by the slope of the curve  $R=f([O_3])$  [17].

The sensor response is nearly linear in the investigated O<sub>3</sub> concentration (200-500 ppb;  $R^2=0.997$ ) and the sensitivity is  $0.0003 \text{ ppm}^{-1}$ .

In Table 3, sensor response and recovery times are tabulated, and it appears evident that they were shorter at lower O<sub>3</sub> amounts. In fact, these values are equal to 6-7 minutes for 0.5 ppm of O<sub>3</sub> and around 1 minute for 0.2 ppm of O<sub>3</sub> exposure. Quicker cinectics of gas adsorption and desorption at smaller concentration of O<sub>3</sub> were noted in literature either for p-type and n-type oxides [18, 19].

**Table 3.** Response and recovery times for BaM under different O<sub>3</sub> concentrations at 250°C.

O <sub>3</sub> concentration (ppb)	$\tau_{\text{ads}}$ (s)	$\tau_{\text{des}}$ (s)
200	71	62
300	136	133
400	258	231
500	482	348

Furthermore, both  $\tau_{\text{ads}}$  and  $\tau_{\text{des}}$  are influenced by the testing T: for the same O<sub>3</sub> level of 0.5 ppm, the  $\tau_{\text{ads}}$  dropped from around 14 minutes at 150°C until around 4.5 minutes at 350°C.

Moreover, evaluation of the selectivity of the BaM sensor was accomplished at 250°C by exposing the BaM sensor upon 50 ppm of NH<sub>3</sub>, 50 ppm of CH<sub>4</sub>, 50% and

90% of relative humidity at 25°C, 15 ppm of N<sub>2</sub>O, 50 ppm of CO<sub>2</sub> and 1.5 ppm of NO<sub>2</sub> and results are illustrated in Figure 11.

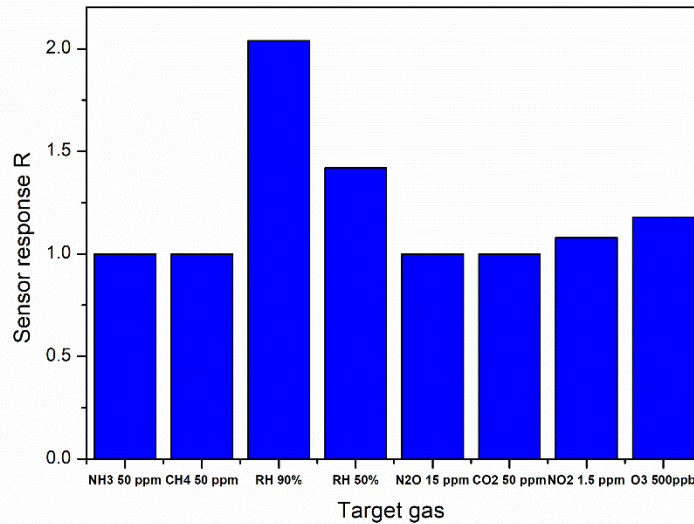


**Figure 11.** Cross sensitivity tests for BaFe<sub>12</sub>O<sub>19</sub> sensor [15].

The highest interference is due to humidity: the interference of water seems consistent still at 250°C where  $Z$  is decreasing from 15.3 M $\Omega$  until 7.5 M $\Omega$  under 90% of RH. These sensor performances are in accordance with [21]. Moreover, a slight interference with respect to NO<sub>2</sub> 1.5 ppm was also identified, with  $R$  of 1.08, in accordance with two previous studies [18, 19]. Interestingly, when BaFe<sub>12</sub>O<sub>19</sub> sensor is exposed to H<sub>2</sub>O and NO<sub>2</sub>, it acts as a n-type semiconductor, while under a stronger electron acceptor like O<sub>3</sub> an inversion of carrier occurs, and BaFe<sub>12</sub>O<sub>19</sub> film impedance decrease under O<sub>3</sub> exposure, exhibiting a p-type semiconductor behavior. For species with lower oxidant characteristics, like NO<sub>2</sub>, the semiconductor behaves as an n-type, since NO<sub>2</sub> molecules catches free electrons from the oxide and the conductance of BaM drops. For O<sub>3</sub>, it takes e<sup>-</sup> from the VB forming holes in the semiconductor conduction band. Here, there is an increase of charge carriers, and BaFe<sub>12</sub>O<sub>19</sub> behaves as a p-type oxide. As a result, the impedance drops by increasing the O<sub>3</sub> amount. This trend was noticed also in [1] where Fe<sub>2</sub>O<sub>3</sub> and Ba-doped Fe<sub>2</sub>O<sub>3</sub> thin film sensors were prepared by magnetron sputtering. As O<sub>3</sub> is a stronger electron acceptor compared to NO<sub>2</sub>, the performances after the injections of O<sub>3</sub> and NO<sub>2</sub> are opposite and the sensor response is higher for O<sub>3</sub> even at lower concentration compared to NO<sub>2</sub> as shown in figure 21.

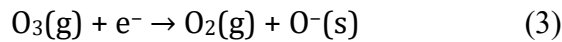
In the Table 4 the principal results from the state of art of Fe-based films for O<sub>3</sub> are presented. The main characteristics as the technological route for the preparation of the sensors, the layer thickness, the crystallite size, the sensor response and the conditions of measurements are outlined in the same table.

**Table 4.** The best performances of Fe-based O<sub>3</sub> MOS sensors.

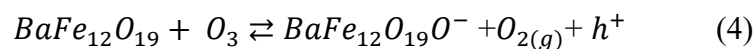
Material	Technological route	Film thickness	Crystallite size	Max R	Conditions of measurements	References
2%wt BaO-doped Fe <sub>2</sub> O <sub>3</sub>	Thin-film, sputtering	500 nm	200 nm	1.8	500 ppb, 225°C	[1]
SmFeO <sub>3</sub>	Thick-film, screen printing	50 μm	100 nm	1.9	10 ppb, 300°C	[2]
BaFe <sub>12</sub> O <sub>19</sub>	Thick-film, screen-printing	23 μm	44 nm	1.18	500 ppb, 250°C, dry	This thesis

Comparing the results obtained with the state of art of Fe-based ozone sensing films, the sensor's maximum response was observed at an intermediate temperature (250°C) [1, 2], where different sintering temperature deposition techniques were carried out. In addition, in this part of the thesis a BaFe<sub>12</sub>O<sub>19</sub> thick film was utilized for the first time for O<sub>3</sub> detection at relatively low temperature despite the sensor response is lower compared with the other works.

When O<sub>3</sub> is injected in the test chamber, the interaction between O<sub>3</sub> and the BaFe<sub>12</sub>O<sub>19</sub> surface follows the equation 3, delineating the electron's acceptor characteristics of O<sub>3</sub> [20]:



In this equation, e<sup>-</sup> represents an electron that contribute to the film conduction, O<sup>-</sup>(s) is an oxygen anion on the surface, and O<sub>3</sub> (g) and O<sub>2</sub>(g) are the adsorbing and desorbing species, respectively [21]. The oxygen situated at the centre of O<sub>3</sub> reacts with the barium hexaferrite surface generating an acceptor, while an O<sub>2</sub> is released as gas, as described in reaction (5). As it is well known, the O<sub>3</sub> reactivity is a consequence of the much lower dissociation energy compared to O<sub>2</sub>: the dissociation energies are respectively 1.1–1.3 eV for O<sub>3</sub> and 5.1 eV for O<sub>2</sub>. So, when O<sub>3</sub> interacts with BaM sensor at 250°C, O<sub>3</sub> is adsorbed onto the BaM surface, that acts as an acceptor of e<sup>-</sup>. The phenomenon probably follows the equation 4:



Oxygen adsorption, in the anionic form of  $\text{O}^-$ , generates a negative charge on the surface for the chemisorption, and an identical positive charge in the crystallites is generated by a HAL in the p-type metal oxide, maintaining the grains neutrality. For this phenomenon, a drop in the film Z was measured when BaM interacts with  $\text{O}_3$ . For BaM film, the 3D porous network provides many channels and surfaces for exchange of  $e^-$  during adsorption of target gas, transforming the layer into a more conducting system during the interaction with  $\text{O}_3$ . According with the state of art, the sensor response of p-type oxides upon oxidants as  $\text{O}_3$  is lower comparing with n-type oxides even if they display smaller optimum working temperature. This was experimentally confirmed in this thesis. As a matter of fact, the sensor response for p-type oxides is generally modelled to be the square root of that for n-type semiconductors. This is due to the different mechanism of conduction between crystallites in the p-type oxides, that happens in the HAL only on the surface, considering that the core of the crystallites displays insulating characteristics.

## 4.2 SWCNTs-ODA sensors

### Abstract

In this section, the results of thin film sensor utilizing Single Walled Carbon Nanotubes (SWCNTs) functionalized with an amino-group polymer for  $\text{O}_3$  detection are described.

Carbon nanotubes (CNTs) present many advantages as sensitive materials in gas sensor technology, such as great surface area for electrical conductivity, moderate cost of production and operative temperatures and the possibility to be functionalized with several functional groups to enhance the sensitivity towards a specific gas. Utilizing CNTs many researchers have fabricated laboratory sensors of gases like  $\text{NH}_3$ ,  $\text{NO}_2$  and  $\text{CO}_2$  That are interesting for environmental monitoring. The major part of these devices works on DC and does not display the selectivity and the sensitivity to run in environment detecting air analytes that contribute to the pollution. In this part, the design and sensing characteristics of  $\text{O}_3$  sensors comprehending pristine SWCNTs functionalized with octadecylamine (ODA) groups by covalent modification is examined. CNTs were firstly dispersed and then sonicated in a paste. This was spray-coated on interdigitated Pt electrodes onto

Al<sub>2</sub>O<sub>3</sub> ceramic substrate. The film Z was measured upon O<sub>3</sub> gas in the range 200-500 ppb, revealing variations > 50% at 75°C and almost entire sensor retractability in desorption. The selectivity was evaluated at the best operating temperature by cross-sensitivity test for reducing gases (methane, ammonia and water vapor) and oxidant species (carbon dioxide and nitrogen dioxide).

#### 4.2.1 Introduction

From the time of the invention of carbon nanotubes (CNTs) [22], the influence of nanotechnology has grown, generating fruitful exploitations to communication, electronics and sensing.

Miniaturized chemical sensors displays a broad area of novel usages for user, medical, industrial and military utilization, empowered by progresses in the development of nanomaterials, such as zeolites, nanoparticles, carbon nanotubes and graphene. Portable and cheap chemical sensors with great selectivity and sensitivity are essential in the environment to monitor pollutants (e.g., O<sub>3</sub>, NO<sub>2</sub> and PM) due to industrial procedures, car emissions and fossil fuel burning. For instance, in the Internet of Things (IoT) dominion cheap wereable and portable sensors are required to monitor both indoor and outdoor air quality together with professional chemical risks [23].

Using CNTs, many researchers have confirmed the validity of laboratory detectors for the monitoring of ordinary environmental gases like NH<sub>3</sub>, NO<sub>2</sub> and CO<sub>2</sub> [23-28], and deadly gases like sarin, the nerve agent [29-31].

Detectors based on CNT use the feature of the interaction involving the analyte and the sensitive film measuring the variation in DC resistance between the electrodes [24-32], i.e. concept forming chemiresistors.

In addition, low-frequency approaches have been examined. In those methods, like inductive near-field coupling [33-36] and chemicapacitor [37-41], the transduction mechanism is due to modifications in capacitance of the CNTs film from intrinsic or induced dipole moments in the case of gas molecule interaction with the CNT sidewalls.

With the aim to extend the influences of sensors based on CNTs over the usual in-lab research step to real outdoor environments, it is demanded to improve the selectivity of CNT in an ambient with several gases. CNTs's chemical functionalization provides often higher selectivity to specific analytes simultaneously with increased sensitivity to the target gas [25, 42].

For improving the sensing performance of CNTs, chemical functionalization appears an effective method. Firstly, it warrants the distinctive features of carbon



nanotubes to be combined with different materials, like metal oxides, metals and conducting polymers, to form composite sensitive elements with increased sensitivity, selectivity and quicker kinetics of adsorption and desorption. Secondly, it can refine the dispersion of CNTs in many solvents, enabling cost-effective way of sensors fabrication by ease technique like dispensing and printing. Noble metals like Pd [43] and Pt [44] have been utilized for O<sub>3</sub> detection at sub ppm level, and Pt-decoration was successfully utilized also for CO, NO [45] and NO<sub>2</sub> [46] detection at concentrations of few ppm. Surface chemical modification of CNTs after the addition of functional species permits to adjust the interaction of CNTs with the surrounding ambient. This ameliorates both the selectivity and the sensitivity of CNTs devices at the same time. For instance, Bekyarova et al. have refined gas sensors using functionalized CNTs evidencing a LOD (limit of detection) of 20 ppb towards NO<sub>2</sub> and 100 ppb towards NH<sub>3</sub>, corresponding to higher sensitivity with respect to the literature [25].

In this part of the thesis, using the innovative SWCNTs functionalization concepts delineated in [25, 42], the design and sensing features of O<sub>3</sub> chemical sensors comprehending pristine CNTs functionalized covalently with octadecylamine (ODA) molecule is explored [47].

#### **4.2.2 Sensor preparation**

The O<sub>3</sub> CNT-chemical sensors were manufactured by the team of E. Bekyarova at Carbon Solutions Inc. using functionalized CNTs to prepare thin films as gas sensor. The films were sprayed onto Pt interdigitated electrodes screen-printed up to  $\alpha$ -alumina substrates as delineated in the paragraph 3.1.5. The carbon nanotubes chosen are SWCNTs (P3-SWNT, from Carbon Solutions (CSI)) treated with HNO<sub>3</sub> for purification and maintained in a strongly functionalized state. This has 1.0-3.0 at% of COOH groups that are derivatizable with a wide range of functional groups. P3-SWNTs are functionalized with ODA with a weight ratio of 1:3 between ODA and P3-CNT. ODA furnish a medium for the adsorption of O<sub>3</sub> that is measured by changes in impedance and conductance of the CNT thin layer.

The ODA-CNTs (CSI's P5-CNT) were developed by adding carboxylate P3-CNTs to ODA. The ODA-CNTs were dispersed in tetrahydrofuran (THF), where they are more dispersible, by means of ultrasonication for breaking the bundles and then realizing the ink for the preparation of the sensor (Figure 12).

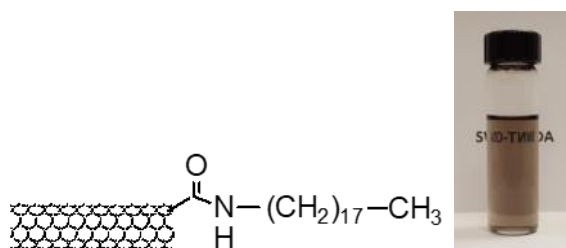


**Figure 12.** Structure of ODA-CNTs (left) and dispersion of ODA-CNTs in THF (right).

Before the deposition of the film, the substrate is put into a manufactured Al plate, that is heated depending on the solvent type. The thin-film of CNTs is sprayed onto the interdigitated electrodes with a commercial air-brush spray coater. DC resistance was checked during the deposition to confirm the generation of the film having the right thickness. Several layers were sprayed till the expected resistance was achieved. The substrate was cool down before annealing at 100°C for 1 h to evaporate the remaining solvent. The definitive resistance was checked after 12 h of equilibration in air. Before testing, the sensors were viewed under an optical microscope to confirm lack of contamination and uniformity.

### 4.2.3 ODA-CNTs characterization

The ODA-CNTs nanomaterial was characterized by SEM, TGA in static air, mid-IR spectroscopy and UV-Vis-NIR spectroscopy. Results are depicted in Figure 13.

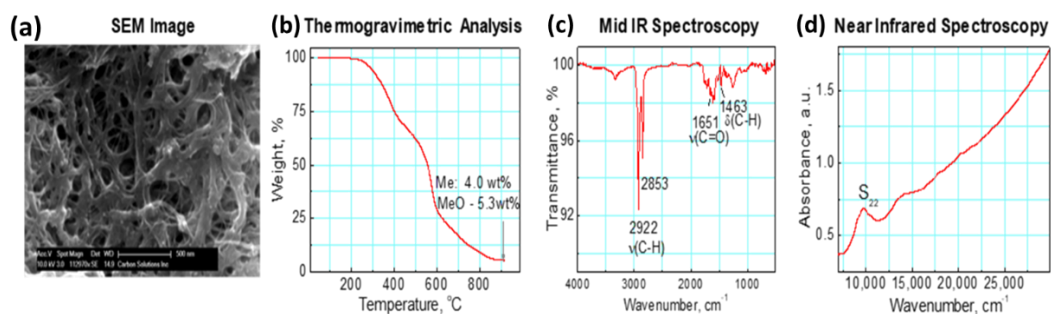


**Figure 13.** Characterization for ODA-CNTs: (a) SEM micrograph displaying the porous nanotube networks, (b) TGA investigation, (c) Mid IR and (d) Near IR Spectroscopy [48].

ODA-CNTs layer morphology displays the generation of a network with high porosity. The TGA investigation demonstrates a best ODA: P3-CNT mass ratio of 1:3, with a mass loss at a temperature higher than 200°C. Moreover, the NIR-IR

analysis confirms the presence of functional groups with oxygen. By functionalizing with alkyl amines, signals between  $2922$  and  $2853\text{ cm}^{-1}$  arise, that are generated by stretching of C-H of the alkyl chain ( $\text{CH}_2$ ). The signal of C-H is shifted to  $1463\text{ cm}^{-1}$  for CNTs and characteristic C=O vibration at  $1651\text{ cm}^{-1}$  confirms that carbonilic groups are bonded to the ammino group.

The TGA analysis confirmed that ODA-SWCNTs nanomaterial is stable until around  $200^\circ\text{C}$ . Consequently, for assessing the temperature dependence of the sensor response, starting from  $25^\circ\text{C}$  the sensor was exposed until  $100^\circ\text{C}$  in steps of  $25^\circ\text{C}$  and at every T, the response of the sensor is determined under  $200\text{ ppb}$  of  $\text{O}_3$  adsorption and desorption. The sensor impedance  $Z$  decreases under  $\text{O}_3$  since ODA-CNTs sensor is a p-type semiconductor. After the adsorption equilibrium,  $\text{O}_3$  is substituted by dry air and in the desorption, an enhanced film impedance was measured.  $Z$  returns almost to the baseline value and this cycle was replicated for each temperature. Since the phase of impedance was close to  $0$ , only the real component is present: impedance is practically equal to resistance.

The sensor response vs the working temperature is depicted in Figure 14a, and the temporal variation in the impedance magnitude is plotted at different temperatures in Figure 14b.

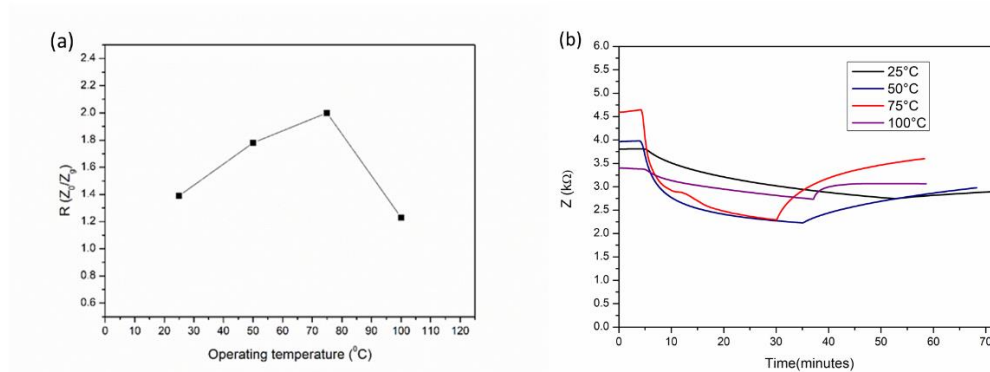


**Figure 14.** Sensor response at different operating temperatures (a) and adsorption and desorption of  $0.2\text{ ppm}$  of  $\text{O}_3$  for ODA-SWCNTs sensor in the temperature range  $25\text{-}100^\circ\text{C}$  [49].

From this plot, either the  $\tau_{\text{ads}}$  and  $\tau_{\text{des}}$ , are shorter with enhancing the working temperature, with optimal sensor response at  $75^\circ\text{C}$ . In fact, the  $\tau_{\text{ads}}$  drop from  $35.8\text{ min}$  at  $25^\circ\text{C}$  to  $15.5\text{ min}$  at  $75^\circ\text{C}$  and the  $\tau_{\text{des}}$  dropped from  $31.7\text{ min}$  to  $28.7\text{ min}$  at  $75^\circ\text{C}$ .  $75^\circ\text{C}$  guarantee the best sensor performances both in terms of sensitivity and kinetic of adsorption and desorption. Furthermore, the ODA-SWCNTs sensors display satisfactory repeatability and reproducibility, since sensor responses standard deviation were lower than  $10\%$  considering  $Z$  after four pulses under the

same O<sub>3</sub> amounts. The presented sensors exhibits comparable characteristics till 75°C, whereas after some hours at 100°C the device starts to be damaged since the sensor response is lower compared to 75°C. Consequently, the best operating temperature is 75°C in further investigations.

In the Figure 15, the impedances' variation of ODA-SWCNTs sensor over an entire cycle of adsorption and desorption at different O<sub>3</sub> concentrations (200, 300, 400, 500 ppb) are illustrated. Since ODA-CNT film's Z can be modelled as a RC circuit in parallel [50], it is possible to extract the conductance of the thin layer from the impedance.

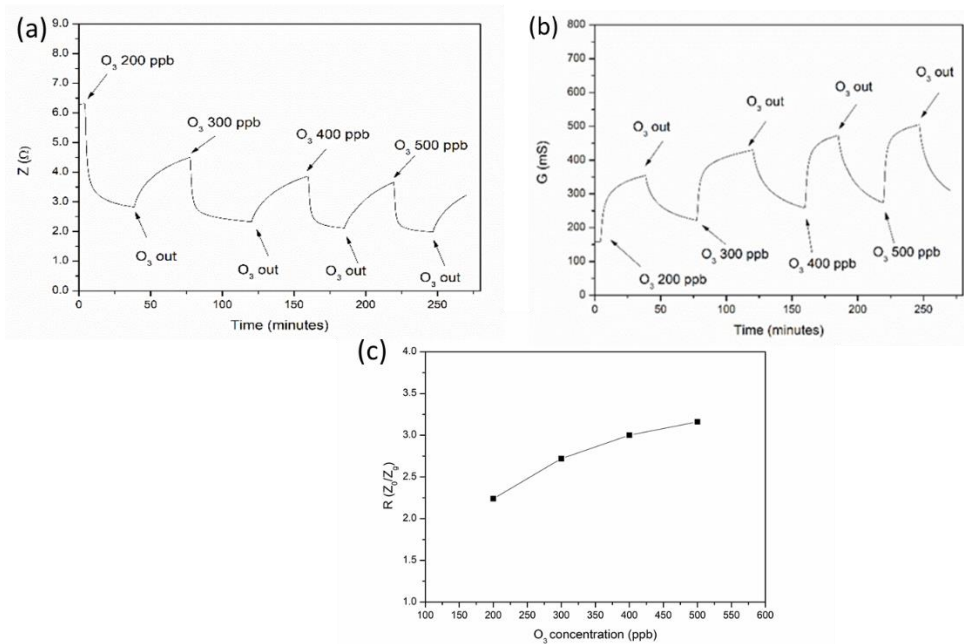


**Figure 15.** Impedance (a) and conductance (b) variation under 200-500 ppb of O<sub>3</sub> and calibration curve at 75°C (c) [49].

Conductance raises at higher O<sub>3</sub> amount and it furnish the same sensor response of  $Z$ .

The variations in conductance were evaluated to comprehend if solely resistive events were present during the gas sensing mechanism. In these tests, the phases of  $Z$  were  $-0.035^\circ$  and  $-0.15^\circ$ , respectively, before and after 200 ppb O<sub>3</sub> interaction with the film, confirming that the real component of  $Z$  is dominant in the sensor signal.

The change in impedance is almost linear with increasing O<sub>3</sub> level ( $R^2$ : 0.95) and the sensitivity is  $0.003 \text{ ppm}^{-1}$ . Adsorption and desorption time are both in the range 7-15 minutes.

The selectivity of ODA-SWCNTs sensor was also investigated by exposing the film to CH<sub>4</sub> 100 ppm, NH<sub>3</sub> 50 ppm, humidity 50%, CO<sub>2</sub> 500 ppm and NO<sub>2</sub> 100 ppb. Results are displayed in Figure 16.

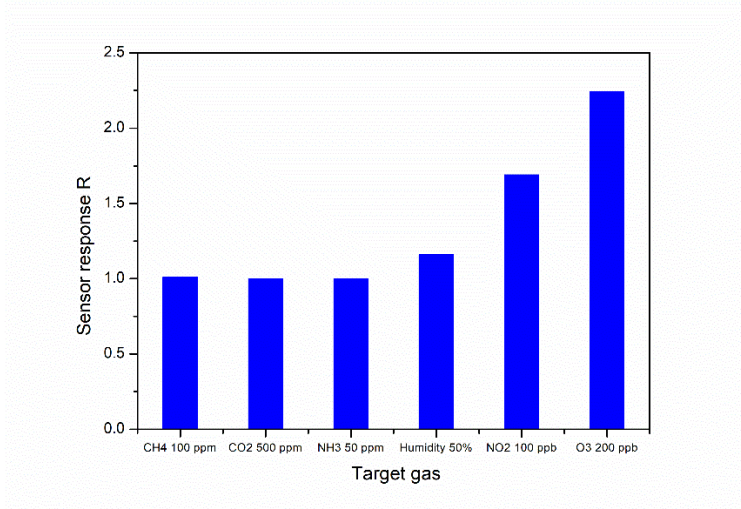


**Figure 16.** Cross sensitivity tests for ODA-SWCNTS sensor.

For environmental monitoring the cross-sensitivity tests are essential, particularly with respect to nitrogen dioxide and humidity. Air with 50% RH was inserted into the sensor chamber until a new equilibrium was reached. Only a modest (R: 1.16) increase in impedance was generated by humidity. Humidity is an acceptor of holes on the CNTs surface, increasing moderately the impedance of the film. This little alteration can be rectified by calibrations in the real environment. The predominant, as expected, interference was measured for 100 ppb NO<sub>2</sub> with a sensor response of 1.69. This is a result of the fact that NO<sub>2</sub> reacts with ODA-SWCNTS on the surface with a similar interaction mechanism as O<sub>3</sub>. Finally, no interferences were measured with CH<sub>4</sub>, CO<sub>2</sub> and NH<sub>3</sub>.

The impedance changes in former SWCNTs and ODA-SWCNTs were put in comparison to evaluate the impact of the polymeric functionalization, and an increase of 8% in the impedance variation was measured under 200 ppb of O<sub>3</sub> at 25°C.

The O<sub>3</sub>-sensing mechanism of the ODA-SWCNT sensors involves:

- oxidizing effect between target molecules and the nanotube surface.
- acid-base interaction for the presence of ODA.

The first effect is due to variations in resistance of the CNTs and can be described via Wolkentein's model [51].

During reactions on the CNTs surface, electrons of the VB are removed, generating a higher conductivity of the nanotubes, i.e., adsorbed oxygen species withdraw electrons from SWCNTs. Consequently, under oxidizing species like O<sub>3</sub> and NO<sub>2</sub>, those gases extract electrons from the surface of nanotubes. This extraction generates an extension of the HAL (hole accumulation layer) in every nanotube. Hence, this enhances the ozone sensitivity and selectivity. Moreover, for ODA-SWCNTs, the protonation of amino group could improve the affinity to O<sub>3</sub> adsorption [47].

In particular, metallic Pt NPs on SWCNTs catalytically favour chemisorption and dissociation of NO<sub>2</sub> species. In addition, the conducting channel in CNTs is modulated in the radial direction by PtO<sub>2</sub> (as shown in Fig. 10(b)), that sensitizes remarkably their electrical transport channels for the detection of oxidant species like NO and NO<sub>2</sub>. These sensitization effects can improve the modulation in resistance for NO<sub>2</sub> comparing with other gases in the Pt NPs-doped SWCNT chemical sensors. For extremely selective sensing of NO<sub>2</sub> gas at ambient T, this study has strengthened the usefulness of the doping of Pt NPs on the SWCNTs surface.

Wongwiriyan et al [52] proofed the ozone detection with SWNT networks grown by CVD on a device platform that was prefabricated. This is comparable to the configuration used in the present thesis, with an Al<sub>2</sub>O<sub>3</sub> substrate with platinum interdigitated electrodes and a heater of platinum underneath. Those devices can sense O<sub>3</sub> until 6 ppb at ambient T. They were characterized by quick  $\tau_{des}$  of few min obtained by heating till the sensor conductivity had recovered the baseline. In the case of Capsula-Colindres et al [44] Pt-doped SWCNTs were realized with sensor's  $\tau_{ads}$  after exposition to O<sub>3</sub> equal to 1 minute, with the detection limit of 10 ppb. In that study, vapor phase impregnation decomposition (VPID) way was carried out to decorate Pt NPs onto CNTs. In [43] the same authors doped with Pd NPs the MWCNTs through the same VPID method. The sensor device consisted on a sensitive film realized by drop coating onto Pt electrodes onto a SiO<sub>2</sub> dielectric substrate. The sensor showed a resistance variation under O<sub>3</sub> with  $\tau_{ads}$  of 1 min with the ability to detect until 20 ppb. Sensor displays the highest performances at 120°C. A comparative study of the obtained results with previous works is represented in Table 5.

**Table 5.** The best features of CNTs-O<sub>3</sub> sensors.

Material	Technological route	Sensitivity	Conditions of measurements	Sensor $\tau_{ads}$	References
SWCNTs	Direct growth	6ppb LOD	Room T	n.d.	[52]
Pd-SWCNTs	vapor impregnation-decomposition	10ppb LOD	120°C	100-1200s	[43]
CNT/Pt sensor	VPID	LOD 10 ppb	120°C	1 min-1min	[44]
ODA-SWCNTs	Spray-coating	16% Z variation, sensitivity 0.003 ppm <sup>-1</sup>	75°C	15.5-35.8 min	This thesis

### 4.3 Conclusions

This chapter has described novel results of barium ferrite (BaM) and ODA-SWCNTs sensors for ozone detection at sub-ppm level at low temperatures. BaM was prepared by sol-gel auto-combustion route utilizing citric acid either as chelant and fuel, and devices were fabricated by screen-printing method upon Al<sub>2</sub>O<sub>3</sub> dielectric. Sensor optimum response was achieved at moderate temperature (250°C) with an impedance variation of 18%.  $\tau_{ads}$  and  $\tau_{des}$  were in the range of 1 min for 200 ppb of O<sub>3</sub> and of 5 minutes for 500 ppb of O<sub>3</sub>. The main criticism is due to water molecules interference that should be decreased in further investigations for improving the sensitivity of BaM for O<sub>3</sub> detection. In addition, a study of the sensor performances of O<sub>3</sub> sensors with pristine CNTs functionalized by octadecylamine groups was performed, verifying a noticeably selectivity for O<sub>3</sub> detection, and only 16% of impedance variation under 50% of relative humidity. The impedance of the sensor, evaluated upon O<sub>3</sub> exposure in the range 200-500 ppb, discloses a significant sensor response and almost complete sensor retractability. Despite of this, the fabrication of sensing elements with superior sensitivity and selectivity for low amounts of toxic and hazardous gases is till a challenge. Such materials should be coupled in an array of sensors where different materials are sensitive towards different gases for extracting the specific contribution due to the target gas present in air.

The proposed materials seem interesting for O<sub>3</sub> monitoring at quite low temperature and sub-ppm levels, eventough the sensor response is lower compared to others n-type ozone sensitive materials (SnO<sub>2</sub>, In<sub>2</sub>O<sub>3</sub>, ZnO).

## References

- [1] Debliquy M., Baroni C., Boudiba A., Tulliani J. M., Oliver M., Zhang C. (2011) Sensing characteristics of hematite and barium oxide doped hematite films towards ozone and nitrogen dioxide. *Procedia Eng.* Pages 219-222.
- [2] Hosoya Y., Itagaki Y., Aono H., Sadaoka Y. (2005) Ozone detection in air using SmFeO<sub>3</sub> gas sensor. *Sens. Actuators B.* Pages 198–201.
- [3] Lopez C., Baroni C., Tulliani J. M. (2013) Ba-doped iron oxide as a new material for NO<sub>2</sub> detection. *Materials.* Pages 4801-4816.
- [4] Primc D., Makovec D., Lisjak D., Drofenik M. (2009) Hydrothermal synthesis of ultrafine barium hexaferrite nanoparticles and the preparation of their stable suspensions. *Nanotech.* Pages 315605.
- [5] Karmakar M., Mondal B., Pal M., Mukherjee K. (2014) Acetone and ethanol sensing of barium hexaferrite particles: A case study considering the possibilities of non-conventional hexaferrite sensor. *Sens Actuators B.* Pages 627– 633.
- [6] Annapureddy V., Kang J.-H., Palneedi H., Kim J.-W., Ahn C.-W., Choi S.-Y., Johnson S. D., Ryu J. (2017) Growth of self-textured barium hexaferrite ceramics by normal sintering process and their anisotropic magnetic properties. *J. Eur. Ceram. Soc.* Pages 4701–4706.
- [7] Özgür Ü., Alivov Y., Morkoç H. (2009) Microwave ferrites, part 1: fundamental properties, *J Mater Sci-Mater El.* Pages 789-834.
- [8] Pullar R. C. (2012) Hexagonal ferrites: a review of the synthesis, properties and applications of hexaferrite ceramics, *Progress in Materials Science.* Pages 1191-1334.
- [9] Harris V. G., Geiler A., Chen Y., Yoon S. D., Wu M., Yang A., Chen Z., He P., Parimi P. V., Zuo X. (2009) Recent advances in processing and applications of microwave ferrites, *J. Magn. Magn. Mater.* Pages 2035-2047.
- [10] Chikazumi S., Physics of Ferromagnetism 2e, Oxford University Press, 2009.



- [11] Maswadeh Y., Mahmood S. H., Awadallah A., Aloqaily A. N. (2015) Synthesis and structural characterization of non-stoichiometric barium hexaferrite materials with Fe:Ba ratio of 11.5 – 16.16. *IOP Conf. Series: Materials Science and Engineering*. Pages 012019.
- [12] Li Y., Wang Q., Yang H. (2009) Synthesis, characterization and magnetic properties on nanocrystalline BaFe<sub>12</sub>O<sub>19</sub> ferrite. *Current Appl. Physics*. Pages 1375-1380.
- [13] Durmus Z., Sozeri H., Toprak M. S., Baykal A. (2011) The effect of condensation on the morphology and magnetic properties of modified barium hexaferrite (BaFe<sub>12</sub>O<sub>19</sub>). *Nano-micro Lett.* Pages 108-114.
- [14] Varma A., Mukasyan A. S., Rogachev A. S., Manukyan K. V. (2016) Solution Combustion Synthesis of Nanoscale Materials. *Chem. Rev.* Pages 14493–14586.
- [15] Ziegler D., Marchisio A., Montanaro L., Palmero P., Tulliani J. M. (2018) Barium hexaferrite thick-films for ozone detection at low temperature. *Solid state ionics*. Pages 24-32.
- [16] Sozeri H., Durmus Z., Baykal A., Uysal E. (2012) Preparation of high quality, single domain BaFe<sub>12</sub>O<sub>19</sub> particles by citrate sol-gel combustion route with an initial Fe/Ba molar ratio of 4. *Mater. Sci. Eng. B*. Pages 949-955.
- [17] IUPAC. Compendium of Chemical Terminology, 2nd ed. (the "Gold Book"). Compiled by A. D. McNaught and A. Wilkinson. Blackwell Scientific Publications, Oxford (1997). XML on-line corrected version: <http://goldbook.iupac.org> (2006-) created by M. Nic, J. Jirat, B. Kosata; updates compiled by A. Jenkins. ISBN 0-9678550-9-8
- [18] Basyooni M. A., Shaban M., El Sayed A. M. (2017) Enhanced gas sensing properties of spin-coated Na-doped zZnO nanostructured films. *Sci. Rep.* Pages 41716.
- [19] Kamble B., Umarji A. M. (2015) Effect of Pt doping on the gas sensing properties of porous chromium oxide films through a kinetic response analysis approach. *RSC Adv.* Pages 27509-27516.
- [20] Becker T., Tomasi L., Braunm C. B.-V., Muller G., Sberveglieri G., Fagli G., Comini E. (1999) Ozone detection using low-power-consumption metal-oxide gas sensors. *Sens. Actuators A*. Pages 229–232.
- [21] I. Petrila, F. Tudorache. (2014) Influence of partial substitution of Fe<sup>3+</sup> with W<sup>3+</sup> on the microstructure, humidity sensitivity, magnetic and electrical properties of barium hexaferrite. *Superlattices Microst.* Pages 46–53.
- [22] Tijima S. (1991) Helical microtubes of graphitic carbon *Nature*. Pages 56-58.
- [23] Bahga A., Madisetti V. K. (2014) Internet of Things: A Hands-on Approach, *Arsheep Bahga & Vijay Madisetti Publishers*.

- [24] Collins P. G., Bradley K., Ishigami M., Zettl A. (2000) Extreme oxygen sensitivity of electronic properties of carbon nanotubes. *Science*. Pages 1801-1804.
- [25] Suehiro J., Zhou G., Imakiire H., Ding W., Hara M. (2005) Controlled fabrication of carbon nanotube NO<sub>2</sub> gas sensor using dielectrophoretic impedance measurement, *Sensors and Actuators B*. Pages 398-403.
- [26] Zhang T., Mubeen S., Bekyarova E., Yoo B. Y., Haddon R. C., Myung N. V., Deshusses M. A. (2007) Poly (m-aminobenzene sulfonic acid) functionalized single-walled carbon nanotube based gas sensor. *Nanotechnology*. Pages 165504-165509.
- [27] Brahim S., Colbern S., Gump R., Grigorian L. (2008) Tailoring gas sensing properties of carbon nanotubes. *J. Appl. Phys.* Pages 1-10.
- [28] Kauffman D. R., Star A. (2008) Carbon nanotube gas and vapor sensors, *Angewandte Chemie, International Edition*. Pages 6550–6570.
- [29] Abdellah A., Yaqub A., Ferrari C., Fabel B., Lugli P., Scarpa G. (2011) Spray deposition of highly uniform CNT films and their application in gas sensing, *in Proc. 11th IEEE Int. Conf. Nanotechnology*, Portland, OR.
- [30] Novak J. P. Snow E. S., Houser E. J., Park D., Stepnowski J. L., McGill R. A. (2003) Nerve agent detection using network of single-walled carbon nanotubes. *Appl. Phys. Lett.* Pages 4026-4028.
- [31] Lee C. Y., Sharma R., Radadia A. D., Masel R. I., Strano M. S. (2008) On-chip micro-gas- chromatograph enabled by a non-covalently functionalized single-walled carbon nanotube sensor array. *Angew. Chem.* Pages 5096 –5099.
- [32] Zhang Q., Fu Y. C., Xu J. Q. (2010) Advances in the chemical sensors for the detection of DMMP – A simulant for nerve agent sarin. *Proc. Engineering*. Pages 179-184.
- [33] Varghese O. K., Kichambre P. D., Gong D., Ong K. G., Dickey E. C., Grimes C. A. (2001) Gas sensing characteristics of multi-walled carbon nanotubes. *Sensors and Actuators B*. Pages 32-41.
- [34] Ong K. G., Zheng K., Grimes C. A. (2002) A wireless passive carbon nanotube-based gas sensor. *IEEE Sensors J*. Pages 82-88.
- [35] Chopra S., Pham A., Gaillard J., Parker A., Rao A. M. (2002) Carbon-nanotube-based resonant-circuit sensor for ammonia. *Appl. Phys. Lett.* Pages 4632-4634.
- [36] Someya T., Small J., Kim P., Nuckolls C., Yardley J. T. (2003) Alcohol vapor sensors based on single-walled carbon nanotube field effect transistors. *Nano Lett.* Pages 877-881.

- [37] Snow E. S., Perkins F. K., Houser E. J., Badescu S. C., Reinecke T. L. (2005) Chemical detection with a single-walled carbon nanotube capacitor. *Science*. Pages 1942-1945.
- [38] Patel S. V., Mlsna T. E., Fruhberger B., Klaassen E., Cemalovic S., Baselt D. R. (2003) Chemicapacitive microsensors for volatile organic compound detection. *Sensors and Actuators B*. Pages 541-553.
- [39] Delapierre G., Grange H., Chambaz B., Destannes L. (1983) Polymer-based capacitive humidity sensor: characteristics and experimental results. *Sensors and Actuators B*. Pages 97-104.
- [40] Hierlemann A., Lange D., Hagleitner C., Kerness N., Brand O., Baltes H. (2000) Application-specific sensor systems based on CMOS chemical microsensors. *Sensors and Actuators B*. Pages 2-11.
- [41] Roninson J. T., Perkins F. K., Snow E. S., Wei Z. Q., Shan P. E. (2008) Reduced graphene oxide molecular sensors. *Nano. Lett.* Pages 3137-3140.
- [42] Bekyarova E., Davis M., T. Burch, M. E. Itkis, B. Zhao, S. Sunshine, R.C. Haddon. (2004) Chemically functionalized single-walled carbon nanotubes for ammonia sensors. *J. Phys. Chem. B*. Pages 19717-19720.
- [43] Capsula-Colindres S., Aguir K., Cervantes-Sodi F., Villa-Vargas L. A., Salazar J. M., Garibay-Febles V. (2014) Ozone sensing based on palladium decorated carbon nanotubes. *Sensors*. Pages 6806-6818.
- [44] Capsula-Colindres S., Aguir K., Cervantes-Sodi F., Villa-Vargas L. A., Garibay-Febles L. A. (2014) Carbon nanotubes functionalized by nanoparticles of platinum. *Materials Science Forum*. Pages 45-50.
- [45] Li K., Wang W., Cao D. (2011) Metal (Pd, Pt)-decorated carbon nanotubes for CO and NO sensing. *Sensors and Actuators B*. Pages 171– 177.
- [46] Choi S-W., Kim J., Byun Y. T. (2017) Highly sensitive and selective NO<sub>2</sub> detection by Pt nanoparticles-decorated single-walled carbon nanotubes and the underlying sensing mechanism. *Sensors and Actuators B*. Pages 1032–1042.
- [47] Bekyarova E., Itkis M. E., Cabrera N., Zhao B., Yu A., Haddon R. C. (2005) Electronic properties of single-walled carbon nanotube networks. *J. Am. Chem. Soc.* Pages 5990-5995.
- [48] [https://www.carbonsolution.com/~carbon/sites/default/files/documents/ACR2002\\_Chemistry.pdf](https://www.carbonsolution.com/~carbon/sites/default/files/documents/ACR2002_Chemistry.pdf) (Accessed on 18th February 2019).
- [49] Ziegler D., Bekyarova E., Naishadham G., Savi P., Marchisio A., Tulliani J. M., Naishadham K. (2018) Nanotechnology-based ozone sensors exploiting low-frequency impedance changes for detection in 17th International Meeting on Chemical Sensors - IMCS 2018. Pages 740-741

- [50] Lee H., Shaker G., Naishadham K., Song X. J., McKinley M., Wagner B., Tentzeris M. M. (2011) Carbon nanotube-loaded antenna-based ammonia gas sensor, *IEEE Trans. Microwave Theory Tech.* Pages 2665-2673.
- [51] Liu X., Chen N., Han B., Xiao X., Chen G., Djerdj I., Wang Y. (2015) Nanoparticle cluster gas sensor: Pt activated SnO<sub>2</sub> nanoparticles for NH<sub>3</sub> detection with ultrahigh sensitivity. *Nanoscale.* Pages 14872-14880.
- [52] Wongwiriyan W. et al. (2006) Ultrasensitive ozone detection using single-walled carbon nanotube networks. *J. J. Appl. Phys.* Pages 3669–3671.

# List of Tables

**Table 1.** Laser granulometry  $d_{10}$ ,  $d_{50}$  and  $d_{90}$  of  $\text{In}_2\text{O}_3$  synthesized via BP, HT-urea, HT-soda, HT-soda-W, SA and SA-W.

**Table 2.** Lattice parameters and crystallite size from Scherrer equation for the samples.

**Table 3.** Positions and relative intensities of the Oxygen signals for the samples.

**Table 4.** HT-W- $\text{In}_2\text{O}_3$  film response and recovery times at different  $\text{O}_3$  amounts (200-500 ppb) at  $100^\circ\text{C}$ .

**Table 5.** State of the art of  $\text{In}_2\text{O}_3$  thick layer heated  $\text{O}_3$  sensors. Elaboration from ref. [2].

# List of Figures

**Figure 1.** Indium oxide cubic structure.

**Figure 2.** Sensor response vs  $[O_3]$ . The sensitive films of heated devices were manufactured by drop-coating technique. 1)  $In_2O_3$  sensors were obtained by sol-gel synthesis from the aged suspension of  $In(OH)_3$ , and 2)  $In_2O_3$  sensors from an aged colloidal solution.

**Figure 3.** Comparison between sintering of  $In_2O_3 - Fe_2O_3$  (97:3 wt%) films at  $900^\circ C$  (left) and  $1300^\circ C$  (right).

**Figure 4.** Correlation between sensor response and operating temperature under 73 ppb of  $O_3$  for screen printing and spin-coating sensors.

**Figure 5.** Diagram of the interaction between  $In_2O_3$  surface and reducing/oxidant species.

**Figure 6.** Nanocomposite by incorporation of the second phase into a different MOS matrix.

**Figure 7.** Crystal structure of  $WO_3$ .

**Figure 8.** Particle size distribution of SA- $In_2O_3$  (a); SA-W- $In_2O_3$  (b); HT- $In_2O_3$  (c); HT-W- $In_2O_3$  (d).

**Figure 9.** FESEM micrographs of wet synthesized  $In_2O_3$  powders: BP (a), HT-urea (b), HT-soda (c), HT-soda-W(d).

**Figure 10.** FESEM observations of the films: SA- $In_2O_3$  (a), SA-W- $In_2O_3$  (b), HT- $In_2O_3$  (c) and HT-W- $In_2O_3$  (d) 100 kx.

**Figure 11.** TG-DTA curve of TG: dashed line; DTA: straight line for  $In(OH)_3$  before calcination.

**Figure 12.** XRD spectra of powders: SA-  $In_2O_3$  and SA-W- $In_2O_3$  (black and red, respectively, a); comparison between HT-  $In_2O_3$  (black) and HT-W- $In_2O_3$  (red) b); XRD spectrum of  $In(OH)_3$ , c); and  $WO_3$  synthesized with the identical procedure without the impregnation of  $In_2O_3$ , d).

**Figure 13.** TEM (a, b) and HRTEM images of SA-W- $In_2O_3$  and of HT-W- $In_2O_3$  (c, d, e, f).

**Figure 14.** Survey XPS spectra of: SA- $In_2O_3$  (a); SA-W- $In_2O_3$  (b); HT- $In_2O_3$  (c); HT-W- $In_2O_3$  (d).

**Figure 15.** HR XPS spectra of  $In_{3d}$  in: SA- $In_2O_3$  (black); SA-W- $In_2O_3$  (red).

**Figure 16.** HR XPS spectra of W4f carried out on SA-W- $In_2O_3$ .

**Figure 17.** HR XPS spectra of  $O_{1s}$  carried out on SA- $In_2O_3$  (a) and SA-W- $In_2O_3$  (b).

**Figure 18.** SA- $In_2O_3$  (a) and HT- $In_2O_3$  sensors.

**Figure 19.** Sensor responses of SA-In<sub>2</sub>O<sub>3</sub>, doped with diverse amounts of WO<sub>3</sub>: 1.25, 2.5 and 5 wt% and fired at 400°C, 500°C and 600°C for 1 h upon 500 ppb of O<sub>3</sub> in dry conditions and 115°C.

**Figure 20.** Sensor response at different working T (25-200°C) upon 0.5 ppm of O<sub>3</sub>: SA-In<sub>2</sub>O<sub>3</sub>, SA-W-In<sub>2</sub>O<sub>3</sub>, HT-In<sub>2</sub>O<sub>3</sub> and HT-W-In<sub>2</sub>O<sub>3</sub>.

**Figure 21.** Changes in impedance of HT-W-In<sub>2</sub>O<sub>3</sub> sensor towards different [O<sub>3</sub>] at 100°C (a) and its calibration curve (b).

**Figure 22.** Cross-sensitivity tests for SA-In<sub>2</sub>O<sub>3</sub>, SA-W-In<sub>2</sub>O<sub>3</sub>, HT-In<sub>2</sub>O<sub>3</sub> and HT-W-In<sub>2</sub>O<sub>3</sub> films at 100°C.

**Figure 23.** Humidity influence at 30-50-70% of RH for the four sensors at 100°C.

**Figure 24.** Sensor realized over CeramTec substrates.

**Figure 25.** 10 μm thick value sensor resistance variation under O<sub>3</sub>, NO<sub>2</sub> and H<sub>2</sub> and different relative humidity levels: 0, 30 and 60% at 75 °C.

**Figure 26.** Calibration curves for 10 μm thick In<sub>2</sub>O<sub>3</sub> sensor upon O<sub>3</sub> (a), NO<sub>2</sub> (b) and H<sub>2</sub> (c) at 75°C under 0%, 30% and 60% RH.

**Figure 27.** Comparison between sensor response towards O<sub>3</sub> and NO<sub>2</sub> for 0%RH (a), 30%RH (b) and 60% RH (c) at 75 °C.

**Figure 28.** 10 μm thick sensor resistance variation under O<sub>3</sub>, NO<sub>2</sub> and H<sub>2</sub> and different relative humidity values: 30 and 60% at 115 °C.

**Figure 29.** Calibration curves for 10 μm thick In<sub>2</sub>O<sub>3</sub> sensor upon O<sub>3</sub> (a), NO<sub>2</sub> (b) and H<sub>2</sub> (c) at 115°C under 30% and 60% RH.

**Figure 30.** Comparison between sensor response towards O<sub>3</sub> and NO<sub>2</sub> for 30%RH (a) and 60% RH (b) at 115 °C.

**Figure 31.** 10 μm thick sensor resistance variation under O<sub>3</sub>, NO<sub>2</sub> and H<sub>2</sub> upon 30 and 60% of RH at 150°C.

**Figure 32.** Calibration curves for 10 μm thick In<sub>2</sub>O<sub>3</sub> sensor under O<sub>3</sub> (a), NO<sub>2</sub> (b) and H<sub>2</sub> (c) at 150°C under 30% and 60% RH.

**Figure 33.** Comparison between In<sub>2</sub>O<sub>3</sub> sensor response towards O<sub>3</sub> and NO<sub>2</sub> for 30% RH (a) and 60% RH (b) at 150 °C.

**Figure 34.** Repeatability test for In<sub>2</sub>O<sub>3</sub> sensor towards O<sub>3</sub> 100-1000 ppb under 30%RH (a) and 60% RH (b) at 150 °C.

**Figure 35.** Calibration curves for ozone and nitrogen dioxide between 75 and 150 °C under 30% RH (a) and 60%RH.

**Figure 36.** 40 μm (a) and 70-100 μm (b) thick In<sub>2</sub>O<sub>3</sub> resistance's variations toward O<sub>3</sub>, NO<sub>2</sub> and H<sub>2</sub> at 150°C and 30% RH.

**Figure 37.** Comparison between sensor responses of 10, 40, 70 and 100 μm thick In<sub>2</sub>O<sub>3</sub> layer under O<sub>3</sub>(a), NO<sub>2</sub> (b) and H<sub>2</sub> (c) at 150°C and 30% RH.

**Figure 38.** N<sub>2</sub>-syn air measurement for HT-In<sub>2</sub>O<sub>3</sub> (black) and HT-W-In<sub>2</sub>O<sub>3</sub> (red) at 115°C and 0% of RH.

**Figure 39.** H<sub>2</sub>O/D<sub>2</sub>O experiment at higher (a) and lower (b) wave numbers.

**Figure 40.** Resistance measurement during DRIFT of In<sub>2</sub>O<sub>3</sub> and W-In<sub>2</sub>O<sub>3</sub> in dry and in 10% of RH.

**Figure 41.** NO<sub>2</sub> 10ppm measurement in dry and 10% of RH at higher (a) and lower (b) wave numbers.

**Figure 42.** N<sub>2</sub>/O<sub>2</sub> 100ppm measurement for In<sub>2</sub>O<sub>3</sub> sensor at higher (a) and lower (b) wave numbers.

**Figure 43.** Substraction of the baseline between 2200-800 cm<sup>-1</sup> for In<sub>2</sub>O<sub>3</sub> sensor under 10ppm NO<sub>2</sub> in dry air.

**Figure 44.** Resistance measurements during DRIFT of In<sub>2</sub>O<sub>3</sub> and W-In<sub>2</sub>O<sub>3</sub> under 10% of relative humidity and 700-1500ppb of O<sub>3</sub> at 150°C.

**Figure 45.** O<sub>3</sub> 700 and 1500ppb O<sub>3</sub> DRIFT measurement of In<sub>2</sub>O<sub>3</sub> sensor under 10% of relative humidity at higher (a) and lower (b) wave numbers.

**Figure 46.** O<sub>3</sub> 700 and 1500ppb O<sub>3</sub> DRIFT measurement of W-In<sub>2</sub>O<sub>3</sub> sensor under 10% of relative humidity at higher (a) and lower (b) wave numbers.

**Figure 47.** Substraction of the baseline between 2500-800 cm<sup>-1</sup> for In<sub>2</sub>O<sub>3</sub> (a) and W-In<sub>2</sub>O<sub>3</sub> (b) films under 1500 ppb of O<sub>3</sub> in 10% RH.



# Chapter 5 - In<sub>2</sub>O<sub>3</sub>-based O<sub>3</sub> sensors

## Abstract

The objective of this part of the thesis is the evaluation of the sensing performances of nanostructured metal oxides. WO<sub>3</sub>-doped In<sub>2</sub>O<sub>3</sub> was selected for its interesting properties, and the results compared with those of pure In<sub>2</sub>O<sub>3</sub>, used as a reference material.

The gas sensing characteristics of commercial and hydrothermally synthesized powders were compared. Those materials were sensitive towards low amounts of O<sub>3</sub> in air at moderate temperature.

An innovative approach is the use of In<sub>2</sub>O<sub>3</sub> and WO<sub>3</sub>-doped In<sub>2</sub>O<sub>3</sub> hydrothermally synthesized for designing thick-film sensors with great selectivity and sensitivity for O<sub>3</sub> monitoring. Nanostructured metal oxide thick films allow an efficient gas diffusion toward the whole surfaces with an extended sensitive area. Consequently, either the gas response and the velocity of the adsorption-desorption should improve at the same time and considerably when enhancing the specific surface area [1].

Despite other metal oxides were investigated for O<sub>3</sub> detection, like WO<sub>3</sub>, ZnO, TiO<sub>2</sub>, CuAlO<sub>2</sub>, SmFeO<sub>3</sub> and BaFe<sub>12</sub>O<sub>19</sub>, In<sub>2</sub>O<sub>3</sub> has displayed the most promising results in terms of sensitivity, cross sensitivity, low humidity interference and  $\tau_{ads}$  due to the chemical stability, the compatibility with standard integrated circuit fabrication and an excellent stability in oxidizing atmosphere [2].

Generally, the highest sensor response towards O<sub>3</sub> of In<sub>2</sub>O<sub>3</sub>-based conductometric sensors has been detected between 200 and 350°C, depending on the technique of layer deposition.

## 5.1 In<sub>2</sub>O<sub>3</sub> and WO<sub>3</sub>-doped In<sub>2</sub>O<sub>3</sub> powders

Firstly, it was assessed that bulk-doping of In<sub>2</sub>O<sub>3</sub> with tungsten oxide (WO<sub>3</sub>) is a suitable way to enhance sensor response towards O<sub>3</sub>, after the creation of new adsorption sites with higher affinity for O<sub>2</sub> using commercial indium oxide (Sigma Aldrich). Then, In<sub>2</sub>O<sub>3</sub> was synthesized by three different methods to decrease the crystallite and agglomeration size for enhancing the sensor response with respect to O<sub>3</sub>. Sensor devices were developed by screen printing technique obtaining films

characterized by different thickness: at Politecnico di Torino, films of around 20  $\mu\text{m}$  of thickness were firstly developed; later, at University of Tübingen, films with thickness in the range 40-100  $\mu\text{m}$  were prepared. In both cases, the optimum operating temperature towards  $\text{NO}_2$ ,  $\text{N}_2\text{O}$ ,  $\text{NH}_3$ ,  $\text{CH}_4$  and  $\text{CO}_2$  was evaluated. This sensor exhibits the maximum sensor performances at low operating temperatures (100-150°C).

As previously written, part of this research was carried out in the Weimar Group in the University of Tübingen laboratory with the supervision of dr. Barsan. Here, the hydrothermally synthesized  $\text{In}_2\text{O}_3$  thick film sensors were tested upon diverse levels of  $\text{O}_3$ ,  $\text{NO}_2$  and  $\text{H}_2$  at diverse T, and the role of the sensor thickness was analyzed in the gas sensor response.

Investigations on the sensing performances of the realized sensors were accomplished by different methods: electrical measurements of DC resistance in University of Tübingen and AC impedance in Politecnico research laboratories. Moreover, Diffuse reflectance infrared fourier transform (DRIFT) spectroscopic investigations for understanding the species interacting during the gas sensing mechanism were accomplished.

### 5.1.1 General aspects of $\text{In}_2\text{O}_3$

Indium (III) oxide ( $\text{In}_2\text{O}_3$ ) is an oxide with amphoteric characteristics.  $\text{In}_2\text{O}_3$  is an n-type MOS and it is present in the form of bixbyite-typology of cubic crystals. The band gap of  $\text{In}_2\text{O}_3$  has newly been re-calculated at 2.9 eV, a lower value compared to the old one of 3.7 eV. Indium oxide finds application in batteries, as resistive element in integrated circuits in semiconductor technology, thin film IR reflectors transparent for visible light, photocatalyst and chemical sensors, optical and antistatic coatings. In addition, it is combined with  $\text{SnO}_2$ , forming indium tin oxide (ITO) that is utilized in transparent coatings with with conductivity. Moreover,  $\text{In}_2\text{O}_3$  is utilized as a component of some stain solutions in microanatomy.

Indium oxide exhibits excellent magnetic and conductive characteristics. Magnetic semiconductors fabricated with chromium-doped indium oxide are characterized by single-phase crystal structure, high-temperature ferromagnetism and high amounts of charge carriers. It has probable exploitation in spin electronics in solid state devices for spin injectors [3].

Indium oxide is a polymorphic compound. It is present in two crystalline phases, i.e. the cubic bixbyite and the rhombohedral. The latter one is generated at elevated P and T or when adopting non-equilibrium growth processes. This phase is characterized by R3c 167 space group with  $a = 0.5487 \text{ nm}$ ,  $b = 0.5487 \text{ nm}$ ,  $c =$

0.57818 nm,  $Z = 6$  and  $7.31 \text{ g/cm}^3$  of density. The cubic phase is characterized by  $Ia\bar{3} 206$  space group with  $a = 1.0117(1) \text{ nm}$ ,  $Z = 16$ . The cubic crystal structure of  $\text{In}_2\text{O}_3$  is depicted in Figure 1.

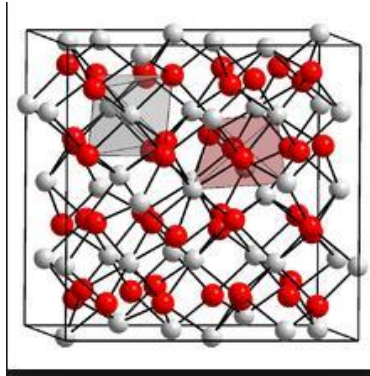


**Figure 1.** Indium oxide cubic structure [4].

Thin polycrystalline films of Zn-doped  $\text{In}_2\text{O}_3$  display high conductivity ( $\sim 10^5 \text{ S/m}$ ) and become superconductive at  $T < 3.3 \text{ K}$ . In fact,  $T_c$  (superconducting transition temperature) is dependent on the doping amount and on the film features. In this condition, the carrier density is in the range  $10^{25} - 10^{26} \text{ m}^{-3}$  [5].

### 5.1.2 Sensing properties of $\text{In}_2\text{O}_3$

$\text{In}_2\text{O}_3$  is characterized by big conductivity and abundance of defects both in the bulk and on the surface, so it is an encouraging candidate for practical usages. Particularly, it exhibits excellent response and selectivity in the detection of oxidant species, while it is mildly sensitive to reductants.

Throughout the design of the microstructure, the sensing features of  $\text{In}_2\text{O}_3$  can be considerably improved, peculiarly for the detection of low amounts of  $\text{O}_3$  at ppb level with quick response and recovery features. Till now, aside from the different structural phases,  $\text{In}_2\text{O}_3$  nanostructures with diverse morphologies like 1D nanowires, 2D nanosheets and 3D hierarchical nanostructures have been realized for  $\text{O}_3$  sensing. For diverse morphologies of  $\text{In}_2\text{O}_3$  nanostructures, many approaches, like chemical vapor deposition, physical evaporation technique, thermal oxidation, template method, sol-gel method, homogeneous precipitation, hydrothermal route, directly synthesis and precursor method, have been extensively described.

In general,  $\text{In}_2\text{O}_3$  has been broadly used in applications related to gas sensing.

Those sensors are constituted by a film sensitive towards gas, that is a porous  $\text{In}_2\text{O}_3$  layer fabricated by different methods. They are equipped with finger electrodes under or on the top of the sensitive element to check variations in the film resistivity caused by the exposure upon gas species. The heater is typically a Pt resistor located on the top or underneath the substrate, furnishing the proper temperature in the sensitive region of the sensor.

A strategy adopted for improving the gas sensor performances is the utilization of UV illumination ( $h\nu \sim E_g$ ) in the course of  $\text{O}_3$  detection intensifying the interaction of  $\text{O}_3$  interaction with metal oxide surface. Therefore, this kind of sensor can operate at room temperature (RT) [7].

The improved sensitivity at RT depends on the UV irradiation conditions all along  $\text{O}_3$  adsorption and it occurs for the  $\text{O}_3$  decomposition that is stimulated by UV illumination or for the desorption of chemisorbed oxygen from the  $\text{In}_2\text{O}_3$  surface previous to the exposure upon  $\text{O}_3$ .

In Korotcenkov et al. [7] it is demonstrated that the sensor response is typically delineated by the relationship  $R \sim C^X$ , in which  $C > 1$ , and  $X$  is dependent on the technique of sensor fabrication.

$X$  varies between 0.2 and 1.53 for ‘saturation’ (see the next Figures 2), for many sensors characterized by elevate sensitivity, the saturation is detected at  $\text{O}_3$  levels higher than 1 ppm.

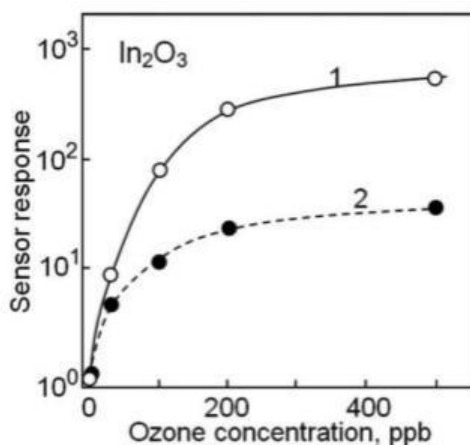


**Figure 2.** Sensor response vs  $[\text{O}_3]$ . The sensitive films of heated devices were manufactured by drop-coating technique. 1)  $\text{In}_2\text{O}_3$  sensors were obtained by sol-gel synthesis from the aged suspension of  $\text{In}(\text{OH})_3$ , and 2)  $\text{In}_2\text{O}_3$  sensors from an aged colloidal solution. Reproduced with permission from [8], published by ACS Publications, 2003.

If the sensitivity of the sensor is very high, the saturation happens at much lower O<sub>3</sub> amounts [9].

This effect causes a reduction in the dynamic measurement range of O<sub>3</sub> amounts with MOS sensors. This phenomenon is often described by the '*Weisz-limitation*' [10].

This limitation is applicable for a great number of MOS and occurs when the surface of the SMO<sub>x</sub> is full of adsorbed species that interact with the CB by capturing electrons, other molecules trying to adsorb in a state where the number of ions adsorbed is restricted to a coverage of 10<sup>-2</sup>–10<sup>-3</sup> monolayers. This process restricts the ionosorption of new oxygens close to the surface.

If the chemisorbed oxygen density on the surface increases, the band bending of the depletion layer is higher, and a thermionic leave of electron from the CB to the surface is prevented.

For instance, for oxygen chemisorption, the accumulation of anions at the oxide surface can result in a BB of up to around 1 eV.

If the adsorbate coverage is higher than 0.1, the repulsion of electrostatic forces represents an obstacle for an adsorption. This is clear in nonlinear effects of surface coverage and in a drop of the adsorption energy. In some cases, the saturation is caused by the characteristics of gas-sensitive layer structure. Particularly, in the case of fully overlapping of the necks between crystallites by the space-charge regions, they cause '*saturation*'.

MOS sensors exhibit one most significant weakness: the lack of selectivity also regarding O<sub>3</sub> sensors [11].

To the best of my knowledge, in literature merely few articles have discussed the interference phenomena in ozone sensors [12-16].

In those papers, authors have demonstrated that the presence of reductants like H<sub>2</sub>, CO or vapors of VOCs modifies the sensor response towards ozone. For instance, at high temperature (T>400°C) VOCs can suppress the sensitivity of SmFeO<sub>3</sub> sensors towards O<sub>3</sub> [14].

For this reason, the maximal O<sub>3</sub> sensitivity and the lowest cross sensitivity is obtainable at lower operating temperature, usually between 200°C and 300°C. The highest interference of O<sub>3</sub> sensors is due to NO<sub>2</sub> in some studies [13,17].

The variation of the working temperature does not ameliorate the selectivity for the detection of O<sub>3</sub>, since the maximum sensitivities towards O<sub>3</sub> and NO<sub>2</sub> appears in the identical range of temperatures.

Two main strategies have been realized in order to surpass this issue. Losche et al [15] proposed to use an individual sensor operating in a temperature cycle-mode,

while Sauter et al. [12] proposed to exploit an array of diverse sensors based on the working principle of an electronic nose.

The problem of those techniques consists in higher and more complex systems.

For O<sub>3</sub> sensors, higher selectivity of O<sub>3</sub> sensor's response can be obtained mainly via surface modification or by bulk doping [18].

For example, Belysheva et al. [19] demonstrated that adding little quantities of Al<sub>2</sub>O<sub>3</sub> and NiO to the In<sub>2</sub>O<sub>3</sub>-α-Fe<sub>2</sub>O<sub>3</sub> improved its sensitivity of three times and selectivity of O<sub>3</sub> detection considering NO<sub>2</sub> and Cl<sub>2</sub> as interfering gases.

Generally [12], In<sub>2</sub>O<sub>3</sub>-based ozone sensors have more selectivity compared to SnO<sub>2</sub>-based ozone sensors considering humidity, SO<sub>2</sub> and CO.

The performances of the sensor are dependent on the procedure utilized for the synthesis and for the sensor fabrication.

In a study performed by Kim et al. [20], In<sub>2</sub>O<sub>3</sub>/Fe<sub>2</sub>O<sub>3</sub> thick layer sensors were fabricated by screen-printing deposition, showing a consistent decrease in the sensor response towards O<sub>3</sub> when enhancing the temperature of calcination from 900 to 1300°C.

During annealing at such temperatures, strong ceramics sintering takes place, resulting in a considerable growth in the area of contact between crystallites and in the crystallite size, together with a reduced porosity, as depicted in Figure 3.

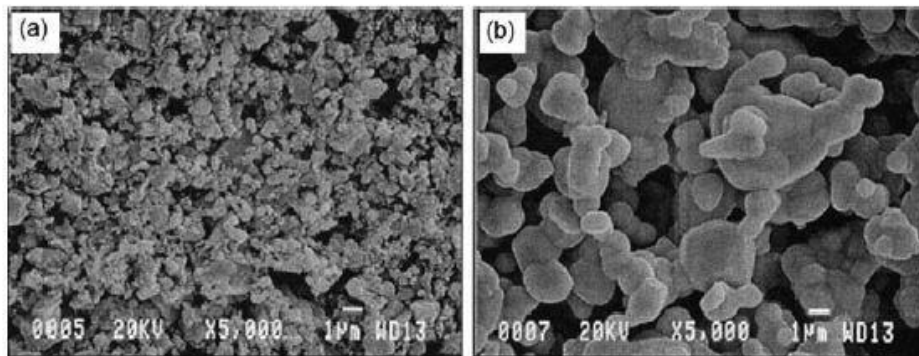


**Figure 3.** Comparison between sintering of In<sub>2</sub>O<sub>3</sub> – Fe<sub>2</sub>O<sub>3</sub> (97:3 wt%) films at 900°C (left) and 1300°C (right). Reproduced with permission from [25], published by Elsevier 2000.

In most papers, powders were calcined at 700–800°C for 1 h in air after synthesis [18].

Annealing at these temperatures ensure the connection between the crystallites, without the creation of wide necks between them.

A comparison of  $\text{In}_2\text{O}_3$ -based sensors realized by screen-printing and spin coating technologies was realized by Sahn et al [26], and the authors noticed an increase in the sensor response towards 73 ppb of  $\text{O}_3$  for screen printing-based sensors when decreasing the operating temperature, and an opposite trend for spin-coated sensors, as illustrated in Figure 4.

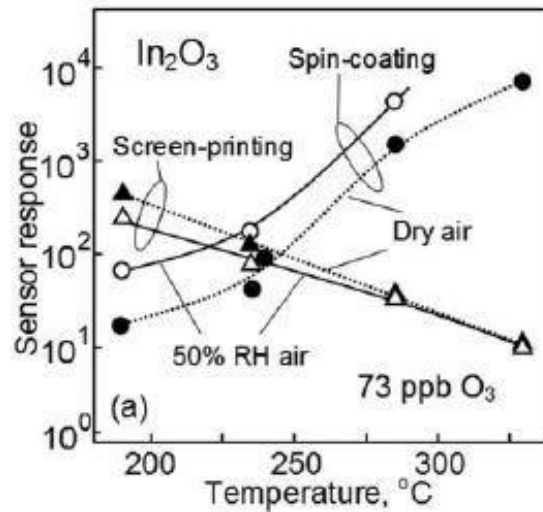


**Figure 4.** Correlation between sensor response and operating temperature under 73 ppb of  $\text{O}_3$  for screen printing and spin-coating sensors [21].

When  $\text{In}_2\text{O}_3$  films remain in an oxygen atmosphere, no phase transformations take place until  $1000^\circ\text{C}$  [22], whereas under 1% of  $\text{H}_2$  it can be reduced to metal form even around  $350^\circ\text{C}$  [23].

When reducing species, like VOCs or  $\text{H}_2$ , interact with  $\text{In}_2\text{O}_3$  surface, they cause a wide reduction of the surface, promoting the generation of an accumulation layer. On the other hand, the interaction with oxidant species like  $\text{O}_3$  and  $\text{NO}_2$  is associated with the recovery of the  $\text{In}_2\text{O}_3$  surface stoichiometry caused by its reoxidation and a depletion layer is created. In Figure 5, a diagram demonstrating variations in the characteristics of the  $\text{In}_2\text{O}_3$  inter-crystallite interfaces upon exposure of reducing or oxidant gases is illustrated.

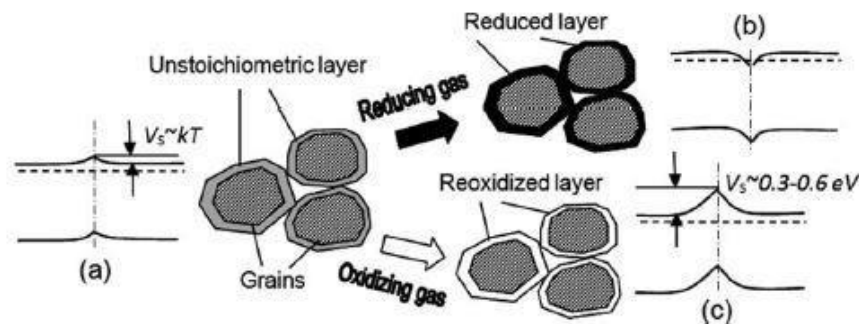


**Figure 5.** Diagram of the interaction between  $\text{In}_2\text{O}_3$  surface and reducing/oxidant species. Reproduced with permission from [24], published by Elsevier, 2007.

According to Brinzari et al [25], a downward BB of respectively 0.3 eV for the (111) and of 0.25 eV for (100) planes were calculated in reducing atmosphere. A small height of the surface potential barrier is the principal cause of the short  $\tau_{\text{des}}$  of  $\text{In}_2\text{O}_3$  sensor even at low temperature.

Considering the stability of  $\text{In}_2\text{O}_3$  sensors, they have obtained great accuracy and repeatability, and prolonged sensor life when properly stored. The stability of  $\text{O}_3$  sensor characteristics can be decreased solely by an excessive small crystallite size in the gas-sensitive film at values below 5 nm.

### 5.1.3 Strategies to optimize $\text{In}_2\text{O}_3$ sensors -surface modification

If catalytically active films are present at the oxide surface, an effective dissociative chemisorption of oxygen is favoured, followed by spillover effect influencing the sensitivity towards ozone [26].

Usually noble metals (Pt, Pd, Au, Rh) act as centres for a dissociative oxygen adsorption at low temperature followed by chemisorbed oxygen on the oxide surface [27].

For achieving an optimal modification of the  $\text{In}_2\text{O}_3$  surface with a strong enhance in the sensor response, the gold nanoparticles (NPs) should have a size in the order of 2–3 nm or even less [28].

In this way, the NPs can be effectively atomically dispersed on the surface.

In Korotcenkov [29] the authors describe the electronic mechanism of sensitization on the  $\text{In}_2\text{O}_3$ : Au ozone sensors. This mechanism is listed as an oxidation of the gold NPs under  $\text{O}_3$  exposure, enhancing the work function. This stimulates the movement of  $e^-$  from the oxide to the Au NPs increasing the resistance of the  $\text{In}_2\text{O}_3$  film.



During the  $O_3$  detection, a relationship between the variation in the resistivity of the film in air and the sensor sensitivity was noticed.

Higher alterations were detected for resistivity under  $O_3$  compared to dry air. This fact advises that the interaction between Au NPs and  $O_3$  is accountable for the improved sensitivity upon  $O_3$  [34].

The spillover effect favors the formation of a negative charge caught by surface species increasing the BB and the resistivity of the polycrystalline oxide film. This phenomenon can often happen during the interaction with  $O_3$ , since the  $\tau_{des}$  for  $O_3$  detection is a function of the lifetime of chemisorbed oxygen, staying on the MOS surface next to the interaction with  $O_3$ , gold stimulates reactions that improve the kinetics of this process.

The interaction between Au NPs and oxygen either as  $O_2$  and  $O_3$  is the main strategy of  $In_2O_3$ -Au-based device sensitization. In addition, this interaction is easier for smaller clusters of Au NPs.

Many researches have displayed that Au NPs with a size lower than 3 nm can be simply oxidized also at low T, whereas bigger clusters are more stable [30].

In accordance with Miller [31], around 10% of the Au is oxidized. If oxidizing species are present, like  $O_3$  [32] and  $NO_2$  [33], this phenomenon is promoted. Au can catalyze the dissociation of  $O_3$  [34].

A way to increase the efficiency of Au sensitization is to decrease strongly the size of  $In_2O_3$  crystallites increasing at the same time the density of Au NPs on the crystallites surface. Furthermore, Au NPs clusters on the oxide surface displays excellent mobility, particularly at high temperatures. Thus, the stability of these systems must be improved.

Nanocomposites can be realized by incorporating the second phase of MOS into an existing MOS matrix as shown in Figure 6.

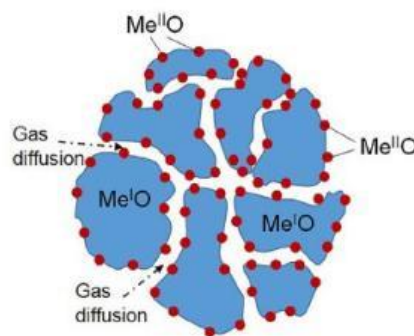


**Figure 6.** Nanocomposite by incorporation of the second phase into a different MOS matrix. Reproduced with permission from [35], published by Elsevier, 2017.

Usually, methods such as wet impregnation, co-condensation, covalent bonding and ion exchange are used. For instance, the addition of a second element by impregnation usually causes its distribution on the main component crystallites surface. In this way, an extremely dispersed doping in the framework of the MOS matrix is fulfilled.

#### **5.1.4 Strategies to optimize In<sub>2</sub>O<sub>3</sub> sensors – bulk doping**

Researchers have demonstrated that bulk doping of In<sub>2</sub>O<sub>3</sub> is the most interesting method for enhancing the O<sub>3</sub> sensor parameters, because it influences the defect chemistry, bulk electrophysical characteristics and the morphology of the MOS layer together with the surface reactivity [36].

This effect is a consequence of the incorporation of the second oxide in the lattice of In<sub>2</sub>O<sub>3</sub>. For achieving a bulk doping, the most effective methods are wet chemical routes like precipitation, sol-gel and hydrothermal route: in this way, an improved tune of the chemical composition, stoichiometry, surface area and crystallite size is accomplished. Incorporation of a secondary phase in the principal MOS matrix, has often an important impact on the kinetics and mechanism of sintering as well as on the definitive features of the oxides.

For instance, the addition of  $\gamma$ -Fe<sub>2</sub>O<sub>3</sub> significantly dropped the working temperature down to 170–200°C, improving the sensitivity towards O<sub>3</sub>, decreasing the cross-sensitivity towards Cl<sub>2</sub> comparing with pure In<sub>2</sub>O<sub>3</sub> and In<sub>2</sub>O<sub>3</sub>- $\alpha$ -Fe<sub>2</sub>O<sub>3</sub>. Often bulk doping by different elements like Co, Ce, La, Fe and others lead to a diminished crystallite size.

In the literature, the highest sensitivity towards O<sub>3</sub> after bulk doping of In<sub>2</sub>O<sub>3</sub> films was obtained by using Fe and Co. In [5] was demonstrated that doping by these elements (3–6 mol%) improved the best response decreasing the optimum working temperature. However, optimized effects for transition metals occur solely at modest amounts of additive elements ( $C_{MeO} < 1-4\%$ ). At higher amounts, a significant drop in sensitivity was detected. Typically, this threshold level is the limit of solubility of additives in the oxide. In some cases, doping could come with the formation of novel compounds, different from the binary oxide phases.

Finally, one of the main parameters that control the activity of the SMO for the detection of gases with a high activity such as O<sub>3</sub> is the porosity, especially the pore size.

The last part of this chapter will investigate the impact of the sensor thickness on the O<sub>3</sub> sensitivity for In<sub>2</sub>O<sub>3</sub> thick film sensor. In fact, for thick film chemical sensors

with higher than 1 microns of thickness, the modest penetrability of the gas sensitive matrix and the limitation to the gas diffusion for analytes with catalytic characteristics are the principal factors that limit the potential to achieve the high sensitivity towards  $O_3$ .

If the sensor is too thick, the interactions with  $O_3$  happen on the surface of the layer and consequently the characteristics of deeper layers are not changing. If the pore size is high, the penetration of the target gas is deep in the matrix. In order to accomplish an increased porosity, volatile components have been incorporated [37]. For example,  $In_2O_3-SnO_2$  (10%) thin layers showed great sensitivity to  $NO_2$  and  $NO$ , improving their selectivity with respect to  $CO$  and  $CH_4$  [38].

Thus, for MOS-based nano-composites it was demonstrated that in the case additives are not able to generate a conductive phase with great sensitive features, the optimized amounts of additive elements in the main matrix would not overcome 1–3 wt%. [39].

For composites, with two sensitive metal oxides, optimal amount of the second phase should be between 10 and 20 wt% [36].

### 5.1.5 General aspects of $WO_3$

$WO_3$  is a n-type semiconductor, that presents interesting chemical, optical and electrical properties. This oxygen-deficient oxide has been studied in many fields. For instance, it finds application in industry as a pigment in ceramics and paints. It is used for instance in the manufacture of tungstates in X-ray screen phosphors and in the realization of fireproofing materials [40, 41].

$WO_3$  is widely used in gas sensor technology. In fact, several papers report elevated signals of  $WO_3$  to both reducing species like ammonia [42], toluene [43], hydrogen sulfide [44], acetone [45] and oxidants like  $O_3$ ,  $NO$  and  $NO_2$  [46, 47]. Moreover, the oxidizing effect of  $H_2O$  at  $300^\circ C$  was deeply investigated in a work by Staerz et al [48].

$WO_3$  shows a cubic perovskite-like crystal structure with corner sharing normal octahedra with W at the centre and oxygens at the corner of every octahedron. The crystal network is formed by the alternation between oxygen and  $WO_2$  planes orthogonally to every crystallographic orientation. The symmetry of  $WO_3$  is lowered compared to the ideal  $ReO_3$  structure by two distortions: displacement of W from centre of its octahedron and tilting of  $WO_6$  octahedra. There is a T-dependence of the crystal structure of  $WO_3$  [49].

In fact,  $WO_3$  is triclinic at between  $-50$  and  $17^\circ C$ , monoclinic between  $17$  and  $330^\circ C$ , orthorhombic in the temperature range  $330-740^\circ C$ , and tetragonal above

this temperature. Among all these phases, the most common crystal structure is monoclinic with space group  $P2_1/n$  as displayed in Figure 7.

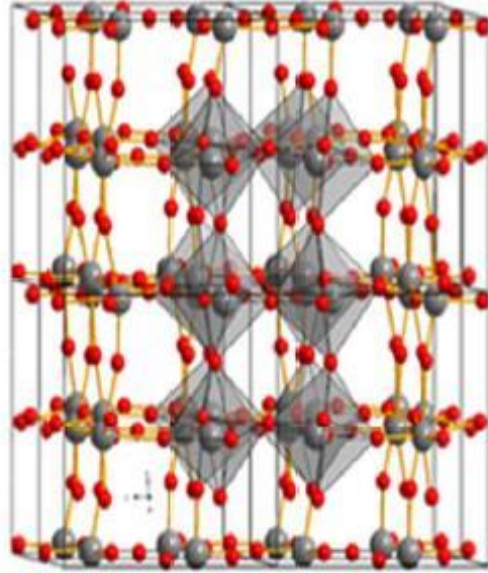


**Figure 7.** Crystal structure of  $WO_3$  [63].

## 5.2 Sensors based on $In_2O_3$ nanostructures

In this part of the work, ozone sensors based on n-type  $In_2O_3$  and 2.5 wt%  $WO_3$ -doped  $In_2O_3$  thick film to measure  $O_3$  at sub-ppm level and at low temperatures were used.

$In_2O_3$  was synthesized by three different methods, trying to decrease the crystallite and agglomeration size enhancing the specific surface area, obtaining a superior sensitivity upon  $O_3$  exposure with respect to the commercial indium oxide. Among the differently synthesized powders, pristine  $In_2O_3$  produced by hydrothermal route (HT) using soda as mineralizer constitutes a precious platform for the realization of  $O_3$  sensors, improving the sensor performances compared to the commercial  $In_2O_3$  (SA) in term of sensor response, optimum operating temperature, response and recovery times. In this work, HT-  $In_2O_3$  was doped with  $WO_3$  by an impregnation route to increase both its selectivity and sensitivity with respect to  $O_3$ .

Powders were characterized by laser granulometry, FESEM, DTA-TG, XRD,  $N_2$  adsorption, TEM and XPS. The cross-sensitivity under different levels of humidity,  $NO_2$ ,  $N_2O$ ,  $NH_3$ ,  $CH_4$ ,  $CO$  and  $CO_2$  were investigated since modest selectivity is usually the principal limit of MOS detectors. Thus, doping with  $WO_3$  by

impregnation route increase the sensor performances of indium oxides sensors towards O<sub>3</sub> and the selectivity with respect to NO<sub>2</sub> and humidity.

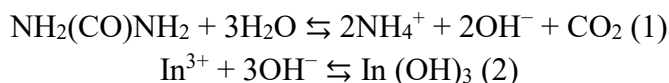
### 5.2.1 Synthesis of In<sub>2</sub>O<sub>3</sub>

Wet-synthesized In<sub>2</sub>O<sub>3</sub> powders were prepared by three different routes [50], with the aim of achieving a finer crystallite size compared to commercial In<sub>2</sub>O<sub>3</sub>, that is one key to increase the sensor response [51].

In the first synthesis, a bath precipitation process (BP) was carried out. Here, In(NO<sub>3</sub>)<sub>3</sub>·5H<sub>2</sub>O was dissolved in H<sub>2</sub>O and urea solution was mixed together for 30 min. The mixture was then transferred in ‘Falcon’ tubes and remained in a silicon oil bath for 8 h at 80°C. Thus, it was transferred in an oven at 80°C for 24 h. The powders were washed in H<sub>2</sub>O and EtOH and dried subsequently in an oven. In<sub>2</sub>O<sub>3</sub> architectures were realized by calcination of the powders for 30 min at 400°C.

In the second procedure, In<sub>2</sub>O<sub>3</sub> were gained by hydrothermal synthesis utilizing urea as mineralizer (HT-urea) [52].

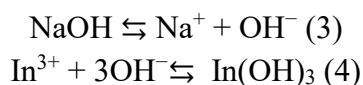
In a typical synthesis, In (NO<sub>3</sub>)<sub>3</sub>·5H<sub>2</sub>O, [(C<sub>16</sub>H<sub>33</sub>)N(CH<sub>3</sub>)<sub>3</sub>]<sup>+</sup>Br<sup>-</sup> (CTAB, utilized as capping agent to provide stability to NPs in the process of crystal growth controlling their morphologies), and urea were dissolved in H<sub>2</sub>O and mixed for 30 min at 25°C. The resulting mixture was put into a Teflon-autoclave and kept at 70°C for 24 h and subsequently at 120°C for 12 h. The synthesized white precipitate was washed and then dried in air. The reactions (1-2) occurred in the In (OH)<sub>3</sub> indium hydroxide formation:



In<sub>2</sub>O<sub>3</sub> nano-powder was formed by calcination of the powder for 30 minutes at 400°C. After this stage, powder varies from white until yellow, denoting the formation of In<sub>2</sub>O<sub>3</sub>.

In the third synthesis, the same procedure was carried out by replacing urea with NaOH (HT-soda) as mineralizer since in [75] a smaller crystallites size was achieved under this condition.

This is probably a consequence of the dilute alkaline environment produced by urea leading to a complete crystallization and a bigger crystallite size when comparing with solutions with higher alkali environment produced by soda where complete crystallization does not happen. Here, the following reactions (3-4) occurred:



An In (NO<sub>3</sub>)<sub>3</sub>.5H<sub>2</sub>O: CTAB: NaOH molar ratio of 1:1.96:3 was chosen in this work, and a molar ratio of 3:1 between NaOH and In<sub>2</sub>(NO<sub>3</sub>)<sub>3</sub> was selected.

The most promising powder (in terms of lower crystallite and agglomeration size) was doped with 2.5 wt% of WO<sub>3</sub> by an impregnation route.

WCl<sub>6</sub> (≥ 99.9% trace metals basis, Sigma Aldrich) was mixed in CH<sub>2</sub>Cl<sub>2</sub> (ACS, ≥ 99.8%, ChemLab) previous to the addition of In<sub>2</sub>O<sub>3</sub>. The suspensions were mixed at 25 °C for 3 h and subsequently dried at 40°C. In order to get rid of the chloride by-product, the powders were washed in H<sub>2</sub>O and EtOH several times by centrifugation. For SA-In<sub>2</sub>O<sub>3</sub>, impregnation was performed with three diverse quantities of WCl<sub>6</sub>, to achieve 1.0, 2.5 and 5.0 wt% of WO<sub>3</sub>-doped In<sub>2</sub>O<sub>3</sub> powders. HT-soda-In<sub>2</sub>O<sub>3</sub> powder was doped at the optimal WO<sub>3</sub> concentration (2.5 wt%) defined for the SA-In<sub>2</sub>O<sub>3</sub>.

Powders were mixed for 3 hours at room temperature, washed many times in water and ethanol and WO<sub>3</sub>-doped In<sub>2</sub>O<sub>3</sub> was obtained after 3 hours of annealing at 400°C (HT-soda-W). Commercial In<sub>2</sub>O<sub>3</sub> powder (SA, Sigma Aldrich, 99.9% purity, particle size < 100 nm) was also submitted to the same WO<sub>3</sub>-doping and used as a reference (SA-W) [53].

## 5.2.2 Characterization of In<sub>2</sub>O<sub>3</sub>

Results of laser granulometry investigation are tabulated in Table 1.

**Table 1.** Laser granulometry d<sub>10</sub>, d<sub>50</sub> and d<sub>90</sub> of In<sub>2</sub>O<sub>3</sub> synthesized via BP, HT-urea, HT-soda, HT-soda-W, SA and SA-W.

	BP	HT-	HT-soda-	HT- W-	SA-In <sub>2</sub> O <sub>3</sub>	SA-W-
Cumulative	In <sub>2</sub> O <sub>3</sub>	urea-	In <sub>2</sub> O <sub>3</sub> (μm)	soda-	(μm)	In <sub>2</sub> O <sub>3</sub>
(%)	(μm)	In <sub>2</sub> O <sub>3</sub>		In <sub>2</sub> O <sub>3</sub>		(μm)
		(μm)		(μm)		
10	0.42	0.83	0.11	0.10	0.29	0.18
50	3.18	1.61	0.41	0.40	3.67	4.02
90	22.2	2.85	8.34	4.55	11.4	16

By hydrothermal synthesis using NaOH as mineralizing agent instead of urea, smaller particles were synthesized in accordance with ref [75]. In fact,  $d_{50}$  decreases from 1.61 to 0.41  $\mu\text{m}$  when urea is replaced by soda.

From now, HT-In<sub>2</sub>O<sub>3</sub> indicates HT-soda-In<sub>2</sub>O<sub>3</sub> and HT-W-In<sub>2</sub>O<sub>3</sub> is HT-soda-W-In<sub>2</sub>O<sub>3</sub>.

Laser granulometry in Figure 8 compares the commercial powder and the HT-soda that shows the lower degree of agglomeration and lowest particle size distribution. Both commercial powders display a trimodal distribution. For the hydrothermally prepared In<sub>2</sub>O<sub>3</sub>, HT-In<sub>2</sub>O<sub>3</sub> particles distribution displays four maxima, at 0.25, 1.5, 8 and 30  $\mu\text{m}$ , whereas the distribution of HT-W-In<sub>2</sub>O<sub>3</sub> is similar to the undoped In<sub>2</sub>O<sub>3</sub>, despite of a rather lower size of agglomerates. This results in a  $d_{90}$  that is the smallest considering all the types of In<sub>2</sub>O<sub>3</sub> proposed.

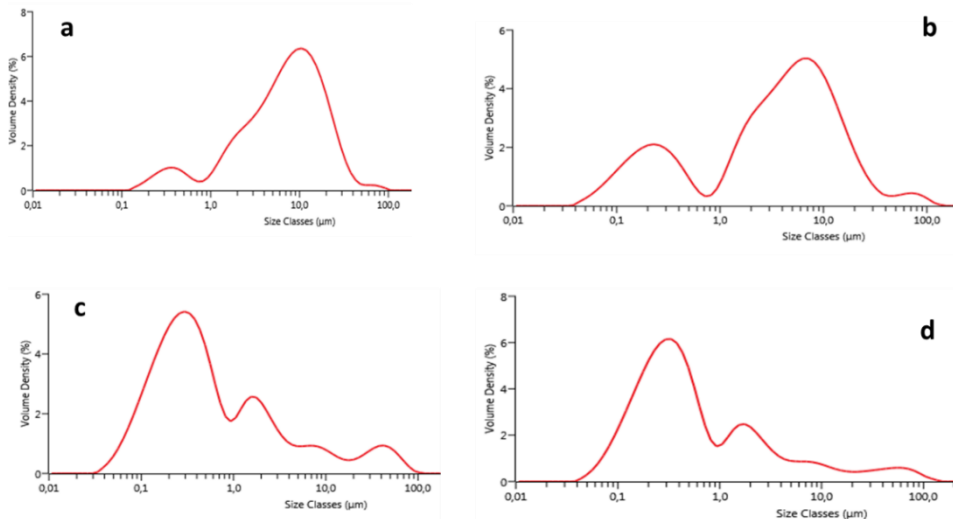


**Figure 8.** Particle size distribution of SA-In<sub>2</sub>O<sub>3</sub> (a); SA-W-In<sub>2</sub>O<sub>3</sub> (b); HT-In<sub>2</sub>O<sub>3</sub> (c); HT-W-In<sub>2</sub>O<sub>3</sub> (d).

Those results were confirmed by FESEM observations shown in Figure 9, which also allowed to observe the different morphologies accomplished. Powders obtained from BP show a wide range of morphologies: cubes of about 1 micron in length, spheres of hundreds of nanometers and panicles with some microns in length and hundreds of nanometers in depth. HT-urea powder presents a regular morphology with cubes of around 1  $\mu\text{m}$  in length and confirmed the narrow distribution in particle size as determined by laser granulometry (Table 1). Finally, the finest particles were measured in the case of HT-W-soda, with grains between 45 and 65 nm slightly agglomerated, with agglomerates in the range of few microns,

in accordance with laser granulometry and the HT-W-soda powder shows the more or less the same morphology of the HT-soda.

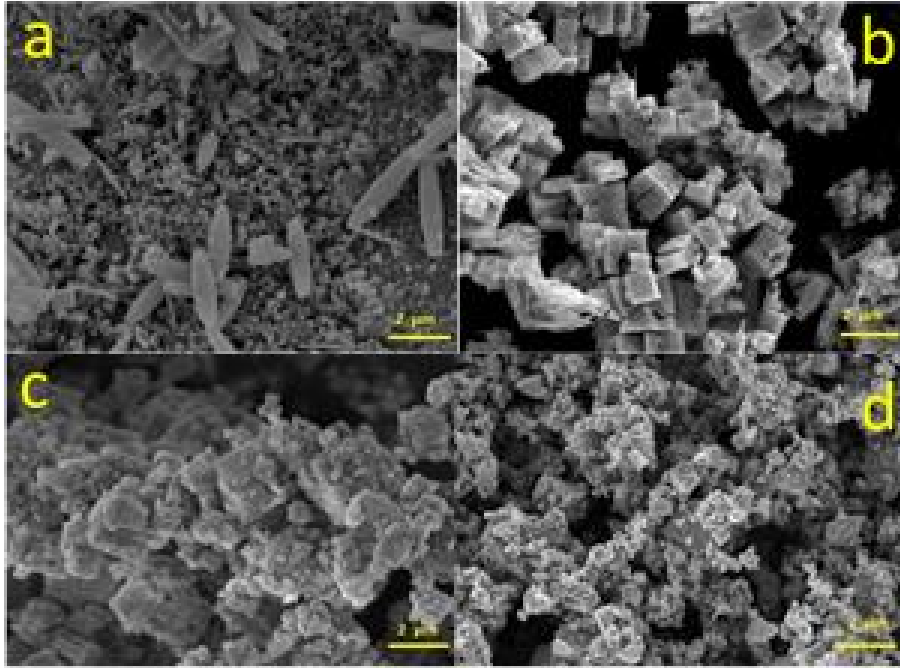


**Figure 9.** FESEM micrographs of wet synthesized  $\text{In}_2\text{O}_3$  powders: BP (a), HT-urea (b), HT-soda (c), HT-soda-W(d).

FESEM observations were carried out on both SA- $\text{In}_2\text{O}_3$  and SA-W- $\text{In}_2\text{O}_3$  films after firing at  $600^\circ\text{C}$  for 1 h (Figures 10 a, b). Nanoparticles display diameters in the range between 50 and 70 nm with spheric and prolonged configurations, and agglomerates of few microns, in agreement with laser granulometry analysis.

The morphology of either HT- $\text{In}_2\text{O}_3$  and HT-W- $\text{In}_2\text{O}_3$  films next to firing at  $600^\circ\text{C}$  for 1 h were also investigated and results are displayed in Figure 10 c, d. In the HT- $\text{In}_2\text{O}_3$ , grains in the range 30-40 nm were measured and they are connected in agglomerates that exhibit smaller size compared to the commercial indium oxide (0.5-1 micron vs 6-10 microns). This is in agreement with laser granulometry analysis. Thus in the synthesized films, an extremely porous structure with cubic and rectangular shapes was noticed. Finally, the W-doped indium oxide film exhibits similar morphology of the undoped  $\text{In}_2\text{O}_3$ , with a surface enrichment of  $\text{WO}_3$  NPs evidenced by point EDX analysis with dimensions from 12 to 16 nm. In fact,  $\text{WO}_3$  appears present also on the surface of  $\text{In}_2\text{O}_3$ .



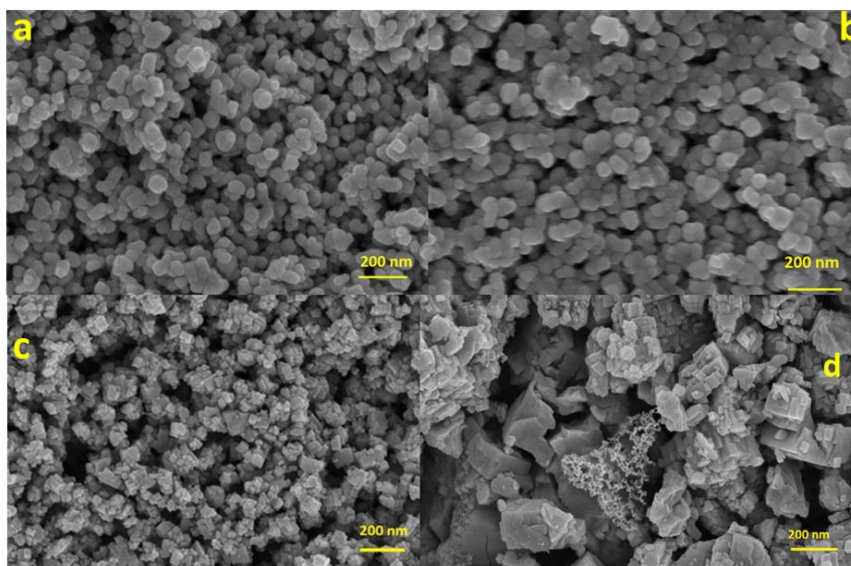


**Figure 10.** FESEM observations of the films: SA-In<sub>2</sub>O<sub>3</sub> (a), SA-W-In<sub>2</sub>O<sub>3</sub> (b), HT-In<sub>2</sub>O<sub>3</sub> (c) and HT-W-In<sub>2</sub>O<sub>3</sub> (d) 100 kx.

Thus, FESEM observations carried out orthogonally to screen-printed films permit to measure the layer thickness that for SA-In<sub>2</sub>O<sub>3</sub> and HT-In<sub>2</sub>O<sub>3</sub> films was  $20.6 \pm 2.7$   $\mu\text{m}$  and  $21.4 \pm 1.9$   $\mu\text{m}$ , respectively.

In Figure 11, DTA-TG curves regarding HT-In<sub>2</sub>O<sub>3</sub> precursor before the calcination at 400°C are displayed. TG curve confirms a whole mass loss equal to 14.8% in the range of T 270°C-350°C, with the highest slope at 305°C (as determined by the differentiate of the TG curve). DTA curve supports TG result, and a broad endothermic signal with maximum at 317°C was found, probably due to the conversion of In(OH)<sub>3</sub> into In<sub>2</sub>O<sub>3</sub>. Furthermore, a small exothermic signal at 207°C that is due to the decomposition of the remaining CTAB still present in the powder [54].

The whole mass loss is lightly lower in comparison with the theoretic value of 16.3% for the formation of In<sub>2</sub>O<sub>3</sub> from In(OH)<sub>3</sub> and for this reason, all powders were calcined at 400°C for 3 h [55].

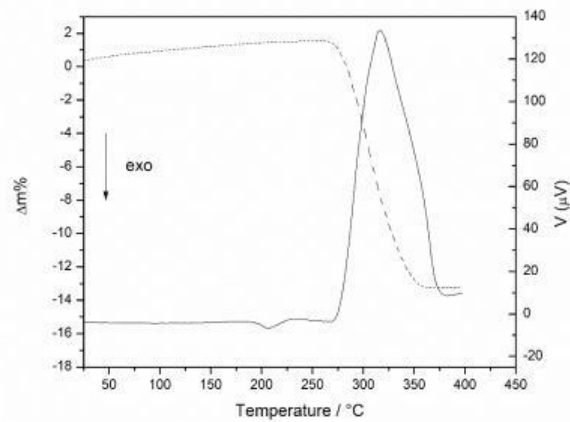


**Figure 11.** TG-DTA curve of TG: dashed line; DTA: straight line for  $\text{In}(\text{OH})_3$  before calcination.

The crystallization of cubic  $\text{In}_2\text{O}_3$  are demonstrated by XRD investigation as depicted in Figure 12. XRD was realized after annealing at  $400^\circ\text{C}$  for 3 h. For comparison, the XRD pattern of the SA- $\text{In}_2\text{O}_3$  and SA-W- $\text{In}_2\text{O}_3$  and HT- $\text{In}_2\text{O}_3$  and HT-W- $\text{In}_2\text{O}_3$ , are depicted in Figure 12a and 12b.

Furthermore, for the HT- $\text{In}_2\text{O}_3$  precursor, the crystallization of  $\text{In}(\text{OH})_3$  previous to annealing was verified in Figure 12c. Finally, the XRD spectrum of  $\text{WO}_3$  achieved with the identical process except for the impregnation of  $\text{In}_2\text{O}_3$  is represented in Figure 12d.

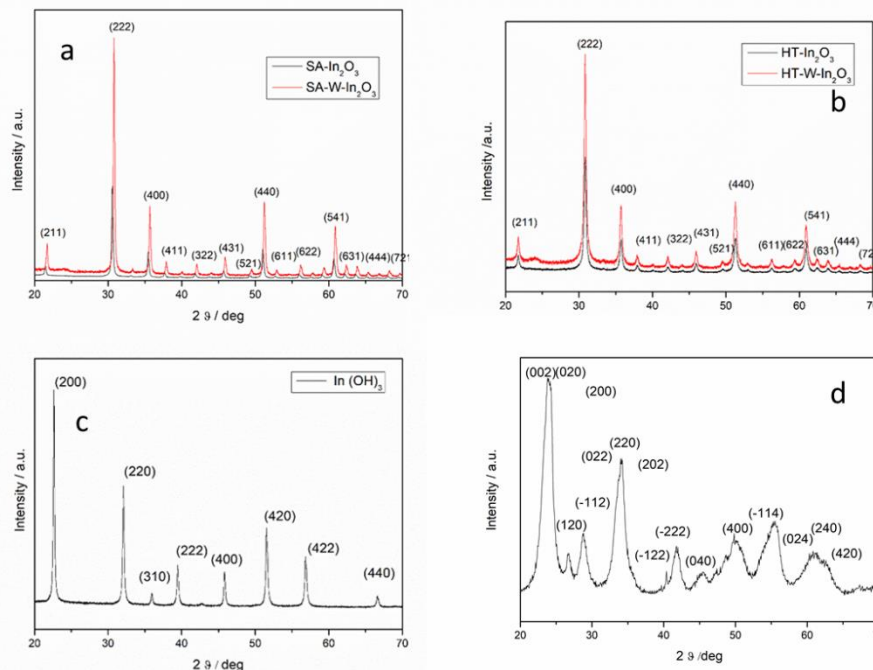


**Figure 12.** XRD spectra of powders: SA-  $\text{In}_2\text{O}_3$  and SA-W- $\text{In}_2\text{O}_3$  (black and red, respectively, a); comparison between HT-  $\text{In}_2\text{O}_3$  (black) and HT-W- $\text{In}_2\text{O}_3$  (red) b); XRD spectrum of  $\text{In}(\text{OH})_3$ , c); and  $\text{WO}_3$  synthesized with the identical procedure without the impregnation of  $\text{In}_2\text{O}_3$ , d).

The XRD spectrum of  $\text{In}_2\text{O}_3$  NPs corroborates the  $\text{In}_2\text{O}_3$  in cubic phase crystallization (JCPDF card n°06-0416). In all samples, the intensity of signals that correspond to the (222) orientation is the principal peak. Korotcenkov et al [2] demonstrated that if the (222) peak is higher than the (400) one, the sensors's  $\tau_{\text{des}}$  towards  $\text{O}_3$  decreases at few minutes. The degree of film texturing is indeed estimated by the ratio between the main peak intensities in the XRD patterns of  $\text{In}_2\text{O}_3$ , eg.  $I(400)/I(222)$ .

This is a result of the film densification caused by the crystallites structure in the texturing layers. In the studied NPs, the ratio  $I(400)/I(222)$  is  $< 1$ , as a consequence  $\text{In}_2\text{O}_3$  nanostructures does not display texturing. Consequently, the sensing characteristics are dependent by the layer thickness (see later) and also by the size of crystallites of the sensitive layer.

The XRD spectrum of HT-powders present broader signals comparing with SA-powders, describing a situation where crystallites are smaller in size and where the degree of crystallization is lower, in accordance with [75]. The Scherrer equation was applied on the diffraction signals such as (211), (222), (400), (440), (541), and

a crystallite size of  $48 \pm 3.5$  nm for SA-In<sub>2</sub>O<sub>3</sub> and SA-W-In<sub>2</sub>O<sub>3</sub> was obtained. This parameter is almost the half ( $26 \pm 2.8$  nm) in the case of synthesized indium oxides. These outcomes are in agreement with Bagheri-Mohagheghi [56], in which the size of crystallites between 3 and 25 nm for In<sub>2</sub>O<sub>3</sub> powders synthesized by hydrothermal route were obtained.

From Figure 12, it is clear that SA-In<sub>2</sub>O<sub>3</sub> and SA-W-In<sub>2</sub>O<sub>3</sub> display quasi identical XRD spectra (Figure 12a) and this is confirmed for the HT-In<sub>2</sub>O<sub>3</sub> and HT-W-In<sub>2</sub>O<sub>3</sub> too (figure 12b). For the doped materials, a small and broad signal due to the convolution of the three main signals of monoclinic WO<sub>3</sub> (reference n<sup>o</sup> 43-1035) was detected, as a confirmation of the beginning of crystallization of WO<sub>3</sub>. (002), (020) and (200) crystallographic planes were present at 23.12, 23.59 and 24.38 of 2 $\theta$ , respectively. In addition, no secondary phases in addition to cubic In<sub>2</sub>O<sub>3</sub> and monoclinic WO<sub>3</sub> were noticed in the doped powders. WO<sub>3</sub> crystallization take place at T < 400°C, as verified by XRD investigation performed on the WCl<sub>6</sub> precursor calcined at 400°C for 3 h without impregnation of indium oxide (Figure 12d) forming monoclinic WO<sub>3</sub> (reference n<sup>o</sup> 43-1035). Thus, XRD was carried out after the HT synthesis and prior to the annealing at 400°C: in this case, every diffraction signal can be indexed as a pure In(OH)<sub>3</sub>, in cubic phase with lattice constant  $a = 0.797$  nm, accordingly with JCPDS n<sup>o</sup> 76-1463. The sharp diffraction pattern is a proof of the good crystallization of the powder.

As corroborated by XRD investigation of the hydrothermally prepared powder after firing at 600°C, the size of crystallites raised till 39 nm from 26 nm, while for the commercial powders this parameter reaches the value of 54 nm from 48 nm. For evaluating an eventual shift of the diffraction signals, the analysis was accomplished with an internal standard method using quartz as reference. Taking into account the six principal signals of (211), (222), (400) (431), (440) and (622) Miller indices, a shift to smaller 2 $\theta$  values (average of 0.03° of 2 $\theta$ ) was measured for the W-In<sub>2</sub>O<sub>3</sub> powders with respect to the undoped ones (not shown). As a result, lattice parameter  $d$  mildly increases in the doped powders (from 1.0078 to 1.0089 nm for the SA-powder and from 1.0083 to 1.0092 nm for the HT-sample). This is probably a consequence of the substitution by W<sup>6+</sup> dopants into the indium oxide cell, in spite of a smaller ionic radius for the octahedral W(VI) (74 pm), in comparison with the octahedral and trigonal prismatic In(III) (94 pm). A lower cation occupancy is required for maintaining the electrical neutrality of the lattice cell when replacing In<sup>3+</sup> by W<sup>6+</sup> ions. This decrease in cation occupancy may be responsible for the distortion of the cell increasing the bond length and resulting in the slight increase of  $a$ .

A brief of these results is tabulated in the Table 2 where the lattice parameters (a) for the In<sub>2</sub>O<sub>3</sub> in bixbyte-cubic form were calculated considering the three main planes (222) (400) and (440) adopting the equation 5 from the XRD data:

$$d_{hkl} = \frac{a}{\sqrt{h^2+k^2+l^2}} \quad (5)$$

Where  $d_{hkl}$  denotes the lattice spacing of the (h k l) plane and a is the lattice spacing.

**Table 2.** Lattice parameters and crystallite size from Scherrer equation for the samples.

Material	Crystallite size (nm)	Lattice parameter (a, nm)
SA-In <sub>2</sub> O <sub>3</sub>	48	1.0078
SA-W-In <sub>2</sub> O <sub>3</sub>	48	1.0089
HT-In <sub>2</sub> O <sub>3</sub>	26	1.0083
HT-W-In <sub>2</sub> O <sub>3</sub>	26	1.0092

In both powders, the addition of WO<sub>3</sub> generates an increase of about 0.1% in lattice parameter. In<sub>2</sub>O<sub>3</sub> crystallizes in a body centred cubic unit cell (BCC) that belongs to the space group Ia3 (number 206). Here, the In atoms stay in the centres of the cube and O lay on the vertices with an oxygen vacancy in every base. The entire system is constituted by two kind of In sorrounded by O in the octahedral and trigonal prismatic coordination, alternated each others. Either coordination groups can be depicted as distorted octaedra and the XRD spectra establish that WO<sub>3</sub> in part is present into the crystal lattice of In<sub>2</sub>O<sub>3</sub>, distorting the BCC cell after impregnation and thermal treatment. This was verified by the shift with internal standard method in the XRD spectrum after WO<sub>3</sub> addition. Moreover, WO<sub>3</sub> in part lay on the In<sub>2</sub>O<sub>3</sub> surface since a small peak as a result of the three mains signals of monoclinic WO<sub>3</sub> was noticed for either doped-powders.

The N<sub>2</sub> adsorption isotherms obtained from the indium oxide powders next to the identical thermal treatment at 600°C were measured and the SSA enhanced from the SA-In<sub>2</sub>O<sub>3</sub> (13.3 m<sup>2</sup>/g) to the SA-W-In<sub>2</sub>O<sub>3</sub> (15.2 m<sup>2</sup>/g). This tendency is even more evident for the HT prepared powders, since SSA were equal to 27.7 and 38 m<sup>2</sup>/g for HT-In<sub>2</sub>O<sub>3</sub> and HT-W-In<sub>2</sub>O<sub>3</sub>, respectively.

The morphology and structure of the powders were investigated by TEM and HRTEM. Figure 13 displays TEM images of SA-W-In<sub>2</sub>O<sub>3</sub> and HT-W-In<sub>2</sub>O<sub>3</sub> (a, b respectively) and HRTEM of SA-W-In<sub>2</sub>O<sub>3</sub> (c, d respectively) and HT-W-In<sub>2</sub>O<sub>3</sub> (e, f) micrographs.

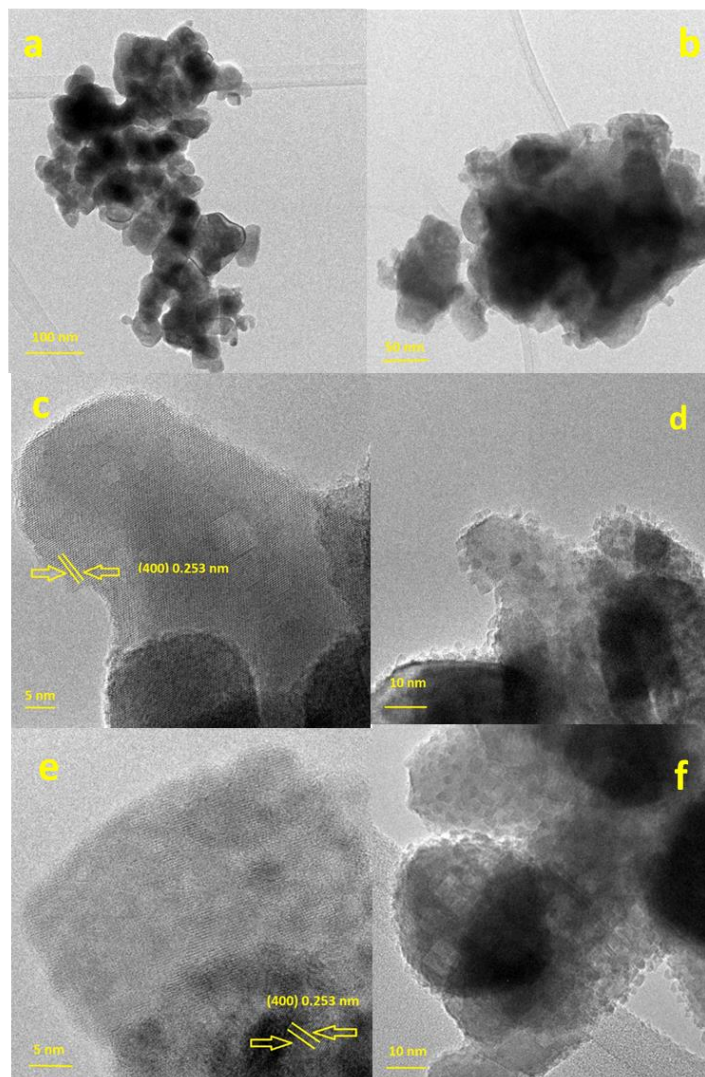


**Figure 13.** TEM (a, b) and HRTEM images of SA-W-In<sub>2</sub>O<sub>3</sub> and of HT-W-In<sub>2</sub>O<sub>3</sub> (c, d, e, f).

Considering the TEM bright-field pictures, it is clear that all samples are agglomerated to a small extent, with clusters of crystallites with diameters in the range 20–60 nm. These results confirm the laser granulometry test and the Scherrer equation applied in the XRD analysis about the crystallite size of the sample discussed above. Thus, one of the principal crystal planes of In<sub>2</sub>O<sub>3</sub> was recognized (400) characterized by a diffraction plane with lattice fringes of 0.253 nm. In

HRTEM images, it is possible to assess the presence of  $\text{WO}_3$  nanoparticles on the surface of indium oxide (e.g. it was verified by a punctual EDX analysis carried out on the NPs) strengthening the finding that  $\text{WO}_3$  is present both in the bulk and on  $\text{In}_2\text{O}_3$  surface.

In addition, no lattice spacing generated by the main crystal planes of  $\text{WO}_3$ , such as (200), (020) and (002), were distinguished probably as a result of the small size of  $\text{WO}_3$  and of the fact that  $\text{W}^{6+}$  forms a solid solution with  $\text{In}_2\text{O}_3$ .

By means of XPS analysis, the chemical states of In and O were investigated in SA- $\text{In}_2\text{O}_3$  and HT- $\text{In}_2\text{O}_3$  samples, whereas the chemical states of In, O and W were studied for SA-W- $\text{In}_2\text{O}_3$  and HT-W- $\text{In}_2\text{O}_3$  powders. Figure 14 presents the XPS survey of the 4 materials (a, b, c, d).

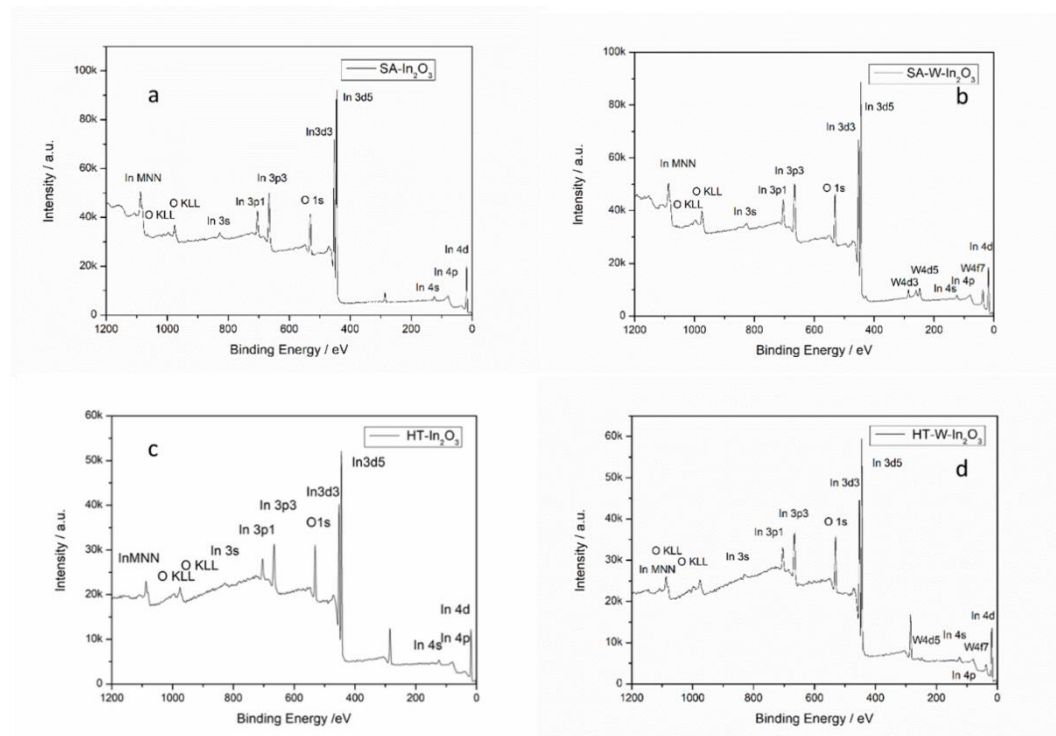


**Figure 14.** Survey XPS spectra of: SA- $\text{In}_2\text{O}_3$  (a); SA-W- $\text{In}_2\text{O}_3$  (b); HT- $\text{In}_2\text{O}_3$  (c); HT-W- $\text{In}_2\text{O}_3$  (d).

The presence of W in the doped materials was verified from the surveys, either for SA-W- $\text{In}_2\text{O}_3$  and HT-W- $\text{In}_2\text{O}_3$ .

Furthermore, spectrum in high-resolution was performed after signals deconvolution for In, O and W for all the powders. In Figure 15 outcomes of spin-orbit split for In  $3d_{5/2}$  and In  $3d_{3/2}$  of In(III) are represented, putting in comparison results achieved for the doped and undoped metal oxides.

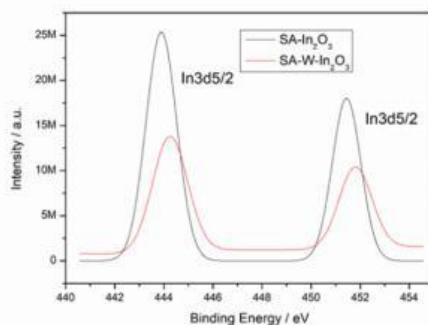


**Figure 15.** HR XPS spectra of  $\text{In}_{3d}$  in: SA- $\text{In}_2\text{O}_3$  (black); SA-W- $\text{In}_2\text{O}_3$  (red).

The 3d characteristic signals were estimated at 443.89 eV and 451.45 eV, respectively. Those are characteristics of the binding energy (BE) of  $\text{In}^{3+}$  in  $\text{In}_2\text{O}_3$  [58].

These signals were measured at 444.25 eV and 451.8 eV for SA-W- $\text{In}_2\text{O}_3$ , with a slight shift at bigger BE, and the identical tendency was detected for HT-  $\text{In}_2\text{O}_3$  and HT-W- $\text{In}_2\text{O}_3$ . This shift can be a result of the differences in the charge density of  $\text{W}^{6+}$  with respect to  $\text{In}^{3+}$ , with a smaller ionic radius for W respect to In, as previously discussed.  $\text{E}^-$  are furnished into the  $\text{In}_2\text{O}_3$  matrix from  $\text{WO}_3$ , resulting in the typical signals of In at bigger BE caused by screening effect [59].

In the Table 3 the positions and relative intensities of the Oxygen signals in high resolution after peak deconvolution are summarized. Taking into account oxygen peaks, XPS investigation performed on the SA- $\text{In}_2\text{O}_3$  and SA-W- $\text{In}_2\text{O}_3$  displays asymmetric  $\text{O}_{1s}$  spectra that can be deconvoluted into three components, as illustrated in figure 17, where  $\text{O}_l$  is the lattice oxygen,  $\text{O}_c$  the chemisorbed oxygen and  $\text{O}_i$  the hydroxyl oxygen according with Table 3 [60].

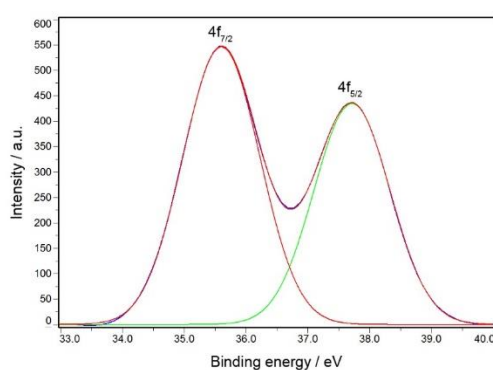


**Table 3.** Positions and relative intensities of the Oxygen signals for the samples.

Material	Peak position	Relative intensity (%)	Type of oxygen	Material	Peak position	Relative intensity (%)	Type of oxygen
SA-In <sub>2</sub> O <sub>3</sub>	529.24	43.97	Lattice	SA-W-In <sub>2</sub> O <sub>3</sub>	529.66	21.63	Lattice
	529.74	31.34	Chemisorbed		530.32	61.85	Chemisorbed
	531.30	24.69	Hydroxyl		531.51	16.53	Hydroxyl
HT-In <sub>2</sub> O <sub>3</sub>	529.62	47.11	Lattice	HT-W-In <sub>2</sub> O <sub>3</sub>	530.00	50.89	Lattice
	530.38	9.39	Chemisorbed		531.29	17.64	Chemisorbed
	531.48	43.51	Hydroxyl		532.11	31.46	Hydroxyl

From this summary, the concentration of O<sub>c</sub> is doubled for the W-In<sub>2</sub>O<sub>3</sub> in comparison with In<sub>2</sub>O<sub>3</sub> (respectively 31.34% for SA-In<sub>2</sub>O<sub>3</sub> and 61.85% for SA-W-In<sub>2</sub>O<sub>3</sub>, 9.39% for HT-In<sub>2</sub>O<sub>3</sub> and 17.64% for HT-W-In<sub>2</sub>O<sub>3</sub> with respect to the total oxygen). Furthermore, the O<sub>i</sub> contribution is reduced for W-doped indium oxides as respect to the undoped ones (from 24.69% till 16.53% for SA-In<sub>2</sub>O<sub>3</sub> and SA-W-In<sub>2</sub>O<sub>3</sub> and from 43.51% until 31.46% for HT-In<sub>2</sub>O<sub>3</sub> and HT-W-In<sub>2</sub>O<sub>3</sub> with respect to the total oxygen, respectively).

Moreover, the W<sub>4f</sub> spectrum of SA-W-In<sub>2</sub>O<sub>3</sub> (and this is true also for HT-W-In<sub>2</sub>O<sub>3</sub>) is a doublet with BE equal to 35.6 eV considering W 4f<sub>7/2</sub> and 37.7 eV of W 4f<sub>5/2</sub> as depicted in Figure 16.

**Figure 16.** HR XPS spectra of W4f carried out on SA-W-In<sub>2</sub>O<sub>3</sub>.

This XPS spectrum confirms the presence of tungsten in the W<sup>6+</sup> oxidation state [61]. Results of high-resolution XPS carried out on O peaks is presented in Figure 17.

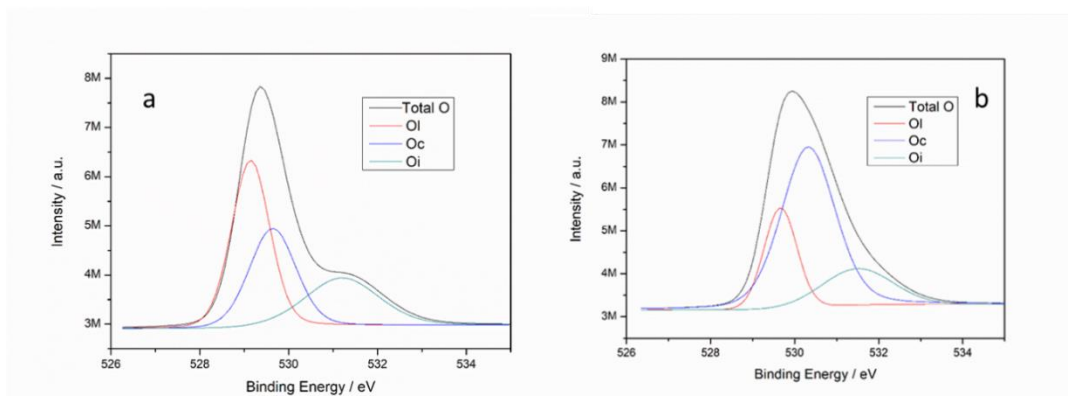


**Figure 17.** HR XPS spectra of  $O_{1s}$  carried out on SA- $In_2O_3$  (a) and SA-W- $In_2O_3$  (b).

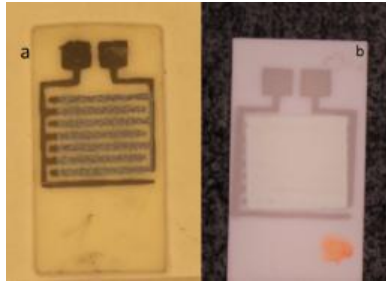
These outcomes are in agreement with XRD analysis, in which shifts in the  $In_2O_3$  spectrum delineate that  $W^{6+}$  is present partially in solid solution in the  $In_2O_3$  lattice, altering to a small extent the lattice parameters.

As illustrated in Figure 17, the SA-W- $In_2O_3$  is characterized by higher levels of  $O_c$  in comparison with the pure SA- $In_2O_3$ . Consequently, the W- $In_2O_3$  is able to adsorb more  $O_2$  on the surface since more vacancies can be filled. The sensing response take place mainly through transfer of electrons and with alterations in the quantity of  $O_c$ , so the sensor characteristics typically are improving when chemisorbed oxygen and defects are higher. In addition,  $WO_3$  on the  $In_2O_3$  surface is able to ameliorate the sensor response towards  $O_3$  through spillover-effect (e.g. increasing the efficiency in the dissociation of  $O_3$  into  $O_2$ ). The identical behavior was assessed on the HT- $In_2O_3$  and HT-W- $In_2O_3$  samples. In this case, the signals generated by  $O_c$  is enhanced from 9.4% till 17.64% of the total oxygen and either In and O signals were shifted at bigger BE for the doped materials.

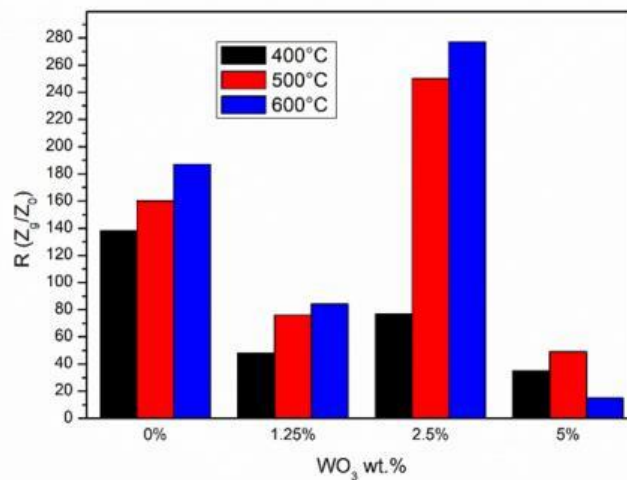
### 5.3 Sensor performances of $In_2O_3$ and $WO_3-In_2O_3$

Firstly, the firing temperature (between 400 and 600°C) and the amount of  $WO_3$  (in the range between 1.25 and 5 wt%) were optimized for SA sensors.

An image of this sensor is illustated in Figure 18, and results for sensor response are summarized in Figure 19.



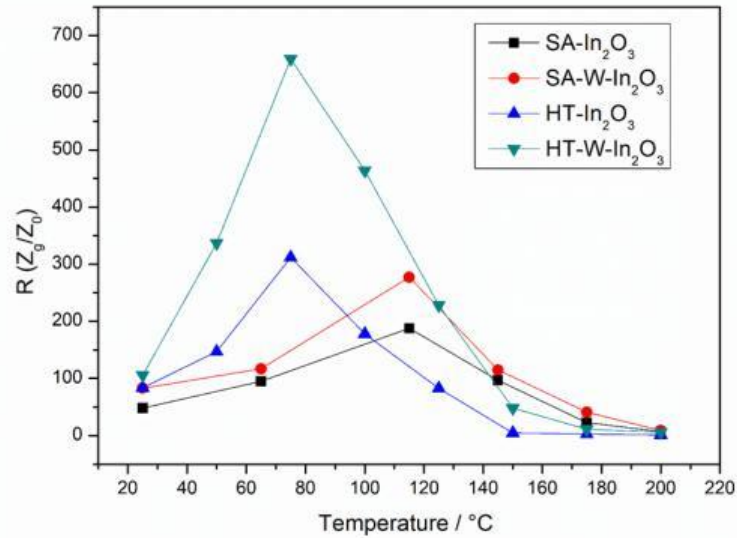
**Figure 18.** SA-In<sub>2</sub>O<sub>3</sub> (a) and HT-In<sub>2</sub>O<sub>3</sub> sensors.



**Figure 19.** Sensor responses of SA-In<sub>2</sub>O<sub>3</sub>, doped with diverse amounts of WO<sub>3</sub>: 1.25, 2.5 and 5 wt% and fired at 400°C, 500°C and 600°C for 1 h upon 500 ppb of O<sub>3</sub> in dry conditions and 115°C.

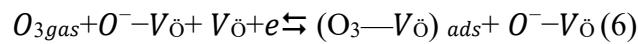
Maximum sensor response was achieved in the case of 2.5 wt% of WO<sub>3</sub> as dopant and 600°C of firing temperature, ameliorating the adhesion of the layer onto the Al<sub>2</sub>O<sub>3</sub> substrate and the ohmic contacts between the thick layer and the Pt interdigitated circuit at the same time. As a result, HT-In<sub>2</sub>O<sub>3</sub> and HT-W-In<sub>2</sub>O<sub>3</sub> were fabricated by firing at 600°C for 1 h the device either both SA-W-In<sub>2</sub>O<sub>3</sub> and HT-W-In<sub>2</sub>O<sub>3</sub> have 2.5 wt% of WO<sub>3</sub> doping.

Figure 20 illustrates the sensor response for all the sensors between 25 and 200°C. Generally, the sensor's impedance (Z) starts from hundreds of Ω in dry conditions of synthetic air and reaches up to tens of kΩ upon O<sub>3</sub> 0.5 ppm. The best operating T was 115°C for SA-In<sub>2</sub>O<sub>3</sub> and SA-W-In<sub>2</sub>O<sub>3</sub>, and equal to 100°C for HT-In<sub>2</sub>O<sub>3</sub> and HT-W-In<sub>2</sub>O<sub>3</sub>, as displayed in Figure 20.



**Figure 20.** Sensor response at different working T (25-200°C) upon 0.5 ppm of O<sub>3</sub>: SA-In<sub>2</sub>O<sub>3</sub>, SA-W-In<sub>2</sub>O<sub>3</sub>, HT-In<sub>2</sub>O<sub>3</sub> and HT-W-In<sub>2</sub>O<sub>3</sub>.

It is noticeable that, by adding 2.5 wt% of WO<sub>3</sub> to both SA-In<sub>2</sub>O<sub>3</sub> and HT-In<sub>2</sub>O<sub>3</sub> with, an amelioration of sensor characteristics was achieved. In fact, in the case of W-doped In<sub>2</sub>O<sub>3</sub> more O<sub>c</sub> is available during the O<sub>3</sub> adsorption that involves the filling of oxygen vacancies in accordance with the equation 6.



In this equation, O<sub>3</sub> has a huge affinity towards oxygen vacancies (V $\ddot{O}$ ) in comparison with the adsorbed oxygen species, O<sup>-</sup>-V $\ddot{O}$ . In accordance with this mechanism, e<sup>-</sup> of the CB are consumed. After the I interaction with O<sub>3</sub>, the depletion layer thickness is enhanced, and the charge carrier amount decreased.

The sensor response increases by 48% after doping for SA-In<sub>2</sub>O<sub>3</sub> at 115°C without variations on the best working T. For the synthesized In<sub>2</sub>O<sub>3</sub> devices, an improvement of 111% of sensor response was fulfilled at 75°C. Thus, for HT-sensors, optimum best working T was considerably lower (i.e. 75°C): this value is remarkably lower compared to the best operating T of commercial ones (i.e. 115°C). In fact, by realizing via hydrothermal synthesis In<sub>2</sub>O<sub>3</sub> nanostructures, a consistent increase of the sensor response and a decrease of the best operating temperature were reached. This is probably a consequence of the lower crystallite and agglomeration size and a superior SSA achieved for the HT-In<sub>2</sub>O<sub>3</sub>. Nonetheless,

the  $\tau_{\text{ads}}$  and  $\tau_{\text{des}}$  at 75°C were too long for real applications (they were in the range 10-12 min), and as a result the optimum best working T was selected to be 100°C. In these conditions, sensor  $\tau_{\text{ads}}$  and  $\tau_{\text{des}}$  were equal to 2 minutes after exposure to 500 ppb of O<sub>3</sub> as tabulated in the Table 4.

The changes in Z of the sensor with the highest sensor response towards O<sub>3</sub>, HT-W-In<sub>2</sub>O<sub>3</sub>, at the optimized temperature of 100°C upon diverse O<sub>3</sub> concentrations (between 200 and 500 ppb), are represented in the next Figure 21a, and the corresponding calibration curve in Figure 21b.

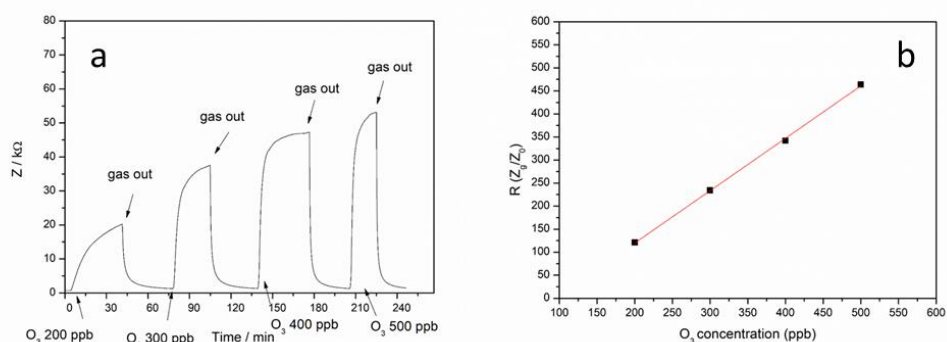


**Figure 21.** Changes in impedance of HT-W-In<sub>2</sub>O<sub>3</sub> sensor towards different [O<sub>3</sub>] at 100°C (a) and its calibration curve (b).

From the Figure 21, the calibration curve of HT-W-In<sub>2</sub>O<sub>3</sub> sensor upon O<sub>3</sub> 0.2-0.5 ppm at 100°C exhibits a linear relationship, and a sensitivity of 0.879 ppm<sup>-1</sup> was obtained, accordingly with IUPAC definition. Sensor  $\tau_{\text{ads}}$  and  $\tau_{\text{des}}$  of HT-W-In<sub>2</sub>O<sub>3</sub> film are both reasonably short. In fact, they are around 1-5 minutes for the different O<sub>3</sub> concentrations studied, as shown in Table 4, and the kinetic of sensing is faster at higher O<sub>3</sub> concentration in accordance with the literature [62].

**Table 4.** HT-W-In<sub>2</sub>O<sub>3</sub> film response and recovery times at different O<sub>3</sub> amounts (200-500 ppb) at 100°C.

O <sub>3</sub> concentration (ppb)	$\tau_{ads}$ (s)	$\tau_{des}$ (s)
200	992	298
300	567	241
400	387	129
500	267	199

Thus, the selectivity of the proposed sensors was investigated, and results are illustrated in Figure 22 after interaction of the sensors with NH<sub>3</sub> 50 ppm, CH<sub>4</sub> 50 ppm, air + RH 50%, CO<sub>2</sub> 500 ppm, N<sub>2</sub>O 15 ppm, CO 10 ppm and NO<sub>2</sub> 250 ppb.

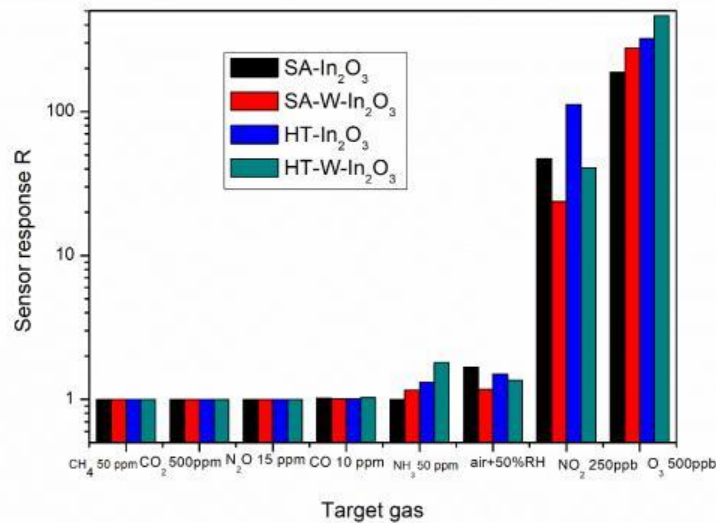


**Figure 22.** Cross-sensitivity tests for SA-In<sub>2</sub>O<sub>3</sub>, SA-W-In<sub>2</sub>O<sub>3</sub>, HT-In<sub>2</sub>O<sub>3</sub> and HT-W-In<sub>2</sub>O<sub>3</sub> films at 100°C.

For all the four types of sensors, the main interferences are nitrogen dioxide, as expected, and humidity. RH is well-known to decrease the baseline resistance for most of the SMOx investigated [63], even if in the case of SA-W-In<sub>2</sub>O<sub>3</sub> and HT-W-In<sub>2</sub>O<sub>3</sub> the interference is noticeably reduced upon interaction with water molecules.

On the opposite, HT-base  $\text{In}_2\text{O}_3$  sensors display a higher sensor response for  $\text{NH}_3$  50 ppm compared to the commercial indium oxides.

Taking into account other oxidant species, no cross sensitivity towards  $\text{CO}_2$  was evidenced and a cross sensitivity towards  $\text{NO}_2$  was assessed, as expected considering that the interaction mechanism is similar of that for  $\text{O}_3$ . Nevertheless, the interference of  $\text{NO}_2$  is decreased for the W- $\text{In}_2\text{O}_3$ , for either SA and HT powders. When  $\text{WO}_3$  acts as dopant into the  $\text{In}_2\text{O}_3$  matrix, the selectivity for  $\text{O}_3$  is higher in terms of RH and  $\text{NO}_2$  but it is decreased with respect to  $\text{NH}_3$ . In general,  $\text{In}_2\text{O}_3$  chemical sensors are remarkably more sensitive upon oxidizing species compared to the reducing ones, in agreement with the state of the art [64,2]. The variation between sensor performances upon  $\text{NO}_2$  and  $\text{O}_3$  can be justified by the diverse oxidant power of those gases.  $\text{WO}_3$  is probably able to favour an effective spillover mechanism upon  $\text{O}_3$  interaction by promoting an efficient dissociation of  $\text{O}_3$  into  $\text{O}_2$  while for  $\text{NO}_2$  the mechanism is different.

In addition, the humidity effect was investigated for the proposed sensors after the interaction of the sensors with different concentrations of RH: 30%, 50% and 70% for 15 min. Outcomes are illustrated in Figure 23 by calculating the sensor response  $R$  like the ratio between the impedance upon dry air ( $Z_0$ ) and the impedance in humid air ( $Z_g$ ) at the equilibrium.

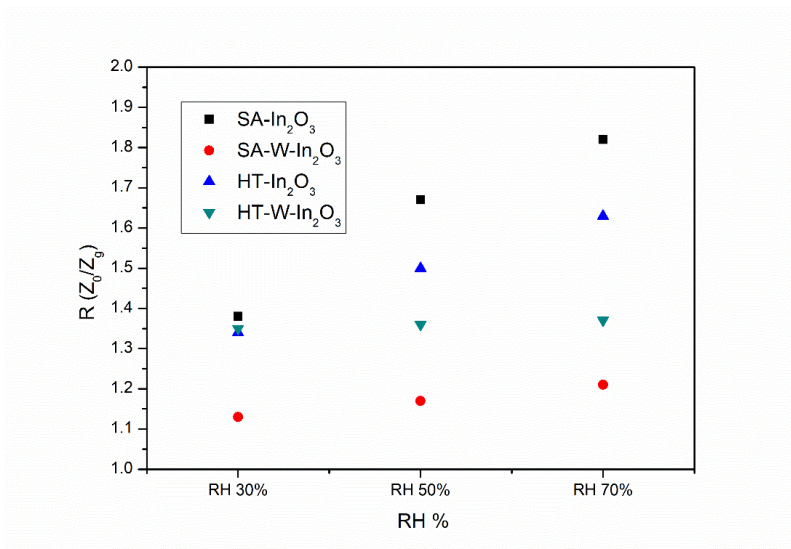


**Figure 23.** Humidity influence at 30-50-70% of RH for the four sensors at 100°C.

The  $\text{WO}_3$ -doped devices display a modest interference due to humidity comparing with the base line impedance value in dry air compared to the undoped materials ones. This is in accordance with XPS investigations where a drop in the

OH amount was measured for W doped-indium oxides. Surprisingly, for HT-W-In<sub>2</sub>O<sub>3</sub>, no variation in Z were measured at higher level of RH than 30%. On the opposite, a linear dependence between sensor response and RH amount was measured for the rest of the devices. In the case of W-In<sub>2</sub>O<sub>3</sub> sensors, saturation caused by water molecules adsorption occur at lower water molecules amounts with respect to the undoped sensors.

Finally, in Table 5, results obtained in this thesis are compared with other studies dealing with In<sub>2</sub>O<sub>3</sub>-based sensor for O<sub>3</sub> monitoring.

**Table 5.** State of the art of In<sub>2</sub>O<sub>3</sub> thick layer heated O<sub>3</sub> sensors. Elaboration from ref. [2].

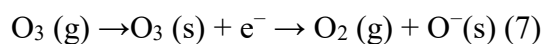
Technological route	Film thickness	Crystallite size	Max sensor response R: (Rg/Ro)	Conditions of measurements	References
Thick film, drop coating	2 μm	12 nm	300	85°C, 250 ppb, dry	[65]
Thick film, drop coating	/	8 nm	1500	200°C, 100 ppb, dry	[9]
Thick film, screen printing	/	8 nm	100	235°C, 1 ppm	[21]
Thick film, screen printing	20 μm	20 nm	120	270°C, 1ppm	[66]
Thick film, screen printing	20.6 μm	25.6 nm	464	100°C, 500 ppb, dry	This work

By comparing the results of this thesis with those of other researchers working with In<sub>2</sub>O<sub>3</sub> thick-films for O<sub>3</sub> detection, the optimum response is usually obtained between 200° and 350°C. Only in the work of Starke [65] achieved the highest response at 85°C, a similar operating T of this thesis (100°C). Nevertheless, the synthesis method was laser ablation, the deposition was drop coating and the thickness of the film (2 instead of 20.6 microns) was different too.

The gas-sensing mechanism of In<sub>2</sub>O<sub>3</sub>-based devices is predominantly controlled by the surface at T<100°C [67], and from [68], it is established that between 100°C and 200°C, it is dominated either by bulk and surface phenomena.



When O<sub>3</sub> interacts with the In<sub>2</sub>O<sub>3</sub>, it is dissociated according with the equation 7:



In which e<sup>-</sup> represent an electron that is accountable for the conduction in the In<sub>2</sub>O<sub>3</sub> layer, O<sup>-</sup>(s) are surface oxygen ions, and O<sub>3</sub> (g) and O<sub>2</sub> (g) are the adsorbing ozone and the desorbing oxygen molecules, respectively [1]. When In<sub>2</sub>O<sub>3</sub>-based devices interact with O<sub>3</sub> molecules, the gas interacts with the O<sub>c</sub>, that are more in number in the W-In<sub>2</sub>O<sub>3</sub> with respect to the undoped In<sub>2</sub>O<sub>3</sub>, as verified in XPS analysis. E<sup>-</sup> are caught from the CB enhancing the film impedance. When the In<sub>2</sub>O<sub>3</sub> sensors are under air flow again, film recover fast to the initial electronic state despite of the low working T.

The chemisorbed oxygens of the metal oxide accelerate the decomposition of O<sub>3</sub> on the sensor surface increasing the sensor response towards ozone.

When electrons are released from the surface of In<sub>2</sub>O<sub>3</sub>, the impedance increases until a determined temperature, over that the exothermic adsorption of gas becomes tricky and the analyte begin desorbing widely, resulting in a consistent decrease in the sensor response up to 150°C as illustrated in figure 20. The improvement of O<sub>3</sub>-sensing properties of the W-doped In<sub>2</sub>O<sub>3</sub> films is probably a result of the synergic effect of the WO<sub>3</sub> and In<sub>2</sub>O<sub>3</sub> NPs. WO<sub>3</sub> is partially present on the In<sub>2</sub>O<sub>3</sub> surface and it avoids the In<sub>2</sub>O<sub>3</sub> agglomeration refining effective pathways for adsorption and diffusion of O<sub>3</sub>. Consequently, hetero-junctions between WO<sub>3</sub> and In<sub>2</sub>O<sub>3</sub> generate a typical e<sup>-</sup> donor–acceptor system. As a consequence, the synergic effect of WO<sub>3</sub> and In<sub>2</sub>O<sub>3</sub> species with diverse sizes are efficient factors to ameliorate the low-T gas sensing performances of the WO<sub>3</sub>-doped In<sub>2</sub>O<sub>3</sub>.

Among different WO<sub>3</sub> concentrations investigated, in accordance with [69] a WO<sub>3</sub>-doping of 3 at%, a comparable amount of the proposed sensor, the lowest value of resistivity and the highest carrier mobility were measured among several WO<sub>3</sub> doping amounts onto In<sub>2</sub>O<sub>3</sub> layer.

When enhancing the concentration of oxygen vacancies in the MOS, more e<sup>-</sup> are disposable, increasing its n-type features. As a result, the Fermi level was shifted nearer to the CB, shifting the VB upward too. Moreover, the electron affinity of the semiconductor is enhanced since more e<sup>-</sup> are provided from WO<sub>3</sub> to In<sub>2</sub>O<sub>3</sub> giving a superior electron affinity by forming the oxygen vacancies.

Presumably, WO<sub>3</sub> promotes the generation of Schottky hetero-junctions with In<sub>2</sub>O<sub>3</sub> at nanoscale. This led to a transfer of electrons to In<sub>2</sub>O<sub>3</sub>, diminishing the energy needed in order to create oxygen vacancies into the lattice. An effective dissociative oxygen chemisorption is favoured by WO<sub>3</sub>, with a spillover mechanism

that is an efficient way to refill the oxygen vacancies. As a result, superior sensitivity and quicker response of the indium oxide sensors were achieved [70].

The baseline  $Z$  of  $\text{WO}_3$ -doped devices is smaller with respect to the undoped ones, proofing the increased number of  $e^-$ , that are inserted into the oxide lattice by interstitial metal atoms or by oxygen vacancies for maintaining the whole neutrality in the  $\text{In}_2\text{O}_3$  crystal.

If we compare the sensitivity of commercial and synthesized  $\text{In}_2\text{O}_3$ , the sensitivity of  $\text{In}_2\text{O}_3$ -based layer (around 20  $\mu\text{m}$ ) upon  $\text{O}_3$  is governed by either the sizes of the crystallites and of the agglomerates.

In accordance with other works in the field of chemical sensors related to highly agglomerated MOS, not solely the crystallite size, but the dimensions of agglomerates and the gas penetrability too are essential factors that control both the kinetics and the sensitivity.

In the case of agglomerated MOS in thick film devices, it is of paramount importance to adjust mainly the dimensions of agglomerates. Laser granulometry investigation assesses the lower size of agglomerates from SA- $\text{In}_2\text{O}_3$  to HT- $\text{In}_2\text{O}_3$ . In addition, XRD analysis confirms that also the dimension of crystallites is smaller for HT- $\text{In}_2\text{O}_3$  with respect to the SA- $\text{In}_2\text{O}_3$  powders and that  $\text{WO}_3$  alters the lattice parameters to some extent inside the cubic  $\text{In}_2\text{O}_3$  crystal.

The  $\text{O}_3$  adsorption mechanism involves both the crystallites and the agglomerates, and for HT- $\text{In}_2\text{O}_3$  devices a significant drop of either parameters was reached enhancing remarkably the sensor performances for  $\text{O}_3$  monitoring [51].

## 5.4 Influence of film thickness on sensor response

With the aim to investigate the influence of the film thickness on the sensor response towards oxidant and reducing species, sensors were manufactured by screen-printing deposition on  $\alpha\text{-Al}_2\text{O}_3$  with Pt interdigitated electrodes and a Pt heater on the backside (CeramTec, DE), received from University of Tübingen.

The same ink was deployed as described in the chapter 3. In order to prepare different film thicknesses, after the deposition of the prime layer, it was dried and another layer was deposited on it subsequently.

In Figure 24 the sensors prepared onto CeramTec substrates and tested at the University of Tübingen are shown. The performances of HT- $\text{In}_2\text{O}_3$  sensors were investigated with respect to  $\text{O}_3$ ,  $\text{NO}_2$ ,  $\text{H}_2$  and humidity between 75°C and 150°C.

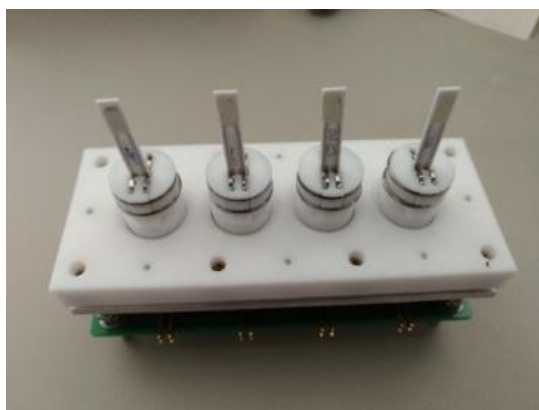


**Figure 24.** Sensor realized over CeramTec substrates.

The resistances of the sensors were measured using Keithley 6517B electrometers and 6487 picoammeters at the University of Tübingen. Various concentrations of  $O_3$ ,  $NO_2$  and  $H_2$  were provided by a computer-regulated gas mixing system with mass-flow controllers in dry air and at diverse relative humidity levels at various temperatures by means of one or more power supplies.  $O_3$  was supplied by a corona discharge generator, while  $NO_2$  and  $H_2$  were supplied by certified gas bottles. Every test gas concentration was pulsed for one hour or one hour and a half. Between the different tests, the test chamber was flowed with synthetic air. The entire protocol of tests was realized in a dry synthetic air background and in 30% and 60% of relative humidity (RH) to evaluate the effect of the humidity on the sensor response.

The sensor response ( $R$ ) was calculated in accordance with the equation (8) for oxidant species and with equation (9) for reductant ones:

$$R: R_g/R_0 \text{ (8)}$$

$$R: R_0/R_g \text{ (9)}$$

Where  $R_g$  and  $R_0$  are the resistances upon analyte and the baseline resistance upon air of the film at the equilibrium, respectively.

Sensors with different thicknesses were realized in the range between 10 and 100  $\mu m$  to study the role of the sensor thickness on the sensing performances. This was verified both towards oxidant gases ( $O_3$  and  $NO_2$ ) and reducing ones ( $H_2$ ). The 10  $\mu m$  (1 layer of deposition) and 20  $\mu m$  thickness (2 layers) were realized at Politecnico di Torino, while 40 (1 layer), 70 (2 layers) and 100  $\mu m$  (3 layers), were prepared at University of Tübingen by screen printing technique using the same ink described above. Sensor thicknesses were determined by cross-sectional FESEM observations at Politecnico di Torino and by means of laser topography (MicroProf

CHR 150 N, with a High-Resolution Optical Sensor, FRT, DE) at the University of Tübingen.

### 5.4.1 Electrical measurements

The first set of measurements was performed at 75°C upon an uniform gas flow of 300 SCCM with the sensor having 10 μm of thickness (1 layer of deposition). Adsorption and desorption times were respectively equal to 1 hour and 1.5 hours. Sensor was exposed to the following concentrations: 100, 200, 400, 800 and 1600 ppb of O<sub>3</sub>; 200, 400, 800 and 1600 ppb of NO<sub>2</sub>; 20, 40 and 80 ppm of H<sub>2</sub>. Results are shown in Figure 25 at different humidity level: 0%RH, 30%RH and 60%RH.

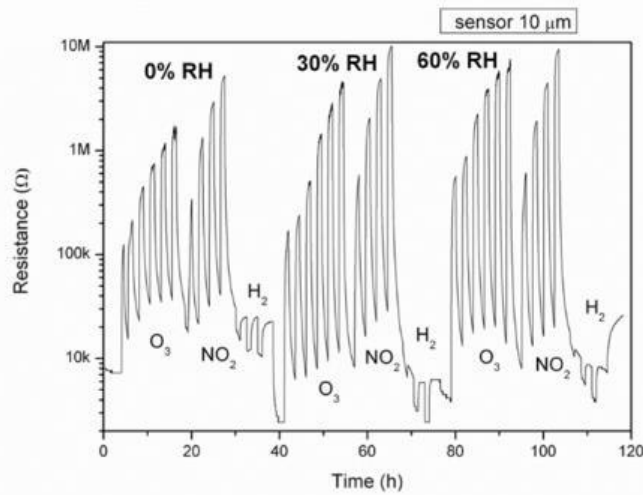


**Figure 25.** 10 μm thick sensor resistance variation under O<sub>3</sub>, NO<sub>2</sub> and H<sub>2</sub> and different relative humidity levels: 0, 30 and 60% at 75 °C.

Under O<sub>3</sub> and NO<sub>2</sub> exposure, the film resistance increases sharply from 10 kΩ to some MΩ while no consistent drop in the resistance was measured under hydrogen exposure. Calibration curves for the 3 gases are illustrated in Figure 26.

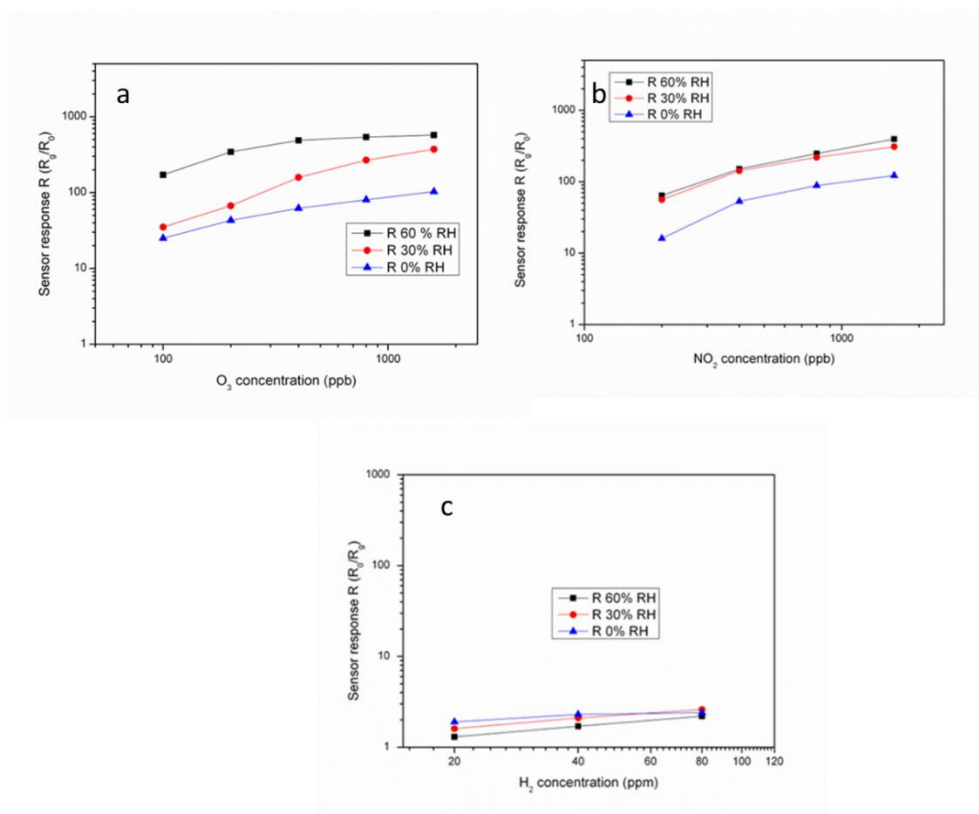


**Figure 26.** Calibration curves for 10 μm thick In<sub>2</sub>O<sub>3</sub> sensor upon O<sub>3</sub> (a), NO<sub>2</sub> (b) and H<sub>2</sub> (c) at 75°C under 0%, 30% and 60% RH.

Best results were achieved at higher humidity values for both oxidant gases, while for H<sub>2</sub> the tendency is the inverse, because of the competition between H<sub>2</sub> and H<sub>2</sub>O for the identical adsorption centres on the In<sub>2</sub>O<sub>3</sub> surface.

A comparison between sensor response towards O<sub>3</sub> and NO<sub>2</sub> under different humidity values is reproduced in Figure 27.

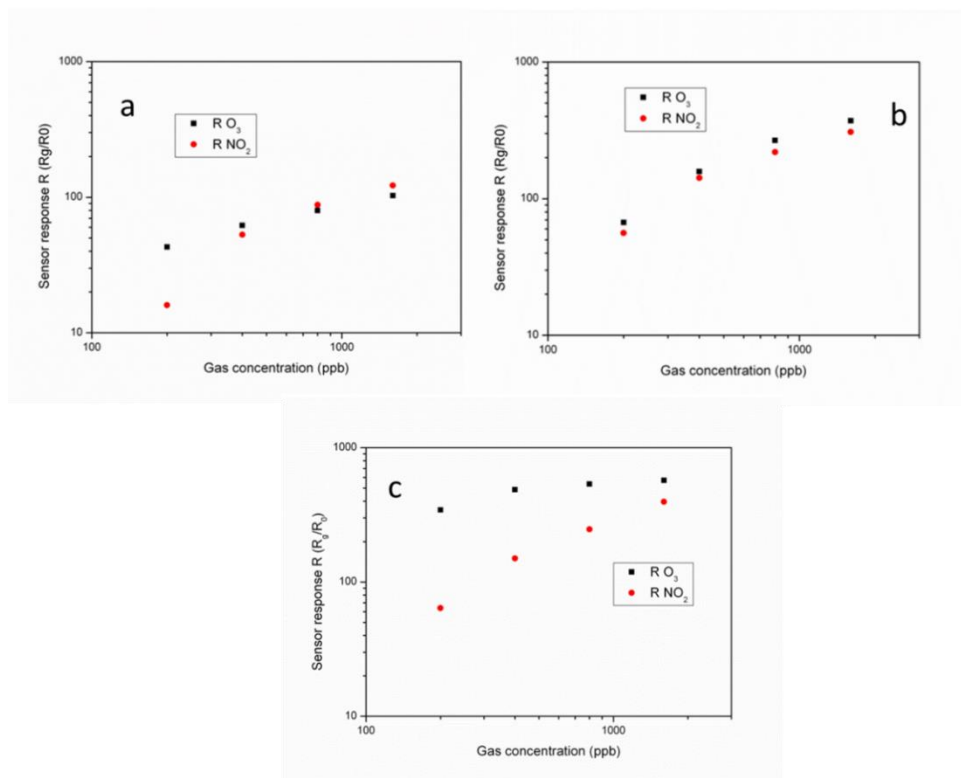


**Figure 27.** Comparison between sensor response towards O<sub>3</sub> and NO<sub>2</sub> for 0%RH (a), 30%RH (b) and 60% RH (c) at 75 °C.

Comparing the results obtained at 75°C, at higher values of humidity the sensor response towards O<sub>3</sub> increases compared to that towards NO<sub>2</sub>, probably because of the decrease in the baseline resistance when In<sub>2</sub>O<sub>3</sub> film is exposed to 60% of relative humidity and a synergic effect of humidity in the sensor response for oxidant species. In addition, O<sub>3</sub> is known to be a stronger oxidant agent than NO<sub>2</sub>. However, the sensitivity (slope of the curve  $R=f([\text{gas}])$ ) is higher for NO<sub>2</sub> respect to O<sub>3</sub>.

The same sensor was tested also at 115°C since at 75°C desorption of O<sub>3</sub> and NO<sub>2</sub> are not complete, even after 90 minutes. Relative humidity values of 30 and 60% were selected since at those levels best results were attained at 75°C. Results are shown in figure 28 for 1 hour-pulses of gas and 1.5 hour of desorption under synthetic air. The sensor interacted with the following gas concentrations: 100, 200, 400, 800 and 1000 ppb of O<sub>3</sub>; 200, 400, 800 and 1000 ppb of NO<sub>2</sub>, 20, 40, 80 and 160 ppm of H<sub>2</sub> (Figure 28).

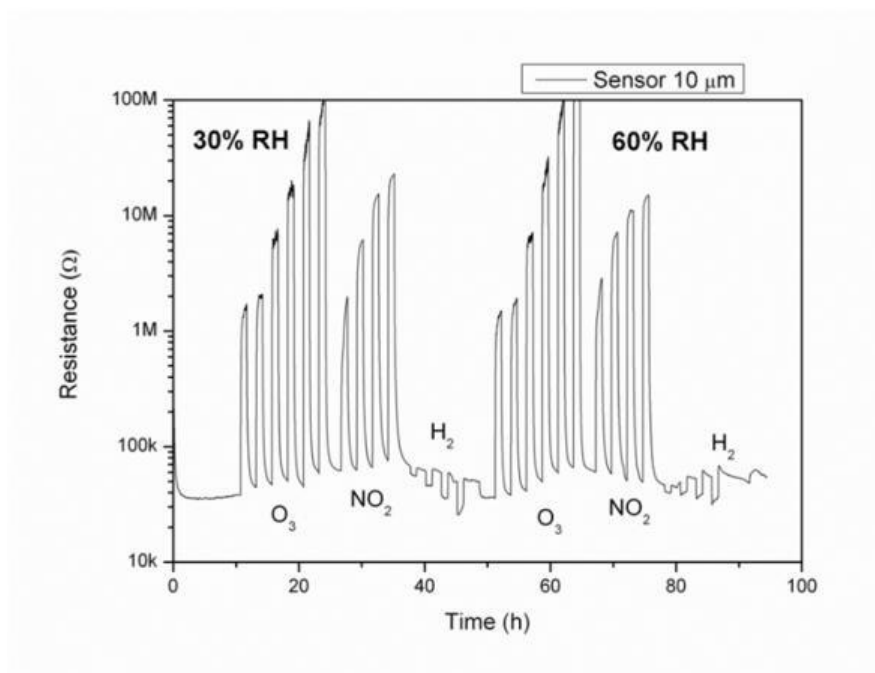


**Figure 28.** 10  $\mu\text{m}$  thick sensor resistance variation under  $\text{O}_3$ ,  $\text{NO}_2$  and  $\text{H}_2$  and different relative humidity values: 30 and 60% at  $115^\circ\text{C}$ .

Under  $\text{O}_3$  and  $\text{NO}_2$  exposure, film resistance enhances sharply from  $30\text{ k}\Omega$  to  $10\text{-}100\text{ M}\Omega$  while only a moderate decrease in the resistance was found under hydrogen exposure. Moreover, almost complete desorption of target gases takes place at this temperature. Calibration curves for the 3 target gases are drawn in Figure 29.

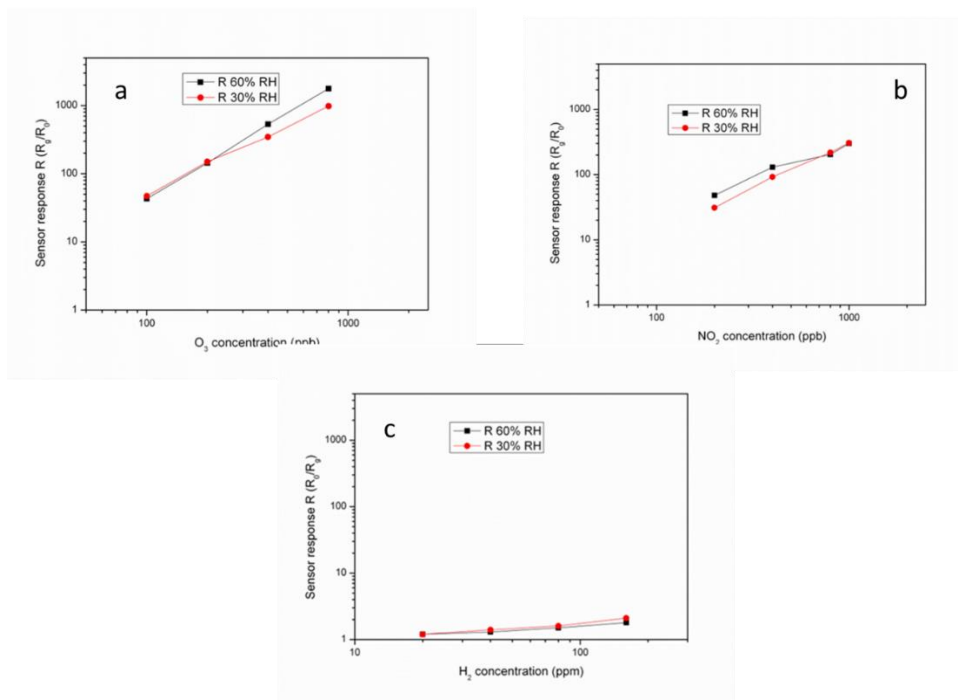


**Figure 29.** Calibration curves for 10  $\mu\text{m}$  thick  $\text{In}_2\text{O}_3$  sensor upon  $\text{O}_3$  (a),  $\text{NO}_2$  (b) and  $\text{H}_2$  (c) at  $115^\circ\text{C}$  under 30% and 60% RH.

No consistent variation among the two humidity values was detected for almost all gases. The comparison between sensor responses towards  $\text{O}_3$  and  $\text{NO}_2$  is reproduced in Figure 30 under 30% and 60% of relative humidity.

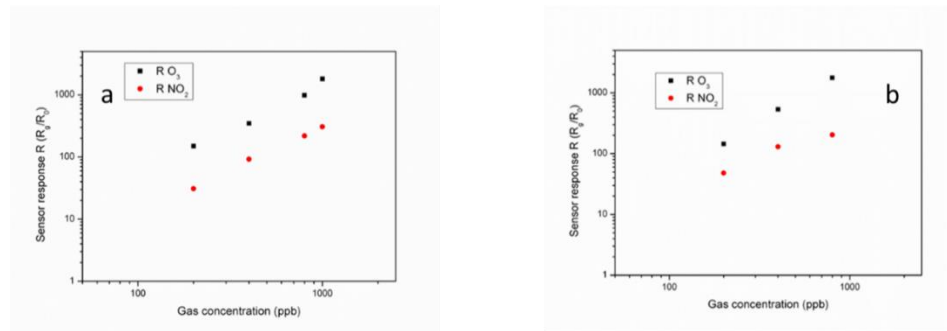


**Figure 30.** Comparison between sensor response towards  $\text{O}_3$  and  $\text{NO}_2$  for 30% RH (a) and 60% RH (b) at  $115^\circ\text{C}$ .

At  $115^\circ\text{C}$ , the relative response under  $\text{O}_3$  is higher compared to the response under  $\text{NO}_2$  under 30 and 60% of humidity. This trend is even more significant at bigger amounts of the analyte.

The same sensor was then tested at  $150^\circ\text{C}$  under the same relative humidity values of 30 and 60%. Results are represented in figure 31 with pulses of gas for 1



hour followed by 1.5 hour of desorption under synthetic air. The sensor was exposed to the following concentrations: 100, 200, 400, 800 and 1000 ppb of O<sub>3</sub>; 200, 400, 800 and 1000 ppb of NO<sub>2</sub>; and finally, 20, 40, 80 and 160 ppm of H<sub>2</sub>. In addition, some repeatability tests were carried out under O<sub>3</sub> 100, 200, 400 and 800 ppb for three times in a row. Results of 10 μm thick film are displayed in Figure 31.

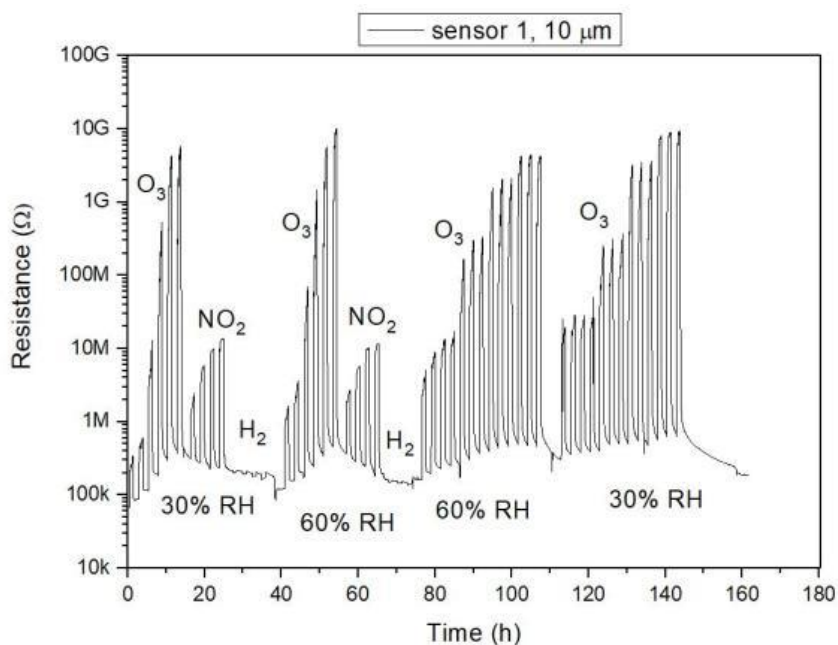


**Figure 31.** 10 μm thick sensor resistance variation under O<sub>3</sub>, NO<sub>2</sub> and H<sub>2</sub> upon 30 and 60% of RH at 150°C.

At 150°C, the sensor response towards O<sub>3</sub> sharply grows, while that towards NO<sub>2</sub> decreases compared to the results obtained at 115°C. As a result, the selectivity of In<sub>2</sub>O<sub>3</sub> sensor at 150°C improves significantly. In fact, the film resistance under 30% of relative humidity was equal to 100 kΩ, while under 1000 ppb of ozone, it reaches almost 10 GΩ.

On the opposite, only a moderate variation in film resistance was observed under 20-160 ppm of hydrogen.

The as-described variation is clear from the calibration curves for the three gases, illustrated in Figure 32.

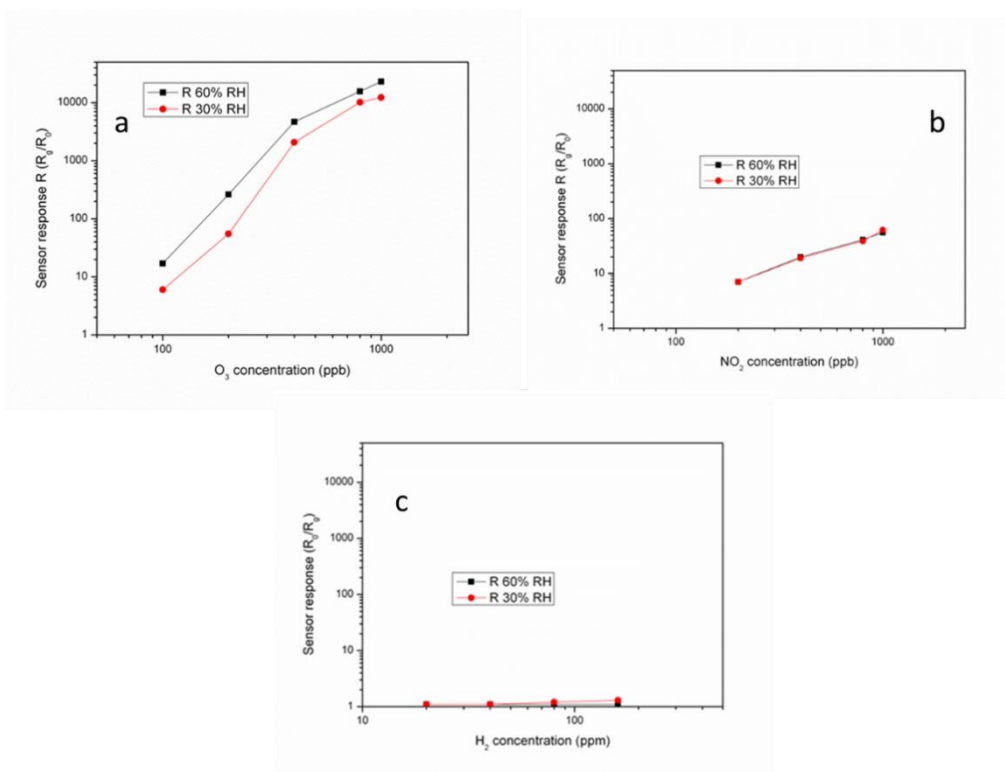


**Figure 32.** Calibration curves for 10 μm thick In<sub>2</sub>O<sub>3</sub> sensor under O<sub>3</sub> (a), NO<sub>2</sub> (b) and H<sub>2</sub> (c) at 150°C under 30% and 60% RH.

No consistent differences between the two humidity levels for sensor response towards hydrogen was detected (the maximum value of sensor response was equal to 1.2), confirming the result obtained at 115°C. Thus, considering NO<sub>2</sub> measurements, at this temperature no differences between 30 and 60% of RH was measured. On the opposite, sensor response under O<sub>3</sub> is considerably higher compared to NO<sub>2</sub>, and this difference increases sharply at higher humidity values. Finally, a comparison between sensor responses towards O<sub>3</sub> and NO<sub>2</sub> is reproduced in Figure 33 under 30% and 60% of relative humidity.

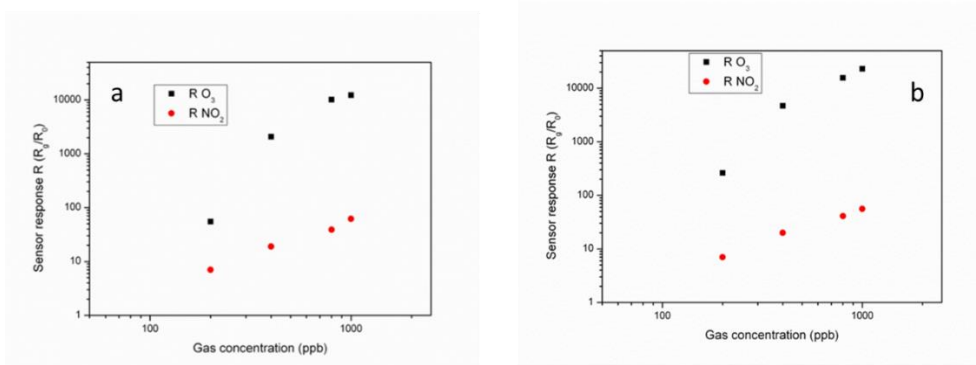


**Figure 33.** Comparison between  $\text{In}_2\text{O}_3$  sensor response towards  $\text{O}_3$  and  $\text{NO}_2$  for 30% RH (a) and 60% RH (b) at 150 °C.

At 150°C, the sensor response under  $\text{O}_3$  is remarkably higher compared to the  $\text{NO}_2$  one and this trend is confirmed both under 30 and 60% of humidity. In humid conditions, the ozone sensitivity clearly increases, and the selectivity for  $\text{O}_3$  detection also improves with respect to  $\text{NO}_2$ .

Results of repeatability test for three  $\text{O}_3$  measurements in the range 100-1000 ppb are illustrated in Figure 34 for 30% and 60% of RH.

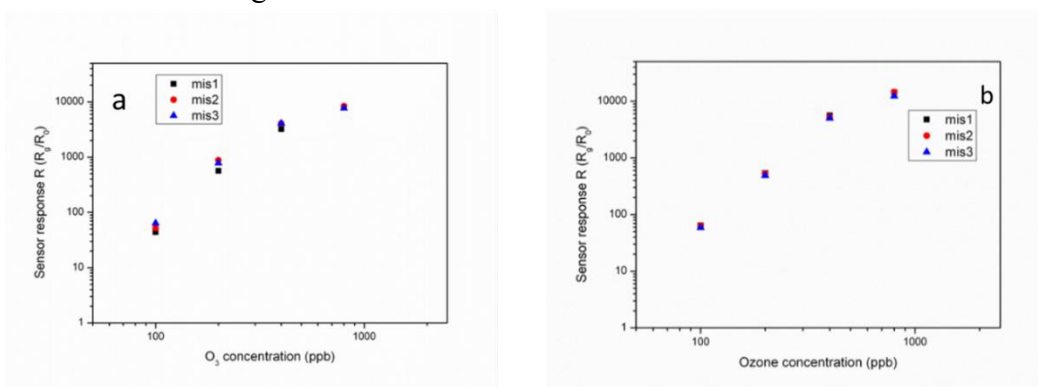


**Figure 34.** Repeatability test for  $\text{In}_2\text{O}_3$  sensor towards  $\text{O}_3$  100-1000 ppb under 30%RH (a) and 60% RH (b) at 150 °C.

Sensors exhibit a good repeatability towards  $\text{O}_3$ , with variation in the sensor response smaller than 7%.

A general comparison among all the measurements performed at different temperatures and concentrations of  $\text{O}_3$  and  $\text{NO}_2$  is shown in Figure 35 for 30% (a) and 60% of RH (b).

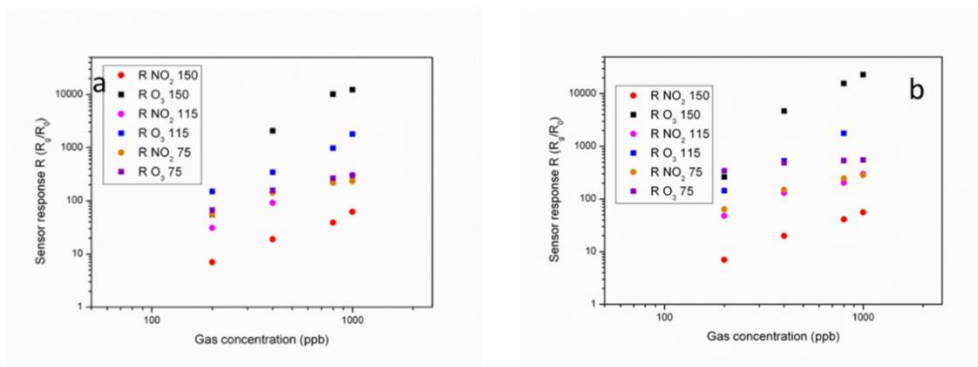


**Figure 35.** Calibration curves for ozone and nitrogen dioxide between 75 and 150°C under 30% RH (a) and 60% RH.

The sensor response under  $\text{O}_3$  increases from 75°C to 150°C, whereas under  $\text{NO}_2$  the sensor response is lower at 150°C compared to 75°C and 115°C both with 30 and 60% of relative humidity. As a result, at 150°C, the selectivity to  $\text{O}_3$  is improved for the HT- $\text{In}_2\text{O}_3$  sensor.

At the best working T of 150°C, devices with different thicknesses were tested (40 and 100  $\mu\text{m}$ ) and the results are displayed in Figure 36.

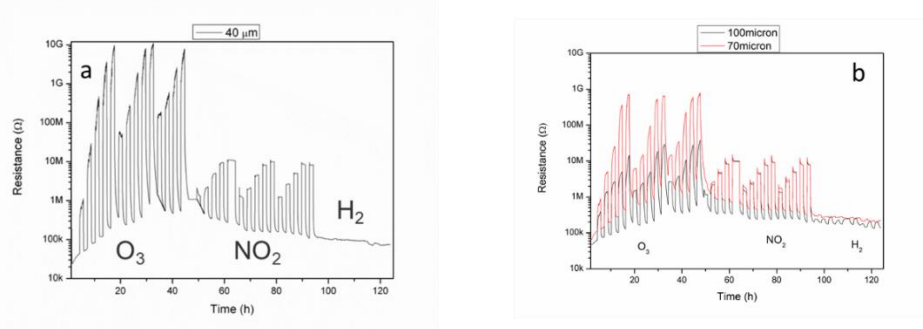


**Figure 36.** 40  $\mu\text{m}$  (a) and 70-100  $\mu\text{m}$  (b) thick  $\text{In}_2\text{O}_3$  resistance's variations toward  $\text{O}_3$ ,  $\text{NO}_2$  and  $\text{H}_2$  at 150°C and 30% RH.

For 40  $\mu\text{m}$  thick sensors, the resistance under 30% of RH is around 30 kΩ and reaches almost 10 GΩ under 1 ppm of  $\text{O}_3$  changing its value by 5 orders of magnitude. On the other side, the influence of  $\text{NO}_2$  is considerably lower and almost no response is detected for  $\text{H}_2$ . Concerning 70 and 100  $\mu\text{m}$  thick sensors, a decrease of the sensor response by increasing the film thickness was noticed, as expected. In fact, the resistance increases from around 100 kΩ to almost 1 GΩ for 70  $\mu\text{m}$  thick film and from similar initial values until 10 MΩ for 100  $\mu\text{m}$  thick film under 1 ppm of  $\text{O}_3$  (Figure 37).

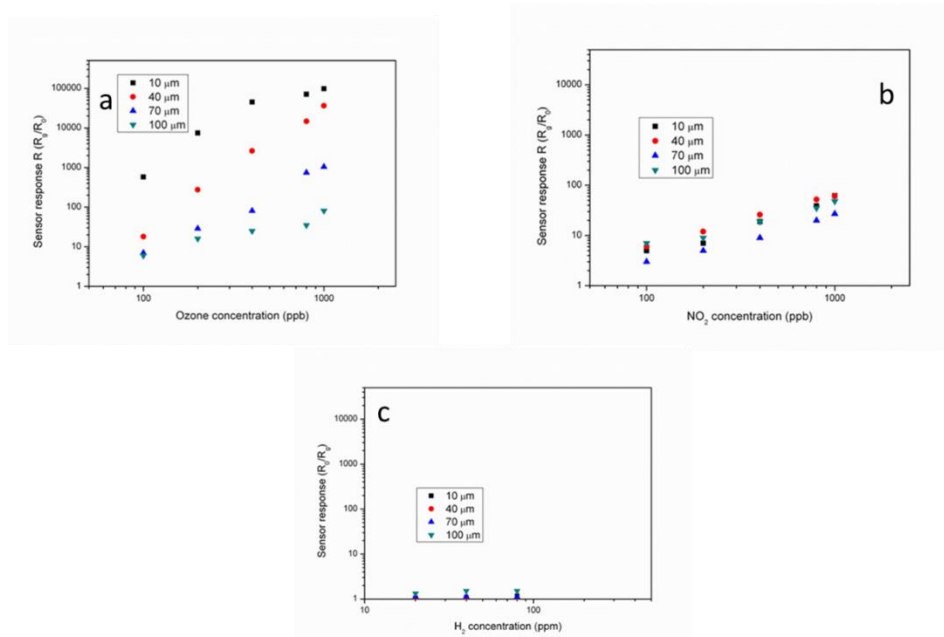


**Figure 37.** Comparison between sensor responses of 10, 40, 70 and 100 μm thick In<sub>2</sub>O<sub>3</sub> layer under O<sub>3</sub>(a), NO<sub>2</sub> (b) and H<sub>2</sub> (c) at 150°C and 30% RH.

Under 30% RH, the impact of film thickness is more pronounced under O<sub>3</sub> with respect to NO<sub>2</sub>, and 10-40-70-100 μm thick films exhibit a logical trend where, by changing the sensor thickness of one order of magnitude, the sensor response changes of three orders of magnitude upon 1000 ppb of O<sub>3</sub>. Upon NO<sub>2</sub>, solely a minute influence of the layer thickness was noticed on the sensitivity. At the end, the cross-sensitivity with H<sub>2</sub> is marginal since the sensor response upon hydrogen does not depend on the layer thickness.

N<sub>2</sub>-syn air measurements were carried out at 115°C at Politecnico under 1000 sccm to understand the oxygen adsorption capability of the indium oxide undoped and doped sensors in dry conditions. Sensors with the same layer thicknesses (20 μm) were evaluated (10-100 μm), and results are presented in Figure 38.

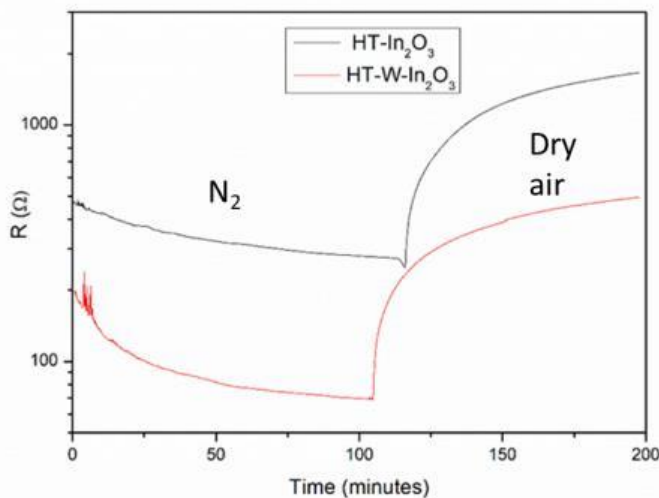


**Figure 38.** N<sub>2</sub>-syn air measurement for HT-In<sub>2</sub>O<sub>3</sub> (black) and HT-W-In<sub>2</sub>O<sub>3</sub> (red) at 115°C and 0% of RH.

The ratio between the value of the resistance under dry air and nitrogen at the equilibrium is equal to 5.8 for undoped indium oxide and 6.9 for the W-doped sensor, describing a good capability of indium oxide sensors for oxygen adsorption, especially for the doped one, confirming the results obtained in the XPS analysis.

## 5.5 DRIFT measurements

The surface reactions of the sensors were studied by operando diffuse reflectance infrared Fourier transform (DRIFT) spectroscopy (Bruker Vertex80v spectrometer), with a home-made test chamber with a KBr window and a liquid nitrogen cooled MCT (mercury cadmium tellurium) detector. The spectral resolution is equal to 4 cm<sup>-1</sup>. Sensors were heated at the best operating temperature (150°C) and the resistance of the sensitive film was measured by an electrometer (Keithley 617). The analytes were supplied with a computer-controlled gas mixing system with a constant flow of 200 SCCM. Spectra were recorded every 15 min. A reference spectrum was recorded before every target gas interaction under dry air, and the spectrum of the sample was registered after each measurement from which the absorbance was calculated following the relationship (10):

$$Absorbance = -\log \frac{(single\ channel\ test\ gas)}{(single\ channel\ reference)} \quad (10)$$

Here the focus of the investigation is to understand the impact of  $O_3$  and  $NO_2$  on the thick-film resistance and which species are formed after the interaction of HT- $In_2O_3$  and HT-W- $In_2O_3$  with those oxidizing gases. Under dry air, the main ions onto the  $In_2O_3$  surface are oxygen species, both  $O_2^-$  or  $O^-$ . Higher amounts of ionosorbed oxygen species further enhances the  $e^-$  trapped through the CB of the n-type  $In_2O_3$  and this increases the film resistance, as measured. In surface-sensitive DRIFTS conditions, the electrical resistance is recorded simultaneously to understand the interaction of  $NO_2$  and  $O_3$  with the surface of  $In_2O_3$  validating clearly the relation between the structure of the surface and the adsorbed species with the sensitivity of the sensor. Deconvolution and fitting of the main spectra was performed by means of LabSpec software (ver 5.0).

HT- $In_2O_3$  and HT-W- $In_2O_3$  devices with the same thickness (10  $\mu m$ ) were tested at the best working T of 150°C for  $O_3$  detection under  $H_2O/D_2O$ ,  $NO_2$  and  $O_3$ .

### 5.5.1 $H_2O/D_2O$ test

For evaluating the role of OH groups, tests of  $H_2O/D_2O$  exchange were performed for either doped and undoped  $In_2O_3$  sensors. The sensors were exposed for 6 hours to 10% relative humidity and then other 6 hours in 10% of  $D_2O$ . Results are depicted in Figure 39.

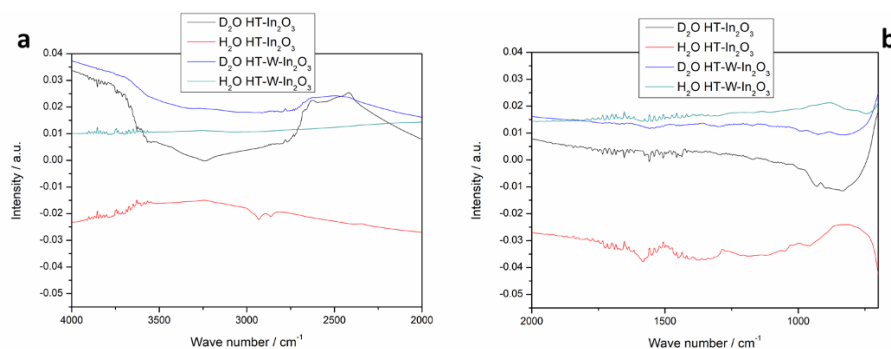
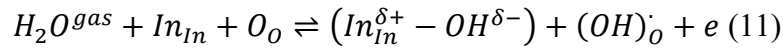


**Figure 39.**  $H_2O/D_2O$  experiment at higher (a) and lower (b) wave numbers.

Comparing  $In_2O_3$  with W- $In_2O_3$ , the later sensor presents a higher degree of exchange  $H_2O/D_2O$  revealing a huge presence of pre-existing OH groups on the MOS surface, especially in the region 3658-3629  $cm^{-1}$  (frequency of the terminals-OH stretching). They interact with other surface species via H bonding.

Indium oxide sensor shows a broad band centred at  $3250\text{ cm}^{-1}$  typical of H bonds. When indium oxide is exposed to water, it reacts with surface oxygens forming OH groups and increasing the conductivity of the film following the equation 11:



### 5.5.2 NO<sub>2</sub> test

Both undoped and doped sensors of  $10\text{ }\mu\text{m}$  in thickness were tested in operando at the best operating temperature,  $150^\circ\text{C}$  under  $10\text{ ppm}$  of NO<sub>2</sub> for 3 hours in dry and 10% of relative humidity conditions. The resistance measurements are shown in Figure 40 for both sensors, where a comparable sensor response for In<sub>2</sub>O<sub>3</sub> and W-In<sub>2</sub>O<sub>3</sub> was measured. However, doped material is more conductive because WO<sub>3</sub> drains a large quantity of electrons to the In<sub>2</sub>O<sub>3</sub> as previously described.

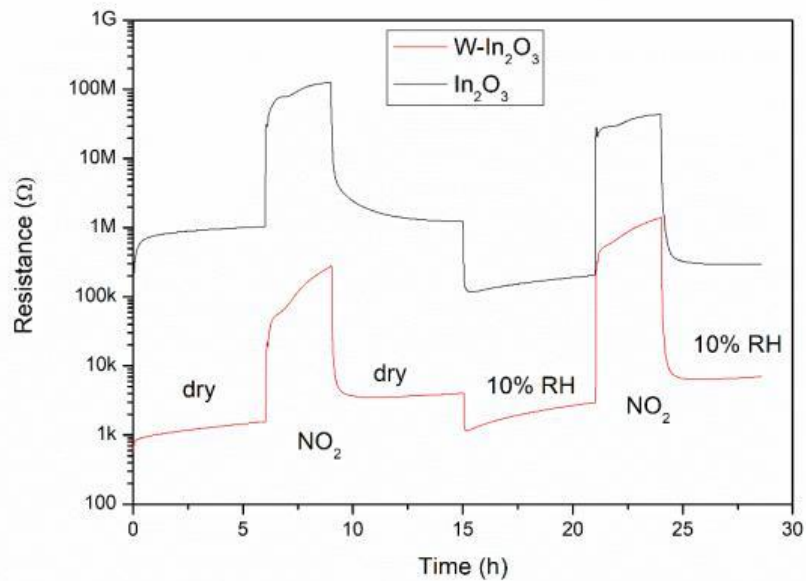


**Figure 40.** Resistance measurement during DRIFT of In<sub>2</sub>O<sub>3</sub> and W-In<sub>2</sub>O<sub>3</sub> in dry and in 10% of RH.

As previously shown, a slight raise in the sensor response was measured in dry conditions for the synergic effect of the water vapor in the adsorption of NO<sub>2</sub> at  $150^\circ\text{C}$ . In Figure 41 the spectra in dry and wet conditions is depicted for both In<sub>2</sub>O<sub>3</sub> and W-In<sub>2</sub>O<sub>3</sub> sensors.



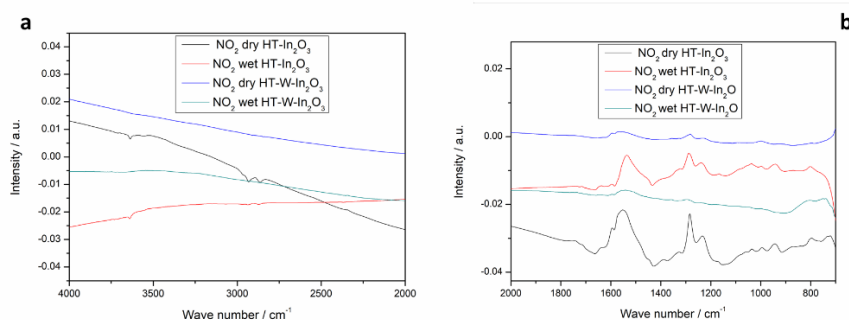


**Figure 41.** NO<sub>2</sub> 10 ppm measurement in dry and 10% of RH at higher (a) and lower (b) wavenumbers.

Generally, In<sub>2</sub>O<sub>3</sub> has more absorption bands than W- In<sub>2</sub>O<sub>3</sub>. For this reason, the deconvolution was performed only on the HT-In<sub>2</sub>O<sub>3</sub>. At 2860 cm<sup>-1</sup> a signal is present, probably due to residual CTAB used as capping agent in the synthesis, and determined only on the undoped material.

N<sub>2</sub>/100 ppm air experiment was also carried out on HT-In<sub>2</sub>O<sub>3</sub> sensor with the aim of distinguishing the In-O bonds due to NO<sub>2</sub>, and those to oxygen. Results are plotted in Figure 42.

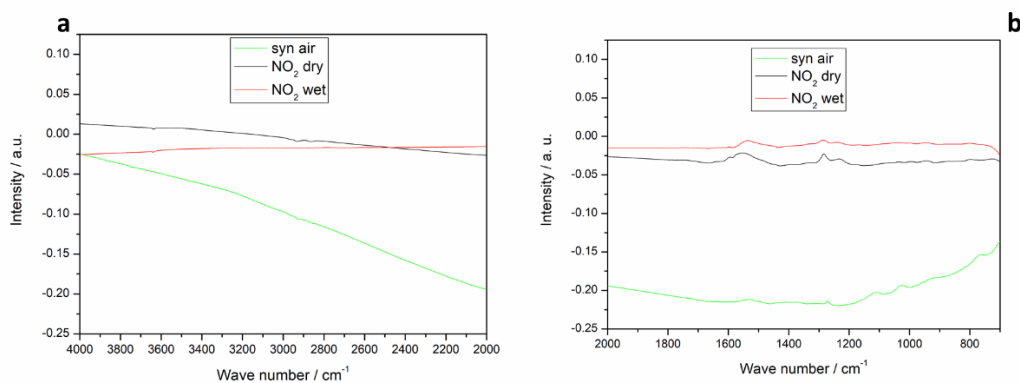


**Figure 42.** N<sub>2</sub>/O<sub>2</sub> 100ppm measurement for In<sub>2</sub>O<sub>3</sub> sensor at higher (a) and lower (b) wavenumbers.

Between 2200-800 cm<sup>-1</sup>, for In<sub>2</sub>O<sub>3</sub> sensor under 10 ppm NO<sub>2</sub> in dry air, the baseline was subtracted as in Figure 43.

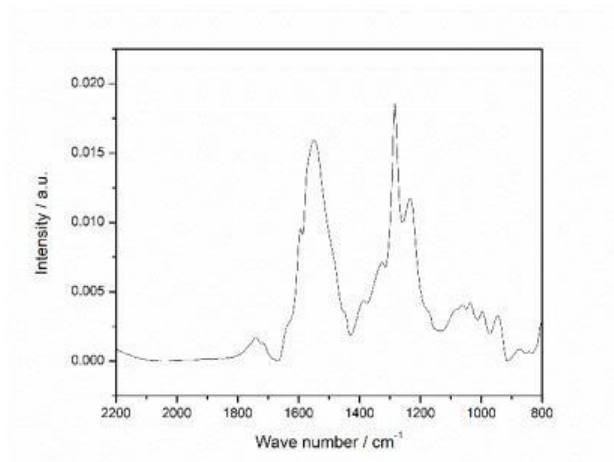


**Figure 43.** Subtraction of the baseline between 2200-800  $\text{cm}^{-1}$  for  $\text{In}_2\text{O}_3$  sensor under 10 ppm  $\text{NO}_2$  in dry air.

The intense signal at  $1547 \text{ cm}^{-1}$  and that at  $1234 \text{ cm}^{-1}$  are probably a consequence of the interaction of surface OH and adsorbed  $\text{H}_2\text{O}$  with adsorbed  $\text{NO}_2$  present as nitrites [71].

In addition, there is no evidence of the bands in the OH region under  $\text{NO}_2$  exposure, proving that OH groups, caused by adsorbed  $\text{H}_2\text{O}$ , play a crucial part during adsorption of nitrogen dioxide and they are consumed when  $\text{NO}_2$  is adsorbed onto  $\text{In}_2\text{O}_3$ . In fact, hydrogen bonds are broken in this process.

To conclude, the “wet“ surface is beneficial for the adsorption of  $\text{NO}_2$  as described in the resistance measurements session, and nitrites adsorption via formation of H bonds with the free OH groups is the main mechanism of adsorption of  $\text{NO}_2$ .

### 5.5.3 $\text{O}_3$ test

Both  $\text{In}_2\text{O}_3$  and W- $\text{In}_2\text{O}_3$  sensors of  $10 \mu\text{m}$  in thickness were tested in DRIFT at the same temperature,  $150^\circ\text{C}$  under 700 and 1500 ppb of  $\text{O}_3$  respectively for 2 hours under 10% of relative humidity. The resistance measurements for the two samples are exhibited in Figure 44.

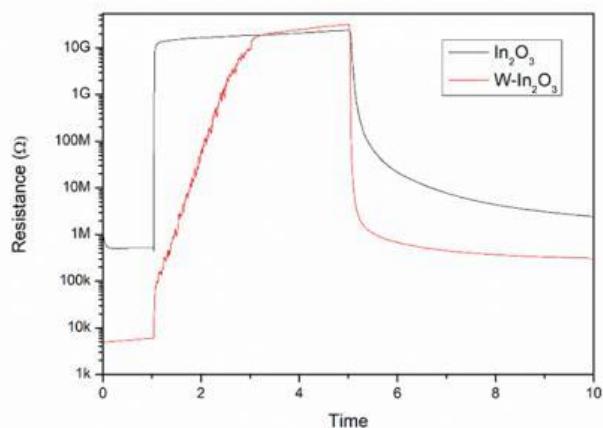


**Figure 44.** Resistance measurements during DRIFT of  $\text{In}_2\text{O}_3$  and  $\text{W-In}_2\text{O}_3$  under 10% of relative humidity and 700-1500 ppb of  $\text{O}_3$  at  $150^\circ\text{C}$ .

The  $\text{W-In}_2\text{O}_3$  sensor response is higher compared to the  $\text{In}_2\text{O}_3$  sensor, since under 10% of relative humidity the film resistance of the doped material is lower than  $10\text{ k}\Omega$  and it reaches  $10\text{ G}\Omega$  under 1.5 ppm of  $\text{O}_3$ , changing the film resistance of 6 orders of magnitude. The undoped indium oxide film resistance change of 4 orders of magnitude under 700 ppb of  $\text{O}_3$ , in accordance with the electrical measurements described above. Thus, the  $\text{In}_2\text{O}_3$   $\tau_{\text{ads}}$  is faster (i.e. in the few minutes range) comparing to the  $\text{W-In}_2\text{O}_3$  (in the order of minutes).

In Figure 45 the spectra in wet conditions are depicted for  $\text{In}_2\text{O}$  sensor under 700 and 1500 ppb of  $\text{O}_3$

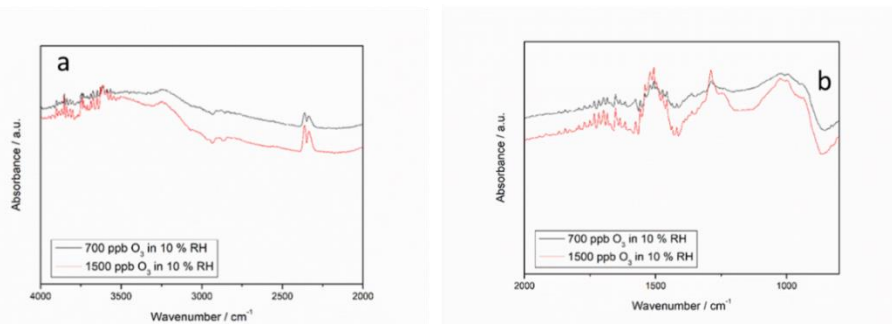


**Figure 45.**  $\text{O}_3$  700 and 1500 ppb  $\text{O}_3$  DRIFT measurement of  $\text{In}_2\text{O}_3$  sensor under 10% of relative humidity at higher (a) and lower (b) wavenumbers.

In addition, in Figure 46 the spectra in wet conditions are illustrated for  $\text{W-In}_2\text{O}$  sensor under 700 and 1500 ppb of  $\text{O}_3$ .

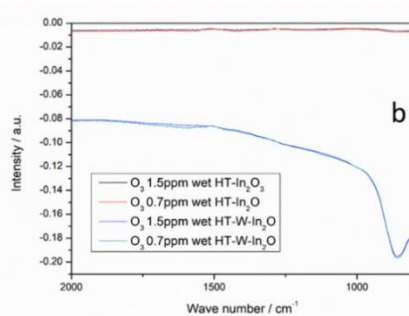
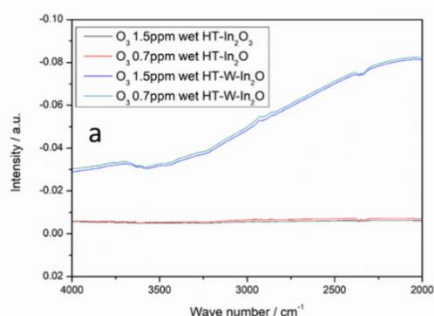


**Figure 46.** O<sub>3</sub> 700 and 1500 ppb O<sub>3</sub> DRIFT measurement of W-In<sub>2</sub>O<sub>3</sub> sensor under 10% of relative humidity at higher (a) and lower (b) wavenumbers.

Peaks deconvolution was performed between 2500-800 cm<sup>-1</sup> for In<sub>2</sub>O<sub>3</sub> and W-In<sub>2</sub>O<sub>3</sub> sensors under 1500 ppb of O<sub>3</sub> and 10% RH where the peak intensity was higher respect to other regions of the spectrum in Figure 47.

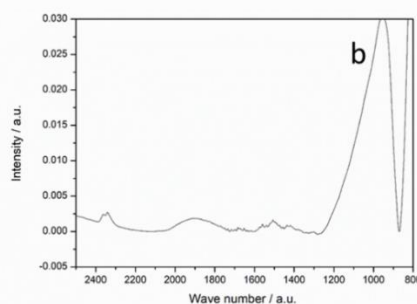
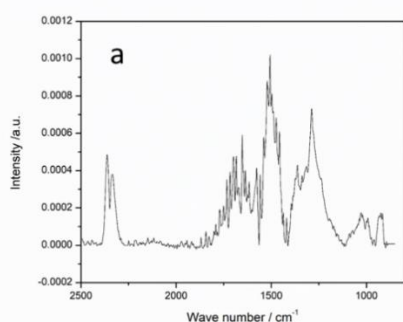
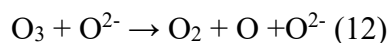


**Figure 47.** Subtraction of the baseline between 2500-800 cm<sup>-1</sup> for In<sub>2</sub>O<sub>3</sub> (a) and W-In<sub>2</sub>O<sub>3</sub> (b) films under 1500 ppb of O<sub>3</sub> in 10% RH.

No signals due to intermediate species like ozonide O<sub>3</sub><sup>-</sup> at 790 cm<sup>-1</sup> and superoxide O<sub>2</sub><sup>-</sup> at 1124 cm<sup>-1</sup> that are probably intermediates in O<sub>3</sub> decomposition on acid sites like In<sup>3+</sup> cations close to the base sites (i.e. surface oxygen) were detected in In<sub>2</sub>O<sub>3</sub> spectra [72].

According to [72] there are two principal ways for O<sub>3</sub> adsorption on the oxide surface: the first is through the terminal oxygen atom of ozone bonding with a OH on the oxide, whereas the second one is through the terminal oxygen atom of ozone bonding with a Lewis active site on the oxide.

Atomic oxygen vibration band appears usually at 1317 cm<sup>-1</sup>, but in this experiment this peak was found at 1288 cm<sup>-1</sup>. This is formed in the possible surface reaction (12):



O<sub>3</sub> behaves as a Lewis base and it can be adsorbed on weak Lewis acid sites decomposing to form oxygen radicals onto Lewis sites. The interaction of O<sub>3</sub> with these sites is a consequence of its resonance structure, in which the great density of e<sup>-</sup> at one of the oxygen atoms acts as strong base, with a great affinity for acid surface sites. These are essentials in the interaction between O<sub>3</sub> and the oxide. Signals 1020 and 994 cm<sup>-1</sup> are presumably generated by peroxide formation during ozone adsorption and decomposition, and their intensity increases by enhancing the O<sub>3</sub> concentration. Moreover, the signal at 1022 cm<sup>-1</sup> with a shoulder at 1054 cm<sup>-1</sup> is probably due to physisorbed O<sub>3</sub> still present at 150°C.

The region between 1282 and 1862 cm<sup>-1</sup> is full of bands due to carbonate-like species generated via reactions of ozone with remaining carbonaceous impurities. Finally, also 2363-2332 cm<sup>-1</sup> large bands are probably generated by CO adsorption.

From this investigation, it appears difficult to extract any additional information after the interaction of W-In<sub>2</sub>O<sub>3</sub> with O<sub>3</sub>, and generally broader peaks were found compared to the undoped indium oxide. For the W-In<sub>2</sub>O<sub>3</sub>, the variation in the resistance values is huge (6 orders of magnitude) under 1.5 ppm of O<sub>3</sub> and even higher compared to the undoped In<sub>2</sub>O<sub>3</sub>, but the fitting of extremely broad peaks could be arbitrary.

## 5.6 Conclusions

In this chapter, the properties of indium oxide-based sensors were investigated. In<sub>2</sub>O<sub>3</sub> was successfully synthesized by hydrothermal route and tungsten-doped indium oxide was realized by impregnation method.  $\tau_{\text{ads}}$  and  $\tau_{\text{des}}$  of the sensor were around 1-5 minutes both for the doped and undoped indium oxides. The gas sensing features towards O<sub>3</sub> of In<sub>2</sub>O<sub>3</sub> NPs synthesized by hydrothermal route using CTAB as capping agent with lower dimensions of crystallites and agglomerates as well as an increased SSA was achieved comparing with the commercial In<sub>2</sub>O<sub>3</sub> in terms of best working temperature, rate of sensor response and selectivity towards O<sub>3</sub>. Furthermore, impregnation with WO<sub>3</sub> at 2.5 wt% results in a partial solid solution generation and WO<sub>3</sub> is present also on the surface improving the decomposition of O<sub>3</sub> by spillover effect ameliorating the selectivity and the sensitivity for ozone detection. In addition, sensors with different thicknesses between 10 and 100  $\mu\text{m}$  were manufactured by screen printing deposition. In this study, an increase in the sensor response of 3 orders of magnitude upon 1000 ppb of O<sub>3</sub> was achieved by decreasing of 1 order of magnitude the film thickness. The maximum sensor response and the higher selectivity with respect to O<sub>3</sub> was measured at 150°C, at relatively low temperature in metal oxide-based sensors. By means of DRIFT

*operando* measurements under nitrogen dioxide and ozone at the optimum operating temperature we have analyzed some of the surface species responsible for NO<sub>2</sub> and O<sub>3</sub> detection. It has been described that the sensing mechanism is rather complex, involving OH groups and adsorbed H<sub>2</sub>O in the mechanism of adsorption of nitrites during NO<sub>2</sub> exposure and carbonate-like species generated through reactions with ozone. Further investigations in *operando* DRIFT at different temperatures under O<sub>3</sub> will elucidate the temperature-dependent species that are formed on In<sub>2</sub>O<sub>3</sub> surface.

## References

- [1] Lee J.-H. (2009) Review Gas sensors using hierarchical and hollow oxide nanostructures: Overview, *Sens. Actuators B*. Pages 319-336.
- [2] Korotcenkov G., Brinzari V., Cho B. K. (2017) In<sub>2</sub>O<sub>3</sub>- and SnO<sub>2</sub>-based ozone sensors: design and characterization. *Crit. Rev. Solid State*. Pages 83-132.
- [3] <http://news.mit.edu/2006/spintronics-0524>, visited 17<sup>th</sup> January 2019.
- [4] Marezio M. (1966) Refinement of the crystal structure of In<sub>2</sub>O<sub>3</sub> at two wavelengths. *Acta Cryst.* Pages 723-728.

- [5] Makise K., Kokubo N., Takada S., Yamaguti T., Ogura S., Yamada K., Shinozaki B., Yano K., Inoue K., Nakamura H. (2008) Superconductivity in transparent zinc-doped  $\text{In}_2\text{O}_3$  films having low carrier density. *Sci. Technol. Adv. Mater.* ID 044208 (6 pages).
- [6] Korotcenkov G. Handbook of gas sensor materials, 1–2. Springer, New York, 2013.
- [7] Korotcenkov G., Brinzari V., Cho B.K. (2016)  $\text{In}_2\text{O}_3$  and  $\text{SnO}_2$ -based thin film ozone sensors. Fundamentals, *J. Sensors*. 3816094
- [8] Gurlo A., Barsan N., Weimar U., Ivanovskaya M., Taurino A., Siciliano P. (2003) Polycrystalline well-shaped blocks of indium oxide obtained by the sol-gel method and their gas-sensing properties. *Chem. Mater.* Pages 4377–4383.
- [9] Epifani M., Comini E., Arbiol J., Diaz R., Sergent N., Pagnier T., Siciliano P., Faglia G., Morante J. R. (2008) Chemical synthesis of  $\text{In}_2\text{O}_3$  nanocrystals and their application in highly performing ozone-sensing devices, *Sens. Actuat. B.* Pages 483–487.
- [10] Weisz P. (1953) Effects of electronic charge transfer between absorbate and solid on chemisorption and catalysis, *J. Chem. Phys.* Pages 1531–1538
- [11] Morrison S. R. (1987) Selectivity in semiconductor gas sensors. *Sens. Actuat. B.* Pages 425–440.
- [12] Sauter D., Weimar U., Noetzel G., Mitrovics J., Gopel W. (2000) Development of modular ozone sensor system for application in practical use, *Sens. Actuat. B.* Pages 1–9.
- [13] Gurlo A., Barsan N., Ivanovskaya M., Weimar U., Gopel W. (1998)  $\text{In}_2\text{O}_3$  and  $\text{MoO}_3$ - $\text{In}_2\text{O}_3$  thin film semiconductor sensors: interaction with  $\text{NO}_2$  and  $\text{O}_3$ . *Sens. Actuat. B.* Pages 92–99.
- [14] Hosoya Y., Itagaki Y., Aono H., Sadaoka Y. (2005) Ozone detection in air using  $\text{SmFeO}_3$  gas sensor. *Sens. Actuat. B.* Pages 198–201.
- [15] Losch M., Baumbach M., Schutze A. (2008) Ozone detection in the ppb-range with improved stability and reduced cross sensitivity. *Sens. Actuat. B.* Pages 367–373.
- [16] Korotcenkov G., Brinzari V., Cho B. K. (2017) Interference effects between hydrogen and ozone in the response of  $\text{SnO}_2$ -based gas sensors, *Sens. Actuat. B.* Pages 507–515.
- [17] Abideen Z. U., Kim J.-H, Kim S. S. (2017) Optimization of metal nanoparticle amount on  $\text{SnO}_2$  nanowires to achieve superior gas sensing properties, *Sens. Actuat. B.* Pages 374–380.
- [18] Marikutsa A., Rummyantseva M., Gaskov A. (2015) Selectivity of catalytically modified tin dioxide to CO and  $\text{NH}_3$  gas mixtures, *Chemosens.* Pages 241–252.

- [19] Belysheva T. V., Bogovtseva L. P., Gutman E. E. (2004) Application of metal oxide semiconducting heterosystems for gas analysis. *Int. Sci. J. Altern. Energy Ecol.* Pages 60–66.
- [20] Kim S.-R., Hong H.-K., Kwon C. H., Yun D. H., Lee K., Sung Y. K. (2000) Ozone sensing properties of  $\text{In}_2\text{O}_3$ -based semiconductor thick films. *Sens. Actuat. B.* Pages 59-62.
- [21] Sahn T., Gurlo A., Barsan N., Weimar U. (2006) Properties of indium oxide semiconducting sensors deposited by different techniques. *Partic. Sci. Technol.* Pages 441–452.
- [22] Korotcenkov G., Brinzari V., Ivanov M., Cerneavski A., Rodriguez J., Cirera A., Cornet A., Morante J. (2005) Structural stability of indium oxide films deposited by spray pyrolysis during thermal annealing. *Thin Solid Films.* Pages 38–51.
- [23] Samsonov G. V. (1973) *The Oxide Handbook*. IFI/Plenum, New York.
- [24] Korotcenkov G., Brinzari V., Stetter J. R., Blinov I., Blaja V. (2007) The nature of processes controlling the kinetics of indium oxide-based thin film gas sensor response, *Sens. Actuat. B.* Pages 51–63.
- [25] Kim S.-R., Hong H.-K., Kwon C. H., Yun D. H., Lee K., Sung Y. K. (2000) Ozone sensing properties of  $\text{In}_2\text{O}_3$ -based semiconductor thick films *Sens. Actuat. B.* Pages 59–62.
- [26] Papakonstantinou G. D., Jaksic J. M., Labou D., Siokou A., Jaksic M. M. (2011) Spillover phenomena and its striking impacts in electrocatalysis for hydrogen and oxygen electrode reactions, *Adv. Phys. Chem.* ID 412165 (22 pages).
- [27] Conner W. C., Falconer Jr. and J. L. (1995) Spillover in heterogeneous catalysis, *Chem. Rev.* Pages 759–788.
- [28] Korotcenkov G., Gulina L. B., Cho B. K., Brinzari V., Tolstoy V. P. (2014) Au nanoclusters on the surface of  $\text{SnO}_2$  and  $\text{In}_2\text{O}_3$  films: Synthesis by SILD method and characterization, *Pure Appl. Chem.* Pages 801–817.
- [29] Korotcenkov G., Brinzari V., Han S. H., Cho B. K. (2016) Gas sensing properties of  $\text{In}_2\text{O}_3$  films modified with gold nanoparticles, *Mater. Chem. Phys.* Pages 188–199.
- [30] Manjula P., Arunkumar S., Manorama S. V. (2011) Au/ $\text{SnO}_2$  an excellent material for room temperature carbon monoxide sensing, *Sens. Actuat. B.* Pages 168-175.
- [31] Miller J. T., Kropf J., Zha Y., Regalbuto J. R., Delannoy L., Louis C., Bus E., van Bokhoven J. A. (2006) The effect of gold particle size on Au-Au bond length and reactivity toward oxygen in supported catalysts, *J. Catal.* Pages 222-234.
- [32] Puckett S. D., Heuser J. A., Keith J. D., Spindel W. U., Pacey G. E. (2005) Interaction of ozone with gold nanoparticles, *Talanta.* Pages 1242-1246.



- [33] Venkov Tz, Fajerweg K., Delannoy L., Klimev Hr, Hadjiivanov K., Louis C. (2006) Effect of the activation temperature on the state of gold supported on titania: an FT-IR spectroscopic study, *Appl. Catal. A-Gen.* Pages 106-114.
- [34] Kim J., Samano E., Koel D. E. (2006) Oxygen adsorption and oxidation reactions on Au (211) surfaces: exposures using O<sub>2</sub> at high pressures and ozone (O<sub>3</sub>) in UHV, *Surf. Sci.* Pages 4622-4632.
- [35] Korotcenkov G., Cho B. K. (2017) Metal oxide composites in conductometric gas sensors: Achievements and challenges. *Sens. Actuat. B.* Pages 182–210.
- [36] Krivetskiy V., Rummyantseva M., Gaskov A. (2013). Design, synthesis and application of metal oxide-based sensing elements: A chemical principles approach. In M. A. Carpenter, S. Mathur, and A. Kolmakov (eds.), *Metal Oxide Nanomaterials for Chemical Sensors*, Springer Science+Business Media, New York. Pages 69–118.
- [37] Lee, I.-S. Han K.-S., Seo D.-W., Woo S.-K. (2003) Improvement of strength in porous ceramics by control of additives, *Mater. Sci. Forum.* Pages 68–73.
- [38] Sberveglieri G., Benussi P., Coccoli G., Gropelli S., Nelli P. (1990) Reactivity sputtered indium tin oxide polycrystalline thin films as NO and NO<sub>2</sub> gas sensors, *Thin Solid Films.* Pages 349–360.
- [39] Liu L., Guo C., Li L., Wang L., Dong Q., Li W. (2010) Improved H<sub>2</sub> sensing properties of Co-doped SnO<sub>2</sub> nanofibers, *Sens. Actuat. B.* Pages 806–810.
- [40] Rao M. C. (2013) Structure and properties of WO<sub>3</sub> thin film for electrochromic device application. *Journal of Non-Oxide Glasses.* Pages 1 – 8.
- [41] Tungsten trioxide. (2006) The Merck Index 14.
- [42] Wang G., Ji Y., Huang X., Yang X., Gouma P. I., Dudley M. (2006) Fabrication and characterization of polycrystalline WO<sub>3</sub> nanofibers and their application for ammonia sensing, *J. Phys. Chem. B.* Pages 23777–23782.
- [43] Choi K.-I., Hwang S.-J., Dai Z., Chan Kang Y., Lee J.-H. (2014) Rh-catalyzed WO<sub>3</sub> with anomalous humidity dependence of gas sensing characteristics, *RSC Adv.* Pages 53130–53136.
- [44] Rout C. S., Hegde M., Rao C. N. R. (2008) H<sub>2</sub>S sensors based on tungsten oxide nanostructures, *Sens. Actuat. B* Pages 488–493.
- [45] Khadayate R. S., Sali J. V., Patil P. P. (2007) Acetone vapor sensing properties of screenprinted WO<sub>3</sub> thick films, *Talanta.* Pages 1077–1081.
- [46] Oison V., Saadi L., Lambert-Mauriat C., Hayn R. (2011) Mechanism of CO and O<sub>3</sub> sensing on WO<sub>3</sub> surfaces: First principle study. *Sens. Actuat. B.* Pages 505–510.
- [47] Akamatsu T., Itoh T., Izu N., Shin W. (2013) NO and NO<sub>2</sub> Sensing Properties of WO<sub>3</sub> and Co<sub>3</sub>O<sub>4</sub> Based Gas Sensors. *Sensors* Pages 12467-12481.

- [48] Staerz A., Berthold C., Russa T., Wicker S., Weimar U., Barsan N. (2016) The oxidizing effect of humidity on WO<sub>3</sub> based sensors. *Sens. Actuat. B.* Pages 54–58.
- [49] Weckhuysen B. M., Jehng J. M., Wachs I. E. (2000) In situ raman spectroscopy of supported transition metal oxide catalysts: <sup>18</sup>O<sub>2</sub>–<sup>16</sup>O<sub>2</sub> isotopic labeling studies. *J. Phys. Chem. B.* Pages 7382–7387.
- [50] Shinde D. V., Ahn D. Y., Jadhav V. V., Lee D. Y., Shrestha N. K., Lee J. K., Lee H. Y., Maneb R. S., Han S. H. (2014) A coordination chemistry approach for shape-controlled synthesis of indium oxide nanostructures and their photoelectrochemical properties. *J of Mater Chem A.* Pages 5490.
- [51] Korotcenkov G., Brinzari V., Cerneavski A. (2004) The influence of film structure on In<sub>2</sub>O<sub>3</sub> gas response. *Thin Solid Films.* Pages 315–323.
- [52] Yan T., Wang X., Long J., Liu P., Fu X., Zhang G., Fu X. (2008) Urea-based hydrothermal growth, optical and photocatalytic properties of single-crystalline In(OH)<sub>3</sub> nanocubes. *J Colloid and Interf Sci.* Pages 425–431.
- [53] Ziegler D., Marchisio A., Palmero P., Tulliani J.-M. (2017) WO<sub>3</sub>-doped indium oxide thick films for ozone detection at low temperature. *Proceedings.* Pages 428-432.
- [54] Cao J.-L., Yan Z.-L., Wang Y., Sun G., Wang X.-D., Bala H., Zhang Z.-Y. (2013) CTAB-assisted synthesis of mesoporous CoFe<sub>2</sub>O<sub>4</sub> with high carbon monoxide oxidation activity, *Materials Letters.* Pages 322–325.
- [55] Ho W. H., Yen S. K. (2006) Preparation and characterization of indium oxide film by electrochemical deposition, *Thin Solid Films.* Pages 80-84.
- [56] Bagheri-Mohagheghi M. M., Shahtahmasebi N., Mozafari E., Shokooch-Saremi M. (2009) Effect of the synthesis route on the structural properties and shape of the indium oxide (In<sub>2</sub>O<sub>3</sub>) nano-particles, *Physica E Low Dimens Syst Nanostruct.* Pages 1757-1762.
- [57] <http://abulafia.mt.ic.ac.uk/shannon/radius>, visited on 19<sup>th</sup> January 2019.
- [58] <https://xpssimplified.com/elements/indium.php>, visited on 19<sup>th</sup> January 2019.
- [59] Zhang Y. D., Jiang G. C., Wong K. W., Zhen Z. (2010) Green synthesis of indium oxide hollow spheres with specific sensing activities for flammable organic vapors, *Sensor Letters.* Pages 355–361.
- [60] Zhang T., Gu F., Han D., Wang Z., Guo G. (2013) Synthesis, characterization and alcohol-sensing properties of rare earth doped In<sub>2</sub>O<sub>3</sub> hollow spheres, *Sens Actuat B.* Pages 1180– 1188.
- [61] <https://xpssimplified.com/elements/tungsten.php>, visited on 19<sup>th</sup> January 2019.
- [62] Wang Ch. Y., Cimalla V., Roehlig C.-C. (2006) A new type of highly sensitive portable ozone sensor operating at room temperature, in Proceedings of the 5th IEEE Conference on Sensors, 81–84, EXCO, Daegu, South Korea.

- [63] Loopstra B. O., Rietveld H. M. (1969) Further refinement of the structure of  $\text{WO}_3$ . *Acta Cryst.* Pages 1420-1421.
- [64] Ivanovskaya M., Gurlo A., Bogdanov P. (2001) Mechanism of  $\text{O}_3$  and  $\text{NO}_2$  detection and selectivity of  $\text{In}_2\text{O}_3$  sensors, *Sens. Actuat. B.* Pages 264–267.
- [65] Starke T. K. H., Coles G. S. V. (2002) High sensitivity ozone sensors for environmental monitoring produced using laser ablated nanocrystalline metal oxides, *IEEE Sensors Journal.* Pages 14–19.
- [66] Oprea A., Gurlo A., Bârsan N., Weimar U. (2009) Transport and gas sensing properties of  $\text{In}_2\text{O}_3$  nanocrystalline thick films: a Hall effect based approach, *Sens. Actuat. B.* Pages 322–328.
- [67] Zhang Y. D., Zheng Z., Yang F. L. (2010) Highly sensitive and selective alcohol sensors based on Ag-doped  $\text{In}_2\text{O}_3$  coating, *Ind. Eng. Chem. Res.* Pages 3539–3543.
- [68] Neri G., Bonavita A., Micali G., Rizzo G., Pinna N., Niederberger M. (2007)  $\text{In}_2\text{O}_3$  and Pt- $\text{In}_2\text{O}_3$  nanopowders for low temperature oxygen sensors. *Sens. Actuat. B.* Pages 455–462.
- [69] Vishwanath S. K., An T., Jin W., Kang J., Kim J. (2017) The optoelectronic properties of tungsten-doped indium oxide thin films prepared by polymer-assisted solution processing for use in organic solar cells. *J. Mater. Chem. C.* Pages 10295-10301.
- [70] Yamazoe J. (2005) Toward innovations of gas sensor technology *Sens. Actuat. B.* Pages 2–14.
- [71] Roso S., Degler D., Llobet E., Barsan N., Urakawa A. (2017) Temperature-dependent  $\text{NO}_2$  sensing mechanisms over indium oxide, *ACS Sens.* Pages 1272–1277.
- [72] Wu J., Su T., Jiang Y., Xie X., Qin Z., Ji H. (2017) In situ DRIFT study of  $\text{O}_3$  adsorption on  $\gamma\text{-CaO}$ ,  $\text{CuO}$ ,  $\alpha\text{-Fe}_2\text{O}_3$  and  $\text{ZnO}$  at room temperature for the catalytic ozonation of cinnamaldehyde, *Appl. Surf. Sci.* Pages 290-305.

# Appendix A

## Abbreviations

SA- In <sub>2</sub> O <sub>3</sub>	SA-W- In <sub>2</sub> O <sub>3</sub>	HT-In <sub>2</sub> O <sub>3</sub>	HT-W- In <sub>2</sub> O <sub>3</sub>
Indium oxide Sigma Aldrich	Indium oxide Sigma Aldrich doped with 2.5 wt.% of WO <sub>3</sub>	Indium oxide hydrothermally synthetized	Indium oxide hydrothermally synthetized doped with 2.5 wt.% of WO <sub>3</sub>

# List of Tables

**Table 1.** SSA and conductivity of OSR700 and SWP 700 biochars.

**Table 2.** Cumulative particle size distribution  $d_{10}$ ,  $d_{50}$  and  $d_{90}$  for the OSR700 and SWP 700 biochars.

**Table 3.** Mass% of elements from XPS analysis.

**Table 4.** Highest values of sensor responses for OSR700, SWP700, PVP, SWP10PVP and SWP20PVP films towards RH.

**Table 5.** Decomposition of peaks in Raman spectrum of CGB powder.

**Table 6.** State of the art of humidity sensors based on carbon-based materials.

# List of Figures

- Figure 1.** RH measurement system used in dynamic test.
- Figure 2.** Image 0.85x1.7 cm of biochar sensor made of SWP700 material.
- Figure 3.** Laser granulometry analysis of OSR700 (a) and SWP700 (b).
- Figure 4.** XRD patterns of SWP700 (red) and OSR700 (black) powders.
- Figure 5.** Raman spectra for OSR700 (a) and SWP700 (b).
- Figure 6.** XPS Survey spectra for OSR700 (a) and SWP700 (b), HR XPS spectra of C1s peaks for (c) OSR700, (d) SWP700.
- Figure 7.** FESEM micrographs of OSR 700 film (a, 2.5k $\times$ ; b, 10k $\times$ ) and SWP700 film (c, 2.5k $\times$ ; d, 10k $\times$ ).
- Figure 8.** FESEM micrographs of SWP700-PVP10% film (a, 2.5k $\times$ ; b, 10k $\times$ ) and SWP700-PVP20% (c, 2.5k $\times$ ; d, 10k $\times$ ).
- Figure 9.** SR% under different RH% for (a) OSR700; (b) SWP700.
- Figure 9.** Sensor response towards relative humidity of (a) OSR700; (b) SWP700 biochars.
- Figure 10.** PVP film impedance's variation towards RH.
- Figure 11.** SWP10PVP and SWP20PVP sensor responses towards RH.
- Figure 12.** SR% of SWP10PVP sensor toward O<sub>3</sub> 0.5 ppm, NH<sub>3</sub> 50 ppm, CH<sub>4</sub> 100 ppm and CO<sub>2</sub> 500 ppm.
- Figure 13.** Conversion process of coffee firstly in WBCP and then in CGB.
- Figure 14.** Particle size distribution of CGB powder.
- Figure 15.** TGA of WBCP under argon.
- Figure 16.** TG (black)-DTA (blue) curves of CGB in static air.
- Figure 17.** XRD pattern of CGB powder.
- Figure 18.** Raman analysis of CGB powder.
- Figure 19.** XPS investigations for CGB powder (a) survey, (b) HR C1s and (c) HR O1s.
- Figure 20.** FESEM images of the CGB powder at: (a) 150  $\times$ , (b) 1 k  $\times$ , (c) 2.5 k  $\times$  and (d) 15 k  $\times$  magnification.
- Figure 21.** A CGB sensor.
- Figure 22.** Changes in impedance (a) and sensor responses at different RH% (b) for CGB film during adsorption and desorption cycles.
- Figure 23.** Cross sensitivity test of CGB sensor towards CO<sub>2</sub> 500 ppm, O<sub>3</sub> 200 ppb, NO<sub>2</sub> ppb and NH<sub>3</sub> 50 ppm.

# Chapter 6 - Humidity sensors

## Abstract

Humidity is a common component in the environment, and the accurate and reliable measurement of its amount is fundamental for several industries and technologies and in environmental monitoring [1, 2].

For instance, a lot of domestic applications requires humidity sensors in the smart control of the buildings and laundry environments, and in the control of microwave ovens. Concerning the car industry, sensors able to detect humidity are utilized in motor assembly lines and in rear-window defoggers. In agriculture, humidity sensors are adopted in air conditioning, protection of vegetation, cereal storage and in control of soil moistures. Thus, in medicine, humidity sensors are employed in several machines like those for respiratory monitoring incubators, sterilizers and pharmaceutical processing. In addition, humidity sensors are applied for monitoring of chemical gas purification, ovens, dryers, textile and paper production as well as processing of food.

A wide range of humidity sensors with several sensing materials have been developed so far.

Since water is an essential component of all living organisms on Earth, as well as for the major part of the materials utilized by people, it can influence substantially the chemical-physical, mechanical and technological features of either biogenic and antropogenic materials [3].

## 6.1 Humidity detection

### 6.1.1 Some definition about humidity

The word '*moisture*' is related to the content of H<sub>2</sub>O in a solid or in a liquid, that is removable without alteration of its chemical characteristics, whereas '*humidity*' is referred to the concentration of water vapor present in gases. The amount of humidity (absolute or relative) is measured by hygrometer, an instrument invented by Sir John Leslie [4] that is sensitive to water molecules.

Absolute humidity is determined as the density of water vapor content in a unit volume or the mass of water vapor ( $m$ ) in a unit volume of wet gas ( $V$ ) (eq 1):

$$dw := \frac{m}{V} \quad (1)$$

The mixing or humidity ratio  $r$  is the mass of water vapor in a unit mass of dry gas. Relative humidity (RH) is the ratio between the current water vapor pressure ( $P_W$ ) and the saturated vapor pressure ( $P_S$ ) (eq. 2):

$$RH := 100 * \frac{P_W}{P_S} \quad (2)$$

RH is similarly determined as the ratio between the actual absolute humidity and the highest possible absolute humidity at a certain temperature; RH reveals the vapor amount as % of the concentration requested to generate the saturated water vapor.

A different method to define RH is as the ratio between the current mole fraction of water vapor and that of water vapor in condition of saturation. The value of  $P_W$  and the partial pressure of dry air  $P_a$  correspond to the pressure in the area or equal to the  $P_{atm}$  (atmospheric pressure), in the case the area is exposed to the atmosphere (eq. 3):

$$P_{atm} = P_W + P_a \quad (3)$$

at temperatures over the boiling point, water pressure could remove all different gases in the area. The atmosphere is completely consisting of super-heated steam. Here,  $P_{atm} = P_W$ . If  $T > 100^\circ\text{C}$ , RH is a fallacious indicator of moisture amount since in this condition  $P_s$  is higher than  $P_{atm}$ , and RH cannot achieve 100%. For this reason, at pressure of 1 atmosphere and  $T$  of  $100^\circ\text{C}$ , the highest RH value is equal to 100%, whereas at  $200^\circ\text{C}$ , this value drops to 6% [5].

The dew point (DP) temperature is the  $T$  where the water vapor's partial pressure is maximum (i.e. it is saturated), compared to to an equilibrium with a flat ice surface. DP is the temperature where RH is equal to 100%. Alternatively, the DP corresponds to temperature that the air must attain to retain the highest quantity of moisture achievable. In the case the  $T$  coincides to the DP, the air is saturated, and frost or fog can be formed. The equations (4, 5 and 6) permits to extract DP from RH and  $T$ :

$$EW = 10^{\left(\frac{0.66077+7.5T}{237+T}\right)} \quad (4)$$

$$DP = \frac{[273.3(0.66077-\log EW_{RH})]}{\log EW_{RH}-8.16077} \quad (5)$$



$$EW_{RH} = \frac{(EW)*(RH)}{100} \quad (6)$$

Where  $EW$  is the saturation vapor pressure over  $H_2O$ , DP corresponds to the dew-point temperature and all temperatures are expressed in Celsius degrees.

The relative humidity is inversely proportional to the temperature. The DP is generally measured by means of a chilled mirror.

The frost point is the T where the vapor condenses at temperatures lower than  $0^\circ C$ .

Finally, a part per million ( $ppm$ ) is the water vapor amount by volume fraction ( $ppmv$ ). By multiplying it with the ratio between the molecular weight of  $H_2O$  and that of air, it is represented as  $ppmw$  [4, 6].

### 6.1.2 Methods to measure humidity

Humidity can be measured by several methods. Some consist in the detection of the partial pressure of vapor in the gas (e.g., RH). Measurements of dry and wet bulb T include the utilization of the psychrometric chart (e.g. air conditioning). Thus, different approaches are based on the effect of humidity on the physical features and behavior of several compounds.

Methods involve the measurement of the dew point, wet and dry bulb temperatures, chemical and physical adsorption methods, hair hygrometer, thermal conductivity meters, electrical conductivity measurements and others [7].

In the *measurement of the dew point*, a mirror or other polished surfaces are cooled gradually. Here, the temperature of the water condensation can be defined. Since at the temperature of dew point the partial pressure of  $H_2O$  in the gas is equal to that of saturated gas at the same T, from the saturation curve on the psychrometric chart is possible to acquire the requested value of humidity.

The accuracy of the formation of dew point determines the reliability of the measurement. This may be accomplished utilizing a photo-resistive optical-sensing bridge. Here, the amount of humidity is extremely low without condensation till the T of the surface is lower than  $0^\circ C$ , the moisture is deposited as a frost; this is detectable by techniques such as  $\alpha$  particles attenuation. For achieving a great command of the cooling of the mirror, a thermoelectric module where heat is relocated distant from the polished surface by Peltier mechanism can be used. In order to reduce the surface temperature, this can be kept around  $0^\circ C$ . The gas is compressed till the partial pressure of the water vapor achieves the saturation when moisture begins to be deposited onto the surface.

In the *measurements of wet and dry bulb temperatures*, a gas stream flows quickly over a small wet surface with no variation in the air characteristics,

establishing a dynamic equilibrium with the heat conveyed from the air equipped by the heat needed for vaporizing H<sub>2</sub>O at the surface. If the air flow rate is high enough, the predominant mechanism for the heat transfer is the convection. In this case, the ratio of the heat and mass transfer coefficients is fixed and the T where the surface drops will be the *wet bulb temperature*. For the air-water arrangement, the *psychrometric ratio* is about equal to 1 and the wet bulb T is the adiabatic saturation T. Therefore, the compositions of every air-water vapor mixtures are represented by the adiabatic-cooling lines on the psychrometric chart.

Air-water vapor mixtures have the identical wet bulb and adiabatic saturation temperatures. So, if the adiabatic cooling line that corresponds to the measured wet bulb T is chosen, the point in this line that correspond to the dry bulb T furnishes the humidity value of the investigated gas.

A wet and dry bulb hygrometer is constituted by two thermometers, the first equipped with a dry bulb and the second equipped with a wet bulb coated with a porous tissue saturated with H<sub>2</sub>O. Air is pulled quickly ( $> 5 \text{ ms}^{-1}$ ) longer the thermometer bulbs and the two temperatures are measured when the temperature of the wet bulbs achieves the equilibrium.

In the case of *chemical/physical adsorption methods*, a measured volume of gas passes through an appropriate absorbent whose increase in weight increase is monitored. The methodology is quite laborious but effective. Absorbents used for water vapor are P<sub>2</sub>O<sub>5</sub> dispersed on pumice and concentrated H<sub>2</sub>SO<sub>4</sub>.

In the *air hygrometers*, variations in shape and physical dimensions in accordance with the content of moisture that the sensitive material have absorbed. The materials used are cellulose-based like wool, hair and cotton, that are hygroscopic.

The length of these materials is influenced by the humidity amount in the environment and this property is exploitable in instruments with direct readings. It is mandatory to calibrate those instruments at frequent intervals due to the drifting, especially if the instrument is utilized over a broad interval of humidity amounts.

In *thermal conductivity meters*, of the degree of heat loss from a heated wire is dependent on the thermal conductivity of the gas, that depends on its moisture composition. A thermistor or a hot wire element is utilized to accomplish the double function of temperature sensor and heat source. So, for a steady applied tension, the T and the resistance of the element are functions of the level of humidity of the gas in contact.

In *electrical conductivity measurements*, the resistance of hygroscopic materials thin layers depends on the moisture content and on the temperature. Those parameters are functions of the content of humidity in atmosphere. An example is

the LiCl cell, constituted of fine fibers with a plastic frame conveying two electrodes attached to the fibers. The current with a steady applied tension through the electrodes results in a resistance measurement. The instrument is calibrated to provide immediate control of humidity amounts. A different option of system consists in a sensor as hydroxyethyl-cellulose film in a carbon particles matrix with high conductivity that swell in dependence of the moisture content in the surrounding environment. The resistance depends on the rate of compression of the matrix and the device can be calibrated to furnish immediate readings of humidity contents.

A wide range of other methods is available and each one is characterized by a diverse application. The pillars of operation are the following:

- selective absorption of IR radiation
- measurement of absorption heat onto a surface
- electrolytic hygrometry in which a measurement of the electricity needed to electrolyze H<sub>2</sub>O that is adsorbed from the environment onto a thin layer of dryer is realized
- piezoelectric hygrometry using a quartz crystal equipped with a hygroscopic layer where moisture is adsorbed from a wet gas and it is desorbed in a dry gas flow, alternatively
- capacitance meters where the electrical capacitance depends on the deposition rate of moisture from the environment
- alterations in color in active substances (e.g. in cobaltous chloride).

In the next session, different humidity chemical sensors will be described more in detail, with a special focus on chemoresistive ones based on ceramic and carbon materials.

### 6.1.3 Chemical humidity sensors

Chemical sensors are analytical devices able to fulfill on-line and real-time informations regarding the presence and concentration of specific compounds in complex matrixes [8].

These devices can additionally furnish a recommendable variant to the analytical method of the lab [9], and moisture and humidity detectors can be applied in several areas of human activity. For this reason, the design and manufacture of chemical sensors is now one of the most productive research areas [6,10].

The major part of chemical sensors for water molecules detection detects water vapor. They are the so-called *humidity sensors*. Those are designed for the determination of water amount in the air [11].

Some humidity sensors can sense water vapor under saturated vapor situations in air [12] and under controlled vapor conditions without air [13].

As previously described, the most used strategy to refer the level of water vapor in the air is to consider the ratio between the actual water vapor pressure and that at saturation at a certain T, by measuring the relative humidity (RH).

Humidity sensors can find many applications such as human breathing monitoring [14] or for humidity measurement in the exhaust gas of industrial textile dryers [15] and in a combustion process in surplus of air [16].

Different humidity sensors could find other applications, including the detection of water leakages, mapping on roofs and humidity measurements in situ on airplanes [17], measurement of water activity in foods [18] and humidity control in electronic devices [19].

In some cases, humidity sensors can measure trace of humidity [20, 21] or detect at elevated temperatures [22, 23].

The conditions for valid humidity sensors for real applications are great sensitivity in a broad interval of H<sub>2</sub>O amount and temperatures, quick cinetic of adsorption and desorption, large reproducibility, modest hysteresis and dependence on the temperature, low manufacturing and maiteinance cost, strenght to pollutants, a linear response, simplicity of manufacture and enduring in time [3]. Nowadays, two ways are possible to fabricate a superior humidity sensing element: the improvement in the features of a known material and the creation of a novel material [24].

A high level of either selectivity and sensitivity are guaranteed by high and specific chemical interaction between the sensitive element and the target gas whereas a proper reversibility and quick adsorption and desorption are advantaged by weak physical-chemical phenomena [25].

Since up to now there have been not a perfect sensing material able to satisfy all those requirements [26], the exploration of innovative humidity sensing elements with great performances is an indispensable need for researchers [27].

Recently, a wide range of materials including ceramics, carbonaceous materials, electrolytes, organic polymers and composite materials have been exploitedas water vapor sensitive elements [27,28].

In this chapter, three innovative carbonaceous materials have been proposed as sensitive and selective elements for humidity detection at room temperature.

#### 6.1.4 Carbon-based humidity sensors

In high-performance sensors, the sensitive elements are the essential components. For this, carbon films have intrigued recently large interest for their potential use as humidity sensors since they possess an extensive sensing area and great chemical inertness [29, 30].

For their fruitful surface chemistry and the several ways to design their structure, carbon materials are very desirable as humidity sensors. Furthermore, carbon nanomaterials, like graphene, carbon nanotubes (CNTs), carbon nanofibers and carbon black, are the principle active elements utilized for the manufacture of high-performance humidity sensors. Peculiarly, graphene and CNTs are assemblable into 1D fibers, 2D films and 3D architectures, permitting an easy sensor's design for several usages.

Thus, they work at room temperature (RT) and are functionalizable for chemical specificity. Furthermore, they have a modest thermal mass favoring quick heating with low power consumption [31]. However, carbon materials have modest selectivity and reproducibility, the propensity to poisoning and a long-term drift in some cases [31].

In addition, cheap carbon materials, like carbon nanofibers and carbon black are exploitable as sensitive elements integrated with tissues. Alongside carbon nanomaterials, different carbon powders proceeded from bio-materials by pyrolysis process have been presented as sensitive materials too, for instance silk [32] and cotton fibers [32].

Biomass is also an adequate carbon source, accessible in high content, and retained an environmental-friendly renewable resource [34]. Moreover, after pyrolysis process biochars is obtained, which are getting disposable from pilot plants generating energy and biogas [35, 36]. Recently, biochars have found applications in several areas [37] even if the principal usage is still as field amendment in agriculture [38]. Alongside, in recent years, biochars have been widely investigated as alternative for carbon materials with higher costs such as graphene, carbon nanotubes and others [39].

In this chapter, the gas sensing properties of three different biochars (two p-type and one n-type semiconductors) will be described with a deep understanding on the properties of the materials that are responsible for their sensitivity towards humidity.

## 6.2 Humidity sensors measurements

The realized sensors were placed in a laboratory apparatus depicted in Figure 1, realized with a hermetic chamber where RH levels can be adjusted between 0 and 100% by 12 steps of 3 minutes both in adsorption and in desorption to investigate the presence of a possible hysteresis between the processes. Test towards water vapor were realized under a steady flow of 1000 SCCM. In this home-made system, compressed air flow (1) is split in two streams: the first is desiccated above a  $\text{Al}_2\text{O}_3$  bed (2), the other goes through two  $\text{H}_2\text{O}$  bubblers (3), resulting respectively in a dry and a humid stream. These fluxes are recombined by means of two precision microvalves (4) in a unique flow with a mixer (5). A commercial probe for humidity and temperature measurements (9), Delta Ohm DO9406 (Caselle di Selvazzano (PD), Italy) was adopted for T and RH measurements as reference in the measuring chamber.

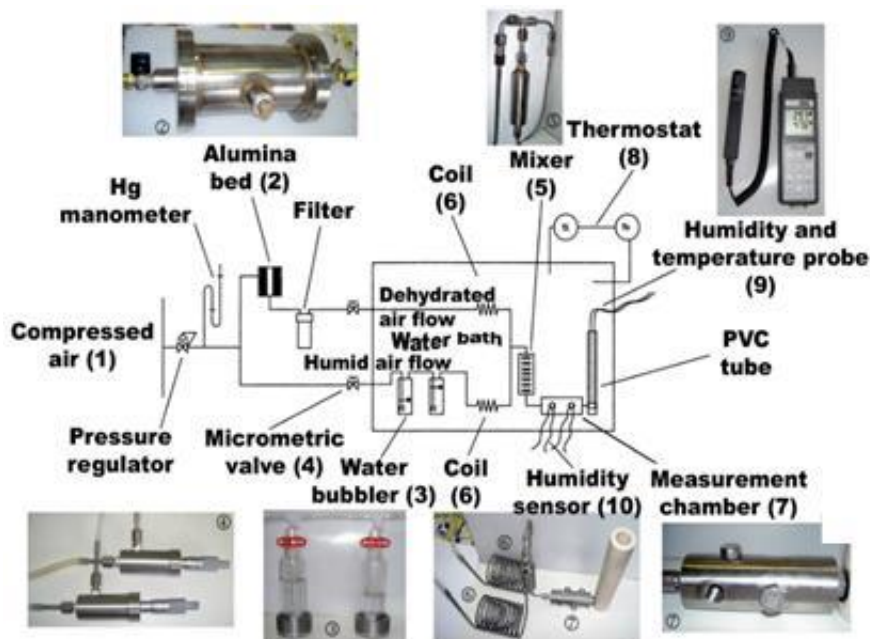


**Figure 1.** RH measurement system used in dynamic tests. Reproduced with permission from [40], published by Elsevier, 2005.

Tests were realized at ambient temperature. During measurements in a dynamic flow upon different concentrations of RH, sensors Z were measured with LCR meter (Hioki 3533-01, Nagano, Japan). All tests were performed at 1 kHz with an AC potential equal to 1 V.

The sensor response (SR%) towards humidity is calculated as follows (Equation (7)):

$$SR(\%) = 100 \times \frac{|Z_0 - Z_g|}{Z_0} \quad (7)$$

where,  $Z_0$  is the initial film impedance in dry air and  $Z_g$  is the impedance in humid conditions.

### 6.3 SWP-OSR Humidity sensors

In this section, the results of thick-films sensor based on two biochars are presented. Part of this paragraph is taken from ref [41]. Biochar-based chemoresistive humidity sensors were realized by drop-coating method.

The sensitive carbon materials and the as-prepared thick films were characterized by means of laser-granulometry measurements, XRD, Raman spectroscopy, XPS, FESEM. Sensors performances were evaluated towards relative humidity (RH) at ambient T and  $\tau_{ads}/\tau_{des}$  were defined, as well as cross-sensitivity measurements towards ozone, ammonia, methane and carbon dioxide.

#### 6.3.1 OSR-SWP biochars

Two typologies of standard biochar were obtained from UK Biochar Research Centre (BRC, Edinburgh, UK) and utilized as novel carbon element for humidity sensing. These materials were chosen among lots of disposable products from BRC, selecting that with the highest value of specific surface area (SSA) and that with the highest value of electrical conductivity. The one with the highest surface area was realized with pyrolyzed mixed softwood pellets (SWP700). It was pyrolyzed at 700°C with 87°C/min of heating rate. The yield in biochar was equal to 17.34% as declared by the producer. The one with the highest electrical conductivity was realized from oil seed rape (OSR700) attained by a 700°C-pyrolysis and 103°C/min of heating rate with 22.62% of yield, as declared by BRC. Table 1 reports the physical characteristics of the selected biochars like SSA and the conductivity, in accordance with their datasheets [35, 36].

**Table 1.** SSA and conductivity of OSR700 and SWP 700 biochars [39].

Biochar	SSA (m <sup>2</sup> /g)	Conductivity (dS/m)
OSR700	25.2	3.11
SWP700	162.3	0.16

Both materials were received as pellets. Firstly, they were pulverized in a planetary mill for 10 minutes. Subsequently, they were ground manually with an agate pestle in an agate mortar for obtaining a homogeneous powder. Furthermore, powders were sieved with a 45  $\mu\text{m}$  apertures sieve.

Polyvinylpyrrolidone (PVP, average  $M_w \sim 1,300,000$  by LS, Sigma Aldrich) was added to the biochar as an organic binder for enhancing the adhesion of the deposited biochar on  $\alpha\text{-Al}_2\text{O}_3$  substrates equipped with Pt interdigitated electrodes. The drop coating technique was realized by mixing 0.1 g of sensing element (OSR700, SWP700, PVP or SWP700-PVP (10 or 20 wt% of PVP with respect to SWP700)) with 10 mL of EtOH. After mixing for 1 h, mixture was concentrated by heating at 80°C and sensors were fabricated by dropping 40  $\mu\text{L}$  of this mixture onto ceramic  $\text{Al}_2\text{O}_3$ . Sensors were then dried at 80°C for 12 h. A picture of the as-obtained biochar device is depicted in Figure 2.



**Figure 2.** Picture (0.85x1.7 cm<sup>2</sup>) of biochar SWP700 sensor [39].

### 6.3.2 Biochars powder and film characterization

Particle size distribution of the OSR700 and SWP700 biochars was performed after manual grinding and sieving. From those analysis, OSR700 displays a bimodal distribution, with maxima respectively at 8 and 20  $\mu\text{m}$ .  $D_{50}$  is equal to 10.5  $\mu\text{m}$ , whereas SWP700 exhibits a trimodal distribution, with  $d_{50}$  of 18.3  $\mu\text{m}$ . Results are depicted in Figure 3 and in Table 2.



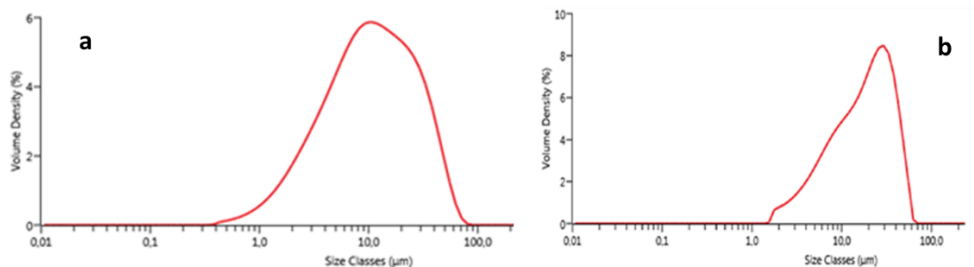


**Figure 3.** Laser granulometry analysis of OSR700 (a) and SWP700 (b) [39].

**Table 2.** Cumulative particle size distribution  $d_{10}$ ,  $d_{50}$  and  $d_{90}$  for the OSR700 and SWP 700 biochars.

Biochar	$d_{10}$ ( $\mu\text{m}$ )	$d_{50}$ ( $\mu\text{m}$ )	$d_{90}$ ( $\mu\text{m}$ )
OSR700	2.61	10.5	33.4
SWP700	4.98	18.3	39.8

XRD analysis was performed to understand if any possible crystallization peaks were present among OSR700 and SWP700 raw materials.

The next Figure 4 reveals the XRD patterns of SWP700 and OSR700. The former one is completely amorphous, whilst in the OSR700 quartz patterns were found, indexed with JCPDS file No 46-1045. The main peaks were determined at  $20.87^\circ$ ,  $26.65^\circ$ ,  $29.43^\circ$ ,  $20.26^\circ$ ,  $59.96^\circ$  and  $67.97^\circ$  of  $2\theta$ .

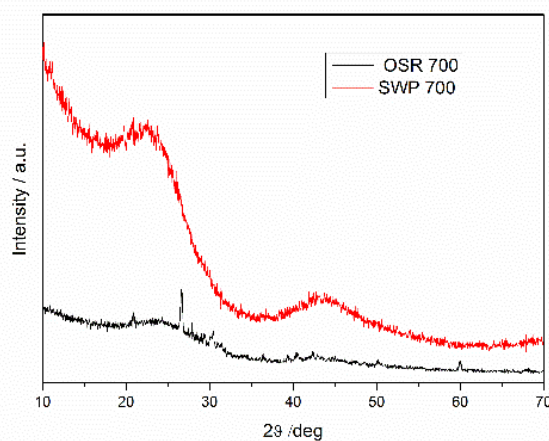


**Figure 4.** XRD patterns of SWP700 (red) and OSR700 (black) powders [39].

The degree of disorder and graphitization of the SWP700 and OSR700 biochar powders was investigated by Renishaw micro Raman performed at room temperature.

Results of Raman investigation are depicted in Figure 5.

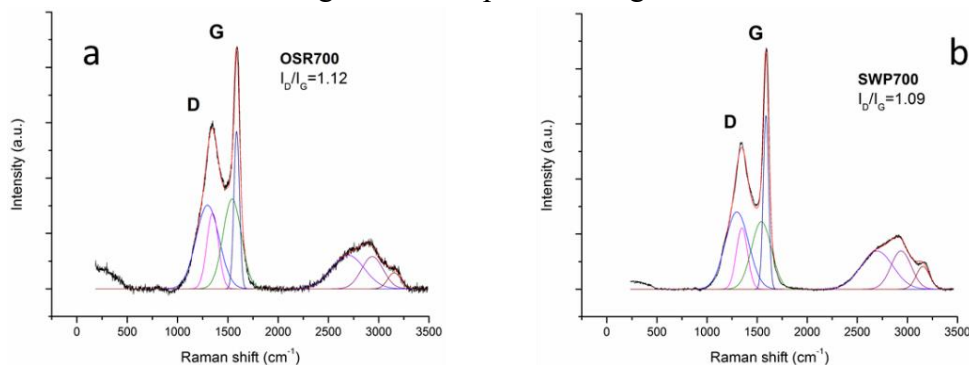


**Figure 5.** Raman spectra for OSR700 (a) and SWP700 (b) [39].

In Raman characterization, with the collaboration of dr. M. Rovere, different areas of the biochars were studied for ensuring the congruity of the results. The first-order Raman band of all  $sp^2$  hybridized carbon materials is represented by G band, generated by  $E_{2g}$ -mode at the  $\Gamma$ -point. G-band is due to the C-C bond stretching typical of graphitic carbon and it is usual in  $sp^2$  carbons. Thus, the D band is defect activated in  $sp^2$  carbon materials. Based on the ratio of D and G bands, it is possible to get an estimate about defect densities.

The D peaks are located around  $1360\text{ cm}^{-1}$  while G peaks  $\sim 1580\text{ cm}^{-1}$ . The peaks were investigated with a home-made method and a validated software which permits (i) to clear the background and (ii) to detect the contribution of different components. The main parameter is the  $I_D/I_G$  relationship of D and G signals, respectively equal to 1.12 for OSR700 and 1.09 for SWP700.

Those are characteristic of carbon-based material with a lot of defects. This investigation did not display great differences between the biochars and it disclosed a slightly higher presence of defects for OSR700 powder.

XPS investigations was accomplished to study the surface chemistry and electronic states of the biochars.

The survey and HR spectra of C1s for OSR700 and SWP700 are shown in Figure 6.

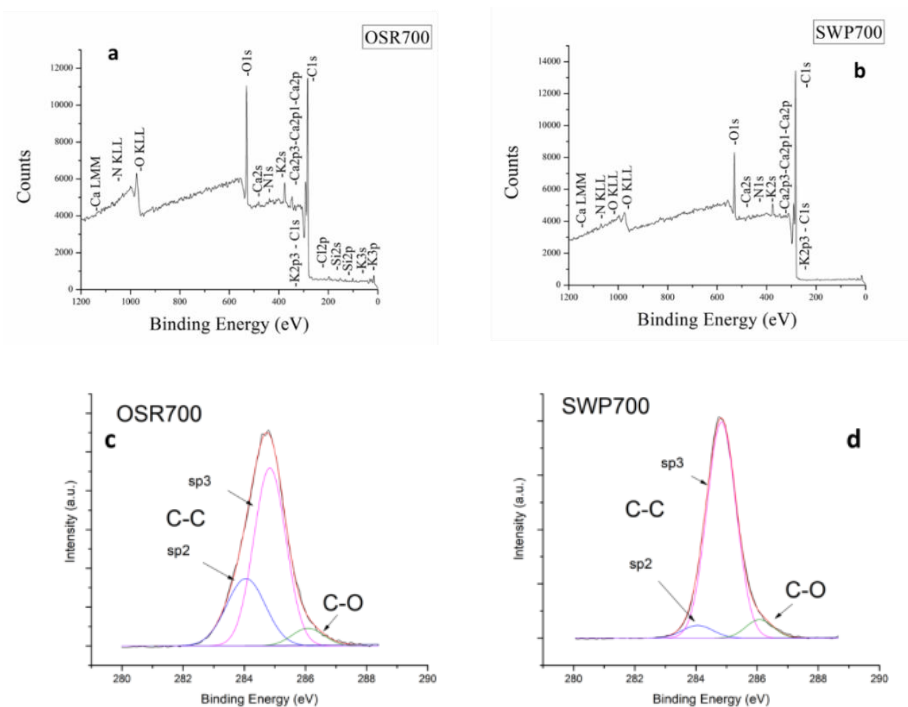


**Figure 6.** XPS Survey spectra for OSR700 (a) and SWP700 (b), HR XPS spectra of C1s peaks for (c) OSR700, (d) SWP700 [39].

From HR XPS analysis on carbon peaks, carbon spectrum can be deconvoluted into three contributions. They correspond respectively to graphite-type  $sp^2$  (284.6 eV); carbon in alcoholic, etheric or phenolic, groups  $sp^3$  (285.6 eV) and carbon in ester or carboxyl or ester functional groups (288.7 eV) [41].

In accordance with previous studies, CO-type functional groups in the surface of carbon-based samples, like hydroxyl, ethers, phenols, quinine and carbonyl groups, provide a positive effect by promoting the hydrophilicity of carbon material. Furthermore, they furnish a supplementary pseudocapacitance generated by Faradic phenomena implicating oxygen groups [42, 43]. XPS analysis revealed the elements tabulated in Table 3.

**Table 3.** Mass% of elements from XPS analysis.

Element	OSR700 (wt%)	SWP700 (wt%)
C <sub>1s</sub>	55.8	72.1
C sp <sup>2</sup>	29.1	5.4
C sp <sup>3</sup>	63.7	87.1
C=O	6.2	7.0
O <sub>1s</sub>	23.3	16.1
K <sub>2s</sub>	15.2	10.3
Ca <sub>2p</sub>	3.2	1.2
Si <sub>2p</sub>	1.9	-
Cl <sub>2p</sub>	traces	-
N <sub>1s</sub>	traces	traces

In the former table, the wt% of all elements were determined by survey analysis, whereas C sp<sup>2</sup>, C sp<sup>3</sup>, and C=O amount were defined by deconvoluting the C 1s signals in Figure 6. From this analysis, the carbon amount is much bigger in SWP700 compared to OSR700. In both materials, surface composition is enriched in oxygen in comparison with the data reported in the datasheets [43, 44]. In fact, from [43, 44] the amount of oxygen was 7.84 wt% and 6.02 wt% for OSR700 and SWP700, respectively.

C in the form of sp<sup>2</sup> bonds is predominant in OSR700 in comparison with SWP700 (29.11% vs. 5.35% of whole C). Furthermore, the content of other elements such as K and Ca in OSR700 is bigger, and Si is present solely in the OSR700 biochar.

Finally, morphologies of biochar films were investigated by FESEM. In figure 7 OSR700 biochar sensors at diverse magnifications (2.5k×, a and 10k×, b) are illustrated. In the same figure SWP700 biochar film images are displayed (2.5k×, c and 10k×, d).

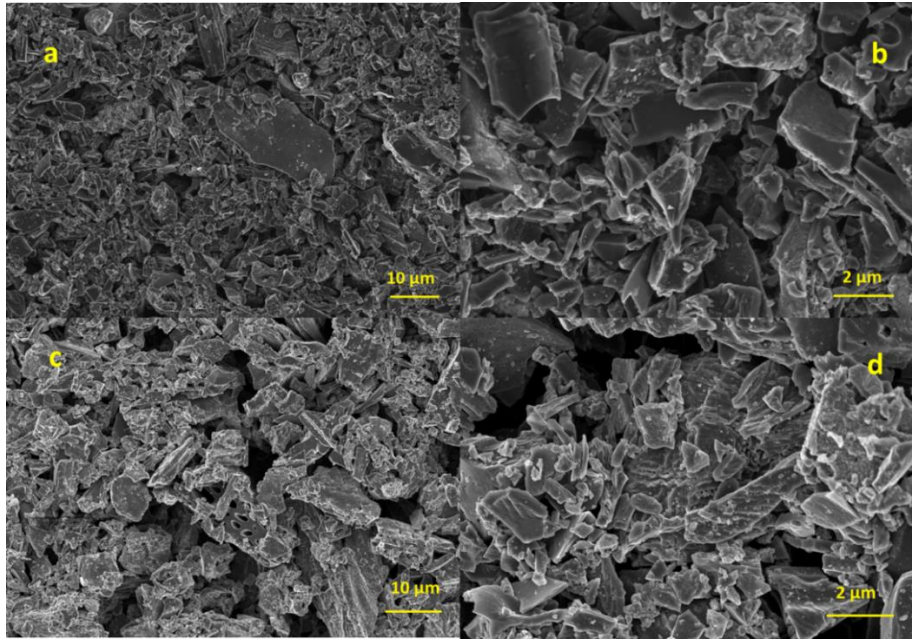


**Figure 7.** FESEM micrographs of OSR 700 film (a, 2.5k $\times$ ; b, 10k $\times$ ) and SWP700 film (c, 2.5k $\times$ ; d, 10k $\times$ ) [39].

A broad particle size distribution was noted in accordance with laser granulometry analysis. Some big, faceted grains enclosed by a finer fraction are present. The grinding step generates small fragments in the 1-50  $\mu\text{m}$  range. The grains display sharp edges, as forecasted in carbon fragile material showing disorderly surfaces subsequently to the milling process.

SWP700-PVP10% (SWP10PVP) and SWP700-PVP20% (SWP20PVP) layer images are shown in Figure 8. In these images, an improved connection between SWP700 grains for the PVP coating was achieved.

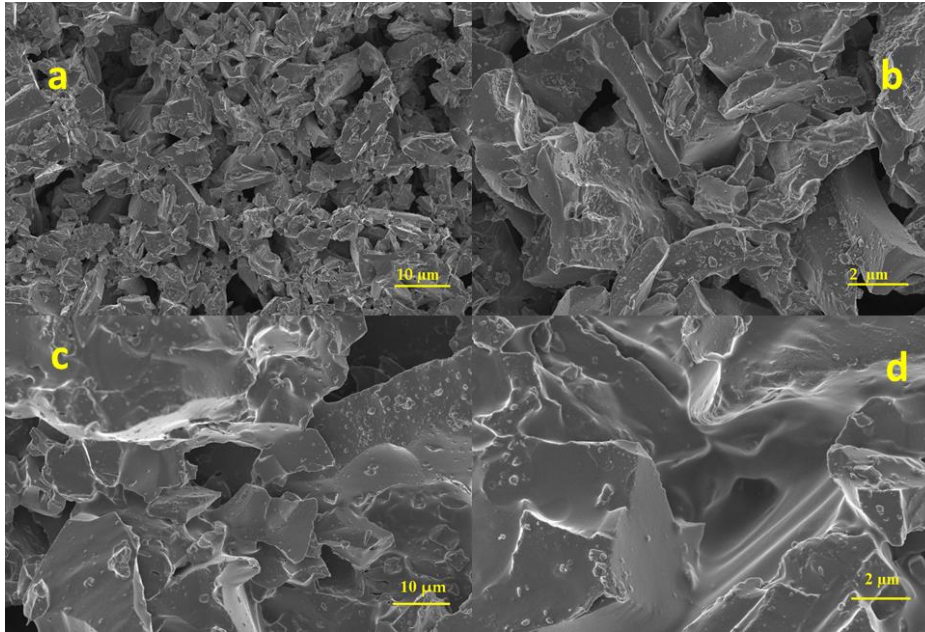


**Figure 8.** FESEM micrographs of SWP10PVP film (a, 2.5k×; b, 10k×) and SWP20PVP (c, 2.5k×; d, 10k×) [39].

### 6.3.3 Biochars gas sensing properties

The SR% vs RH% graphs are depicted in Figure 9 for OSR700 (a) and SWP700 (b) sensors.

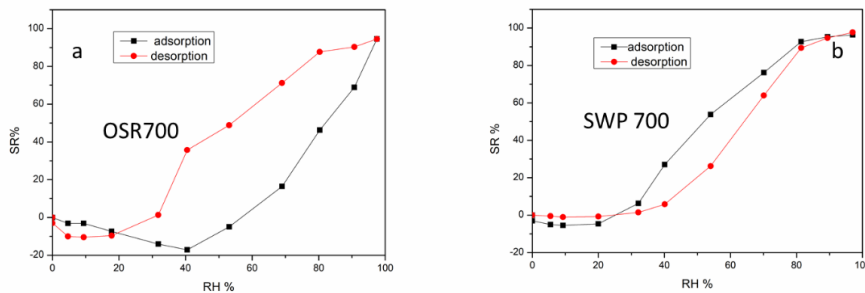


**Figure 9.** SR% under different RH% for (a) OSR700; (b) SWP700 [39].

Both biochars exhibit high sensitivity towards humidity from low RH amounts. As a matter of fact, Z starts to raise (i.e., the slope of SR% is negative) in both cases from 5 RH%. Impedance of the film increased till around 40 RH% for OSR700 and up to 25 RH% in the case of SWP700. For either biochars, they show p-type semiconductor behavior upon low concentration of humidity. On the opposite, at bigger RH contents, Z dropped starting around 40 RH% for OSR700 and from 25

RH% in the case of SWP700 sensor. OSR700, the biochar with the higher conductivity, has an initial  $Z$  under dry air of  $163.9 \text{ k}\Omega$ , and the final value dropped until  $9 \text{ k}\Omega$  under  $99 \text{ RH}\%$ , with a SR% of  $94.5\%$ , and a highest value of hysteresis equal to  $52\%$  upon  $59 \text{ RH}\%$ , as shown in Figure 9a. For SWP 700 sensor, a bigger change in  $Z$  was measured probably as a consequence of the higher SSA and porosity. In fact,  $Z$  declined from  $9.5 \text{ M}\Omega$  at  $0\% \text{RH}$  until  $222 \text{ k}\Omega$  under  $97\% \text{RH}$ , resulting in a SR% of  $97.6\%$ . This biochar displays a smaller hysteresis ( $23\%$  under  $55 \text{ RH}\%$ ) in accordance with figure 9b.

The  $\tau_{\text{ads}}$  and the  $\tau_{\text{des}}$  were respectively  $50$  and  $70 \text{ s}$  for OSR700 sensor, whereas for SWP700 sensor were around  $1$  minute.

Comparing the sensor performances of the examined biochars, SWP700 was the most sensitive towards humidity especially at higher humidity levels. For this material, sensors with different concentrations of PVP were fabricated for improving the adhesion of the film onto alumina dielectric. PVP is a n-type polymer that exhibits highly conductivity and hydrophilicity [44,45] utilized in this thesis in  $10$  and  $20 \text{ wt}\%$  in comparison with SWP700. Thereafter, the films prepared using SWP700 and  $10$  and  $20 \text{ wt}\%$  of PVP are named SWP10PVP and SWP20PVP, respectively.

Furthermore, a pure PVP sensor was realized to understand the sensing characteristics of this conductive polymer. Results are depicted in Figure 10.

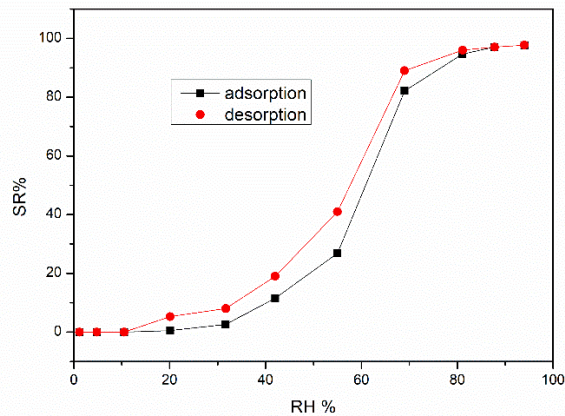


**Figure 10.** PVP film impedance's variation towards RH [39].

This thick-film PVP sensor has an impedance of  $19 \text{ M}\Omega$  under dry air and it drops until  $420 \text{ k}\Omega$  upon  $98\% \text{RH}$  with a cut-off at  $40 \text{ RH}\%$ . SR% vs RH% of PVP sensor are displayed in Figure 10, confirming its n-type polymer semiconducting

nature: in fact, the films became more conductive when increasing RH amount. The maximum hysteresis of 13% was measured under 55% RH.

In the next Figure 11 SR% vs RH% for SWP10PVP and SWP20PVP films are reported.

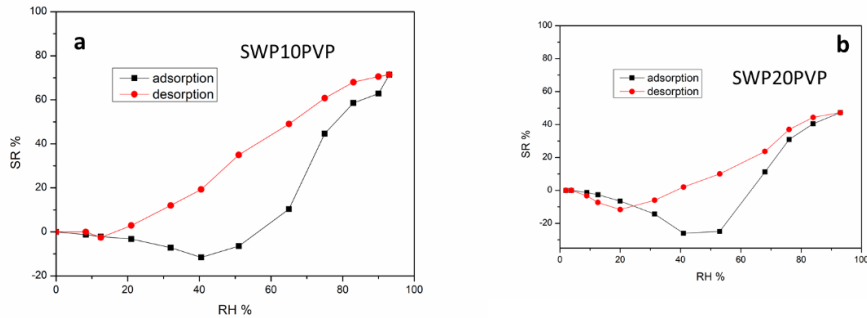


**Figure 11.** SWP10PVP and SWP20PVP sensor responses towards RH [39].

The sensitivity of the SWP sensor diminished compared to the pure SWP700 to the two PVP-biochar composites (SWP10PVP and SWP20PVP). Maximum values of hysteresis were equal to 42% under 50 RH% for the former sensor and to 35% under 53 RH% for the former composite. In the Table 4, maximum sensor responses are tabulated for the five proposed sensors.

**Table 4.** Highest values of sensor responses for OSR700, SWP700, PVP, SWP10PVP and SWP20PVP films towards RH.

Sensor	SR%
OSR700	94.5
SWP700	97.7
PVP	98.0
SWP10PVP	65.2
SWP20PVP	47.3

SWP10PVP sensor represents a satisfactory compromise between the adhesion of the sensitive elements over the alumina substrate and the sensitivity towards humidity. For this, the evaluation of selectivity for SWP10PVP film was carried out.

Cross sensitivity tests are displayed in Figure 12.



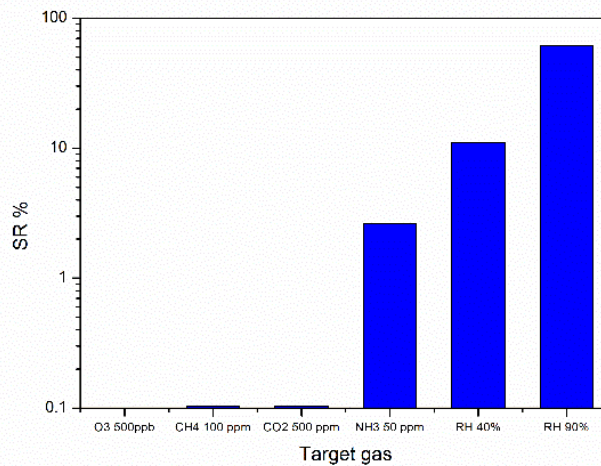


**Figure 12.** SR% of SWP10PVP sensor toward O<sub>3</sub> 0.5 ppm, NH<sub>3</sub> 50 ppm, CH<sub>4</sub> 100 ppm and CO<sub>2</sub> 500 ppm [39].

No cross-sensitivities were identified at room temperature upon 0.5 ppm O<sub>3</sub>, 100 ppm CH<sub>4</sub> and 500 ppm CO<sub>2</sub>, whereas under 50 ppm of NH<sub>3</sub>, a modest increase of 2.6% in Z was measured. Under 40% of RH the maximum increase in impedance was measured (from 1.12 to 1.24 MΩ) and under 90% RH drop to 398 kΩ.

H<sub>2</sub>O can be adsorbed on the carbon-based layers surface of after a weak bonding of H atoms of the water with the C atoms of OSR700 and SWP700 biochars [29]. Additionally, defects in carbon particles improves the sensing performances for humidity adsorption, as confirmed in Raman spectroscopy analysis depicted in figure 5. Defects are known to generate favorable adsorption sites to H<sub>2</sub>O adsorption [29].

The large amount of oxygen derivatives detected by XPS investigation on carbon surface improves the carbon hydrophilicity [29]. In addition, at small RH amounts, not many water vapor species are chemically adsorbed on the carbon surfaces behaving like a p-type semiconductor. This is a result of the charge transfer between adsorbate and carbon film, as described by Pati et al. [46].

In the low RH range (below 40% RH) an exchange of e<sup>-</sup> with a p-type semiconductor occur, increasing the sensor impedance [29]. On the opposite, when RH amount is higher than 40 RH% more H<sub>2</sub>O molecules are adsorbed on the carbon surface forming clusters that generate a liquid-like multilayer of H-bonded H<sub>2</sub>O [47].

In addition, the water molecules physisorbed onto the surface of p-type semiconductor biochar condensed into pores with a size of 1-250 nm. Since many

clusters of water molecules are formed at this humidity levels and the hydration of  $H^+$  into  $H_3O^+$  is a thermodynamically spontaneous process in liquid water,  $H^+$  are the main charge carriers in the  $H_2O$  adsorbed into mesopores. The concentration of  $H^+$  increases at higher water content, and  $H^+$  ions can dislocate freely in liquid water, decreasing the resistance of particle surface by increasing RH content [47]. This mechanism demonstrates why the measured impedance drops at high humidity values.

In summary, at low humidity levels an electronic conduction prevails, whereas at higher RH ionic conduction predominate.

Moreover, the ratio  $sp^2/sp^3$  measured by means of XPS analysis can influence the SR% at low RH (5–30%). The hydrophilic characteristic is verified indeed by a bigger  $sp^2/sp^3$  ratio, measured in OSR700 ( $sp^2/sp^3 = 0.45$ ) respect to SWP700 ( $sp^2/sp^3 = 0.06$ ), according with [48].

As a result, OSR700 shows a higher affinity for the  $H_2O$  adsorption at lower levels of RH in comparison with SWP700.

From figure 11, a considerable variation in the hysteresis between OSR700 and AWP700 was noticed. This could be a consequence of the differences in the pore size distribution: for the OSR700, a higher hysteresis was calculated (52% vs 23%) since  $H_2O$  desorption is tricky and slower for the lower specific surface area (SSA). However, this feature was not investigated deeper in this thesis. In fact, the effect of SSA on the sensitivity of a quartz crystal microbalance-based polyacrylic acid device for  $NH_3$  detection was studied in [49]. The results of this work assessed that the  $NH_3$  sensitivity was improved quickly by increasing the SSA [49]. In our study, the higher value of SSA for SWP700 biochar supports  $H_2O$  adsorption decreasing faster the film impedance up to 25 RH%, in comparison with the 40 RH% for OSR700 film.

The PVP presents a N atom in its molecule and high hydrophilicity [50, 51]. Hence, this polymer can adsorb easily  $H_2O$  molecules. As described before, at low RH amounts, only few  $H_2O$  molecules can be adsorbed onto PVP in order to produce  $H^+$  and  $H_3O^+$  ions. In accordance with figure 10, PVP shows a n-type semiconductor behavior with electrons acting as main conduction carriers [50, 51]. If RH increases,  $H_2O$  molecules can provide more ionic carriers ( $H^+$  and  $H_3O^+$ ) on the PVP surface contributing to the PVP conduction [52]. Over 94 RH%, PVP can be swelled by  $H_2O$ , creating several conductive ions [53]. When PVP is combined with SWP700 to form an optimum composite, an improved connection between biochar grains was achieved as exhibit in FESEM images.

This result in a drop in the initial Z value for the SWP10PVP film in comparison with the SWP700. Furthermore, when n-p heterojunctions are generated between

two semiconductors (i.e., p-type SWP700 and n-type PVP),  $e^-$  from PVP are transferred to SWP700 and  $p^+$  are transferred in the opposite way, in order to equilibrate the Fermi levels of either semiconductors [54].

A potential barrier is generated at the heterojunctions, increasing the Z of the p-n composite respect to SWP700 [60].

In the composite SWP10PVP, the variation in impedance for the adsorption of few  $H_2O$  molecules is enhanced, resulting in an improved sensitivity at lower RH concentrations.

This is in accordance with the results obtained in this thesis, where higher sensor responses were measured in the case of SWP10PVP and SWP20PVP respect to the pristine biochar.

## 6.4 Waste coffee ground sensors

In this paragraph, for the first time, results of preparation of a humidity sensor realized with waste coffee ground biochar are summarized. Part of this paragraph is taken from [55].

Nowadays, coffee consumption is higher than 11 billion tons/year worldwide [57], and usually exhaust coffee concludes as landfill. Coffee is an essential commodity and extensively utilized drinks all around the world [57]. The global production has reached 11–13 million tons [58, 59]. The chemical composition of coffee is dependent on physiological traits such as the degree of maturation [60–62]. In the time process of roasting that takes place at high temperatures, complex chemical phenomena occur modifying considerably the chemical composition of coffee: after this process, 950 different compounds have been recognized [63]. Conversely, an estimated 380,000 tons of brewed coffee waste is discarded each year [64]. Coffee waste is a source of an ecological issue in coffee-using countries [65].

A lot of studies on the use of coffee waste have found many applications for coffee by-products in a variety of ways [66]. Coffee waste residue is constituted prevalently by lignocellulose [67]. Nowadays, many scientists consider these residues as a raw material for other processes [68]. Waste brewed coffee powder (WBCP) is a qualified raw material as a carbon material source for environmentally friendly treatments, like pyrolysis [69]. Nevertheless, the distinguished structural features of its surface constituted by channels become coffee ground biochar exploitable for the adsorption of  $H_2O$  molecules. The utilization of coffee ground biochar as a low-cost resource for carbon is delineated and the synthesized

coffee ground biochar (CGB) was characterized by techniques like laser granulometry, TGA, XRD, Raman spectroscopy, XPS and FESEM for acquiring an exhaustive understanding of its properties and chemical composition. Humidity sensors were fabricated by screen printing deposition.

#### 6.4.1 Coffee ground biochar (CGB)

In this paragraph, the humidity sensing features of CGB realized from the pyrolysis of WBCP were studied at room T in a RH range 0-98%. A WBCP (Caffe Vergnano, Italy) was utilized as starting carbon material for carbonization as schematized in Figure 13.



**Figure 13.** Conversion process of coffee firstly in WBCP and then in CGB [55].

The leftover chemicals in waste coffee powder after brewing may influence the natural structure of coffee during the carbonization step [70].

In order to remove the chemicals leftover in waste coffee powder after brewing, the WBCP was washed many times with H<sub>2</sub>O by centrifugation and filtered. The WBCP was dried for 10 h at 90°C. WBCP was pyrolyzed at 700°C for 1 h in N<sub>2</sub> (120 mL/min) after two -30 min-dwells at 250°C and 400°C, respectively. The heating ramp degree in the tubular furnace was set at 5°C/min [71].

Subsequently to the pyrolysis, the CGB powder was manually ground e to improve its homogeneity.

#### 6.4.2 CGB powder and film characterization

For the characterization of CGB powder and film, the same instruments described in the session 5.2.2 were used. In addition, TGA was carried out on the WBCP powder under a 100 SCCM flow of Ar in the range 25-700°C with 10°C/min of heating ramp.

Furthermore, TG-DTA was accomplished on CGB in the same range of temperature and with the same heating ramp under static air.

Laser granulometry of CGB denoted that this powder displays a bimodal distribution, with the maxima respectively at 23 and 192  $\mu\text{m}$  and  $d_{10}$ ,  $d_{50}$  and  $d_{90}$  (equal to 8.9, 32.6 and 215  $\mu\text{m}$ , respectively). Particle size distribution curve is illustrated in Figure 14.

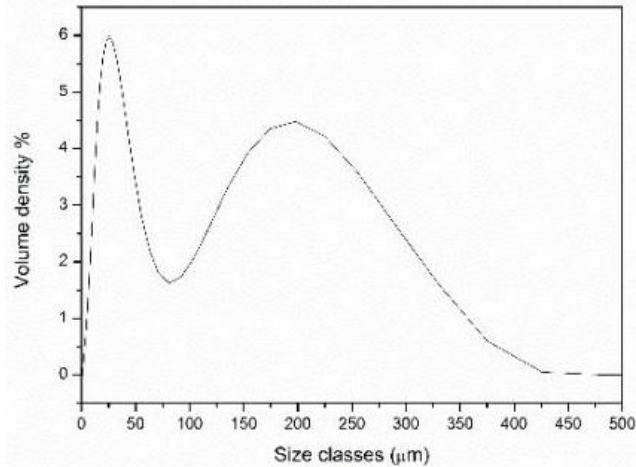


**Figure 14.** Particle size distribution of CGB powder.

TGA under Ar 50 SCCM was realized with the aim to understand the carbonization process and to set the right pyrolysis parameters. The ramp of heating was  $10^{\circ}\text{C}/\text{min}$  until  $700^{\circ}\text{C}$ . Since no mass losses were detected after  $700^{\circ}\text{C}$ , the pyrolysis was performed with 1 h dwell at  $700^{\circ}\text{C}$ . The TG-DTG plots are depicted in Figure 15.

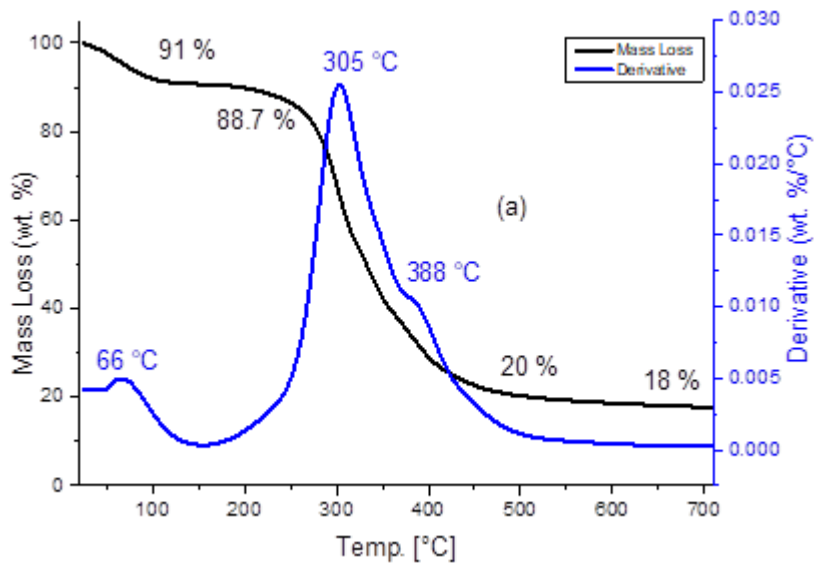


**Figure 15.** TGA of WBCP under argon [55].

From this plot, it is possible to notice that the total weight loss was equal to 82%, in accordance with the yield of WBCP pyrolysis to CGB (18 wt%). The first derivative of TG curve evidences three exothermic peaks respectively at 66°C, 305°C and 388°C. The maximum weight loss rate was recognized at 305°C.

The pyrolysis phenomenon occurs in three decomposition stages. The first one happens in the range 25-200°C and is related to a modest mass loss of 9% caused by the dehydration with VOCs (i.e. volatile organic compounds) emitted from WBCP. The second one (200-500°C) is the major mass loss of 71%, due to the devolatilization of main biomass components such as lignin, cellulose and hemicellulose [72].

In the third zone (500-700°C), the decomposition of the remaining biomass and the formation of the char take place.

The DTA-TG curves of CGB powder is illustrated in the Figure 16.

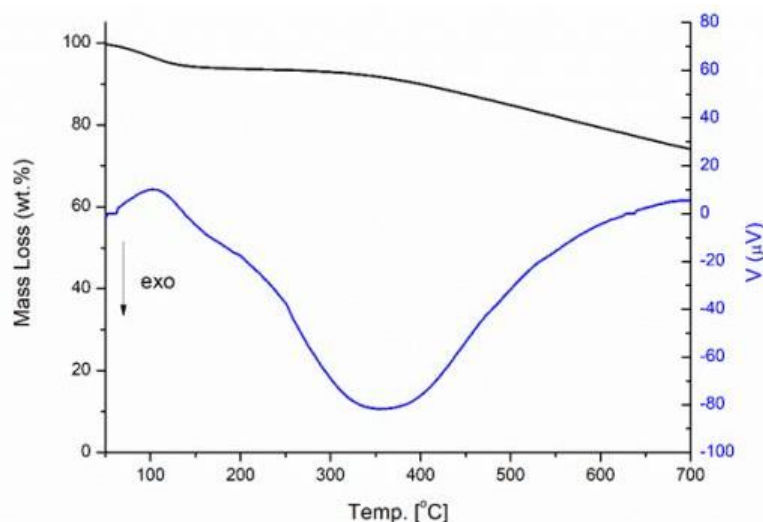


**Figure 16.** TG (black)-DTA (blue) curves of CGB in static air [55].

From the TG-DTA investigation in static air, carried out until 700°C, a 25% of mass loss was measured (black curve). The DTA curve (in blue) reveals a broad endothermic signal centered at 102°C for the evaporation of free water, whereas a shoulder around 250°C may be a result of the evaporation of molecular bound water in the CGB powder. A still broader exothermic signal at 350°C could be generated by the combustion of the residual cellulose and hemicellulose by means of the formation and emission of volatile compounds [73].

The amorphous structure of CGB powder is disclosed by the XRD pattern in Figure 17.

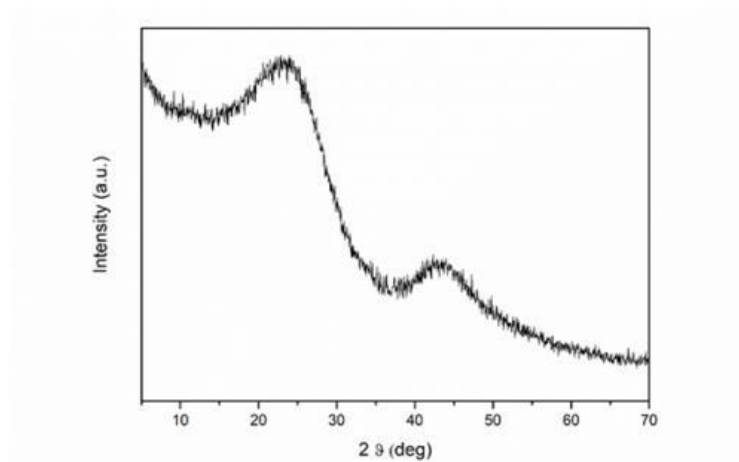


**Figure 17.** XRD pattern of CGB powder [55].

The XRD profile of the CGB powder demonstrates a high background intensity indicating that the as-pyrolized carbon powder contains highly disordered carbon with the characteristic broad humps at 23.5° and 43° of  $2\theta$  expected from amorphous carbonaceous materials.

In the Raman spectroscopy, different regions of the spectrum for CGB powder are identified and the outcomes are presented in Figure 18 and Table 5.

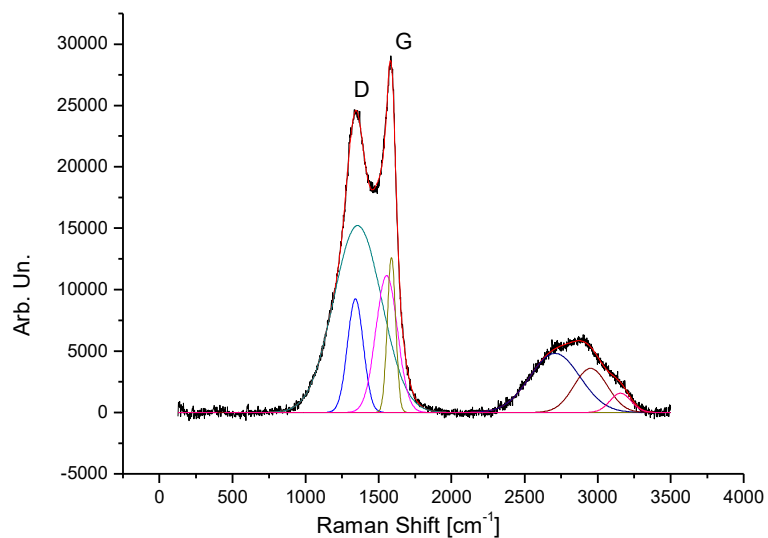


**Figure 18.** Raman analysis of CGB powder [55].

**Table 5.** Decomposition of peaks in Raman spectrum of CGB powder.

Label	Area [a.u.]	Center [ $\text{cm}^{-1}$ ]	Width [ $\text{cm}^{-1}$ ]
D1	1.2	1341	54
D2	6.6	1365	166
G1	1.8	1559	68
G2	0.8	1589	28
2D	2.1	2708	168
D+G	0.8	2932	97
2G	0.5	3130	85

The output of Raman spectroscopy confirms a  $\text{sp}^2$  carbon-based disordered composition. The two main area of interest are between 1000 and 1800  $\text{cm}^{-1}$ , where the D and G peaks are detected, and in the region 2400–3200  $\text{cm}^{-1}$  where their overtones are displayed (2D, D+G and 2G peaks). The first region cannot be correctly fitted with two peaks, but preferably four are necessary, one for each Raman mode in accordance with Table 5. As per the overtone region it can be recognized that even if the signal is relatively broad, specific features support the exhistance of some ordered regions with a supremacy of disordered regions. In this area, one peak for each mode was utilized for extract information on the relative intensities. The  $I_d/I_g$  ratio value is equal to 2.94 (higher than OSR700 and SWP700, respetively 1.12 and 1.09). Moreover, the Gaussias peak shapes confirms the disordered feature of CGB powders.

The chemical and electronic composition of the surface of CGB powder was investigated by XPS, survey and high-resolution C and O displayed in Figure 19.



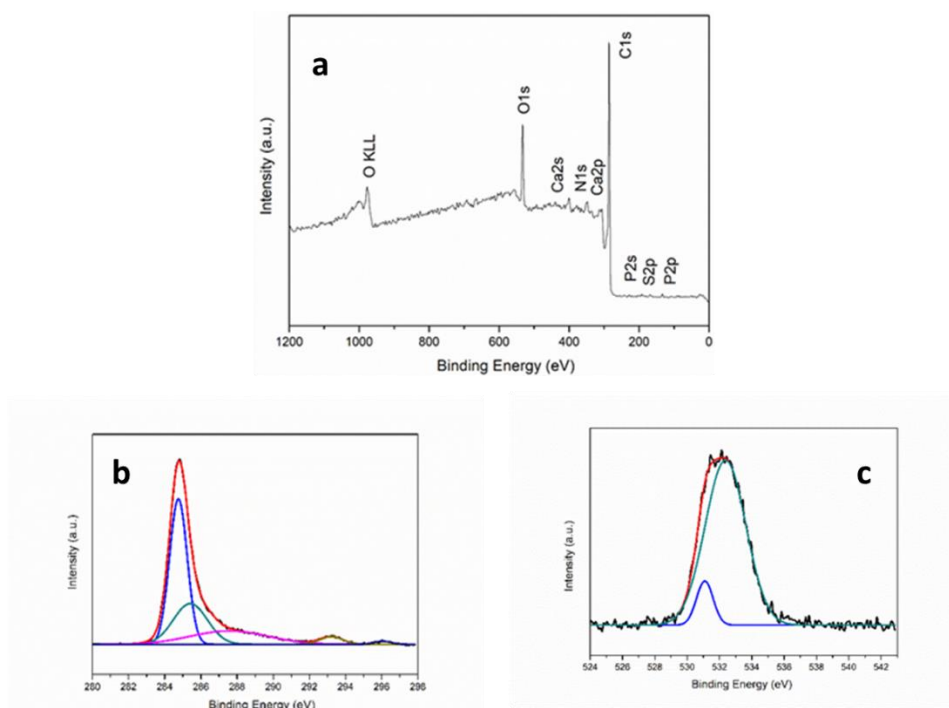


**Figure 19.** XPS investigations for CGB powder (a) survey, (b) HR C1s and (c) HR O1s [55].

From the survey, the major components are C (84.7%) and O (11%) with small concentration of elements like N (2.9 wt%), P (0.5 wt%) and Ca (0.9 wt%). Moreover, from the high-resolution spectra of C1s peaks, disordered  $sp^2$  carbon is predominant compared to the  $sp^3$  (equal to 67.8% at 284.8 eV and 16.2% at 286.2 eV of the total carbon, respectively). The ratio between  $sp^2$  and  $sp^3$  carbon is equal to 4.1. The peak generated by C-O bonds at 288.3 eV, at 290.5 eV the characteristic peak of C=O and at 293.1 eV the COOR signal were detected, accounting to 9.3%, 2.8% and 3.9% of the total carbon, respectively. Considering the deconvolution of the O1s peak in two signals, the peak at 532.8 eV generated by C-O is higher (61.6% of total O) respect to the signal at 531.2 eV due to C=O (38.4% compared to the entire O), in accordance with the high-resolution C peaks. Finally, FESEM micrographs performed on the CGB powder are depicted in Figure 20.

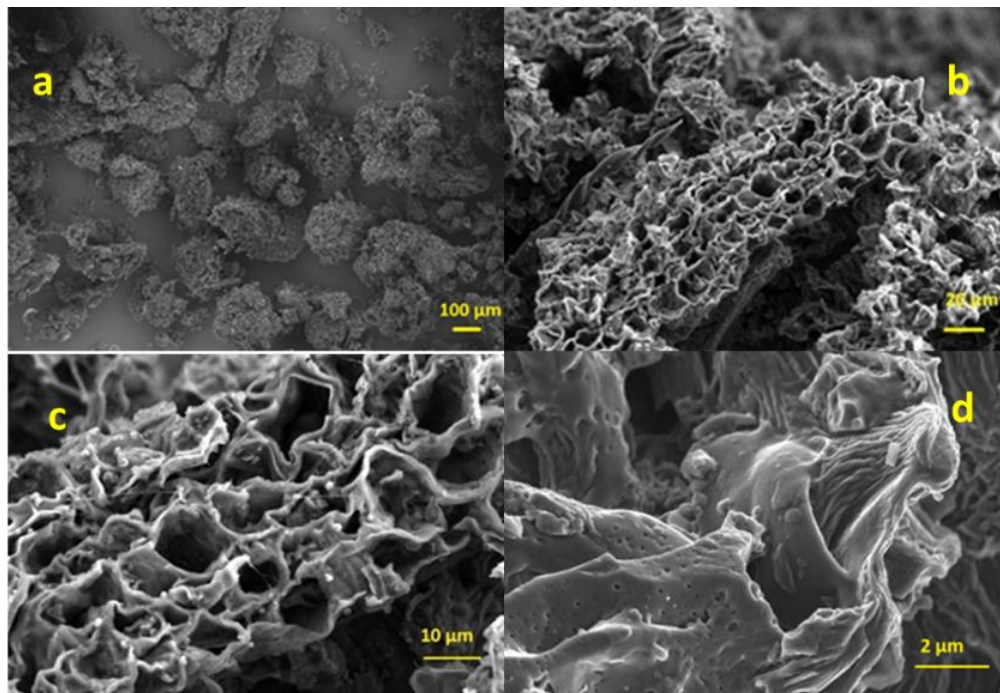


**Figure 20.** FESEM images of the CGB powder at: (a) 150 ×, (b) 1 k ×, (c) 2.5 k × and (d) 15 k × magnification [55].

In Figure 20, it is possible to appreciate that CGB powder displays a consistent degree of porosity with cavities of around 7 μm of average diameter.

The agglomerates' diameters are in the range 10-40 μm, in accordance with laser granulometry. Those agglomerates have nanometric scale pores formed during the pyrolysis of WBCP powder. The overall structure appears suitable for the adsorption of humidity both inside and outside of the channels.

### 6.4.3 CGB gas sensing properties

For the manufacturing of CGB sensors, an ink with CGB powder was realized using the same binder and solvent. In this frame, the CGB ink was utilized to screen-print onto the ceramic  $\alpha$ -Al<sub>2</sub>O<sub>3</sub> substrates with Pt electrodes, as shown in Figure 21. Screen-printed sensors were heat-treated at 300°C for 1 h in air resulting in sensitive CGB thick film of  $20.3 \pm 1.6$  μm of thickness.



**Figure 21.** A CGB sensor [22].

The results of CGB sensor adsorption and desorption towards different humidity levels (3 minutes for each of the 12 steps, as described previously in section 5.2) are illustrated in the following Figure 22, where the impedance ( $Z$ ) changes over time (a) and SR% vs RH% (b) in the range 0%-97% RH are displayed.

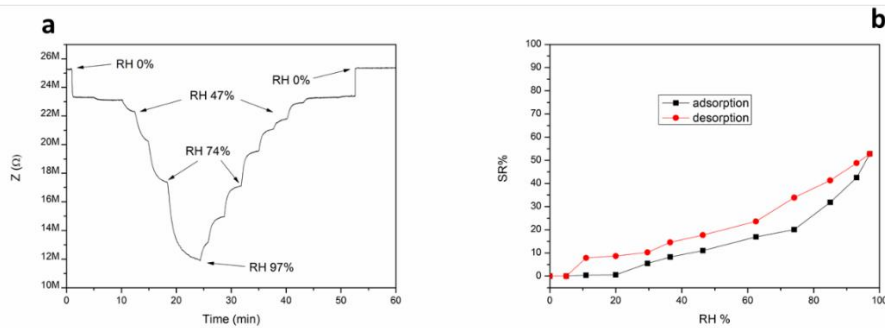


**Figure 22.** Changes in impedance (a) and sensor responses at different RH% (b) for CGB film during adsorption and desorption cycles [55].

When CGB sensors interact with humidity at room temperature ( $27^{\circ}\text{C}$ ), they exhibit a n-type semiconductor behavior. In fact, the SR% slope is positive, i.e. the conductivity of the screen-printed thick films increases at higher RH.

In fact, sensor response begins around 20% RH, with SR% of 51% under 98% RH.  $Z$  drops from 25.2  $\text{M}\Omega$  in 0% RH till 12.3  $\text{M}\Omega$  in 97% RH.

The desorption process was also studied and a maximum hysteresis of 15% was detected upon 74% of RH, establishing that the speed of desorption is similar to that for adsorption. Sensor  $\tau_{\text{ads}}$  and  $\tau_{\text{des}}$  were determined and were equal to 15 and 20 s under 50% of RH and equal to 4.5 min and 1 min under 90% of RH, respectively. The quick kinetics of adsorption and desorption can be a result of the considerable porosity of the film with long channels where humidity can easily come in and physisorbed onto the CGB surface. Furthermore, aging of the sensor was assessed after 1 year of storage at room temperature and the sensor performances were comparable under 90% of RH (42 vs 39% of impedance variation).

Moreover, cross-sensitivity tests were performed on the CGB film to evaluate the selectivity of the film for RH and the following histogram describes the results (Figure 23).

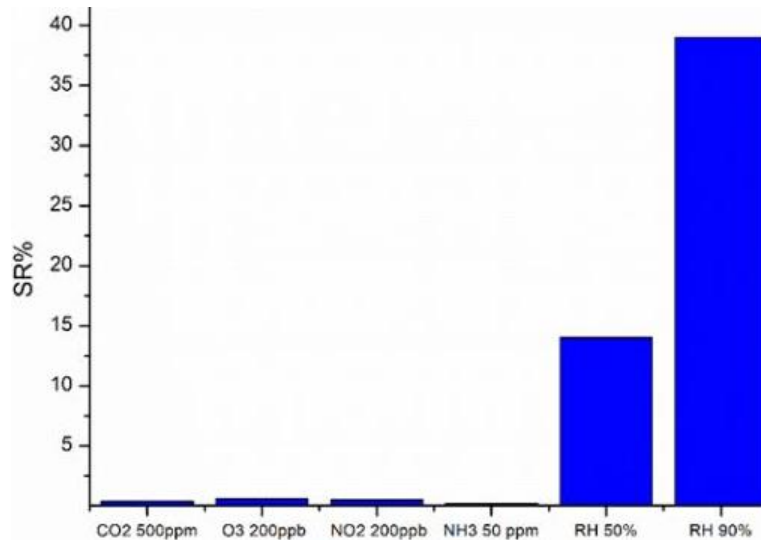


**Figure 23.** Cross sensitivity test of CGB sensor towards CO<sub>2</sub> 500 ppm, O<sub>3</sub> 200ppb, NO<sub>2</sub> ppb and NH<sub>3</sub> 50 ppm [55].

Generally, negligible cross-sensitivities were detected for CO<sub>2</sub> 500 ppm, O<sub>3</sub> 200 ppb, NO<sub>2</sub> ppb and NH<sub>3</sub> 50 ppm.

CGB sensor exhibits a high ratio  $sp^2/sp^3$ , as confirmed by Raman and XPS analyses. This is a proof of the large amount of defects in the CGB surface that enhance the sensor response towards humidity as previously described. In fact, a ratio  $sp^2/sp^3$  equal to 4.2 was calculated from XPS investigation. These defects act as adsorption sites for water molecules. In addition, oxygen derivatives after the pyrolysis improve the hydrophilic properties of the carbon surface [70].

When the RH levels are above 20–30%, an electronic transfer between water vapour and the disordered carbon structure of CGB grains takes place.

The CGB sensor morphology is constituted by connected channels, forming a wide number of paths through the tubes (i.e. percolation paths). The water molecules are reducing agents and a charge transfer from H<sub>2</sub>O to CGB generates a shift of the VB of CGB far from the Fermi level, causing an electron accumulation layer decreasing Z when increasing the H<sub>2</sub>O amounts [71].

There is an exponential trend of the SR% with RH% that can be a consequence of the fact that up to 60% of RH more H<sub>2</sub>O molecules are adsorbed on the CGB surface, with the generation of clusters of multi-layer H<sub>2</sub>O molecules that are hydrogen-bonded [74].

In this situation, the ionic conduction prevails after the creation of clusters of water and the formation of  $\text{H}_3\text{O}^+$  from  $\text{H}^+$ . Protons are the dominant charge carriers into the mesopores of the CGB film, and as a result, a quick rise in the layer conductivity at high RH was noticed. As a synergic effect, the hydrophilicity is enhanced by high values of  $\text{sp}^2/\text{sp}^3$  ratio [39, 48].

Up to now, solely in a previous research a biochar was used as chemoresistive humidity sensor. In Afify et al [69], innovative humidity sensors by screen-printed technique were fabricated with pyrolyzed bamboo. These devices exhibited a high sensitivity upon RH at ambient T with a cut-off RH around 10%. The resistance of the film decreased from around 937 kOhm in dry atmosphere until 89 kOhm under 95% RH. The maximum hysteresis was equal to 28.9% under 33 RH%. The  $\tau_{\text{ads}}$  and the  $\tau_{\text{des}}$  were both around 2 min and  $\tau_{\text{des}}$  were shorter compared to  $\tau_{\text{ads}}$ . This is a consequence of the porosity of the layer that furnish considerable availability for  $\text{H}_2\text{O}$  molecules adsorption. Probably physisorption was the main process for  $\text{H}_2\text{O}$  molecules bonding to the sensitive film since fast recovery times were measured. Nevertheless, the adhesion onto  $\text{Al}_2\text{O}_3$  substrates of pyrolyzed bamboo films was inadequate for practical applications. A comparison of the gas sensing features of the proposed sensors with the state of art on disordered carbonaceous materials was accomplished in the next Table 6.

**Table 6.** State of the art of humidity sensors based on carbon-based materials.

Sample	Resistance/impedance variation	$\tau_{ads}$ (s)	$\tau_{des}$ (s)	Ref.
C nanosheets produced by physical vapor deposition	Increase of 225% under 95 RH%	30 s when RH% increases from 11% to 40%	90 s when RH% decreases from 40% to 11%	[29]
Na-modified C films obtained by spray pyrolysis	Decrease of 97% under 60 RH%	n.d.	n.d.	[75]
Screen-printed commercial composite ink (ESL RS12113) made of epoxy resin and carbon powder	Increase of 4.8% under 80 RH%	n.d.	n.d.	[76]
Carbon quantum dots film made by electrochemical ablation of graphite	Resistivity decrease of 48% under 90 RH%	25 s when RH% increases from 7% to 43%	60 s when RH% decreases from 43% to 7%	[77]
Hydrogenated amorphous carbon (a-C:H) film	Decrease of 97.3% under 80 RH%	n.d.	n.d.	[78]
Pyrolyzed bamboo	Decrease of 91% under 95% RH	2 min	2 min	[69]
Oil seed rape	Decrease of 94.5% under 99% RH	50 s	70 s	This thesis
Pyrolyzed mixed softwood pellets	Decrease of 97.7% under 97.5% RH	1 min	1 min	This thesis
Pyrolyzed mixed softwood pellets/10% PVP (Polyvinylpyrrolidone) composite	Decrease of 65.2% under 94% RH	32 s	45 s	This thesis
Coffee ground biochar	Decrease of 51% under 98%RH	4.5 min	1 min	This thesis

## 6.5 Conclusions

In this chapter, humidity was firstly defined and different strategies to measure its amounts were described. Chemical humidity sensors, with a special focus on carbon-based materials were described in order to measure humidity with a sensitive, reliable and cheap method.

Two p-type biochars (OSR700 and SWP700) were selected as innovative materials for the manufacture of humidity sensors by dip coating method. Their humidity gas sensitive characteristics were studied at room T in the RH range 0–99%. Both biochars are sensitive and selective towards humidity from low RH amounts. Considering OSR700 sensor, impedance starts to raise from 5 RH% and a growth in Z was measured till around 40 RH%, while for SWP700 film, Z increases until 25 RH%. In both cases, biochars exhibit a p-type behavior upon small concentration of RH. Conversely, at higher RH amounts, Z dropped since several conductive layers were formed on the biochar surface. Thus, the cross-sensitivity towards species like methane, ammonia, carbon dioxide and ozone were negligible. PVP was added up acting as a polymeric binder to SWP700, forming a p-n heterojunction between the materials, increasing the sensitivity at small RH amounts for the sensors SWP10PVP and quicker sensor response compared to the pristine SWP700. This trend suggest the exploitation of these sensors for industrial usages in which low RH concentrations are requested such as drying of clothes (0–40 RH%), stocking of cereals (0–45 RH%), pharmaceuticals (20–40 RH%), humidity monitoring in factories, electronic parts, ceramic powders, dried foodstuffs (0–50 RH%) and layer drying (0–30 RH%)... [47].

In the final part, coffee ground biochar (CGB) was proposed for the first time as a n-type resistive humidity sensing material. Sensors were realized by a screen-printing and the humidity sensing features were studied at room temperature. The proposed CGB biochar was realized from pyrolysis at 700 °C of waste brewed coffee powder (WBCP). The sensor impedance variation under humidity starts from 20% RH. The CGB sensor is sensitive towards humidity in the range 20–100 RH% with an exponential trend by increasing humidity amount. The kinetics of adsorption and desorption were extremely fast upon 50% RH (15–20 s), and the cross-sensitivity towards ammonia, nitrogen dioxide, carbon dioxide and ozone were negligible.

In the future, the adhesion of the CGB film should be improved by utilizing a valuable binder.

# References

- [1] Stetter J. R., Penrose W. R., Yao S. (2003) Sensors, Chemical Sensors, Electrochemical Sensors and ECS. *J. Electrochem. Soc.* Pages S11-S16.
- [2] Carr-Brion K. (1986) Moisture sensors in process control; Elsevier Applied Science Publishers: London, UK.
- [3] Blank T. A., Eksperiandova L. P., Belikov K. N. (2016) Recent trends of ceramic humidity sensors development: A review. *Sens. Actuat. B.* Pages 416–442.
- [4] Carter E. F., (1989) ed. Dictionary of Inventions and Discoveries. Crane, Russak and Co., New York, 1966. 3. Baughman E. H. and Mayes, D. NIR applications to process analysis. *Am. Lab.*, Pages 54–58.
- [5] Afify A. S. S., (2016) Elaboration and characterization of humidity sensors for environmental monitoring, PhD dissertation.
- [6] Moseley P. T., Norris J. O. W., Norris D. E., (1991) Techniques and mechanisms in gas sensing, Adam Hilger Bristol, Philadelphia and New York. Pages 189-190.
- [7] Richardson J. F., Humidity measurements. <http://www.thermopedia.com/content/855/> doi: 10.1615/AtoZ.h.humidity\_measurement. Accessed on 22th of February 2019.
- [8] Wolfbeis O. S., Weidgans B. M. (2006) Fiber optic chemical sensors and biosensors: a view back, in: F. Baldini, A.N. Chester, J. Homola, S. Martellucci (Eds.), *Optical Chemical Sensors*, NATO Science Series II: Mathematics, Physics and Chemistry, Springer, Netherlands. Pages 16–44.
- [9] Casalbore-Miceli G., Chen Y. S., Girotto E. M., Li Y., Rinaldi A. W., Yang M. J., Zanelli A. (2006) Prompt responsive sensors for water detection in organic solvents. *Sens. Actuat. B.* Pages 577–582.
- [10] Cha S., Choi M. G., Jeon H. R., Chang S.-K. (2011) Negative solvatochromism of merocyanine dyes: application as water content probes for organic solvents. *Sens. Actuat. B.* Pages 14–18.
- [11] Wong W. C., Chan C. C., Chen L. H., Li T., Lee K. X., Leong K. C. (2012) Polyvinyl alcohol coated photonic crystal optical fiber sensor for humidity measurement, *Sens. Actuat. B.* Pages 563–569.
- [12] Tang J., Skotadis E., Stathopoulos S., Roussi V., Tsouti V., Tsoukalas D. (2012). PHEMA functionalization of gold nanoparticles for vapor sensing: chemi-resistance, chemi-capacitance and chemi-impedance, *Sens. Actuat. B.* Pages 129–136.
- [13] Parikh K., Cattanach K., Dong-Seok R. R., Aimei S., Sanjeev W., Manohar K. (2006) Flexible vapour sensors using single walled carbon nanotubes, *Sens. Actuat. B.* Pages 55–63.



- [14] Akitaa S., Sasaki H., Watanabea K., Seki A. (2010) A humidity sensor based on a hetero-core optical fiber, *Sens. Actuat. B.* Pages 385–391.
- [15] Zipsper L., Wächter F., Franke H. (2000) Acoustic gas sensors using airborne soundproperties, *Sens. Actuat. B.* Pages 162–167.
- [16] Hassen M. A., Clarke A. G., Swetnam M. A., Kumar R. V., Fray D. J. (2000) High temperature humidity monitoring using doped strontium cerate sensors, *Sens. Actuat. B.* Pages 138–143.
- [17] Yang B., Aksak B., Lin Q., Sitti M. (2006) Compliant and low-costhumidity nanosensors using nanoporous polymer membranes, *Sens. Actuat. B.* Pages 254–262.
- [18] Bedoya M., Díez M. T., Moreno- Bondi M. C., Orellana G. (2006) Humidity sensing with a luminescent Ru(II) complex andphase-sensitive detection, *Sens. Actuat. B.* Pages 573–581.
- [19] Zhang M., Hu C., Hong L., Xiong Y., Zhang Z. (2009) A rapid-response humidity sensor based on BaNbO<sub>3</sub> nanocrystals, *Sens. Actuat. B.* Pages 128–132.
- [20] Mohan P., Shinta R., Fujiwara J., Takahashi H., Mott D., Matsumura Y., et al. (2012) Boehmite nanorod/gold nanoparticlenanocomposite film for an easy-to-use optical humidity sensor, *Sens. Actuat. B.* Pages 429–435.
- [21] Islam T., Kumar L., Khan S. A. (2012) A novel sol-gel thin filmporous alumina based capacitive sensor for measuring trace moisture in therange of 2.5–25 ppm, *Sens. Actuat. B.* Pages 377–384.
- [22] Chen X. X., Rieth L., Miller M. S., Solzbacher F. (2009) High temperature humidity sensors based on sputtered Y-doped BaZrO<sub>3</sub> thin films, *Sens. Actuat. B.* Pages 578–585.
- [23] Chen X. X., Rieth L., Miller M. S., Solzbacher F. (2010) Comparison of Y-doped BaZrO<sub>3</sub> thin films for high temperature humidity sensors by RF sputtering and pulsed laser deposition, *Sens. Actuat. B.* Pages173–180.
- [24] He Y., Zhang T., Zheng W., Wang R., Liu X., Xia Y., Zhao J. (2010) Humidity sensing properties of BaTiO<sub>3</sub> nanofiber prepared via electrospinning, *Sens. Actuat. B.* Pages 98–102.
- [25] Oprea A., Bârsan N., Weimar U. (2009) Work function changes ingas sensitive materials: Fundamentals and applications, *Sens. Actuat. B.* Pages 470–493.
- [26] Yuk J., Troczynski T. (2003) Sol–gel BaTiO<sub>3</sub> thin film for humidity sensors, *Sens. Actuat. B.* Pages 290–293.
- [27] Yuan Q., Li N., Geng W., Chi Y., Tu J., Li X., Shao C. (2011) Humidity sensing properties of mesoporous iron oxide/silicacomposite prepared via hydrothermal process, *Sens. Actuat. B.* Pages 334–340.

- [28] Erol A., Okur S., Yağmırcukardes N., Arıkan M. C. (2011) Humidity-sensing properties of a ZnO nanowire film as measured with a QCM, *Sens. Actuat. B*. Pages 115–120.
- [29] Chu J., Peng X., Feng P., Sheng V, Zhang J. (2013) Study of humidity sensors based on nanostructured carbon films produced by physical vapor deposition. *Sens. Actuat. B*. Pages 508–513.
- [30] Jian M., Wang C., Wang Q., Wang H., Xia K., Yin Z., Zhang M., Liang X., Zhang Y. (2017) Advanced carbon materials for flexible and wearable sensors. *Sci China Mater*. Pages 1026–1062.
- [31] Korotcenkov G., Brinzari V., Ham M.-H. (2018) Materials acceptable for gas sensor design: advantages and limitations. *Key Eng. Mater*. Pages 80-89.
- [32] Wang C., Li X., Gao E., Jian M., Xia K., Wang Q., Xu Z., Ren T., Zhang Y. (2016) Carbonized silk fabric for ultrastretchable, highly sensitive, and wearable strain sensors. *Adv. Mater*. Pages 6640–6644.
- [33] Zhang M., Wang C., Wang H., Jian M., Hao X., Zhang Y. (2017) Carbonized cotton fabric for high-performance wearable strain sensors. *Adv. Funct. Mater*. Pages 1604795.
- [34] Nanda S., Dalai A. K., Berruti F., Kozinski J. A. (2015) Biochar as an exceptional bio resource for energy, agronomy, carbon sequestration, activated carbon and specialty materials. *Waste Biomass Valor* Pages 201–235.
- [35] [https://www.biochar.ac.uk/cms/i/user/standard\\_materials/21\\_SWP%20700-web.pdf](https://www.biochar.ac.uk/cms/i/user/standard_materials/21_SWP%20700-web.pdf) (Visited on 2<sup>nd</sup> of February 2017).
- [36] [https://www.biochar.ac.uk/cms/i/user/standard\\_materials/19\\_OSR\\_700-web.pdf](https://www.biochar.ac.uk/cms/i/user/standard_materials/19_OSR_700-web.pdf) (Visited on 2<sup>nd</sup> of February 2017).
- [37] Ahmad S., Khushnood R.A., Jagdale P., Tulliani J.-M., Ferro G. A. (2015) High performance self-consolidating cementitious composites by using micro carbonized bamboo particles. *Mater. Des*. Pages 223-229.
- [38] Chan K. Y., Van Zwieten V, Meszaros I., Downie A., Joseph S. (2007) Agronomic values of green waste biochar as a soil amendment. *Aust. J. Soil Res*. Pages 629-634.
- [39] Ziegler D., Palmero P., Giorcelli M., Tagliaferro A., Tulliani J.-M. (2017) Biochars as innovative humidity sensing materials. *Chemosens*. Pages 35-50
- [40] Tulliani J.-M., Bonville P. (2005) Influence of the dopants on the electrical resistance of hematite-based humidity sensors. *Ceram. Int*. Pages 507–514.
- [41] Gao Y., Yue Q., Gao B. (2015) High surface area and oxygen-enriched activated. *RSC Adv*. Pages 31375.
- [42] Ruiz V., Blanco C., Raymundo-Pinero E., Khomenko V., Beguin F. , Santamaria R. (2007) Effects of thermal treatment of activated carbon on the

- electrochemical behaviour in supercapacitors. *Electrochim. Acta*. Pages 4969–4973.
- [43] Bleda-Martinez M. J., Macia-Agullo J. A., Lozano-Castello D., Morallon E., Cazorla-Amoros D., Linares-Solano A. (2005) Role of surface chemistry on electric double layer capacitance of carbon material. *Carbon*. Pages 2677–2684.
- [44] Azmer M.I., Zafar Q., Ahmad Z., Sulaiman K. (2016) Humidity sensor based on electro spun MEH-PPV: PVP micro structured composite. *RSC Adv*. Pages 35387–35393.
- [45] De Queiroz A. A. A., Soares D. A. W., Trzesniak P., Abraham G. A. (2001) Resistive-type humidity sensors based on PVP–Co and PVP–I<sub>2</sub> complexes. *J. Polym. Sci. Part B Polym. Phys*. Pages 459–469.
- [46] Pati R., Zhang Y., Nayak S. K., Ajayan P. M. (2002) Effect of H<sub>2</sub>O adsorption on electron transport in a carbon nanotube. *Appl. Phys. Lett*. Pages 2638–2640.
- [47] Traversa E. (1995) Ceramic sensors for humidity detection. *Sens. Actuat. B*. Pages 135–156.
- [48] Paul R., Das S. N., Dalui S., Gayen R. N., Roy R. K., Bhar R., Pal A. K. (2008) Synthesis of DLC films with different sp<sup>2</sup>/sp<sup>3</sup> ratios and their hydrophobic behaviour. *J. Phys. D: Appl. Phys*. Pages 055309.
- [49] Jia Y., Yu H., Cai J., Li Z., Dong F. (2017) Explore on the quantitative analysis of specific surface area on sensitivity of polyacrylic acid-based QCM ammonia sensor. *Sens. Actuat. B*. Pages 1042–1045.
- [50] Li Y., Hong L., Chen Y., Wang H., Lu X., Yang M. (2007) Poly(4-vinylpyridine)/carbon black composite as a humidity sensor. *Sens. Actuat. B*. Pages 554–559.
- [51] Zhang J., Shen G., Wang W., Zhou X., Guo S.J. (2010) Individual nanocomposite sheets of chemically reduced graphene oxide and poly (N-vinyl pyrrolidone): preparation and humidity sensing characteristics. *Mater. Chem*. Pages 10824–10828.
- [52] Fei T., Zhao H., Jiang K., Zhou X., Zhang T. J. (2013) Polymeric humidity sensors with nonlinear response: properties and mechanism investigation. *Appl. Polym. Sci*. Pages 2056–2061.
- [53] Pan X., Xue Q., Zhang J., Guo Q., Jin Y., Lu W., Li X., Ling C. (2016) Effective enhancement of humidity sensing characteristics of novel thermally treated MWCNTs/Polyvinylpyrrolidone film caused by interfacial effect. *Adv. Mater. Interfaces*. Pages 1–7.
- [54] Kim J. H., Lee J. H., Mirzaei A., Kim H. W., Kim S. S. (2017) Optimization and gas sensing mechanism of n-SnO<sub>2</sub>-p-Co<sub>3</sub>O<sub>4</sub> composite nanofibers. *Sens. Actuat. B*. Pages 500–511.

- [55] Jagdale P., Ziegler D., Rovere M., Tulliani J. M., Tagliaferro A. (2019) Waste coffee ground biochar: a material for humidity sensors. *Sensors*. Pages 801-816.
- [56] Hu B., Wang K., Wu L., Yu S.-H., Antonietti M., Titirici M.-M. (2010) Engineering carbon materials from the hydrothermal carbonization process of biomass. *Adv. Mater.* Pages 813–828.
- [57] Murthy P. S., Naidu M. (2012) Sustainable management of coffee industry by-products and value addition—A review. *Resour. Conserv. Recycl.* Pages 45–58.
- [58] Halstead T. Coffee: World Markets and Trade. Available online: <https://www.fas.usda.gov/data/coffee-world-markets-and-trade> (Visited on 14th of October 2018).
- [59] Farah A. (2012) Coffee constituents. in coffee: emerging health effects and disease prevention; Yi-Fang Chu, Ed.; IFT Press series; Wiley: Oxford, UK. ISBN 9780470958780.
- [60] Clifford M. N., Ramirez-Martinez J. R. (1991) Phenols and caffeine in wet-processed coffee beans and coffee pulp. *Food Chem.* Pages 35–42.
- [61] Clifford M. N., Kazi T. (1987) The influence of coffee bean maturity on the content of chlorogenic acids, caffeine and trigonelline. *Food Chem.* Pages 59–69.
- [62] Duarte G., Pereira A., Marques V., Farah A. (2008) Comparison of chlorogenic acids contents in *Coffea arabica*, *Coffea canephora* and hybrids resistant to *Meloidogyne exigua*. 22nd Int. Conf. Coffee Sci. ASIC 2008, Campinas, SP, Brazil. Pages 508–512.
- [63] Lindinger Y. C., Jordan A. (2002) Analysing the headspace of coffee by proton-transfer-reaction mass-spectrometry. *Int. J. Mass Spectrom.* Pages 223–224, 115–139.
- [64] Clarke R.J. Coffee; Clarke, R. J., Ed.; (1987) Volume 1.; Springer: Netherlands. ISBN 978-9401086936.
- [65] Figueroa G. A., Homann T., Rawel H. M. (2016) Coffee production wastes: potentials and perspectives. *Austin Food Sci.* Pages 1014–1018.
- [66] Kondamudi N., Mohapatra S. K., Misra M. (2008) Spent coffee grounds as a versatile source of green energy. *J. Agric. Food Chem.* Pages 11757–11760.
- [67] Mussatto S. I., Machado E. M. S., Martins S., Teixeira J. A. (2011) Production, composition, and application of coffee and its industrial residues. *Food Bioprocess Technol.* Pages 661–672.
- [68] Mussatto S. I., Dragone G., Roberto I. C. (2006) Brewers' spent grain: generation, characteristics and potential applications. *J. Cereal Sci.* Pages 1–14.
- [69] Afify A. S., Ahmad S., Khushnood R. A., Jagdale P., Tulliani J.-M. (2017) Elaboration and characterization of novel humidity sensor based on micro-carbonized bamboo particles. *Sens. Actuat. B.* Pages 1251–1256.

- [70] Kemp K. C., Bin B. S.; Lee W.-G., (2015) Meyyappan M., Kim K. S. Activated carbon derived from waste coffee grounds for stable methane storage. *Nanotechnology*. Pages 385602.
- [71] Jagdale P., Sharon M., Kalita G., Maldar N. N. S. M. (2012) Carbon nano material synthesis from polyethylene by chemical vapor deposition. *Adv. Mater. Phys. Chem*. Pages 1–10.
- [72] Parascanu M. M., Sandoval-Salas F., Soreanu G., Valverde J. L., Sanchez-Silva L. (2017) Valorization of Mexican biomasses through pyrolysis, combustion and gasification processes. *Renew. Sustain. Energy Rev*. Pages 509–522.
- [73] Shah J., Kotnala R. K., Singh B., Kishan H. (2007) Microstructure-dependent humidity sensitivity of porous  $\text{MgFe}_2\text{O}_4\text{-CeO}_2$  ceramic. *Sens. Actuat. B*. Pages 306–311.
- [74] Traversa E., Sadaoka Y., Carotta M. C., Martinelli G. (2000) Environmental monitoring field tests using screen-printed thick-film sensors based on semiconducting oxides. *Sens. Actuat. B*. Pages 181–185.
- [75] Lukaszewicz J. P. (1999) Carbon-film-based humidity sensor containing sodium or potassium. Recovery effect. *Sens. Actuat. B*. Pages 184–190.
- [76] Llobet E., Barberà-Brunet R., Etrillard C., Létard J. F., Debéda H. (2014) Humidity sensing properties of screen-printed carbon-black an Fe(II) spin crossover compound hybrid films. *Procedia Eng*. Pages 132–135.
- [77] Zhang X., Ming H., Liu R., Han X., Kang Z., Liu Y., Zhang Y. (2013) Highly sensitive humidity sensing properties of carbon quantum dots films. *Mater. Res. Bull*. Pages 790–794.
- [78] Epeloa J., Repetto C. E., Gómez B. J., Nachez L., Dobry A. (2018) Resistivity humidity sensors based on hydrogenated amorphous carbon films. *Mater. Res*. Pages 025604.

# Appendix A

## Abbreviations

SWP700	OSR700	WBCP	CGB
pyrolyzed mixed softwood pellets	oil seed rape	waste brewed coffee powder	coffee ground biochar

# List of Tables

**Table 1.** Variations in impedance, response and recovery times at different operating T in dry air and 50 ppm of NH<sub>3</sub>.

**Table 2.** Co<sub>3</sub>O<sub>4</sub> R upon NH<sub>3</sub> 1, 2.5, 5, 10, 25 and 50 ppm at 225°C and its response and recovery times.

**Table 3.** Cross-sensitivity tests for Co<sub>3</sub>O<sub>4</sub> film at the optimal operating T.

**Table 4.** Comparison of the NH<sub>3</sub> sensing features of Co<sub>3</sub>O<sub>4</sub> from the state of the art.

**Table 5.** Cumulative particle size equal to d<sub>10</sub>, d<sub>50</sub> and d<sub>90</sub> for AC-ZnO and HT-ZnO.

**Table 6.** Sensor response, response and recovery times at different operational T in dry air and 250 ppb of NO<sub>2</sub> for AC-ZnO and HT-ZnO sensors.

**Table 7.** Comparison of the NO<sub>2</sub> sensing performances of ZnO films working at low T.

.

# List of Figures

**Figure 1.** CuBr sensor for NH<sub>3</sub> monitoring in which NH<sub>3</sub> evaporated in the lungs and exhaled in the device where the interaction with Cu<sup>+</sup> occurs.

**Figure 2.** Crystal structure of Co<sub>3</sub>O<sub>4</sub>.

**Figure 3.** TG-DSC curve of Co<sub>3</sub>O<sub>4</sub> annealed at 600°C for 4 h in static air.

**Figure 4.** XRD analysis of Co<sub>3</sub>O<sub>4</sub> powder pretreated at 250°C for 20 minutes (a), annealed at 600°C for 4 h in static air (b) and then subsequently fired at 700°C for 1 hour (c).

**Figure 5.** Raman spectroscopy of Co<sub>3</sub>O<sub>4</sub> pretreated at 600°C for 4 h in static air.

**Figure 6.** HR XPS spectra of Co<sub>3</sub>O<sub>4</sub> calcined at 600°C for 4 h in static air: O<sub>1s</sub> (a) and Co<sub>2p</sub>.

**Figure 7.** TG curves of water-adsorption tests carried out for Co<sub>3</sub>O<sub>4</sub> calcined at 600°C for 4 h in static air: blank test (a), Co<sub>3</sub>O<sub>4</sub> at 30°C (b), Co<sub>3</sub>O<sub>4</sub> at 250°C (c).

**Figure 8.** FESEM images of Co<sub>3</sub>O<sub>4</sub> powder: low magnification, 25 kx (a); high magnification, 100 kx (b); and of Co<sub>3</sub>O<sub>4</sub> film: low magnification, 25 kx (c); high magnification, 100 kx (d).

**Figure 9.** Co<sub>3</sub>O<sub>4</sub> sensor (0.85x1.7cm).

**Figure 10.** Co<sub>3</sub>O<sub>4</sub> sensor response at different working T (150-250°C) towards 50 ppm NH<sub>3</sub> in dry air.

**Figure 11.** Impedance's variations upon different ammonia concentrations exposure (1, 2.5, 5, 10, 25 and 50 ppm) at 225°C.

**Figure 12.** Calibration curve of Co<sub>3</sub>O<sub>4</sub> sensor towards NH<sub>3</sub> at 225°C.

**Figure 13.** Long term stability and repeatability of Co<sub>3</sub>O<sub>4</sub> film upon 5 ppm of NH<sub>3</sub> after 9 months from the fabrication.

**Figure 14.** Polar plot of Co<sub>3</sub>O<sub>4</sub> cross sensitivity measurements at 225°C.

**Figure 15.** Changes in impedance for Co<sub>3</sub>O<sub>4</sub> film upon 90% of RH and 25 and 1 ppm of NH<sub>3</sub> at 225°C.

**Figure 16.** Baseline effect of humidity in the sensor response of Co<sub>3</sub>O<sub>4</sub> film upon 1-5 ppm of NH<sub>3</sub>.

**Figure 17.** Effects of NO<sub>2</sub> exposure on human lungs.

**Figure 18.** ZnO crystal phases: wurtzite (a), zinc blende (b), rocksalt (c).

**Figure 19.** ZnO particle size distributions of AC-ZnO (a) and HT-ZnO (b).

**Figure 20.** TG-DTA curve in static mode of AC-ZnO powder heated at 300°C for 30 minutes (10°C/min): TG continue line, DTA dashed line.

**Figure 21.** XRD pattern of HT-ZnO (blue line) and AC-ZnO (black line).



**Figure 22.** FESEM observations of AC-ZnO powder at low (25kx, a) and high (150kx, b) magnifications. Images of AC-ZnO sensor at low (25kx, c) and high (150kx, d) magnifications.

**Figure 23.** FESEM observations of HT-ZnO powder at low (25kx, a) and high (80kx, b) magnifications. Images of HT-ZnO sensor at low (25kx, c) and high (200kx, d) magnifications.

**Figure 24.** Images of screen-printed sensors AC-ZnO (a) and HT-ZnO (b).

**Figure 25.** Sensor response at different working T (50-250°C) upon 250 ppb NO<sub>2</sub> in dry air.

**Figure 26.** Impedance variations upon different NO<sub>2</sub> concentrations exposure (50-500 ppb) at 225°C.

**Figure 27.** Calibration curves of AC-ZnO (black) and HT-ZnO (blue) sensors.

**Figure 28.** Cross sensitivity test of AC-ZnO (black) and HT-ZnO (blue) sensors.

# Chapter 7 - NH<sub>3</sub> and NO<sub>2</sub> sensors

## Abstract

From chapter 5, the main gas interferences for the proposed indium oxide-based O<sub>3</sub> sensors are humidity, ammonia and nitrogen dioxide. For this reason, in the previous chapter 6 three solutions based on biochar for humidity detection were presented.

On the opposite, in this last chapter, results of the development of NH<sub>3</sub> and NO<sub>2</sub> Semiconducting metal oxides (SMOx) thick films are described, by using respectively Co<sub>3</sub>O<sub>4</sub> synthesized by autocombustion sol-gel route and ZnO prepared by auto-combustion sol-gel and hydrothermal route. Part of this paragraph is taken from [1].

Compounds of nitrogen are released as NO<sub>x</sub> and NH<sub>3</sub>. The former are the main acidifying constituents causing eutrophication of ecosystems, while the latter is the solely base gas in troposphere. Eutrophication is an enrichment of nutrients, caused by reactive N compounds in air, that damages the ecosystems.

## 7.1 Ammonia detection

In this section, results of nano-crystalline Co<sub>3</sub>O<sub>4</sub> spinel synthesized by auto combustion synthesis and for ammonia detection are presented. After synthesis, the powder was annealed for 4 hours at 600°C and characterized by TG-DSC, XRD, Raman spectroscopy, XPS, nitrogen adsorption, H<sub>2</sub>O adsorption and FESEM. Sensors were fabricated by screen-printing method on  $\alpha$ -Al<sub>2</sub>O<sub>3</sub> dielectric substrates with Pt electrodes and fired at 700°C for 1 h in air. The sensor response was determined between 150°C and 250°C under 1 – 50 ppm of ammonia. The optimum operating temperature was 225°C, with R ( $Z_g/Z_0$ ) of 1.83 under 50 ppm NH<sub>3</sub> and sensor response of 1.1 under 1 ppm of NH<sub>3</sub> in dry conditions.  $\tau_{ads}$  and  $\tau_{des}$  were quite short (few minutes), and cross-sensitivity tests upon CH<sub>4</sub>, CO, N<sub>2</sub>O, RH, O<sub>3</sub>, CO<sub>2</sub> and NO<sub>2</sub> exposure at the optimum working T were evaluated. The sensor displays superior selectivity for ammonia, with a modest cross-sensitivity towards humidity. Since it can detect up to 1 ppm also under 90% of RH, it is proposed both as a cheap and portable solution for human breath monitoring and in ammonia determination in soils.

### 7.1.1 NH<sub>3</sub> issue

Ammonia (NH<sub>3</sub>) is a natural gas originated both from biogenic and anthropogenic sources.

In 2011, the European Environment Agency (EEA) stated that agriculture (especially animal husbandry) was accountable for 93.6% of total NH<sub>3</sub> emissions in the environment considering the 33-member nations [2].

NH<sub>3</sub> is produced mainly in soils from bacteria that decompose organic matter, and it is also present in the troposphere because of many human activities. In fact, this weak basic gas is emitted in the troposphere from wastes, road transportations and particularly in automobile exhaust and industrial manufactures. Furthermore, NH<sub>3</sub> is also widely utilized as refrigerant gas [3] for its vaporization properties. Ammonia is a precursor of nitrogenous compounds like nitric acid (utilized mainly for fertilizer and explosives), urea, amino acids, acrylonitrile, phenol, hydrazine, hydrogen cyanide and ammonium carbonate.

NH<sub>3</sub> finds applications as a cleaner for many surfaces, in the fermentation industry, it is a strong antimicrobial agent for food products and it is widely employed to scrub SO<sub>2</sub> from the burning of fossil fuels resulting in an ammonium sulfate used as fertilizer. It assists in providing enhanced yields of crops like maize and wheat when it is used in soils. Finally, this gas is also used in the neutralization of the nitrogen oxide (NO<sub>x</sub>) pollutants from diesel engines, in woodworking, as respiratory stimulant, energy carrier and lifting gas, in addition to the treatment of cotton materials.

NH<sub>3</sub> is a common air pollutant. In fact, when its concentration in the troposphere exceeds 25 ppm, it damages the mucosa of respiratory tract, irritates eyes and skin, causing laryngospasms and bronchiectasis. In the worse cases, it can even induce death in humans [4-6]. As a consequence, the time-weighted average (TWA) over 8 h should not overcome 25 ppm and the short-term exposure over 15 minutes is limited to 25–35 ppm [3].

Nonetheless, NH<sub>3</sub> is normally present in human body mostly in form of NH<sub>4</sub><sup>+</sup> that is detoxified by the liver and transformed into urea to be excreted by kidneys. A small part of ammonia in human body is in the form of gas, and it can pass through cellular membranes including the blood-brain barrier. This phenomenon is enhanced if hepatic diseases take place. The detection of ammonia in human breath provides early screening test for hepatic diseases since NH<sub>3</sub> acts as a biomarker characteristic for the blood urea nitrogen (BUN). It is adopted in non-invasive clinical diagnostics [7], like in end-stage renal disease (ESRD) monitoring [8], in halitosis [9], determination of *Helicobacter pylori* presence [10] and in the diagnosis of hepatic injury, cirrhosis and encephalopathy [11].

In the exhaled breath, the concentration of NH<sub>3</sub> varies from 0.4–1.8 ppm in healthy humans and 0.82–14.7 ppm for ESRD patients [12].

In this frame, strategies for NH<sub>3</sub> detection are extremely appropriate to combustion, environmental, and health industries [4]. There is a strong need to realize cheap environmental NH<sub>3</sub> detectors.

Thus, the industry of transportation is engaged in monitoring NH<sub>3</sub> from air quality control, exhaust emissions and in innovative lean-burn combustion motors, in which the exhaust gas processing implies the addition of NO<sub>x</sub> to NH<sub>3</sub>.

Several principles of measurement have been used for ammonia detection, consisting of optical spectroscopy, electro-chemistry and wet-chemistry approaches. A markedly intriguing application for analytical devices is the monitoring of NH<sub>3</sub> in the human breath. [13]. In fact, single breath markers need to be detected at trace

levels with high selectivity to other breath compounds and in the presence of high RH amounts (typically 89 - 97%) [14, 15].

The current applied technologies are constituted by three main categories (i.e. mass spectrometry (MS) or gas chromatography-based (GC) methods, laser-adsorption spectroscopic methods and chemical sensors [16]).

Nevertheless, the drawback of the former two technologies is their incapability to analyze breath in real-time.

Other technologies like proton transfer reaction mass spectrometry (PTR-MS) [17], proton transfer reaction time-of-flight mass spectrometry (PTR-TOF-MS) [18] and selective ion flow tube mass spectrometry (SIFT-MS) [19] are limited because of their cost, complexity in application and furthermore they are not portable systems. For this goal, chemoresistive gas sensors based on MOS are very intriguing for their low-cost, simplicity and miniaturization in portable breath analyzers [16].

However, in order to be applied to human breath, some features must be accomplished, such as great sensitivity, low limit of detection and elevated selectivity to the target marker in the complex mixture of breath in humid conditions. In the human breath many species are present such as acetone, CO, HCN, NO, ethane, DMS (dimethylsulphur) CO<sub>2</sub> and many others [16].

Up to now, MOS like n-type WO<sub>3</sub> [20–22], SnO<sub>2</sub> [23, 24], In<sub>2</sub>O<sub>3</sub> [25,26], ZnO [27,28], TiO<sub>2</sub> [29], MoO<sub>3</sub> [30] together with p-type Cr<sub>2</sub>O<sub>3</sub> [31], NiO [32], CuO [33], have been investigated as sensitive elements for ammonia detection.

One of the most interesting prototypes was developed by Fujitsu [34] for breath analysis. It consists in a p-type resistive CuBr sensor, with humidity and pressure-temperature sensors connected with a low-energy Bluetooth module and a battery for data transmission to a smartphone. Sensitivity in the range 100-1000 ppb was achieved and the principle of measure is displayed in Figure 1.

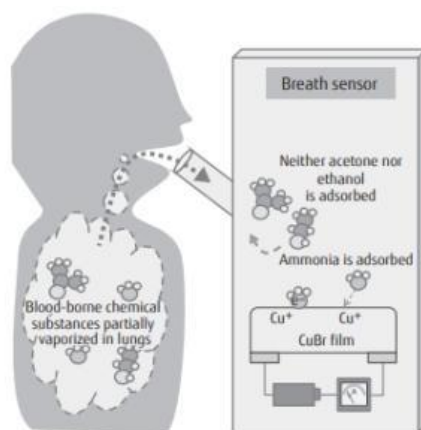


**Figure 1.** CuBr sensor for NH<sub>3</sub> monitoring in which NH<sub>3</sub> evaporated in the lungs and exhaled in the device where the interaction with Cu<sup>+</sup> occurs [34].

By tailoring the material characteristics (i.e. particle size, morphology and phase composition) in the synthesis, and by optimizing the operational parameters, the above requirements for sensor performance can be satisfied.

This development was recently reported with a portable device based on  $\text{WO}_3$  as breath detector for acetone which relates with accuracy to blood glucose before breakfast test [35].

### 7.1.2 $\text{Co}_3\text{O}_4$ characteristics and synthesis

Among SMOx, p-type semiconductors with great catalytic activity and important solubility of  $\text{O}_2$  can be adopted efficiently to fabricate ammonia sensors with high-performance.

Cobalt oxide,  $\text{Co}_3\text{O}_4$ , has reported great consideration by reserachers for its great strenght towards corrosion, large availability l and non-toxicity.

$\text{Co}_3\text{O}_4$  is a antiferromagnetic mixed valence oxide and is  $\text{CoO}\cdot\text{Co}_2\text{O}_3$  is its formula. The crystal structure is that of the characteristics spinel, with  $\text{Co}^{2+}$  in tetrahedral (8a) and  $\text{Co}^{3+}$  in the octahedral interstices (16d) of the CCP lattice (cubic close-packed) space group  $\text{O}_h^7 - \text{Fd}3\text{m}$ . Finally, the 32  $\text{O}^{2-}$  ions occupy 32(e) sites [35]. An image of its crystal structure is illutrated in Figure 2.

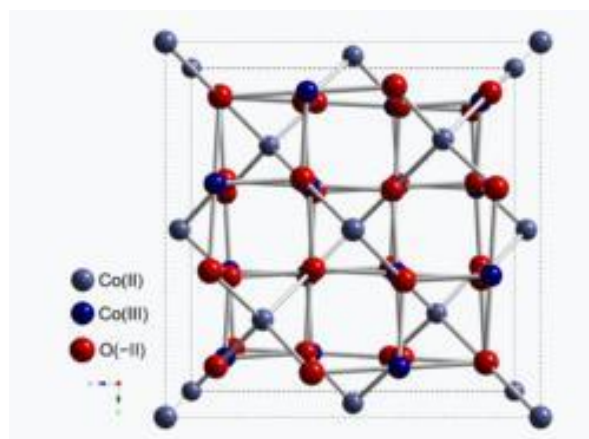


**Figure 2.** Crystal structure of  $\text{Co}_3\text{O}_4$  [36].

$\text{Co}_3\text{O}_4$  is a promising metal oxide that finds application in Li-ion batteries [37], catalysts [38], and gas sensors [39, 40].

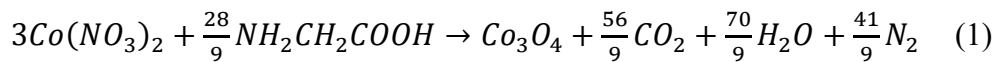
$\text{Co}_3\text{O}_4$  exhibits a great catalytic activity as oxidant [38], and it is designable for improving the sensing features such as gas response and selectivity [41, 42].

Nevertheless, most reports on the  $\text{Co}_3\text{O}_4$  sensors indicate applications in high operational temperature (i.e., above  $300^\circ\text{C}$ ).

Several nanostructures of  $\text{Co}_3\text{O}_4$  have been studied so far. They include microspheres [43], nanofiber [44], nanowires [38], nanotube [37], nanobelt [45], nanorods [46], and nano-sheets [47] using various synthesis methods such as hydrothermal synthesis, thermal oxidation, electrospinning and inverse microemulsion.

In this thesis nano-crystalline  $\text{Co}_3\text{O}_4$  spinel was obtained by sol-gel combustion route and utilized as  $\text{NH}_3$  sensitive MOS. Combustion route is an easy, interesting and intriguing method for realizing several inorganic nanomaterials with high purity. Moreover, it is adaptable to different supports for the manufacture of

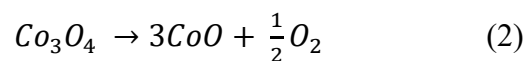
structured catalysts or chemical sensors [48, 49]. The synthesis route consists in the chemistry of propellant. A self-propagating exothermic reaction indeed begins typically in an aqueous or in a sol-gel system next to a quick thermal treatment, producing nanocrystalline materials with high purity [50, 51]. This process is facily tunable, extremely versatile and efficient, permitting a fine-control of the characteristics of the final compounds. Combustion route is a green, scalable and sustainable technique, in agreement with the principles of circular economy [52].  $\text{Co}_3\text{O}_4$  was obtained by combustion route by mixing glycine ( $\text{NH}_2\text{CH}_2\text{COOH}$ ,  $\geq 99\%$  purity, Sigma-Aldrich) - the organic fuel- with cobalt nitrate ( $\text{Co}(\text{NO}_3)_2 \cdot 6\text{H}_2\text{O}$ ,  $\geq 98\%$  purity, Sigma-Aldrich) -the oxidizer- in an aqueous medium.  $\frac{1}{4}$  of the stoichiometric glycine was added [53], in accordance with the following reaction (eq. 1):



Glycine keep the mixture at the proper level of homogeneity avoiding the precipitation of ions in the first step of the combustion. In addition, it reacts with nitrate during the combustion, in accordance with the chemistry of propellants [49, 53]. Firstly, all reagents were dissolved in an aqueous solution by mixing at  $120^\circ\text{C}$  till a gel was obtained. The mixture was subsequently put at  $250^\circ\text{C}$  in an oven to initiate the reaction. After 20 minutes, a fine powder was obtained [54]. The obtained powder was subsequently manually milled in an agata mortar with an agata pestle. At the end, cobalt spinel precursor was calcined at  $600^\circ\text{C}$  for 4 h in static air resulting in a black and fine powder.

### 7.1.3 $\text{Co}_3\text{O}_4$ powder and film characterization

Figure 3 shows TG-DSC curve of the pre-annealed under static air cobalt oxide powder for 4 h at  $600^\circ\text{C}$ . TG curve shows a first mass loss of around 2% in the range  $300^\circ\text{C}$ - $650^\circ\text{C}$ , generated by the combustion of precursors residues still present. Thus, a second weight loss was detected at higher temperature, between  $900^\circ$  and  $930^\circ\text{C}$ , when  $\text{Co}_3\text{O}_4$  decompose into  $\text{CoO}$  according to equation (2):



The mass loss of this step of decomposition is 6.3 wt%, similar to the theoretic 6.6 wt%. The whole mass loss is circa 8%. DSC curve shows one minute exothermic signal at  $310^\circ\text{C}$  that may be attributable to the combustion of residual carbonaceous material and a sharp endothermic peak with maximum at  $918^\circ\text{C}$  that is due to the decomposition of spinel into  $\text{CoO}$ , e.g. a thermal reduction of  $\text{Co}^{3+}$  to  $\text{Co}^{2+}$  as previously described [55].

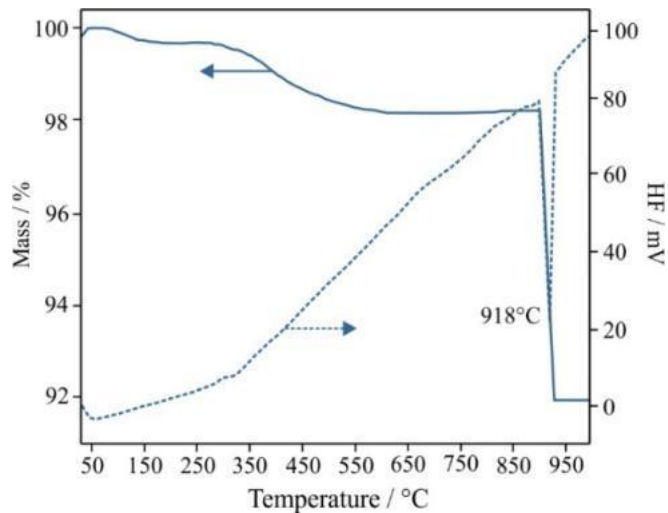


**Figure 3.** TG-DSC curve of  $\text{Co}_3\text{O}_4$  annealed at  $600^\circ\text{C}$  for 4 h in static air [1].

The formation as well as the crystallization of  $\text{Co}_3\text{O}_4$  phase after an heat treatment at  $250^\circ\text{C}$  for 20 min, after calcination at  $600^\circ\text{C}$  for 4 h and after additional annealing at  $700^\circ\text{C}$  for 1 h (with the identical thermal treatment of the fabricated thick layers) are demonstrated by XRD investigation illustrated in Figure 4.

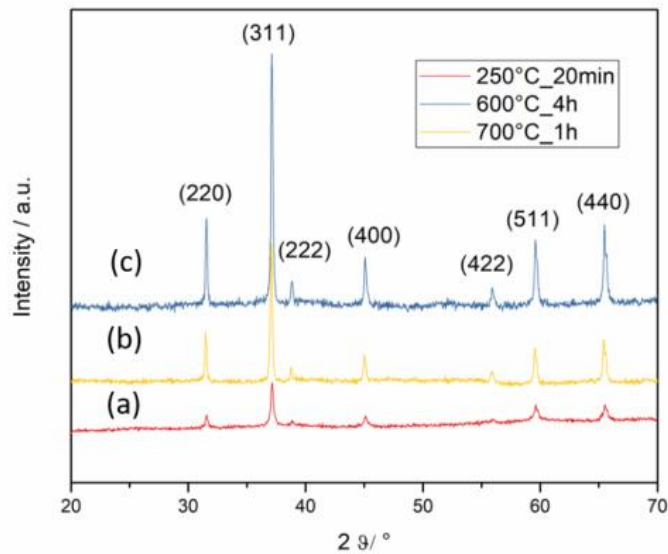


**Figure 4.** XRD analysis of  $\text{Co}_3\text{O}_4$  powder pretreated at  $250^\circ\text{C}$  for 20 minutes (a), annealed at  $600^\circ\text{C}$  for 4 h in static air (b) and then subsequently fired at  $700^\circ\text{C}$  for 1 hour (c) [1].

The XRD pattern of  $\text{Co}_3\text{O}_4$  assess the crystallization of the cubic  $\text{Co}_3\text{O}_4$  phase in the  $\text{Fd}3\text{m}$  space group (JCPDF file n°01-080-1533). The mean crystallite sizes, calculated by Scherrer equation, are 50 nm considering the powder heated at  $250^\circ\text{C}$  for 20 min, 76 nm for the sample calcined at  $600^\circ\text{C}$  for 4 h and 77 nm for powder fired at  $600^\circ\text{C}$  for 4 h and subsequently at  $700^\circ\text{C}$  for 1 h, respectively. The latter calcination at  $700^\circ\text{C}$  affect mildly the crystallite size of the cubic  $\text{Co}_3\text{O}_4$  NPs.

Furthermore, the Raman analysis of the  $\text{Co}_3\text{O}_4$  strengthens the formation of  $\text{Co}_3\text{O}_4$ , revealing five main Raman peaks at 196, 483, 525, 623, and 692  $\text{cm}^{-1}$ , that correspond respectively to the  $\text{F}_{2g}$ ,  $\text{E}_g$ ,  $2\times\text{F}_{2g}$ , and  $\text{A}_{1g}$  modes of crystalline  $\text{Co}_3\text{O}_4$ , outlined in Figure 5 [56].

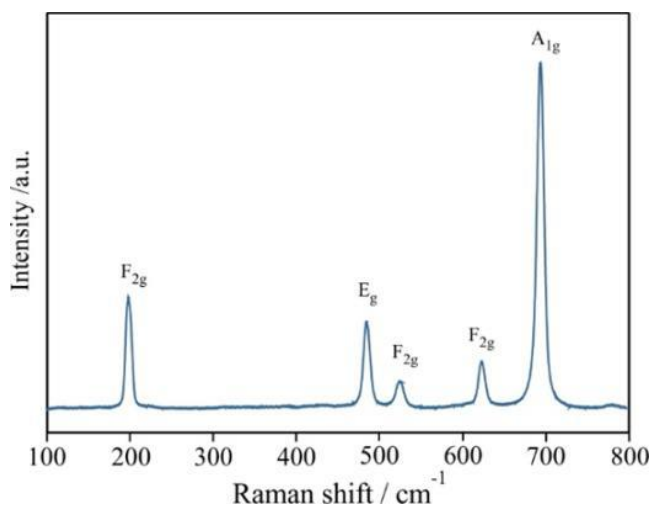


**Figure 5.** Raman spectroscopy of  $\text{Co}_3\text{O}_4$  pretreated at 600°C for 4 h in static air [1].

The chemical and electronic states of Co and O in  $\text{Co}_3\text{O}_4$  sample were studied by XPS analysis. The next Figure 6 displays the high-resolution spectra for O and Co, respectively.

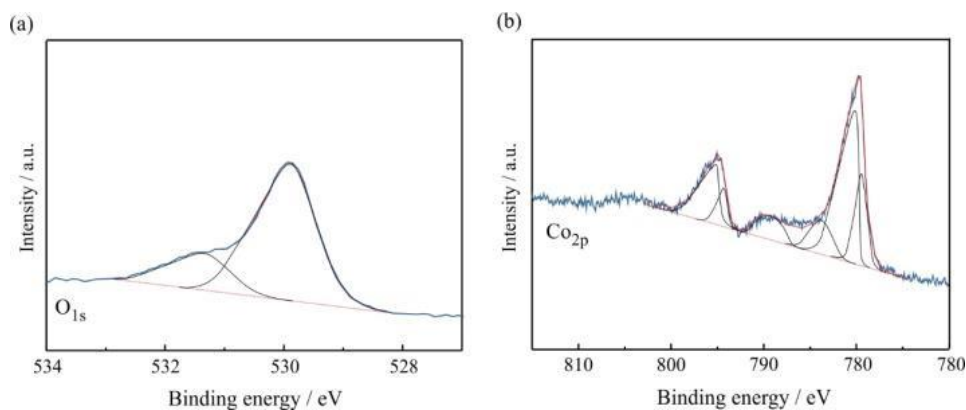


**Figure 6.** HR XPS spectra of  $\text{Co}_3\text{O}_4$  calcined at 600°C for 4 h in static air:  $\text{O}_{1s}$  (a) and  $\text{Co}_{2p}$  (b) [1].

In the case of O, the HR XPS spectrum illustrates asymmetric  $\text{O}_{1s}$  peak that can be deconvoluted into two components, a principal and a minor one, as illustrated in Figure 6a, at 529.7 and 531.6 eV, respectively. The first signal at the lower BE is due to  $\text{O}^{2-}$  ions in the  $\text{Co}_3\text{O}_4$ , enclosed by Co atoms, corresponding to oxygen lattice (O<sub>i</sub>) [57].



The peak at 531.6 eV is generated by  $O^{2-}$  ions in oxygen-deficient areas in the  $Co_3O_4$  that are oxygen vacancies and oxygen species respectively in adsorbed  $Co-OH$  and  $Co-H_2O$  [40, 58].

After the deconvolution of the  $Co_{2p}$  spectrum in high resolution, two main components at 780 and 795 eV were obtained. Those are generated by  $Co_{2p_{3/2}}$  and  $Co_{2p_{1/2}}$ , respectively (Figure 5b) [42, 43]. This pattern is characteristic of the  $Co_3O_4$  spinel arrangement with no  $CoO$  phase [58]. After the deconvolution of  $Co_{2p_{3/2}}$  signal into components generated by  $Co^{2+}$  (with a broad signal at 780.6 eV) and  $Co^{3+}$  (with a broad signal at 779.6 eV), the ratio  $Co^{2+}/(Co^{2+} + Co^{3+})$  is 0.21. This value is much below the theoretic value of 0.67 for  $Co_3O_4$ . Small  $Co^{2+}$  values can be a result of the sub-stoichiometric quantity of glycine utilized in the autocombustion process [59].

From  $N_2$  adsorption measurements on  $Co_3O_4$  powder, the SSA was equal to  $4.5\text{ m}^2\text{g}^{-1}$ .

The results of TGA water adsorption test carried out at  $30^\circ\text{C}$  and  $250^\circ\text{C}$  are illustrated in Figure 7.

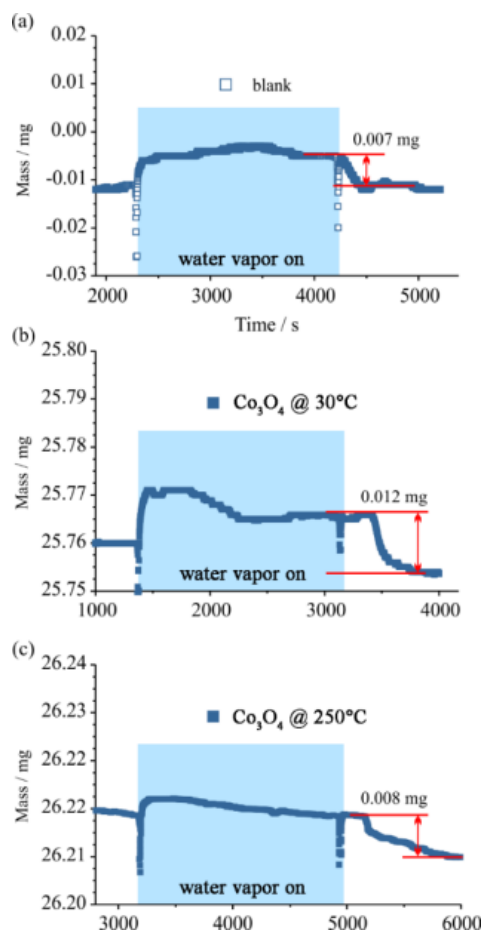


**Figure 7.** TG curves of water-adsorption tests carried out for  $Co_3O_4$  calcined at  $600^\circ\text{C}$  for 4 h in static air: blank test (a),  $Co_3O_4$  at  $30^\circ\text{C}$  (b),  $Co_3O_4$  at  $250^\circ\text{C}$  (c) [1].

After the introduction of 1 vol% of  $H_2O$  in Ar, the response of the system was investigated by carrying out firstly a blank test. The apparent alteration in the weight of the blank test was 0.007 mg (in Figure 7a). This value was subtracted from the

weight of adsorbed H<sub>2</sub>O measured for Co<sub>3</sub>O<sub>4</sub> sample (in Figure 7b, c). Taking into account the modest SSA value (4.5 m<sup>2</sup>g<sup>-1</sup>) of the Co<sub>3</sub>O<sub>4</sub>, a surface concentration of 1 and 0.3 reversibly adsorbed H<sub>2</sub>O molecule per nm<sup>2</sup> was calculated respectively at 30°C and 250°C [60].

This result assesses that water adsorption is modest on spinel surface, and water vapor represents a modest interference on sensing process both at room T and at 250°C.

The Co<sub>3</sub>O<sub>4</sub> powder and sensor morphologies were investigated by FESEM respectively in Figure 8a, b and 8c, d.

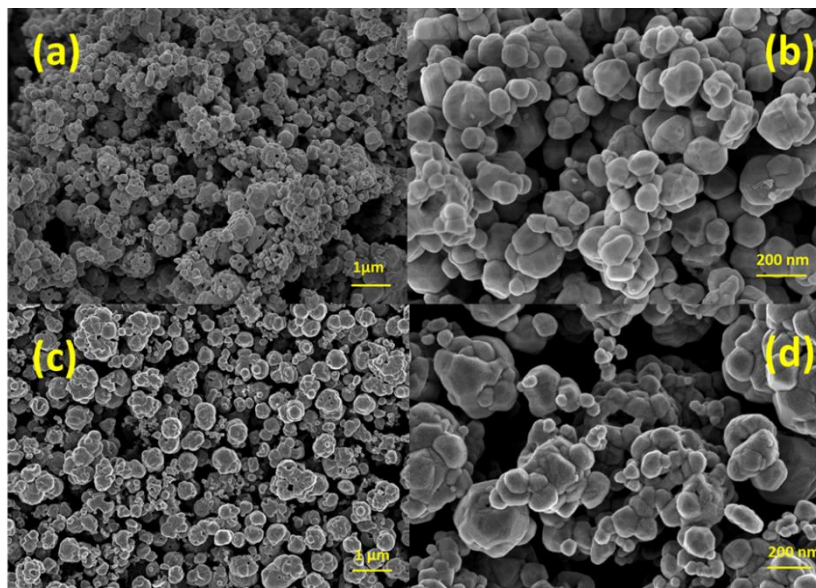


**Figure 8.** FESEM images of Co<sub>3</sub>O<sub>4</sub> powder: low magnification, 25 kx (a); high magnification, 100 kx (b); and of Co<sub>3</sub>O<sub>4</sub> film: low magnification, 25 kx (c); high magnification, 100 kx (d) [1].

The powder, after calcination at 600°C for 4 h, is constituted by clusters of crystals having the typical rombicuboctahedral shapes of the particles.

The crystals exhibit a heterogenous architecture, with edges not clearly delimited, that are generated by the liberation of gases in the auto-combustion procedure [49, 50]. FESEM analysis was carried out on the fabricated sensors fired at 700°C for 1 h (Figure 8c, d) disclosing that Co<sub>3</sub>O<sub>4</sub> grains possess their characteristics rombicuboctahedral morphology, with no modifications after the screen-printing deposition and thermal cycle.

Moreover, FESEM observations were also carried out ortogonally to screen-printed films and permitted to estimate the thickness of the film, that was  $20.6 \pm 2.7$  μm.

### 7.1.4 Co<sub>3</sub>O<sub>4</sub> gas sensing properties

Sensors were realized by screen printing method, as previously described, and after 700°C firing for 1 h, a satisfying adhesion of the film over the alumina substrate was achieved. An image of Co<sub>3</sub>O<sub>4</sub> spinel sensor is depicted in Figure 9.



**Figure 9.** Co<sub>3</sub>O<sub>4</sub> sensor (1x2 cm<sup>2</sup>).

Sensors were firstly tested towards NH<sub>3</sub> 50 ppm between 150 and 250°C, defining the best operating temperature. Subsequently, sensor was exposed towards diverse NH<sub>3</sub> amounts at the best working T, in the range 1-50 ppm, and results were compared with those of similar studies.

In Table 1 the sensor response, response and recovery times at different T are tabulated.

**Table 1.** Variations in impedance, response and recovery times at different operating T in dry air and 50 ppm of NH<sub>3</sub>.

Temperature (°C)	Z <sub>0</sub> (kΩ)	Z <sub>g</sub> (kΩ)	R (Z <sub>g</sub> /Z <sub>0</sub> )	τ <sub>ads</sub> (s)	τ <sub>des</sub> (s)
150	13.19	17.07	1.29	280	585
175	5.36	9.42	1.76	210	850
200	1.82	3.16	1.73	381	592
225	1.83	3.35	1.83	61	396
250	0.96	1.17	1.24	261	83

Co<sub>3</sub>O<sub>4</sub> sensor exhibits a p-type semiconductor behavior and its impedance was enhanced from about 0.96 until 13.19 kΩ, up to 1.17-17.07 kΩ upon exposure to NH<sub>3</sub> 50 ppm in dependence of the working T in dry air (Table 1). Taking into account the sensor's response together with τ<sub>ads</sub> and τ<sub>des</sub>, the best operating T corresponds to 225°C as illustrated in Figure 10 and Table 1.

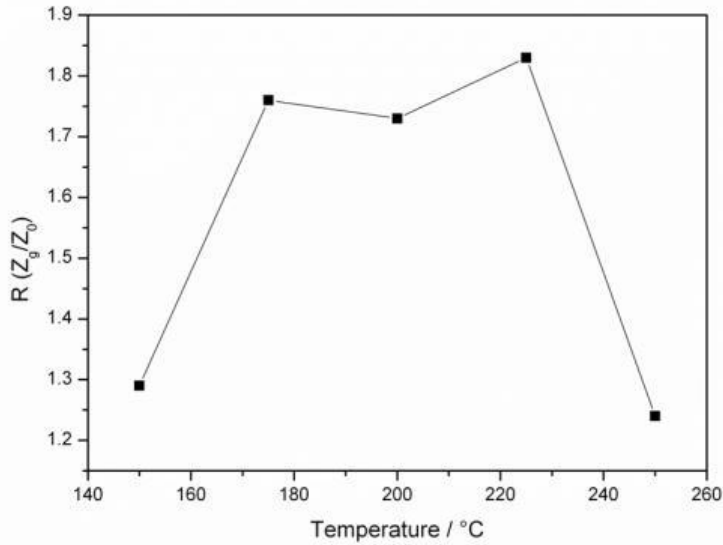


**Figure 10.** Co<sub>3</sub>O<sub>4</sub> sensor response at different working T (150-250°C) towards 50 ppm NH<sub>3</sub> in dry air [1].

At 225°C, under 50 ppm of NH<sub>3</sub> the  $\tau_{des}$  was not the fastest in literature (6 minutes and 36 seconds), while the  $\tau_{ads}$  was quite fast (around 1 minute). Those results are illustrated in Figure 11 and Table 1.

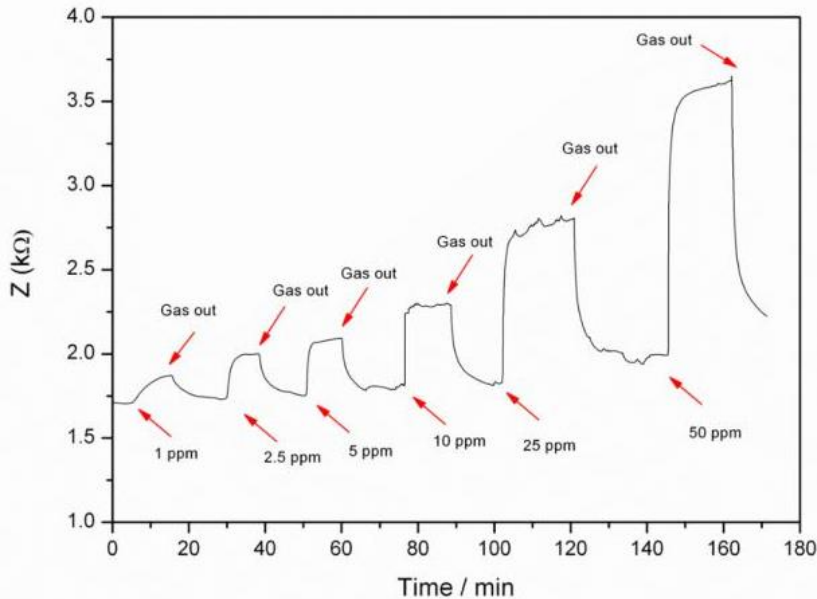


**Figure 11.** Impedance's variations upon different ammonia concentrations exposure (1, 2.5, 5, 10, 25 and 50 ppm) at 225°C [1].

Table 2 collects the Co<sub>3</sub>O<sub>4</sub> sensor performances upon NH<sub>3</sub> 1, 2.5, 5, 10, 25 and 50 ppm at 225°C in terms of initial and final impedance, sensor response, response and recovery times. Outcomes were utilized in order to evaluate the sensitivity of the Co<sub>3</sub>O<sub>4</sub> device. In accordance with the IUPAC, sensitivity of the Co<sub>3</sub>O<sub>4</sub> sensor was defined by the slope of the interpolation curve  $R=f([NH_3])$ , as depicted in Figure 12. The calibration curve is expressed as  $y=a+bx^c$  in the NH<sub>3</sub> interval of

concentration under investigation (1-50 ppm;  $R^2=0.998$ ) and the sensitivity is  $0.051 \text{ ppm}^{-1}$ .

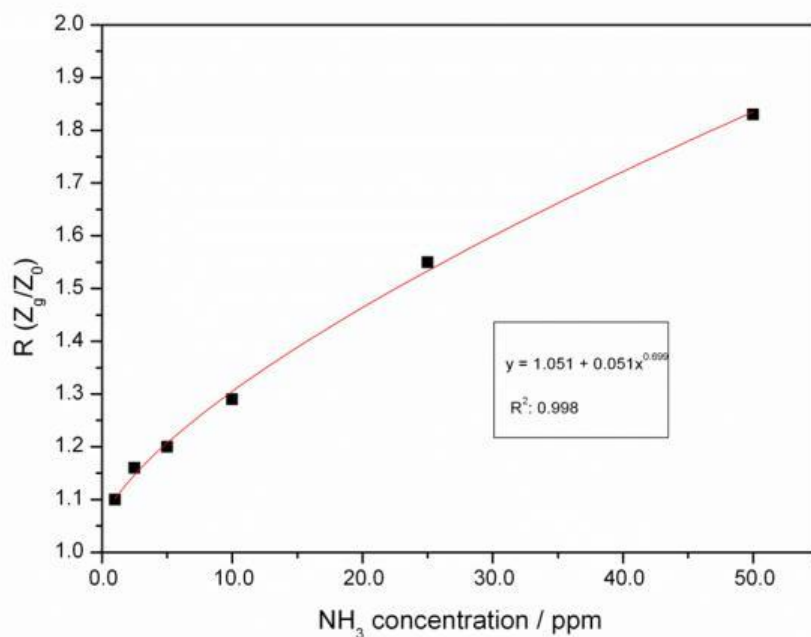


**Figure 12.** Calibration curve of  $\text{Co}_3\text{O}_4$  sensor towards  $\text{NH}_3$  at  $225^\circ\text{C}$  [1].

**Table 2.**  $\text{Co}_3\text{O}_4$  R upon  $\text{NH}_3$  1, 2.5, 5, 10, 25 and 50 ppm at  $225^\circ\text{C}$  and its response and recovery times.

$[\text{NH}_3]$	$Z_0(\text{k}\Omega)$	$Z_g(\text{k}\Omega)$	$R(Z_g/Z_0)$	$\tau_{\text{ads}}(\text{s})$	$\tau_{\text{des}}(\text{s})$
$\text{NH}_3$ 1 ppm	1.7	1.87	1.1	183	249
$\text{NH}_3$ 2.5 ppm	1.73	2	1.16	161	302
$\text{NH}_3$ 5 ppm	1.75	2.1	1.2	124	313
$\text{NH}_3$ 10 ppm	1.78	2.29	1.29	112	367
$\text{NH}_3$ 25 ppm	1.81	2.8	1.55	83	345
$\text{NH}_3$ 50 ppm	1.83	3.35	1.83	61	396

Furthermore, the long-term stability of  $\text{Co}_3\text{O}_4$  thick film was also studied, by exposing the  $\text{Co}_3\text{O}_4$  sensor upon 3 pulses of 5 ppm of  $\text{NH}_3$  after 9 months from the fabrication, as depicted in Figure 13.

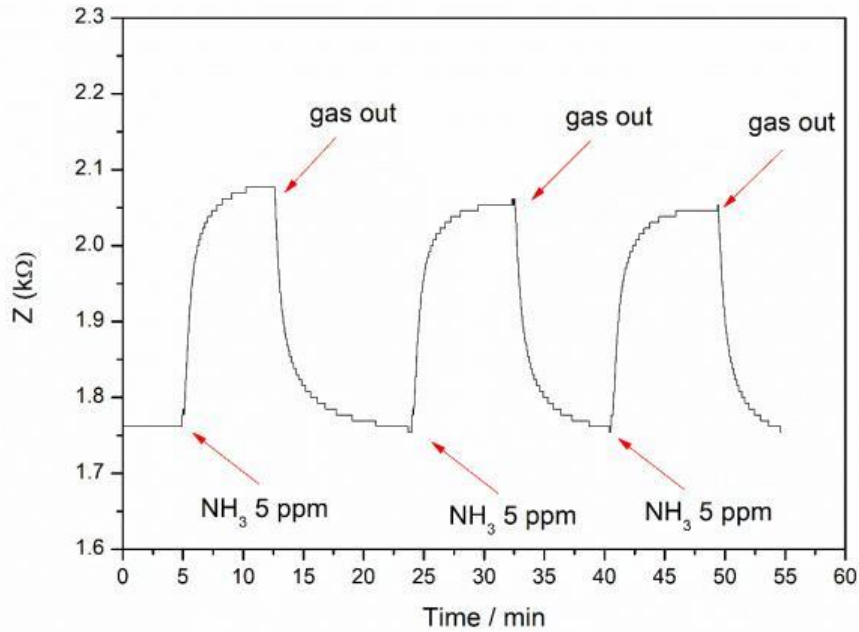


**Figure 13.** Long term stability and repeatability of  $\text{Co}_3\text{O}_4$  film upon 5 ppm of  $\text{NH}_3$  after 9 months from the fabrication [1].

The R upon 5 ppm of ammonia in dry environment is similar to the previous test ( $R = 1.19$  versus  $R = 1.2$ ). Thus, the as-fabricated  $\text{Co}_3\text{O}_4$  sensor exhibits a great repeatability between three pulses.

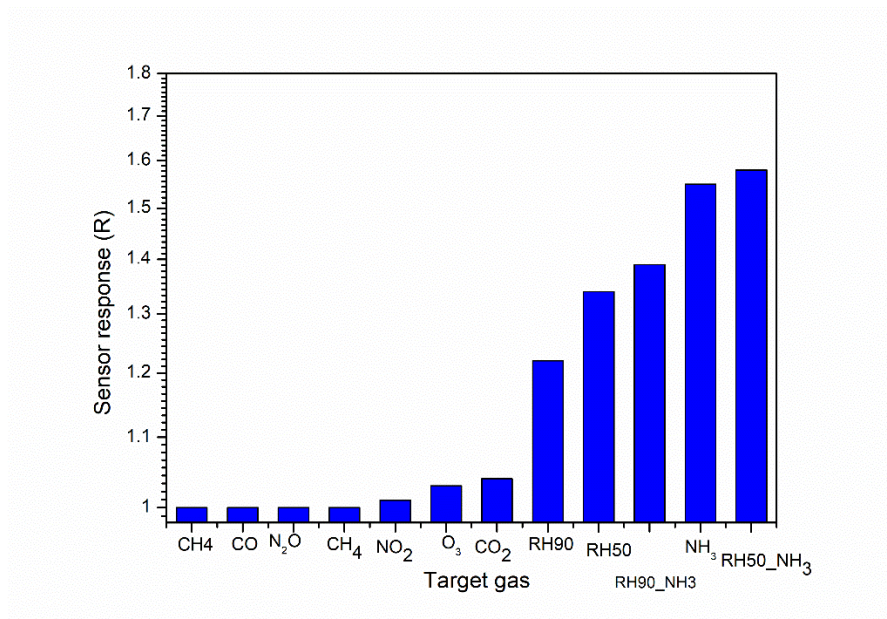
Since the evaluation of the MOS devices selectivity is essential for practical applications, diverse cross-sensitivity tests were performed at the best operational T of  $225^\circ\text{C}$ . Variations in the impedance of the  $\text{Co}_3\text{O}_4$  thick film were recorded after exposing the sensor for 10 min towards different gases and putting in comparison its Z under dry air over the identical period of time and results are tabulated in Table 3.

**Table 3.** Cross-sensitivity tests for  $\text{Co}_3\text{O}_4$  film at the optimal operating T.

Gas	$Z_o$ (k $\Omega$ )	$Z_g$ k $\Omega$	R	$\tau_{ads}$ (s)	$\tau_{des}$ (s)
$\text{CH}_4$ 100 ppm	1.83	1.83	1.00	n.d.	n.d.
CO 10 ppm	1.84	1.84	1.00	n.d.	n.d.
$\text{O}_3$ 0.5 ppm	1.83	1.78	1.03	n.d.	n.d.
$\text{NO}_2$ 0.1 ppm	1.85	1.88	1.02	18	54
$\text{N}_2\text{O}$ 15 ppm	1.85	1.85	1.00	n.d.	n.d.
$\text{CO}_2$ 500 ppm	1.83	1.76	1.04	127	102
RH 50%	1.86	2.5	1.34	276	291
$\text{NH}_3$ 25 ppm	1.81	2.80	1.55	83	345
$\text{NH}_3$ 25 ppm + RH 50%	1.86	2.94	1.58	784	456
RH 90%	1.87	2.28	1.22	157	162
$\text{NH}_3$ 25 ppm + RH 90%	1.87	2.60	1.39	321	290

NB: n.d. = not determined.

Thus, a hystogram of the selectivity measurements carried out at  $225^\circ\text{C}$  is illustrated in Figure 14 assessing an excellent selectivity for  $\text{NH}_3$  of the  $\text{Co}_3\text{O}_4$  thick layer also in humid environments (50% and 90% of RH).

**Figure 14.** Cross sensitivity of  $\text{Co}_3\text{O}_4$   $225^\circ\text{C}$  [1].

In Figure 14, NH<sub>3</sub> stands for 25 ppm of ammonia, CH<sub>4</sub> for 100 ppm of methane, CO for 10 ppm of carbon monoxide, N<sub>2</sub>O for 15 ppm of nitrous oxide, RH50 for 50% of relative humidity, RH90 for 90% of RH, O<sub>3</sub> for 0.5 ppm of ozone, NO<sub>2</sub> for 0.1 ppm of nitrogen dioxide and CO<sub>2</sub> for 500 ppm of carbon dioxide.

Surprisingly for common SMOx, Co<sub>3</sub>O<sub>4</sub> displays a great selectivity for NH<sub>3</sub> detection at ppm range, only in partial accordance with other studies [61-63]. These results are in accordance with water-adsorption tests performed on spinel cobalt oxide that exhibits an hydrophobic behavior, thus decreasing the interference towards RH. More in detail, a mild interference is due to H<sub>2</sub>O molecules, that are reducing agents on the Co<sub>3</sub>O<sub>4</sub> surface at 225°C, in accordance with TGA water adsorption experiments. As a matter of fact, when it interacts with 25 ppm of NH<sub>3</sub>, Co<sub>3</sub>O<sub>4</sub> sensor response is 1.55 with  $\tau_{ads}$  of 83 s, whereas upon 25 ppm of NH<sub>3</sub> in humid environment (50 RH%) the sensor response is almost the same, even if the  $\tau_{ads}$  enhances considerably till 784 s. This is a confirmation of the competition between ammonia and water as reductants for the identical Co<sub>3</sub>O<sub>4</sub> adsorption centres. Thus, the variations of the sensor response upon 25 and 1 ppm of NH<sub>3</sub> in a baseline of 90% RH was tested and Z changes are shown in the Figure 15.

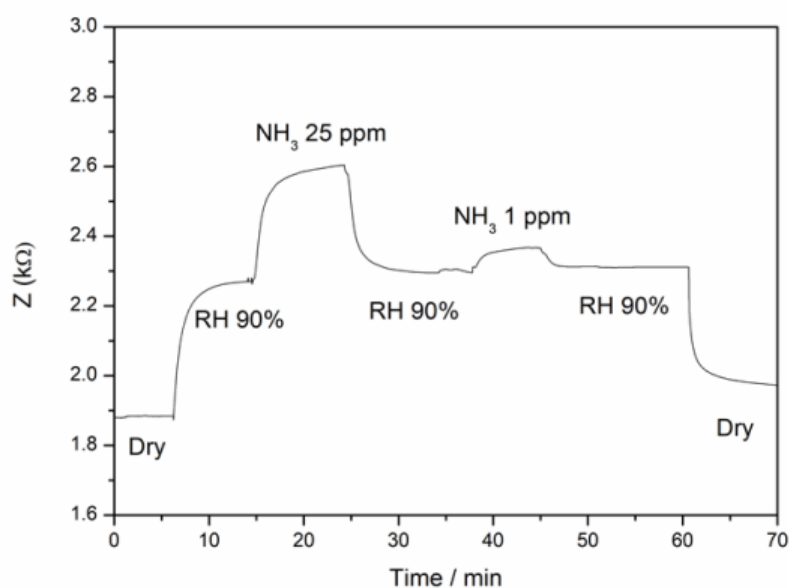


**Figure 15.** Changes in impedance for Co<sub>3</sub>O<sub>4</sub> film upon 90% of RH and 25 and 1 ppm of NH<sub>3</sub> at 225°C [1].

The spinel Co<sub>3</sub>O<sub>4</sub> sensor was put in a 90% RH condition and R was 1.14 (whereas R=1.55 in dry environment) demonstrating the competition between H<sub>2</sub>O and NH<sub>3</sub> for the identical sites of adsorption and also in this case the sensor displays a change in impedance of 3% when interacts with 1 ppm of NH<sub>3</sub> in 90% of RH.

The effect of the baseline humidity for the cobalt oxide sensor response in the range 1-5 ppm is reported in Figure 16.



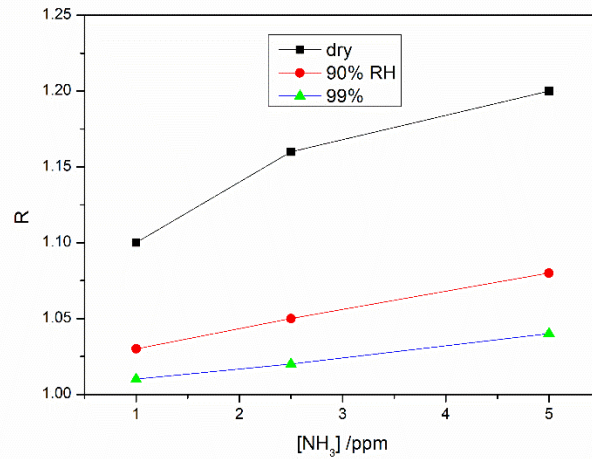


**Figure 16.** Baseline effect of humidity in the sensor response of  $\text{Co}_3\text{O}_4$  film upon 1-5 ppm of  $\text{NH}_3$  [1].

From the calibration curves, the sensor is still sensitive to  $\text{NH}_3$  1 ppm under strong humid conditions (90 and 99%) with sensitivity respectively equal to  $0.012$  and  $0.0076 \text{ ppm}^{-1}$  ( $0.051 \text{ ppm}^{-1}$  in dry conditions). These results confirm the exploitation of the as-realized sensor for breath monitoring, distinguishing the healthy human (ammonia concentration lower than 1 ppm) with respect to the ESRD patients. Moreover, these results support the utilisation of  $\text{Co}_3\text{O}_4$  as sensitive and selective metal oxide that can detect  $\text{NH}_3$  at ppm level in soils, where interferences with respect to  $\text{CH}_4$  and  $\text{N}_2\text{O}$  must be avoided.

At the end, , results of this thesis were put in comparison with other studies on  $\text{Co}_3\text{O}_4$ -based sensor for  $\text{NH}_3$  monitoring, and results are tabulated in Table 4.

**Table 4.** Comparison of the NH<sub>3</sub> sensing features of Co<sub>3</sub>O<sub>4</sub> from the state of the art.

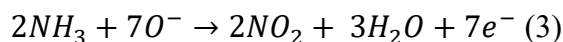
Technological route	Film thickness	Sensitivity (ppm <sup>-1</sup> )	Sensor response (R=Rg/Ro)	Conditions of measurements	Reference
Co <sub>3</sub> O <sub>4</sub> /polyethyleneimine-carbon nanotubes composites by hydrothermal synthesis	Thin film	n.d.	Ca. 1.35	R.T., 50 ppm	[35]
Hierarchical Co <sub>3</sub> O <sub>4</sub> by hydrothermal synthesis	Thick film	n.d.	Ca. 7	160°C, 50 ppm	[38]
Co <sub>3</sub> O <sub>4</sub> sol gel spin coated films technique	Thin film	n.d.	1.28	200°C, 50 ppm	[39]
Co <sub>3</sub> O <sub>4</sub> by precipitation route and annealing	Pellet	n.d.	Ca. 28.5	R.T., 60.6 ppm	[40]
Hybrid Co <sub>3</sub> O <sub>4</sub> /SnO <sub>2</sub> core-shell nanospheres by hydrothermal synthesis	Thick film	n.d.	Ca. 7.5	200°C, 50 ppm	[41]
Nano-sheet arrays of Co <sub>3</sub> O <sub>4</sub> by hydrothermal synthesis	5.2 μm	0.0819	Ca. 5.6	R.T., 60 ppm	[42]
Dumbbell-like Co <sub>3</sub> O <sub>4</sub> by hydrothermal synthesis	n.d.	n.d.	Ca. 1.4	R.T., 50 ppm	[43]
Co <sub>3</sub> O <sub>4</sub> thick film by combustion synthesis	20.6 μm	0.051	1.83	225°C, 50 ppm	This work

NB: R.T. = room temperature.

Comparing the results of this thesis with other studies related to Co<sub>3</sub>O<sub>4</sub> sensors for ammonia detection, the higher sensor response is typically obtained in the 150°-200°C range of T, even if in [35] and in [40] the highest response at ambient temperature were measured. These findings can be a result of a synergic effect of oxygen adsorption and electron transport in the Co<sub>3</sub>O<sub>4</sub>/polyethyleneimine-carbon nanotubes composites, and another explanation can be that the tested sensors were in the form of pellets. In [42] intriguing results were obtained operating at ambient T. Taking into consideration table 4, it seems that the fabrication of sensitive materials through hydrothermal route allow to achieve higher sensing performances compared to other methods of fabrications. This may be a result of the higher value of SSA obtained by these solutions. Nevertheless, one limit of hydrothermal route is the small quantity of product that can be synthesized in every batch (as described in the chapter 5). Therefore, the presented combustion synthesis is an intriguing procedure since it permits to overcome restrictions in the quantity of product synthesized in one batch when comparing with the HT route. This is a big advantage for manufacture of chemical sensors at industrial scale, where there is a need of large amounts of material.

In all impedance measurements performed, no variations in capacitance was measured and imaginary part was almost negligible.

When  $\text{Co}_3\text{O}_4$  thick film interacts with ammonia,  $\text{NH}_3$  reacts with the surface adsorbed species  $\text{O}^{2-}$  and  $\text{O}^-$  in order to generate  $\text{NO}_2$  and  $\text{H}_2\text{O}$  [41], permitting the trapped  $e^-$  to return to the CB (eq. 3).



This step decreases the density of holes, increasing the impedance of the film [41]. When  $\text{NH}_3$  molecules are removed from the surface, the re-adsorption of oxygen species allows fast recovering of the initial  $Z$ .

Generally, the  $\text{O}^-$  and  $\text{O}^{2-}$  adsorption on  $\text{Co}_3\text{O}_4$  generates a HAL and conduction occur principally across the near-surface of HAL. As a result, the chemo-resistive alterations of p-type MOS are smaller comparing with those generated at the electron-depletion layers of n-type MOS. Nevertheless, p-type metal oxides display the advantage to operate at lower temperature.

$\text{Co}_3\text{O}_4$  thick film exhibits peculiar catalytic activities that support the selective oxidation of  $\text{NH}_3$  as a consequence of the great affinity with oxygen and the possibility to present multivalent oxidation states.

Under oxidant gases (like  $\text{NO}_2$  and  $\text{O}_3$ ), the impedance of p-type semiconductors begin to drop. This is a result of an increase in the quantity of holes in the layer after ionosorption of oxidant gases. However, chemo-resistive changes of p-type MOS upon oxidant gases are quite small if we consider the gas sensing mechanism. This may justify the lack of sensor response upon  $\text{O}_3$  and  $\text{NO}_2$  species in  $\text{Co}_3\text{O}_4$  thick film devices [4].

For all those reasons, the proposed  $\text{Co}_3\text{O}_4$  sensor could find an usage in breath analysis in which a selective control of  $\text{NH}_3$  is needed at ppm concentration also considering to humidity and  $\text{CO}_2$  [46]. In addition, this sensor can exploit an efficient monitoring of  $\text{NH}_3$  content in soils where selectivity for ammonia is crucial among gases such as humidity,  $\text{CH}_4$  and  $\text{N}_2\text{O}$ .

## 7.2 Nitrogen dioxide detection

### Abstract

In this section, results of ZnO in wurtzite-like crystalline structure sensors are reported for  $\text{NO}_2$  detection at ppb-level. Sensor performances of ZnO sensors obtained by auto combustion sol-gel synthesis (AC-ZnO) and by hydrothermal route (HT-ZnO) are compared each other. After synthesis, powders were characterized by laser granulometry, DTA-TG, XRD and nitrogen adsorption. Thick film devices were manufactured by screen-printing on  $\alpha\text{-Al}_2\text{O}_3$  substrates equipped with Pt electrodes and fired at  $500^\circ\text{C}$  for 1 h in air. Morphologies of the fabricated thick film were investigated by FESEM. Sensor characteristics were studied between  $50^\circ\text{C}$  and  $250^\circ\text{C}$  under 250 ppb of  $\text{NO}_2$ . The optimum operating temperature was achieved at  $150^\circ\text{C}$ , with  $R (Z_g/Z_0)$  equal to 22.84 for AC-ZnO and 46.73 for HT-ZnO under 250 ppb of  $\text{NO}_2$  in dry conditions. Response and recovery

times were also defined, and cross-sensitivity tests by exposing the film towards CH<sub>4</sub>, CO<sub>2</sub>, N<sub>2</sub>O, humidity and O<sub>3</sub> at the best operating temperature. The sensor exhibits high sensitivity for nitrogen dioxide detection, supporting the exploitation of these sensors as nitrogen dioxide detectors in the sub-ppm level of NO<sub>2</sub>.

### 7.2.1 NO<sub>2</sub> issue

NO<sub>x</sub> plays an essential function in the generation of O<sub>3</sub>. Thus, those oxidant species produce part of the secondary inorganic aerosols (SIA), through formation of nitrates, increasing the amounts of PM<sub>10</sub> and PM<sub>2.5</sub> [64].

Among NO<sub>x</sub>, nitrogen dioxide (NO<sub>2</sub>) is the specie of highest concern considering the protection of human health.

NO<sub>2</sub> is soluble in water, it is characterized by a reddish-brown color, with a characteristic pungent smell. Nitric oxide (NO) generates spontaneously NO<sub>2</sub> if it is exposed to air.

NO<sub>2</sub> is an important atmospheric trace gas for many reasons:

- it absorbs visible radiation from the sun and can damage the visibility.
- Since it is a visible radiation adsorber, it has a potential direct capacity in global warming if its amounts are elevated.
- it is one of the main regulator of the oxidizing role of the troposphere by governing the presence of radicals such as OH.
- it is fundamental to determine O<sub>3</sub> levels in troposphere since the NO<sub>2</sub> photolysis is the main initiator of the photochemical generation of O<sub>3</sub>, in both polluted and unpolluted environments [65].

NO<sub>2</sub> is transformed further in atmosphere forming strong oxidant species that participate in the generation of HNO<sub>3</sub> and of its ammonium salts. Thus, NO<sub>2</sub> is activated through the photochemical reactions activated by solar radiation, generating a wide range of pollutants that are a source of particles in PM. As a result, NO<sub>2</sub> is an essential precursor of several secondary pollutants of whom consequences on human health are deeply studied.

Globally, emissions of NO<sub>x</sub> from biogenic sources far surpass those produced by antropogenic activities. Biogenic sources cover intrusion of stratospheric NO<sub>x</sub>, volcanic and bacterial phenomena and lightning. Nevertheless, the resulting background atmospheric concentrations is low since biogenic emissions are spread over the whole earth surface. The main sources of anthropic NO<sub>x</sub> in troposphere are the creactions of ombustion both in stationary (heating and power production) and in mobile systems (internal combustion motors in ships and vehicles). In the major part of ambient situations, in atmosphere NO is emitted and oxidized quickly into NO<sub>2</sub>, by oxidants like O<sub>3</sub>. As a result, this reaction is the main route for atmospheric NO<sub>2</sub> generation, even if different contributions from specific non-combustion industrial phenomena like HNO<sub>3</sub> manufacturing, utilization of explosives and welding have been considered. Altshuller [66] calculated that 50% conversion of NO takes in less than 1 minute at [NO] 0.1 ppm in the presence of an [O<sub>3</sub>] of 0.1 ppm.

Indoor sources of NO<sub>x</sub> involve tobacco smoking and the utilization of gas-fired instruments and oil stoves.

In Figure 17, a scheme of acute and chronic effects in human lungs after NO<sub>2</sub> exposure is shown.

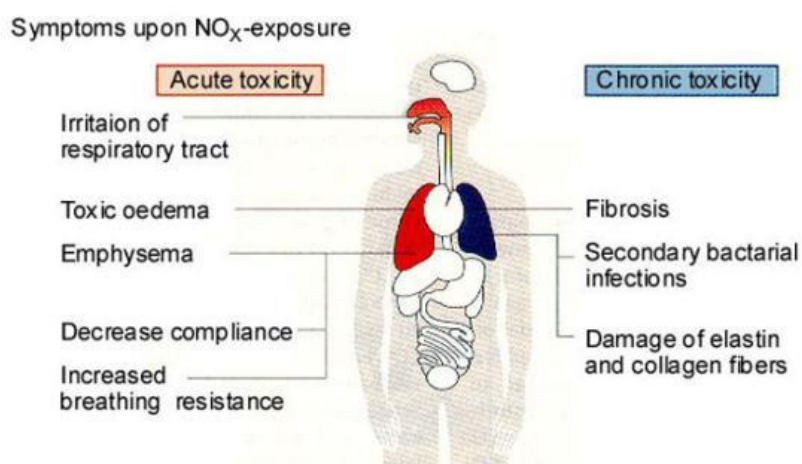


**Figure 17.** Effects of NO<sub>2</sub> exposure on human lungs [67].

NO<sub>2</sub> exerts several biological consequences on metabolism of lungs, structure, function, inflammation and resistance upon host towards respiratory infections for its oxidant character.

In addition, human health consequences can outcome both aftershort-term (e.g. degeneration of lung performance in humans) and long-term exposure (e.g. higher vulnerability towards pulmonary infections). Epidemiological investigations have confirmed that symptoms of bronchitis in kids with asthma are higher after long-term exposure towards NO<sub>2</sub>.

NO<sub>2</sub> is able to diffuse in the epithelial lining fluid (ELF) of the respiratory epithelium, reacting with antioxidants and lipids in the ELF. The consequences on health of NO<sub>2</sub> are due to the reaction byproducts or their metabolites. Those are reactive nitrogen species and results in inflammations, bronchoconstriction, diminished immune response, and may also have bad consequences towards cardio-circulatory system [68].

If NO<sub>2</sub> is directly exposed to the skin, it can result in irritations and burns. Instantaneous distress are caused by high amounts of the gaseous form: 10–20 ppm results in mild irritation of the nose and throat, 25–50 ppm give rise to edema causing pneumonia or bronchitis, and concentrations up to 100 ppm provokes death for asphyxiation. Frequently, no symptoms during exposure occur different from fatigue, nausea or transient cough, but over hours of inflammation in the lungs, edema is produced [69].

A main source of indoor NO<sub>2</sub> is constituted by gas stoves for cooking or heating, and exposure to NO<sub>2</sub> is particularly dangerous for children affected by asthma. In an epidemiological study [70] it was assessed that high levels of NO<sub>2</sub> were responsible for greater levels of respiratory complications, exemplifying that NO<sub>2</sub> toxicity is harmful for kids.

The excess in the reactive nitrogen deposition can generate a surplus of nutrients in ecosystems, resulting in eutrophication in both terrestrial and aquatic communities, including biodiversity loss [71].

Considering NO<sub>2</sub>, two threshold limits and an alert threshold are determined for the human health safety. The threshold limits are defined for short-term (1 hour) and long-term (1 year) exposure and EU Member States were required to accept them before January 1<sup>st</sup>2010. The 1h limit can be surpassed not more than 18 times in a year earlier than the limit is violated and the concentration of NO<sub>2</sub> TLV is equal to 106 ppb. A critical level is also fixed for average of NO<sub>x</sub> in a year for protecting the vegetation, equal to 16 ppb.

Thus, the 2008 Air Quality Directive (EU, 2008c) also determined an alert threshold limit of 213 ppb. In the case of three successive hours of excesses in areas of not less than 100 km<sup>2</sup> or in a whole air quality management region, authorities must enforce short-term action plans. These can involve measures such as decreasing motor vehicle traffic, and the utilization of industrial products or plants and household heating. Definite actions pointing at the preservation of weak groups, such as kids, by diminishing their exposure time towards elevated NO<sub>2</sub> amounts can also be accounted in those actions. Finally, in EU, the TLV annual mean [NO<sub>2</sub>] concentration is set at 21 ppb.

Nowadays, wide spatial NO<sub>x</sub> detection is restrained since the equipment for measurements is limited, considering techniques like continuous chemiluminescence monitors, that occupy big volumes and have high costs. Furthermore, they need elaborate infrastructures, technical-scientific support and constant power supply. For overcoming the above-mentioned deficiency, passive samplers have been profitably utilized for large scale detection of NO<sub>x</sub> in the environment [72].

### **7.2.2 ZnO characteristics and synthesis**

The current technological advances are correlated to the fundamental study of known materials and substantial alterations in their preparation methods, resulting in the design and realization of innovative materials including nanostructures. In this framework, ZnO exhibits a great interest for its possibility to tune and manage different characteristics. A peculiar feature of ZnO is its capacity to generate nanostructures with diverse sizes and morphology: wires, tubes, ribbon, rods and tetrapods. ZnO is characterized by a wide bandgap equal to 3.4 eV, it is characterized by a stable wurtzite structure with lattice spacing  $a = 0.325$  nm and  $c = 0.521$  nm. Thus, for its unique properties, it finds applications in many fields like in piezoelectrics, ultraviolet (UV) light emitters, transparent and spin electronics and gas sensors [73].

ZnO exhibits many promising characteristics such as wide bandgap, considerable electron mobility, great transparency and effective luminescence at room T. Those features are usable in novel applications for heat-protecting windows, transparent

electrodes in liquid crystal displays, in energy-saving systems, in electronics in light-emitting diodes and as thin layer transistors.

Crystalline ZnO exhibits thermochromic characteristics, since when it is heated in air it changes reversibly its color from white to yellow [74].

Furthermore, it is an amphoteric ceramic, almost insoluble in H<sub>2</sub>O but it can be dissolved in many acids.

ZnO crystallizes in three different forms as depicted in Figure 18: hexagonal wurtzite, cubic zinc blende and the infrequently observed cubic rocksalt.

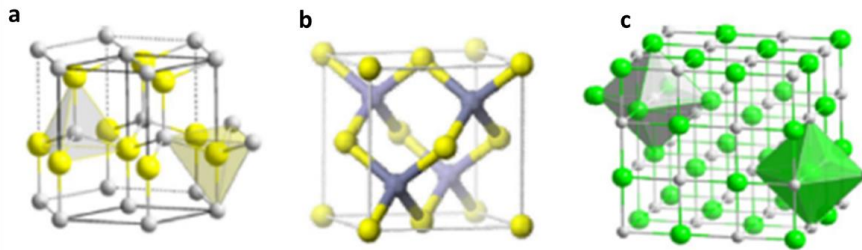


**Figure 18.** ZnO crystal phases: wurtzite (a), zinc blende (b), rocksalt (c) [75].

The most stable structure at room temperature is the wurtzite, while the zinc blende phase is stabilizable after growing ZnO onto substrates having cubic lattice structure. In both situations, Zn and O centers are tetrahedral. The rocksalt structure is stable exclusively at elevated P (around 10 GPa) [76].

The hexagonal wurtzite structure has a point group 6mm and the space group is P6<sub>3</sub>mc. The lattice constants are  $a = 0.325$  nm and  $c = 0.52$  nm, with a ratio  $c/a \sim 1.60$  similar to the theoretic value of 1.633 typical for hexagonal cells.

ZnO is largely utilized as an additive in several materials like cements, lubricants, glass, ceramics, rubbers, plastics [77] foods, batteries, paints, adhesives, sealants, pigments, ferrites and fire retardants. Even if it is present in nature in the form of mineral zincite, most ZnO is synthetically obtained [78].

In addition to the aforementioned properties, ZnO displays peculiar characteristics for gas sensing like large exciton binding energy (60 meV), great photoelectric response, outstanding chemical and thermal stability [79–84].

ZnO can also be synthesized easily, cheaply and it is appropriate for high mass production.

Furthermore, ZnO chemoresistive sensor typically works between 300 and 500° C [85–87], because high thermal energy of surface redox reaction is needed to surpass the  $E_a$  enhancing the velocity of the process [88].

High-operation temperature adversely restricts its vast application, because of the highest power required and increased risk of gas explosion [89].

The pressing need is to decrease the working temperature of ZnO chemical sensors, realizing smaller and cheaper devices, in accordance with the actual developing direction [90]. Most of all, low operational T furnish a reduction in power consumption and in the risk of gas explosion. In addition, it refines the long-term stability of the device.

For instance, ZnO, ZnO nanowires [91] were successfully realized for H<sub>2</sub> detection at low temperature. Selectivity towards H<sub>2</sub> gas was obtained by sputtering Pd clusters on the nanorods's surface. By adding Pd NPs, an efficient catalytic dissociation of H<sub>2</sub> into atomic hydrogen was achieved, enhancing its sensitivity. It can detect H<sub>2</sub> amounts till 10 ppm at room T, with no interference with respect to oxygen.

Recently, [92] ZnO nanowires were synthesized by hydrothermal route as sensitive element. The produced sensors displayed ultra high SR% equal to 98% towards 100 ppm of H<sub>2</sub> at 250°C. In [93] W-doped ZnO thin layer were realized by magnetron sputtering. This hybrid sensor exhibited considerable superior sensing characteristics upon 5–10 ppm NO<sub>2</sub> exposure at 150°C.

In order to develop sensitive ZnO thick films sensors, two synthesis routes were carried out. In the first one, ZnO nanoparticles were obtained by a sol-gel autocombustion synthesis, while in the other one, a hydrothermal route was carried out for synthesizing ZnO nanopowder.

In the first synthesis, zinc nitrate hexahydrate (Zn (NO<sub>3</sub>)<sub>2</sub>·6H<sub>2</sub>O, Sigma Aldrich, 99.9%) and soluble potato starch ((C<sub>6</sub>H<sub>10</sub>O<sub>5</sub>)<sub>n</sub>, Sigma Aldrich) were utilized with no additional purification.

Large variations in structure and composition of starches from diverse botanical sources were noticed, but all are based on two main components, amylose and amylopectin. Those are both polymers of α-glucose units in the 4C1 conformation. In amylose, these are linked (1→4), with all ring oxygen atoms disposed on the identical part, while in amylopectin one residue every twenty is linked (1→6) too, generating branch-points.

Two different solutions were prepared, the first containing 0.037 moles of Zn (NO<sub>3</sub>)<sub>2</sub>·6H<sub>2</sub>O dissolved in 100 mL of H<sub>2</sub>O, the second with 0.42 mole of potato starch in the identical quantity of H<sub>2</sub>O. Potato starch solution was heated at 80°C and maintained under vigorous magnetic agitation for 1 h to provide the complete dissolution of starch. Starch becomes water soluble at this temperature and the semi-crystalline architecture is missing. Subsequently to the addition of zinc nitrate into the starch solution, metal cations are drawn by oxygen of the OH branches [94]. After complete starch dissolution, the two mixtures were maintained further stirred for 15 min and subsequently mixed each other directly in an Al<sub>2</sub>O<sub>3</sub> crucible. The resultant mix is turbid, since starch begin to become gel during mixing. Thus, the crucible was put in a H<sub>2</sub>O bath at 90°C and under stirring continuously through magnetic heater-stirrer for 5 h.

During this time, water evaporates from the mixture and the viscosity increases. The resultant product after water removal is a dense white-yellowish gel. Then, the crucible was rapidly (10 °C/min) heated at 300°C for 30 min to remove the residual H<sub>2</sub>O starting the ignition of reagents. The combustion reaction ended after 1 minute from the ignition. A large amount of smoke was produced during this reaction. The product obtained is a spongy brown friable mix of ZnO, partially unreacted reagents and carbon as confirmed by TGA analysis.

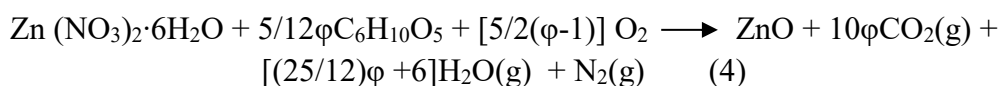


Then, the mix was manually milled and finally thermally treated in a furnace at 500°C (10°C/min) for 2 h. The resultant product is a bright white fine product of ZnO that was manually milled.

This novel synthesis route exhibits high yields of products. In fact, a yield of 90% was obtained.

The amounts of reactants and their relative proportions were chosen according to the reaction stoichiometry. The proportion fuel/oxidant ( $\phi$ ), i.e. zinc nitrate/potato starch, was imposed equal to 2.25. In this case, a highly rich mixture with a significant lack of oxidant was used. In these conditions, the amount of the oxidant  $\text{Zn}(\text{NO}_3)_2 \cdot 6\text{H}_2\text{O}$  is not enough to ensure the complete oxidation of the starch, acting as a fuel. As a result, additional oxygen from the air is required, but in the synthesis conditions (static air and closed environment inside the crucible and furnace's chamber) this additional amount is not provided properly. The result is a partial pyrolysis of the fuel, instead of the complete oxidation [95-97].

For the value of the parameter ( $\phi$ ), the equation (4), derived according to the principles of the combustion processes [95-97], describes the overall process:



In accordance with the eq. 4, the whole reaction causes the production of large amounts of gases. These caused the spongy structure of the mix of products obtained during the reaction in fuel rich conditions [95,96]. For the sake of clarity, the eq. 1 is a theoretic one. The real reaction should take into account the formation of carbonaceous materials. These carbonaceous products create a matrix where ZnO particles and unreacted reagents are trapped. This and the large amount of gases produced avoid aggregation and sintering of ZnO particles during this stage of the synthesis. Moreover, the carbonaceous matrix is burned during heating the intermediate products at 500°C for 1 h. In these conditions, another abundant production of gases is induced (supposing the complete oxidation of the carbonaceous material to produce  $\text{CO}_2$  and  $\text{H}_2\text{O}$ ) and this is the reason of the fluffy appearance of the pure ZnO obtained at the end of the whole process (AC-ZnO).

In the hydrothermal synthesis, all the reagents were utilized without any further purification. In a typical synthesis, potassium hydroxide (KOH, 1 M, Merck) and zinc nitrate hexahydrate ( $\text{ZnNO}_3 \cdot 6\text{H}_2\text{O}$ , 0.5 M, Sigma-Aldrich) were dissolved individually in distilled water. Zinc nitrate was then dropped slowly into KOH under continuous stirring, forming a white gel. The mixture was put in a Teflon container at 70°C for 4 h. Subsequently, ZnO powder was collected by filtration from the solution, washed several times with  $\text{H}_2\text{O}$  till the pH reaches the value of 7 and then dried at 90 °C overnight. ZnO white powder (HT-ZnO) was produced after calcination for 2 h at 450°C.

### 7.2.3 ZnO powder and film characterization

Results of laser granulometry for AC-ZnO and HT-ZnO are depicted in Figure 19 and in Table 5.

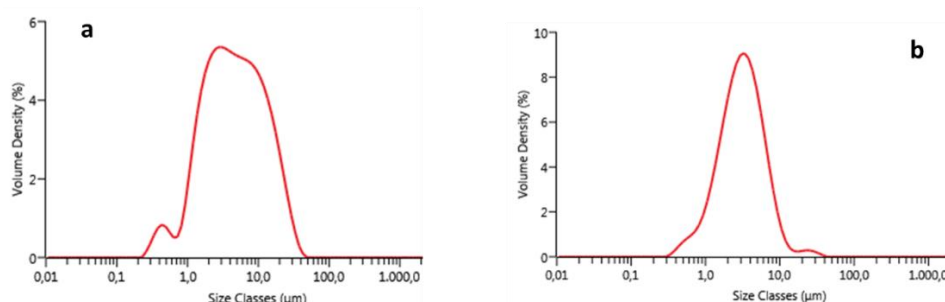


**Figure 19.** ZnO particle size distributions of AC-ZnO (a) and HT-ZnO (b).

**Table 5.** Cumulative particle size equal to  $d_{10}$ ,  $d_{50}$  and  $d_{90}$  for AC-ZnO and HT-ZnO.

Cumulative %	AC-ZnO (μm)	HT-ZnO (μm)
$d_{10}$	1.26	1.22
$d_{50}$	4.40	3.06
$d_{90}$	16.20	6.96

Comparing the particle size distributions in volume of the synthesized ZnO powders, the AC-ZnO powder exhibits a trimodal distribution, with maxima at 0.4, 2.9 and 11.9 μm. This powder shows a higher degree of agglomeration compared to the quasi-monomodal distribution of HT-ZnO with maximum at 3.3 μm. DTA-TG analysis was carried out over the AC-ZnO powder pre-calcined at 300°C for 30 min. Results are displayed in Figure 20.

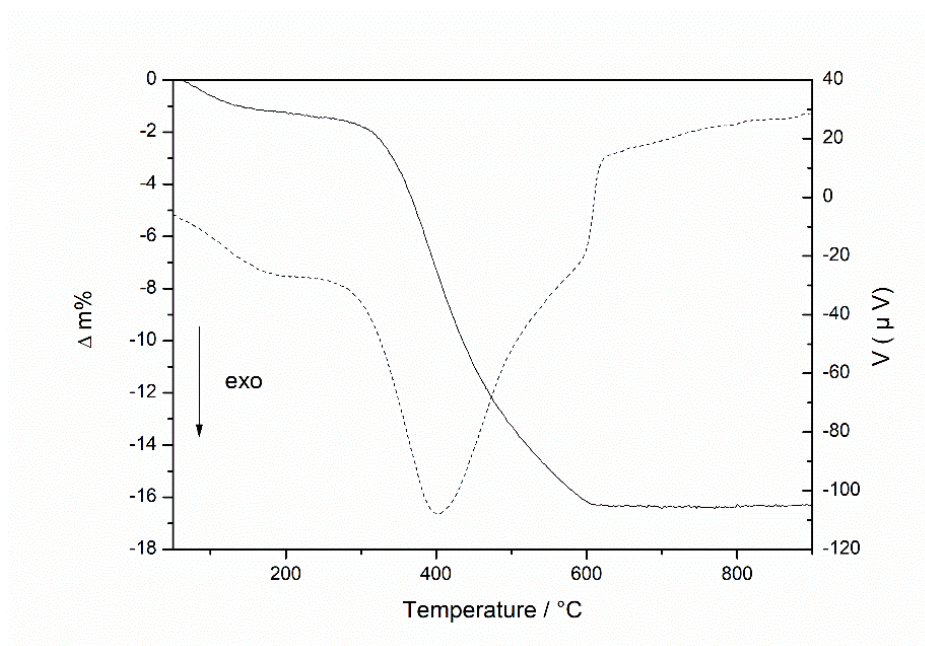


**Figure 20.** TG-DTA curve in static mode of AC-ZnO powder heated at 300°C for 30 minutes (10°C/min): TG continue line, DTA dashed line.

The TG curve decreases until about 600°C, with a final mass loss equal to 16.27%. The TG and DTA signals display three principal regions. The first one (until 180°C) is generated by the decomposition of chemically bound groups. The second one between 180° to 400°C is generated by the degradation of organic groups of starch, and the generation of the pyrochlore phases. The third mass loss above 400°C is produced by the decomposition of the pyrochlore phases and the zinc oxide production. Finally, no mass loss in the range 600-900°C was observed from the TG signal, demonstrating the probable formation of ZnO.

XRD spectra of HT-ZnO and AC-ZnO powders are reported in Figure 21.

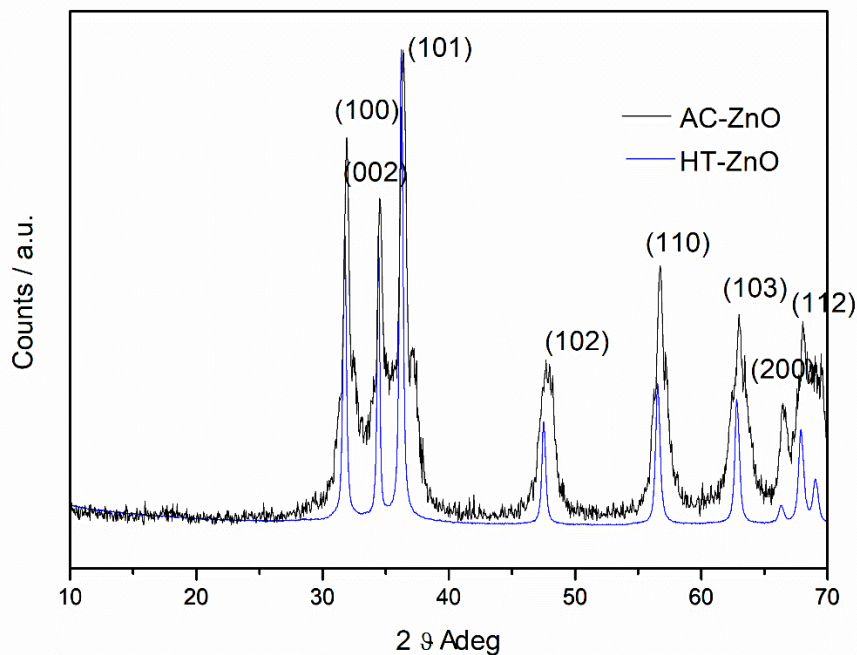


**Figure 21.** XRD pattern of annealed HT-ZnO (blue line) and AC-ZnO (black line).

The diffraction pattern demonstrates a great crystallinity of the HT-ZnO, with the hexagonal wurtzite structure with high purity (JCPDS N<sup>o</sup> 80-0074).

By means of Scherrer equation applied to (100), (002), (101), (102), (110) and (103) peaks, a value of  $38.6 \text{ nm} \pm 2.1$  for crystallite size was obtained. In the case of AC-ZnO, after calcination for 1 h at  $500^\circ\text{C}$ , crystallization of the same hexagonal wurtzite structure was confirmed, even though with a lower degree of crystallization and with smaller crystallites ( $14.8 \text{ nm} \pm 1.7$ ) considering the same six peaks.

The decrease in crystallite size for AC-ZnO compared to HT-ZnO can be related to the different synthesis route, since the annealing was performed at similar T ( $450^\circ\text{C}$  for HT-ZnO and  $500^\circ\text{C}$  for AC-ZnO). In fact, in the case of autocombustion synthesis, the carbonaceous materials from starch create a matrix where ZnO particles and unreacted reagents are trapped. This phenomenon prevents aggregation and sintering of ZnO particles during this stage of the synthesis.

The SSA, as measured by N<sub>2</sub> adsorption, was  $19.58 \text{ m}^2/\text{g}$  and a pore size distribution peaking at around 4 nm for HT-ZnO, whereas for AC-ZnO this value is equal to  $15.4 \text{ m}^2/\text{g}$  with mean pore size of about 1 nm.

FESEM images of the AC-ZnO powder and film are depicted in Figure 22.

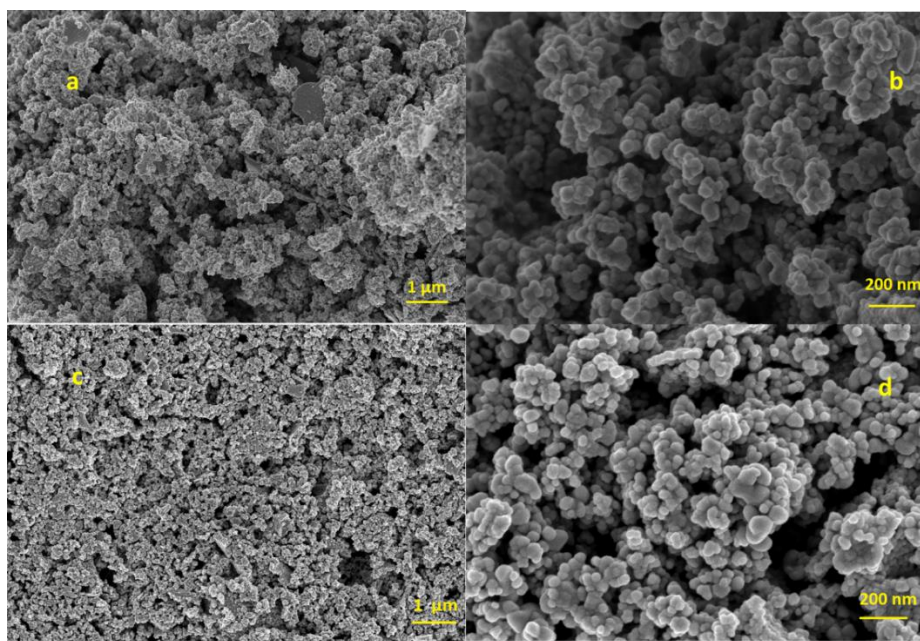


**Figure 22.** FESEM observations of AC-ZnO powder at low (25kx, a) and high (150kx, b) magnifications. Images of AC-ZnO sensor at low (25kx, c) and high (150kx, d) magnifications.

FESEM observations confirm a porous structure of the ZnO thick film, typical of gases run-out during autocombustion. Furthermore, neither variations in the morphology after screen-printing deposition nor evidence of grain growth after firing at 500°C for 1 h were detected. These two factors are essentials for the characteristics of the as-prepared nanostructures: carbon matrix formation during the first stage of the reaction and its combustion during the final heat treatment contribute to obtain a final product, AC-ZnO, constituted by small particles. Those were highlighted by FESEM observations, where particles less than 50 nm in diameter were measured by high magnification micrographs. The as-synthesized ZnO nanoparticles were organized in fluffy and spongy structures rich of micro and nanopores and voids. Sensor thickness was measured in cross-section and a value of  $18.7 \pm 1.8 \mu\text{m}$  was attained as an average of 10 measurements. Moreover, FESEM investigation was performed for the HT-ZnO powder and thick film after firing at 500°C, as illustrated in Figure 23.

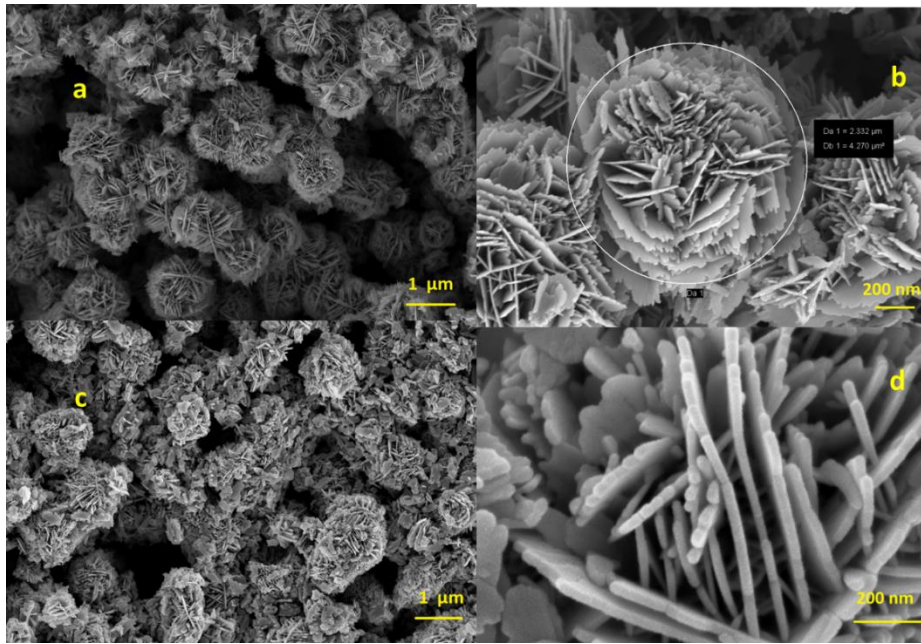


**Figure 23.** FESEM observations of HT-ZnO powder at low (25kx, a) and high (80kx, b) magnifications. Images of HT-ZnO sensor at low (25kx, c) and high (200kx, d) magnifications.

FESEM investigations carried out on AC-ZnO powder and thick-film reveal a flower-like-desert rose shape of the nanoparticles. ZnO powder is constituted of almost spherical grains with constant nanostructured prism-shaped planes as building blocks [98].

The nanostructured branched morphology of ZnO is till well preserved subsequently to the fabrication of the thick film sensor, with petals width of about 10 nm and rose-diameter of about 2-3  $\mu\text{m}$ . In accordance with laser granulometry, in this case an extremely regular 3D dimension of nanoparticle and agglomerates was reached. No variations in the morphology and grain size were detected after screen printing and firing stages at 500°C. Sensor thicknesses of  $19.9 \pm 2.1 \mu\text{m}$  were measured in FESEM cross section measurement.

#### 7.2.4 ZnO gas sensing properties

Sensors were realized by screen-printing deposition, as previously described, and after 500°C firing for 1 h, a satisfying adhesion of the film over the  $\alpha$ -alumina substrate was achieved and confirmed by scotch-tape test. Images of AC-ZnO and HT-ZnO sensor are displayed in Figure 24.

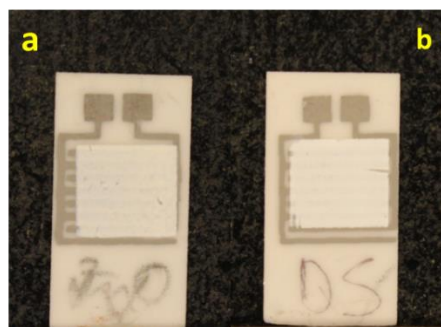


**Figure 24.** Images of screen-printed sensors AC-ZnO (a) and HT-ZnO (b).

AC-ZnO and HT-sensors were firstly tested towards NO<sub>2</sub> 250 ppb in dry conditions at temperatures in the range 50-250°C, investigating the best operating T. Different NO<sub>2</sub> amounts were then tested at the best working T, between 50 and 500 ppb, putting in comparison these results with the literature. Dynamic tests were performed and after the film have reached the equilibrium in dry air (baseline impedance), NO<sub>2</sub> was inserted into the sensor chamber until the equilibrium on the sensor surface. Then, NO<sub>2</sub> was switched off and dry air was fluxed towards the sensor until a novel equilibrium between the sensor surface and the adsorbed species was reached.

In Figure 25 the sensor response R ( $Z_g/Z_o$ ) at different operating temperatures is reported for AC-ZnO and HT-ZnO sensors.

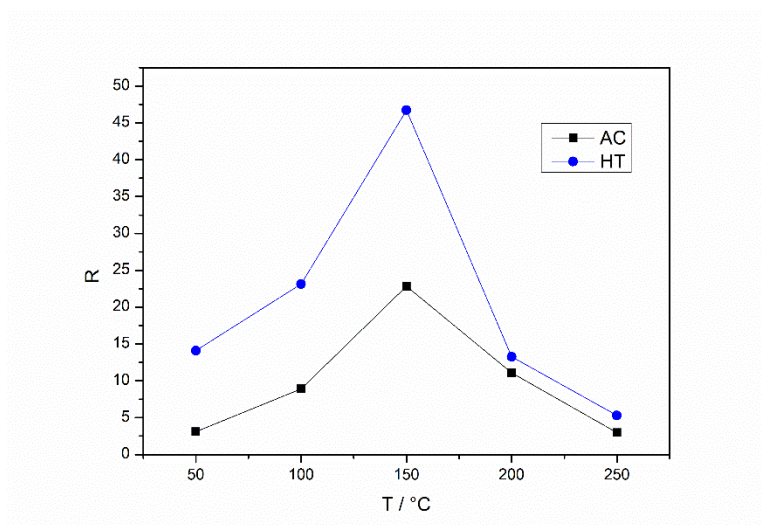


**Figure 25.** Sensor response at different working T (50-250°C) upon 250 ppb NO<sub>2</sub> in dry air.

In the next Table 6 the sensor response, response/recovery times at different T are illustrated for the AC-ZnO and HT-ZnO sensors.

**Table 6.** Sensor response, response and recovery times at different operational T in dry air and 250 ppb of NO<sub>2</sub> for AC-ZnO and HT-ZnO sensors.

Temperature (°C)	R (AC-ZnO)	R (HT-ZnO)	$\tau_{ads}$ AC-ZnO (s)	$\tau_{ads}$ HT-ZnO (s)	$\tau_{des}$ (s)	$\tau_{des}$ (s)
50	3.11	14.09	1,502	404	12,034	5,099
100	8.91	23.14	1,098	361	3,207	2,122
150	22.84	46.73	652	341	788	451
200	11.1	13.26	609	236	105	273
250	2.96	5.3	289	1,602	24	106

ZnO sensors behave as n-type semiconductors in the entire investigated temperature range. In fact, when AC-ZnO and HT-ZnO films were exposed to NO<sub>2</sub>, the impedance and resistance increased after an electron removal from the CB of ZnO. Considering the sensor response R ( $Z_g/Z_0$ ), it is maximum at 150°C with the typical gaussian trend for both sensors. In all cases,  $\tau_{des}$  decrease when increasing the operating temperature, as expected. Furthermore, the kinetic of adsorption follows a comparable trend, excepting HT-ZnO at higher temperatures than 150°C. In fact, when the hydrothermal synthesized ZnO is exposed to NO<sub>2</sub> at 200°C, the adsorption become slower compared to 150°C probably because of the competition between adsorption and desorption processes at the same time. Impedance variations upon different nitrogen dioxide concentrations (50-500 ppb) at 150°C are displayed in Figure 26.

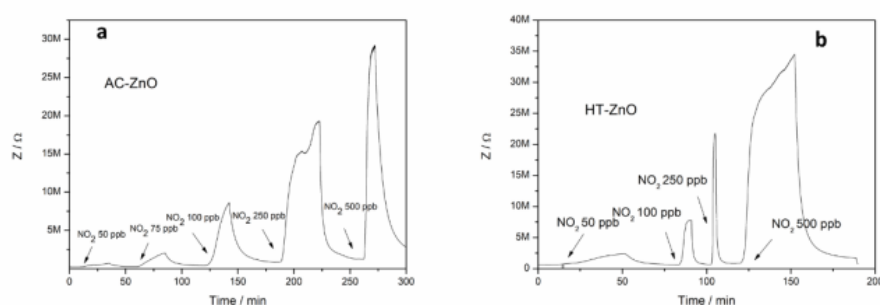


**Figure 26.** Impedance variations upon different NO<sub>2</sub> concentrations exposure (50-500 ppb) at 225°C.

Comparing the sensor performances under 250 ppb of NO<sub>2</sub> in dry conditions, the HT-ZnO shows a higher sensor response with respect to nitrogen dioxide (R: 46.73 vs 22.84) and a quicker response and recovery ( $\tau_{ads}/\tau_{des}$  respectively of 341 and 451) compared to AC-ZnO sensor (652 and 788 s, respectively). This is probably a result of the higher surface area (19.6 vs 15.4 m<sup>2</sup>/g) and of the smaller agglomerates



of the flower-like ZnO hydrothermally prepared confirmed by laser granulometry and FESEM investigations. Moreover, in accordance with Korotcenkov [99], the rate of sensor response towards oxidant species like O<sub>3</sub> and NO<sub>2</sub> increases by increasing the pore size.

In fact, from N<sub>2</sub> adsorption measurement, the average pore size was 4 times higher for the HT-ZnO than for the AC-ZnO.

The calibration curves are presented in Figure 27.

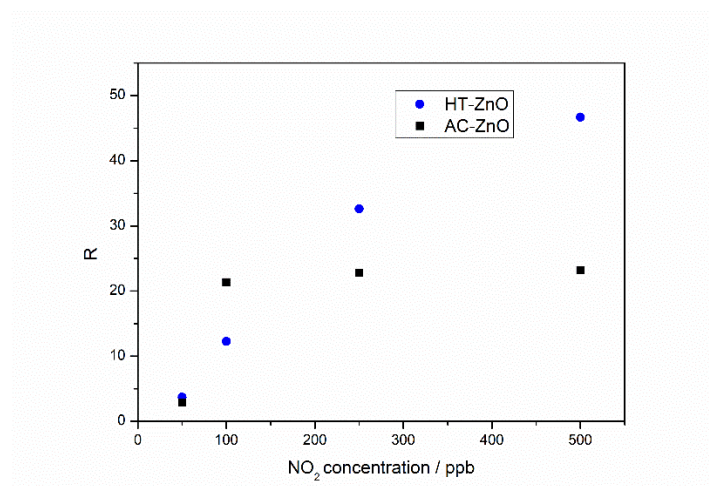


**Figure 27.** Calibration curves of AC-ZnO (black) and HT-ZnO (blue) sensors.

AC-ZnO exhibits a sigmoidal trend in the investigated concentration range, with a quasi-saturation for concentrations higher than 100 ppb, whereas the HT-ZnO shows an enhanced sensitivity with respect to NO<sub>2</sub>, and in agreement with the IUPAC definition, the sensitivity is determinable from the slope of the curve  $R=f([NO_2])$ . The sensor response of the HT-ZnO device follows a calibration curve described by  $y=a+bx^c$  in the 50-500 ppb range of nitrogen dioxide concentration ( $R^2=0.956$ ) and the sensitivity is  $0.094 \text{ ppb}^{-1}$ .

Since selectivity is essential for environmental monitoring, cross-sensitivity measurements were performed at the best operational temperature of 150°C. For this reason, variations in film impedance were measured upon different gases. CH<sub>4</sub> 100 ppm, CO<sub>2</sub> 500 ppm, O<sub>3</sub> 200 ppb, RH 50%, N<sub>2</sub>O 15 ppm and NH<sub>3</sub> 50 ppm were introduced into the sensor chamber and results are presented in Figure 28.

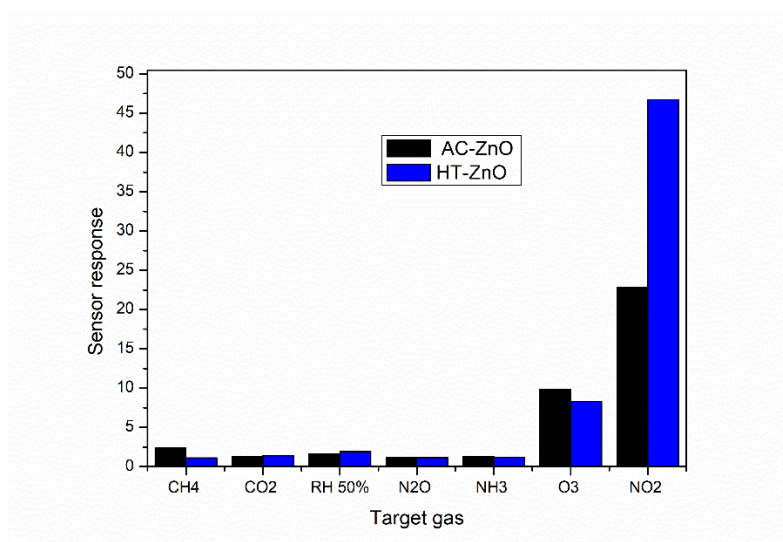


**Figure 28.** Cross-sensitivity test of AC-ZnO (black) and HT-ZnO (blue) sensors.

Generally, HT-ZnO sensor exhibits an enhanced selectivity for nitrogen dioxide detection than AC-ZnO one. In particular, the sensor response towards O<sub>3</sub> is comparable with that one for NO<sub>2</sub> in the case of AC-ZnO, whereas HT-ZnO sensor response is almost double for NO<sub>2</sub> 250 ppb than for O<sub>3</sub> 200 ppb. However, humidity interference is higher for HT-ZnO than for AC-ZnO (R: 1.94 and 1.63, respectively).

Since only few studies have reported sensitivity of ZnO sensors for NO<sub>2</sub> at low T, in Table 7 results of this work are confronted with similar studies.

**Table 7.** Comparison of the NO<sub>2</sub> sensing performances of ZnO films working at low T.

Morphology	Synthesis method	NO <sub>2</sub> concentration (ppm)	Sensor response (R=Rg/Ro)	Operating temperature (°C)	$\tau_{ads}$ (s)	$\tau_{des}$ (s)	Reference
Nanopetals	Chemical precipitation	20	119	25	85	103	[100]
Nanowalls	Solution route	5	6.54	25	23	11	[101]
PH3HT-ZnO	Spin coating	50	1.8	25	n.d	n.d.	[102]
ZnO nanorods	Hydrothermal	0.1	1.24	100			[103]
ZnO film	Ion layer adsorption and reaction (SILAR)	10	1.01	150			[104]
ZnO glass-ceramic	Melt quenching	1 ppm	17	150	5 min e 10 s	n.d.	[105]
Desert rose	Hydrothermal	0.25	46.73	150	341	451	This work
Rectangular-romboedric shape	Sol-gel autocombustion	0.25	22.84	150	652	788	This work

NB: n.d. = not determined.

Comparing the present work with the state of art regarding low-temperature ZnO sensors for NO<sub>2</sub>, AC-ZnO and HT-ZnO sensors' response and recovery times are longer, even though a noticeable increase in the sensor response at sub-ppm level was attained.

The optimum operating temperature is on the boundary between the molecular-oxygen region (at  $T < 150^\circ\text{C}$ ) and the ionic species (at  $T > 150^\circ\text{C}$ ) [106].

These species form a depletion layer at the surface of AC-ZnO and HT-ZnO oxide due to electrons trapping [107,108].

The measured impedances' variations are caused by direct chemisorption process of  $\text{NO}_2$  molecules without involving the reaction with oxygen species [109].

A known series of reactions that form nitrates and nitrites is described in [110]: in this process,  $\text{NO}_2$  reacts firstly at the oxygen vacancy (forming nitrites,  $\text{NO}_2^-$ ) and only then it participates in the formation of nitrates ( $\text{NO}_3^-$ ) after reaction with  $\text{O}_2^-$ .

Electrons from the CB of ZnO are trapped while surface species are generated, but not during the oxidation from nitrites to nitrates.

After the formation of nitrates, a further equilibrium is reached, for the dissociation of nitrates to NO. Since the impedance and resistance increased upon exposure to 50-500 ppb of  $\text{NO}_2$ , the detection mechanism can be attributed to the as-described reactions.

### 7.3 Conclusions

In this chapter,  $\text{Co}_3\text{O}_4$  and ZnO thick film sensors were successfully realized respectively for ammonia and nitrogen dioxide detection. The nanocrystalline  $\text{Co}_3\text{O}_4$  was obtained by solution combustion synthesis (SCS) and adopted as  $\text{NH}_3$  sensitive metal oxide. Sensors were realized by screen-printing the sensitive element on  $\alpha$ -alumina substrates with Pt interdigitated electrodes and fired at  $700^\circ\text{C}$  for 1 h in air. Best performances were achieved at  $225^\circ\text{C}$ , with sensor response  $R$  ( $Z_g/Z_0$ ) of 1.83 upon 50 ppm of  $\text{NH}_3$  exposure and 10% of  $Z$  variation upon 1 ppm of  $\text{NH}_3$  exposure in dry conditions. Sensors are still sensitive towards 1 ppm of  $\text{NH}_3$  in strongly humid conditions (90-99% RH). For this reason, and for the superior selectivity of the as-prepared sensor, this device can find application in breath analysis, as well as for environmental monitoring.

The sensing properties towards  $\text{NO}_2$  were studied for two different ZnO nanostructures. One was obtained by auto-combustion sol-gel route, and the other one by hydrothermal process, resulting in ZnO flower-like microstructures with enhanced specific surface area respect to the sol-gel powders.

Both ZnO were obtained by easy, reproducible and cheap processes, thus resulting in wurtzite-like crystalline nanostructures as verified by accurated morphological investigation. Best results for nitrogen dioxide detection were reached at  $150^\circ\text{C}$ , and by increasing specific surface area of the nanopowder, an enhanced sensor response towards  $\text{NO}_2$  was obtained.

# References

- [1] Ziegler D., Marchisio A., Ercolino G., Specchia S., Tulliani J. M. (2019) Ammonia selective sensors based on cobalt spinel prepared by combustion synthesis. *Solid State Ionics*. Pages 91-100.
- [2] <https://www.eea.europa.eu/data-and-maps/indicators/eea-32-ammonia-nh3-emissions-1/assessment-4>. (Visited on 23th of February 2019).
- [3] <https://www.cdc.gov/niosh/pel88/7664-41.html>. (Visited on 23th of February 2019).
- [4] Timmer B., Olthuis W., Van Den Berg A. (2005) Ammonia sensors and their applications—a review, *Sens. Actuat. B*. Pages 666–677.
- [5] Pauluhn J. (2013) Acute inhalation toxicity of ammonia: revisiting the importance of RD50 and LCT01/50 relationships for setting emergency response guideline values, *Regulatory Toxicology and Pharmacology*. Pages 315–325.
- [6] Tonelli A. R., Pham A. (2009) Bronchiectasis, a long-term sequela of ammonia inhalation: a case report and review of the literature, *Burns*. Pages 451–453.
- [7] Bayrakli I., Turkmen A., Akman H., Sezer M. T., Kutluhan S. (2016) Applications of external cavity diode laser-based technique to non invasive clinical diagnosis using expired breath ammonia analysis: chronic kidney disease, epilepsy, *J. Biomed. Opt.* Pages 087004.
- [8] Davies S., Spanel P., Smith D. (1997) Quantitative analysis of ammonia on the breath of patients in end-stage renal failure, *Kidney Int*. Pages 223–228.
- [9] Amano A., Yoshida Y., Oho T., Koga T. (2002) Monitoring ammonia to assess halitosis, *Oral Surg. Oral Med. Oral Pathol. Oral Radiol. Endodontol*. Pages 692–696.
- [10] Kearney D. J., Hubbard T., Putnam D. (2002) Breath ammonia measurement in *Helicobacter pylori* infection, *Dig. Dis. Sci*. Pages 2523–2530.
- [11] DuBois S., Eng S., Bhattacharya R., Rulyak S., Hubbard T., Putnam D., Kearney D. J. (2005) Breath ammonia testing for diagnosis of hepatic encephalopathy, *Dig. Dis. Sci*. Pages 1780–1784.
- [12] Güntner A. T., Righettoni M., Pratsinis S. E. (2016) Selective sensing of NH<sub>3</sub> by Si-doped  $\gamma$ -MoO<sub>3</sub> for breath analysis, *Sens. Actuat. B*. Pages 266–273.
- [13] Di Natale C., Paolesse R., Martinelli E., Capuano R. (2014) Solid-state gas sensors for breath analysis: a review, *Anal Chim Acta*. Pages 1–17.
- [14] Ferrus L., Guenard H., Vardon G., Varene P. (1980) Respiratory water loss, *Respir. Physiol.*, Pages 367-381.
- [15] Cao W., Duan Y. (2007) Current status of methods and techniques for breath analysis, *Crit. Rev. Anal. Chem.*, Pages 3-13.
- [16] Righettoni M., Amann A., Pratsinis S. E. (2015) Breath analysis by nanostructured metal oxides as chemo-resistive gas sensors, *Mater. Today*, Pages 163-171.

- [17] Lindinger W., Hansel A. Jordan A. (1998) On-line monitoring of volatile organic compounds at pptv levels by means of proton-transfer-reaction mass spectrometry (PTR-MS) medical applications, food control and environmental research, *Int. J. Mass. Spectrom. Ion. Processes.*, Pages 191-241.
- [18] Herbig J., Mueller M., Schallhart S., Titzmann T., Graus M. Hansel A. (2009) On-line breath analysis with PTR-TOF, *J. Breath Res.*, Pages 027004.
- [19] Smith D., Spanel P. (1996) The Novel selected-ion flow tube approach to trace gas analysis of air and breath, *Rapid. Commun. Mass. Spectrom.* Pages 1183-1198.
- [20] Wang G., Ji Y., Huang X., Yang X., Gouma P.-I., Dudley M. (2006) Fabrication and characterization of polycrystalline WO<sub>3</sub> nanofibers and their application for ammonia sensing, *J. Phys. Chem. B* Pages 23777–23782.
- [21] Marquis B. T., Vetelino J. F. (2001) A semiconducting metal oxide sensor array for the detection of NO<sub>x</sub> and NH<sub>3</sub>, *Sens. Actuat. B.* Pages 100–110.
- [22] Llobet E., Molas G., Molinas P., Calderer J., Vilanova X., Brezmes J., Sueiras J. E., Correig X. (2000) Fabrication of highly selective tungsten oxide ammonia sensors, *J. Electrochem. Soc.* Pages 776–779.
- [23] Zhang J., Wang S., Xu M., Wang Y., Xia H., Zhang S., Guo X., Wu S. (2009) Polypyrrole-coated SnO<sub>2</sub> hollow spheres and their application for ammonia sensor, *J. Phys. Chem. C* Pages 1662–1665.
- [24] Van Hieu N., Thuy L. T. B., Chien N. D. (2008) Highly sensitive thin film NH<sub>3</sub> gas sensor operating at room temperature based on SnO<sub>2</sub>/MWCNTs composite, *Sens. Actuat. B.* Pages 888–895.
- [25] Li C., Zhang D. H., Lei B., Han S., Liu X. L., Zhou C. W. (2003) Surface treatment and doping dependence of In<sub>2</sub>O<sub>3</sub> nanowires as ammonia sensors, *J. Phys. Chem. B.* Pages 12451–12455.
- [26] Elouali S., Bloor L. G., Binions R., Parkin I. P., Carmalt C. J., Darr J. A. (2012) Gas sensing with nano-indium oxides (In<sub>2</sub>O<sub>3</sub>) prepared via continuous hydrothermal flow synthesis, *Langmuir.* Pages 1879–1885.
- [27] Law J. B., Thong J. T. (2008) Improving the NH<sub>3</sub> gas sensitivity of ZnO nanowire sensors by reducing the carrier concentration, *Nanotechnology* Pages 205502.
- [28] Patil S. L., Pawar S. G., Mane A. T., Chougule M. A., Patil V. B. (2010) Nanocrystalline ZnO thin films: optoelectronic and gas sensing properties, *J. Mater. Sci.: Mater. Electr.* Pages 1332–1336.
- [29] Pawar S. G., Patil S. L., Chougule M. A., Raut B. T., Pawar S. A., Mulik R. N., Patil V. B. (2011) Nanocrystalline TiO<sub>2</sub> thin films for NH<sub>3</sub> monitoring: microstructural and physical characterization, *J. Mater. Sci.: Mater. Electr.* Pages 273–279.
- [30] Prasad A. K., Kubinski D. J., Gouma P. I. (2003) Comparison of sol-gel and ion beam deposited MoO<sub>3</sub> thin film gas sensors for selective ammonia detection, *Sens. Actuat. B.* Pages 25–30.
- [31] Moseley P. T., Williams D. E. (1990) A selective ammonia sensor, *Sens. Actuat. B.* Pages 113–115.

- [32] Wang J., Yang P., Wei X., Zhou Z. (2015) Preparation of NiO two-dimensional grain y films and their high-performance gas sensors for ammonia detection, *Nan. Res. Lett.* Pages 119.
- [33] Singh I., Bedi R. K. (2011) Influence of pH on the synthesis and characterization of CuO powder for thick film room-temperature NH<sub>3</sub> gas sensor, *J. Mater. Sci.* Pages 5568–5580.
- [34] Tsuboi O., Momose S., Takasu R. (2017) Mobile sensor that quick and selectively measures ammonia gas components in breath, *FUJITSU Tech J.*, Pages 38-43.
- [35] Righettoni M., Schmid A., Amann A., Pratsinis S. E. (2013) Correlations between blood glucose and breath components from portable gas sensors and PTR-TOF-MS, *J. Breath Res.* Pages 037110.
- [36] Greenwood N. N.; Earnshaw A. (1997). Chemistry of the elements (2nd ed.). Butterworth-Heinemann. p. 1118. ISBN 0-08-037941-9.
- [37] Lou X. W., Deng D., Lee J. Y., Feng J., Archer L. A. (2008) Self-supported formation of needlelike Co<sub>3</sub>O<sub>4</sub> nanotubes and their application as lithium-ion battery electrodes. *Adv. Mater.* Pages 258-262.
- [38] Sun Y., Lv P., Yang J. Y., He L., Nie J. C., Liu X. W., Li Y. D. (2011) Ultrathin Co<sub>3</sub>O<sub>4</sub> nanowires with high catalytic oxidation of CO, *Chem. Commun.* Pages 11279-11281.
- [39] Jeong H. M., Kim H. J., Rai P., Yoon J. W., Lee J. H. (2014) Cr-doped Co<sub>3</sub>O<sub>4</sub> nanorods as chemiresistor for ultra selective monitoring of methyl benzene, *Sens. Actuat. B.* Pages 482-489.
- [40] Li Z., Lin Z., Wang Z., Wang N., Liu J., Sun W., Fu K., Qing Y., Zhiguo W. (2016) High precision NH<sub>3</sub> sensing using network nano-sheet Co<sub>3</sub>O<sub>4</sub> arrays-based sensor at room temperature, *Sens. Actuat. B.* Pages 222-231.
- [41] Deng J. N., Zhang R., Wang L. L., Lou Z., Zhang T. (2015) Enhanced sensing performance of the Co<sub>3</sub>O<sub>4</sub> hierarchical nanorods to NH<sub>3</sub> gas, *Sens. Actuat. B.* Pages 449-455.
- [42] Jeong H. M., Kim H. J., Rai P., Yoon J. W., Lee J. H. (2014) Cr-doped Co<sub>3</sub>O<sub>4</sub> nanorods as chemiresistor for ultra selective monitoring of methyl benzene, *Sens. Actuat. B.* Pages 482-489.
- [43] Sun C. W., Rajasekhara S., Chen Y. J., Goodenough J. B. (2011) Facile synthesis of monodisperse porous Co<sub>3</sub>O<sub>4</sub> microspheres with superior ethanol sensing properties, *Chem. Commun.* Pages 12852-12854.
- [44] Yoon J. W., Choi J. K., Lee J. H. (2012) Design of a highly sensitive and selective C<sub>2</sub>H<sub>5</sub>OH sensor using p-type Co<sub>3</sub>O<sub>4</sub> nanofibers, *Sens. Actuat. B.* Pages 570-577.
- [45] Huang H., Zhu W. J., Tao X. Y., Xia Y., Yu Z. Y., Fang J. W., Gan Y. P., Zhang W. K. (2012) Nanocrystal-constructed mesoporous single-crystalline Co<sub>3</sub>O<sub>4</sub> nanobelts with superior rate capability for advanced lithium-ion batteries, *ACS Appl. Mater. Inter.* Pages 5974-5980.
- [46] Deng J. N., Zhang R., Wang L. L., Lou Z., Zhang T. (2015) Enhanced sensing performance of the Co<sub>3</sub>O<sub>4</sub> hierarchical nanorods to NH<sub>3</sub> gas, *Sens. Actuat. B.* Pages 449-455.

- [47] Fan Y. Q., Shao H. B., Wang J. M., Liu L., Zhang J. Q., Cao C. A. (2011) Synthesis of foam-like freestanding  $\text{Co}_3\text{O}_4$  nanosheets with enhanced electrochemical activities, *Chem. Commun.* Pages 3469-3471.
- [48] Specchia S., Galletti C., Specchia V. (2010) Solution combustion synthesis as intriguing technique to quickly produce performing catalysts for specific applications. *Stud. Surf. Sci. Catal.* Pages 59-67.
- [49] Specchia S., Ercolino G., Karimi S., Italiano C., Vita A. (2017) Solution combustion synthesis for preparation of structured catalysts: A mini-review on process intensification for energy applications and pollution control. *Int. J. Self-Propag. High-Temp. Synth.* Pages 166–186.
- [50] González-Cortés S. L., Imbert F. E. (2013) Fundamentals, properties, and applications of solid catalysts prepared by solution combustion synthesis (SCS). *Appl. Catal. A Gen.* Pages 117–131.
- [51] Varma A., Mukasyan A. S., Rogachev A. S., Manukyan K. V. (2016) Solution combustion synthesis of nanoscale materials. *Chem. Rev.* Pages 14493–14586.
- [52] Deganello F., Tyagi A. K. (2018) Solution combustion synthesis, energy and environment: Best parameters for better materials. *Prog. Crystal Growth Charact. Mater.* Pages 23–61
- [53] Wen W., Wu J-M. (2014) Nanomaterials via solution combustion synthesis: a step nearer to controllability. *RSC Adv.* Pages 58090-58100.
- [54] Ercolino G., Grodzka A., Grzybek G., Stelmachowski P., Specchia S., Kotarba A. (2017) The effect of the preparation method of Pd-doped cobalt spinel on the catalytic activity in methane oxidation under lean fuel conditions. *Top. Catal.* Pages 333–341.
- [55] Makhlof M. T., Abu-Zied B. M., Mansoure T. H. (2013) Direct fabrication of cobalt oxide nanoparticles employing sucrose as a combustion fuel. *J. Nanoparticles.* Pages 384350–384357.
- [56] Hadjiev V. G., Iliev M. N., Vergilov I. V. (1988) The Raman spectra of  $\text{Co}_3\text{O}_4$ . *J. Phys. C. Solid State Phys.* Pages 199–201.
- [57] Hagelin-Weaver H. A. E., Hoflund G. B., Minahan D. M., Salaita G. N. (2004) Electronenergy loss spectroscopic investigation of Co metal, CoO, and  $\text{Co}_3\text{O}_4$  before and after  $\text{Ar}^+$  bombardment. *Appl. Surf. Sci.* Pages 420–448.
- [58] Zhou T., Zhang T., Zhang R., Lou Z., Deng J., Wang L. (2017) Ultrahigh-sensitive sensing platform based on p-type dumbbell-like  $\text{Co}_3\text{O}_4$  network. *Appl. Surf. Sci.* Pages 951-956.
- [59] Ercolino G., Stelmachowski P., Grzybek G., Kotarba A., Specchia S. (2017) Optimization of Pd catalysts supported on  $\text{Co}_3\text{O}_4$  for low-temperature lean combustion of residual methane. *Appl. Catal. B Environ.* Pages 712–725.
- [60] Zasada F., Piskorz W., Cristol S., Paul J.-F., Kotarba A., Sojka Z. (2010) Periodic density functional theory and atomistic thermodynamic studies of cobalt spinel nanocrystals in wet environment: Molecular interpretation of water adsorption equilibria. *J. Phys. Chem. C.* Pages 22245–22253.
- [61] Wicker S., Großmann K., Bârsan N., Weimar U. (2013)  $\text{Co}_3\text{O}_4$  - A systematic investigation of catalytic and gas sensing performance under variation of

temperature, humidity, test gas and test gas concentration. *Sens. Actuat. B.* Pages 644-650.

[62] Lin Y., Kan K., Song W., Zhang G., Dang L., Xie Y., Shen P., Li L., Shi K. (2015) Controllable synthesis of Co<sub>3</sub>O<sub>4</sub>/polyethyleneimine-carbon nanotubes nanocomposites for CO and NH<sub>3</sub> gas sensing at room temperature. *J. Alloy. Compd.* Pages 187-196.

[63] Li Z., Lin Z., Wang N., Wang J., Liu W., Sun K., Fu Y. Q., Wang Z. (2016) High precision NH<sub>3</sub> sensing using network nano-sheet Co<sub>3</sub>O<sub>4</sub> arrays-based sensor at room temperature. *Sens. Actuat. B.* Pages 222–231.

[64] Air quality in Europe – EEA Report No 4/2012, 104 pp., ISBN 978-92-9213-328-3.

[65] World Health Organization, (2005) Regional Office for Europe, Copenhagen, Denmark, Nitrogen dioxides Chapter 12, Global update, 2005.

[66] Altshuller A. P. (1956) Thermodynamic considerations in the interactions of nitrogen oxides and oxy-acids in the atmosphere. *J. Air Poll. Control Ass.*, Pages 97-100.

[67] <https://www.desktopclass.com/health-care/pollutants-effects-environment.html> (Visited on 25th of February 2019).

[68] U.S. EPA. Integrated science assessment for oxides of nitrogen – health criteria (2016 Final Report). U.S. Environmental Protection Agency, Washington, DC, EPA/600/R-15/068, 2016.

[69] Toxnet Nitrogen dioxide: Human Health Effects (Visted on 25<sup>th</sup> of February 2019).

[70] Hansel N. N., Breyse P. N., McCormack M. C., Matsui E. C., Curtin-Brosnan J., Williams D. A. L., Moore J. L., Cuhnan J. L., Diette G. B. (2016) A longitudinal study of indoor nitrogen dioxide levels and respiratory symptoms in inner-city children with asthma. *Environ. Health Perspect.* Pages 1428–1432.

[71] The European environment state and outlook 2010, European Environment Agency (<http://www.eea.europa.eu/soer>, visited on 23th of February 2019).

[72] Air pollution in Europe 1990-2004, EU air quality directive 2001/81/CE.

[73] Ushio Y., Miyayama M., Yanagida H. (1994) Effects of interface states on gas sensing properties of a CuO/ZnO thin-film heterojunction, *Sens. Actuat. B.* Pages 221-226.

[74] Wiberg E., Holleman A. F. (2001). *Inorganic Chemistry*. Elsevier. ISBN 978-0-12-352651-9

[75] <https://whatiszincoxide.weebly.com/structure.html> (Visited on 18th of February 2019).

[76] Özgür Ü., Alivov Y. I., Liu C., Teke A., Reshchikov M., Dogan S., Avrutin V., Cho S.-J. Morkoç H. (2005) A comprehensive review of ZnO materials and devices, *J. Appl. Phys.* Pages 041301.

[77] Hernandezbattez A, Gonzalez R., Viesca J., Fernandez J., Diazfernandez J., MacHado A., Chou R., Riba J. (2008). CuO, ZrO<sub>2</sub> and ZnO nanoparticles as antiwear additive in oil lubricants. *Wear.* Pages 422–428.



- [78] De Liedekerke M. (2006) 2.3. Zinc oxide (zinc white): pigments, inorganic, 1 in Ullmann's Encyclopedia of Industrial Chemistry. Wiley-VCH, Weinheim.
- [79] Rai P., Kim Y.-S., Song H.-M, Song M.-K., Yu Y.-T. (2012) The role of gold catalyst on the sensing behavior of ZnO nanorods for CO and NO<sub>2</sub> gases, *Sens. Actuat. B*. Pages 133–142.
- [80] Wang Z. L. (2008) Splendid one-dimensional nanostructures of zinc oxide: a new nanomaterial family for nanotechnology, *ACS Nano*. Pages 1987–1992.
- [81] Zheng J., Jiang Z.-Y., Kuang Q., Xie Z.-X., Huang R.-B., Zheng L.-S. (2009) Shape-controlled fabrication of porous ZnO architectures and their photocatalytic properties, *J. Solid State Chem*. Pages 115–121.
- [82] Kundu S., Nithyanantham U. (2014) DNA-mediated fast synthesis of shape-selective ZnO nanostructures and their potential applications in catalysis and dye-sensitized solar cells, *Ind. Eng. Chem. Res*. Pages 13667–13679.
- [83] Ganesh R. S., Durgadevi E., Navaneethan M., Patil V. L., Ponnusamy S., Muthamizhchelvan C. et al. (2017) Low temperature ammonia gas sensor based on Mn-doped ZnO nanoparticle decorated microspheres, *J. Alloys Compd*. Pages 182–190.
- [84] Das M., Sarkar D. (2017) One-pot synthesis of zinc oxide-polyaniline nanocomposite for fabrication of efficient room temperature ammonia gas sensor, *Ceram. Int*. Pages 11123–11131.
- [85] Patil P., Gaikwad G., Patil D. R., Naik J. (2016) Synthesis of 1-D ZnO nanorods and polypyrrole/1-D ZnO nanocomposites for photocatalysis and gas sensor applications, *Bull. Mater. Sci*. Pages 655–665.
- [86] Zhu L., Zeng W. (2017) A novel coral rock-like ZnO and its gas sensing, *Mater. Lett*. Pages 244–246.
- [87] Zhu L., Li Y., Zeng W. (2018) Hydrothermal synthesis of hierarchical flower-like ZnO nanostructure and its enhanced ethanol gas-sensing properties, *Appl. Surf. Sci*. Pages 281–287.
- [88] Liu X., Sun J., Zhang X. (2015) Novel 3D graphene aerogel-ZnO composites as efficient detection for NO<sub>2</sub> at room temperature, *Sens. Actuat. B*. Pages 220–226.
- [89] Hosseini Z. S., Zad A. I., Mortezaali A. (2015) Room temperature H<sub>2</sub>S gas sensor based on rather aligned ZnO nanorods with flower-like structures, *Sens. Actuat. B*. Pages 865–871.
- [90] Zhu L., Zeng W. (2017) Room-temperature gas sensing of ZnO-based gas sensor: A review. *Sens. Actuat. A* Pages 242–261.
- [91] Tien L. C., Sadik P. W., Norton D. P., Voss L. F., Pearton S. J., Wang H. T., Kang B. S., Ren F., Jun J. et al. (2005). Hydrogen sensing at room temperature with Pt-coated ZnO thin films and nanorods. *Appl. Phys. Lett*. Pages 222106.
- [92] Sinha M., Mahapatra R., Mondal B., Maruyama T., Ghosh R. (2016) Ultrafast and reversible gas-sensing properties of ZnO nanowire arrays grown by hydrothermal technique, *J. Phys. Chem*. Pages 3019–3025.
- [93] Tesfamichael T., Cetin C., Piloto C., Arita M., Bell J. (2015) The effect of pressure and W-doping on the properties of ZnO thin films for NO<sub>2</sub> gas sensing, *Appl. Surf. Sci*. Pages 728–734.

- [94] Zak A. K., Majid W. H. A. (2013) Mahmoudian M. R., Darroudi M., Yousefi R. Starch-stabilized synthesis of ZnO nanopowders at low temperature and optical properties study. *Adv. Powd. Tech.* Pages 618–624.
- [95] Varma A., Mukasyan A. S., Rogachev A. S., Manujyan K. V. (2016) Solution combustion synthesis of nanoscale materials, *Chem. Rev.* Pages 14493-14586.
- [96] Wen W., Wu J.-M. (2014) Materials via solution combustion synthesis: a step near to controllability, *RSC Adv.* Pages 58090-58100.
- [97] Conkling J. A., Mocella C. J. (2011) Chapter 2: Basic chemical principles, in *Chemistry of pyrotechnics: basic principles and theory*, second edition, CRC Press Taylor and Francis group. Pages 7-57.
- [98] Pugliese D., Bella F., Cauda V., Lamberti A., Sacco A., Tresso E., Bianco S. (2013) A chemometric approach for the sensitization procedure of ZnO flowerlike microstructures for dye-sensitized solar cells. *ACS Appl. Mater. Interf.* Pages 11288-11295.
- [99] Korotcenkov G., Brinzari V., Cho B. K. (2017) In<sub>2</sub>O<sub>3</sub>- and SnO<sub>2</sub>-based ozone sensors: design and characterization. *Critical Reviews in Solid State and Materials Sciences* Pages 83-132.
- [100] Sonker R. K., Sabhajeet S. R., Singh S., Yadav B. C. (2015) Synthesis of ZnO nanopetals and its application as NO<sub>2</sub> gas sensor, *Mater. Lett.* Pages 189–191.
- [101] Yu L., Guo F., Liu S., Yang B., Jiang Y., Qi L., Fan X. (2016) Both oxygen vacancies defects and porosity facilitated NO<sub>2</sub> gas sensing response in 2D ZnO nanowalls at room temperature, *J. Alloys Compd.* Pages 352–356.
- [102] Wang J., Li X., Xia Y., Komarneni S., Chen H., Xu J. et al. (2016) Hierarchical ZnO nanosheet-nanorod architectures for fabrication of poly(3-hexylthiophene)/ZnO hybrid NO<sub>2</sub> sensor, *ACS Appl. Mater. Interface.* Pages 8600–8607.
- [103] Öztürk S., Kılınç N., Öztürk Z. Z. (2013) Fabrication of ZnO nanorods for NO<sub>2</sub> sensor applications: Effect of dimensions and electrode position. *J. Alloys Compd.* Pages 196–201.
- [104] Patil V. L., Vanalakara S. A., Patil P. S., Kim J. H. (2017) Fabrication of nanostructured ZnO thin films based NO<sub>2</sub> gas sensor via SILAR technique. *Sens. Actuat. B.* Pages 1185–1193.
- [105] Hassan M., Afify A., Ataalla M., Milanese D., Tulliani J.-M. (2017) New ZnO-based glass ceramic sensor for H<sub>2</sub> and NO<sub>2</sub> detection. *Sensors* Pages 2538;
- [106] Bârsan N., Weimar U. (2001) Conduction model of metal oxide gas sensors. *J. Electroceram.* Pages 143–167.
- [107] Xue X., Nie Y., He B., Xing L., Zhang Y., Wang Z. L. (2013) Surface free-carrier screening effect on the output of a ZnO nanowire nanogenerator and its potential as a self-powered active gas sensor. *Nanotech.* Pages 225501.
- [108] Wang P., Fu Y., Yu B., Zhao Y., Xing L., Xue X. (2015) Realizing room-temperature self-powered ethanol sensing of ZnO nanowire arrays by combining their piezoelectric, photoelectric and gas sensing characteristics. *J. Mater. Chem. A.* Pages 3529–3535
- [109] Berger O., Hoffmann T., Fischer W.-J., Melev V. (2003) Influence of microstructure of tungsten oxide thin films on their general performance as ozone

and NO<sub>x</sub> gas sensor. In *Smart Sensors, Actuators, and MEMS, Proceedings of the Microtechnologies for the New Millennium*, Maspalomas, Gran Canaria, Canary Islands, Spain, Chiao, J.-C., Varadan, V.K., Cané, C., Eds.; Society of Photo-Optical Instrumentation Engineers (SPIE): Washington, DC, USA, 2003. Pages 870–881.

[110] Chiorino A., Ghiotti G., Prinetto F., Carotta M.C., Gnani D., Martinelli G. (1999) Preparation and characterization of SnO<sub>2</sub> and MoO<sub>x</sub>-SnO<sub>2</sub> nanosized powders for thick films gas sensors. *Sens. Actuat. B*. Pages 338–349.

# Appendix A

## Abbreviations

AC-ZnO	HT-ZnO
Zinc oxide synthetized by auto- combustion sol-gel route	Zinc oxide synthetized by hydrothermal route

# General Conclusions

In this PhD thesis, different solutions for ozone environmental monitoring were presented. The ozone concentration in the troposphere is a huge issue because of its dangerous effects on the human health. The analytical techniques present in the market are expensive and they require technicians able to use the proper analytical instrumentation. For this reason, reserachers's interest on chemical sensors is growing. Chemical sensors possess peculiar properties such as low cost, great reliability, the possibility to reuse them and to integrate them in portable electronics. They must fullfull requirement such as high sensitivity, long term stability and selectivity for the target gas. For this reason, during this thesis, novel ceramics and carbon-based materials (also produced from biochar) were proposed for ozone and its main interences monitoring: ammonia, humidity and nitrogen dioxide. A deep understandandng of the material properties in terms of morphology, crystallite and agglomeration size, presence of defects and electronic states was achieved. Those characteristics were correlated with the observed sensing phenomena. In the future, it will be possible to discriminate the contribution due to ozone in a real environment by means of an array of the proposed chemical gas sensors.

# List of publications

## Refereed Journal Articles

- D. Ziegler, A. Marchisio, G. Ercolino, S. Specchia, J. M. Tulliani, Ammonia selective sensors based on cobalt spinel prepared by combustion synthesis. In Solid State Ionics 337 (2019) 91-100. <https://doi.org/10.1016/j.ssi.2019.03.026>
- J. M. Tulliani, B. Inserra, D. Ziegler, Carbon-based materials for humidity sensing: a short review. In Micromachines 10 (2019) 232. <https://doi.org/10.3390/mi10040232>
- P. Jagdale, D. Ziegler, M. Rovere, J. M. Tulliani, A. Tagliaferro, Waste coffee ground biochar: a material for humidity sensors. In Sensors 19 (2019) 801 [doi https://doi.org/10.3390/s19040801](https://doi.org/10.3390/s19040801)
- D. Ziegler, A. Marchisio, L. Montanaro, P. Palmero, J.M. Tulliani, Barium hexaferrite thick-films for ozone detection at low temperature. In Solid state ionics 320 (2018) 24-32 [doi 10.1016/j.ssi.2018.02.028](https://doi.org/10.1016/j.ssi.2018.02.028)
- D. Ziegler, P. Palmero, M. Giorcelli, A. Tagliaferro, J.M. Tulliani, Biochars as innovative humidity sensing materials in Chemosensors 5 (2017) 1-16. [doi 10.3390/chemosensors5040035](https://doi.org/10.3390/chemosensors5040035)
- D. Ziegler, A. Formia, J.M. Tulliani, P. Palmero, Environmentally-friendly dense and porous geopolymers using fly ash and rice husk ash as raw materials. In Materials 9 (2016) 466-486 [doi 10.3390/ma9060466](https://doi.org/10.3390/ma9060466)
- G. Gozzo, D. Ziegler, Teorie e pratiche per la ridefinizione di una nuova epoca geologica: l'antropocene. In Culture della sostenibilità 18 (2016) 174-186 [doi 10.7402/CDS.18.013](https://doi.org/10.7402/CDS.18.013).

## Referred Conference Articles

- D. Ziegler, P. Palmero, J.-M. Tulliani, A. Staerz, A. Oprea, U. Weimar and N. Barsan, Investigation of the film thickness influence on the sensor response of In<sub>2</sub>O<sub>3</sub>-based sensors for O<sub>3</sub> detection at low temperature and operando DRIFT study. Proceedings 14 (2019) 45 [doi:10.3390/proceedings2019014045](https://doi.org/10.3390/proceedings2019014045)
- D. Ziegler, P. Palmero, J.M. Tulliani, In<sub>2</sub>O<sub>3</sub> and WO<sub>3</sub>-doped In<sub>2</sub>O<sub>3</sub> hydrothermally synthesized as promising ozone sensitive materials in Workshop for Young Ceramists Promoting your research results, CNR Bologna 2018, 19-22 ISBN 978-88-7586-599-3
- D. Ziegler, E. Bekyarova, A. Marchisio, J.M. Tulliani, K. Naishadham, Highly selective ozone sensors based on functionalized carbon nanotubes in 2018 IEEE SENSORS [doi 10.1109/ICSENS.2018.8589868](https://doi.org/10.1109/ICSENS.2018.8589868)
- D. Ziegler, E. Bekyarova, G. Naishadham, P. Savi, A. Marchisio, J.M. Tulliani, K. Naishadham, Nanotechnology-based ozone sensors exploiting low-frequency impedance changes for detection in 17th International Meeting on Chemical Sensors - IMCS 2018, 740-741 [doi 10.5162/IMCS2018/P2EC.22](https://doi.org/10.5162/IMCS2018/P2EC.22)
- D. Ziegler, A. Marchisio, G. Ercolino, S. Specchia, J.M. Tulliani, Cobalt spinel via solution combustion synthesis as an ammonia sensing material in 17th International Meeting on Chemical Sensors - IMCS 2018, 555-556 [doi 10.5162/IMCS2018/P1GS.19](https://doi.org/10.5162/IMCS2018/P1GS.19)
- D. Ziegler; A. Marchisio; P. Palmero, J.-M. Tulliani, WO<sub>3</sub>-doped indium oxide thick films for ozone detection at low temperature in Proceedings 1 (2017) 1-5 [doi 10.3390/proceedings1040428](https://doi.org/10.3390/proceedings1040428).